INAUGURAL - DISSERTATION

zur

Erlangung der Doktorwürde

der

Naturwissenschaftlich-Mathematischen

Gesamtfakultät

der

Ruprecht-Karls-Universität

Heidelberg

Vorgelegt von

M. Sc. Anke Roiger

aus: München

Tag der mündlichen Prüfung: 27.10.2011

Biomass burning pollution in the summer time Arctic atmosphere:

Development and deployment of a novel airborne CI-ITMS instrument for PAN detection

Gutachter: Prof. Dr. Ulrich Platt

Prof. Dr. Frank Arnold

Abstract

The present work aims for a better understanding of the reactive nitrogen and ozone budgets of the Arctic summer atmosphere. Special focus is paid to the organic nitrogen compound PAN (**P**eroxy**a**cetyl **n**itrate), which as temporary reservoir species plays a key role especially during long-range transport of pollutants. For the first time, a chemical ionization - ion trap mass spectrometer (CI-ITMS) was equipped with an I^- ion source for the detection of PAN. The new FASTPEX (**Fast** Measurement of **Pe**rox**x**yacyl nitrates) instrument successfully was deployed aboard the research aircraft Falcon during POLARCAT - GRACE campaign (**Pol**ar Study using **A**ircraft, **R**emote Sensing, Surface Measurements and Models, of **C**limate, Chemistry, **A**erosols, and **T**ransport - **Gr**eenland **A**erosol and **C**hemistry **E**xperiment) in summer 2008, which was conducted within the framework of the International Polar Year (IPY) 2007 - 2009. Continuous in-flight calibrations were performed using a newly set-up isotopic PAN calibration source. An in-flight intercomparison during GRACE showed very good agreement between the PAN measurements of the new FASTPEX instrument and the PAN measurements aboard the research aircraft NASA DC8. The GRACE measurements revealed that the Arctic free troposphere in summer is heavily perturbed by aged inflow from the boreal fire regions of Canada and Siberia. PAN was found to be the dominant reactive nitrogen species at altitudes between ~ 4 and 9 km. While nitrogen oxide (NO) in the free troposphere was close to the detection limit of several pmol mol^{-1}, PAN was abundant at median mixing ratios of ~ 300 pmol mol^{-1}. Low photochemical ozone formation was observed in imported pollution plumes. This is the result of fast conversion of NO_x ($NO_x = NO + NO_2$) to PAN in young fire emissions, in combination with the high thermal stability of PAN during subsequent transport towards Greenland. A detailed case study provided first observational evidence of an efficient transport pathway for surface emissions into the lowermost stratosphere, which was previously suggested by model simulations. The anthropogenic pollution was detected by enhanced mixing ratios of PAN and CO above the tropopause. Air mass trajectory calculations showed that the Asian emissions were lifted within a warm conveyor belt (WCB) and reached the lowermost stratosphere within a few days after emission.

Kurzfassung

Die vorliegende Arbeit beschäftigt sich mit dem Budget von reaktivem Stickstoff und Ozon in der arktischen Atmosphäre im Sommer. Besonderer Fokus liegt hierbei auf der organischen Stickoxidkomponente PAN (**P**eroxy**a**cetyl **n**itrate), der als temporärer Reservoirverbindung besondere Bedeutung beim Ferntransport von verschmutzten Luftmassen zukommt. Für die PAN Messungen wurde ein Chemisches Ionisations - Ionenfallen Massenspektrometer (CI-ITMS) zum ersten Mal mit einer I^--Ionenquelle gekoppelt. Das neue FASTPEX System (**Fast** Measurement of **Pe**ro**x**yacyl nitrates) wurde dann im Rahmen der POLARCAT - GRACE Kampagne (**Pol**ar Study using **A**ircraft, **R**emote Sensing, Surface Measurements and Models, of **C**limate, Chemistry, **A**erosols, and **T**ransport - **Gr**eenland **A**erosol and **C**hemistry **E**xperiment) erfolgreich auf dem Forschungsflugzeug Falcon eingesetzt, die im Rahmen des International Polar Year (IPY) 2007 - 2009 durchgeführt wurde. Mithilfe einer neu aufgebauten isotopischen PAN Kalibrationsquelle wurden permanente In-Flug Kalibrationen durchgeführt. Ein Vergleichsflug während der GRACE Messkampagne zeigte sehr gute Übereinstimmung zwischen den PAN Messungen des neuen FASTPEX Systems und den PAN Messungen auf dem Forschungsflugzeug NASA DC8. Die GRACE Messungen zeigten dass die arktische freie Troposphäre stark durch den Eintrag von gealterten borealen Waldbrandemissionen aus Kanada und Sibirien beeinflusst war. PAN war in Höhen zwischen 4 und 9 km die dominierende reaktive Stickstoff verbindung. Während Stickstoffmonoxid (NO) in der freien Troposphäre nur im Bereich weniger $\mathrm{pmol\,mol^{-1}}$ vorhanden war, wurden mittlere PAN Mischungsverhältnisse von $\sim 300\,\mathrm{pmol\,mol^{-1}}$ nachgewiesen. Die Messungen in den importierten Waldbrandfahnen deuten auf nur geringe photochemische Ozonbildung hin. Ursache hierfür sind die schnelle Umwandlung von NO_x ($NO_x = NO + NO_2$) in PAN in den frischen Waldbrandemissionen, in Kombination mit der hohen thermischen Stabilität von PAN während des folgenden Ferntransports nach Grönland. Eine GRACE-Fallstudie bestätigte zum ersten Mal experimentell einen effizienten Transportweg von Bodenemissionen in die untere Stratosphäre, welcher bisher nur von Modellrechnungen gezeigt wurde. Die anthropogene Verschmutzung aus Asien wurde durch erhöhte Mischungsverhältnisse von PAN und Kohlenmonoxid überhalb der Tropopause detektiert. Mithilfe von Trajektorienrechnungen konnte nachgewiesen werden dass die asiatischen Emissionen in einem warm conveyor belt (WCB) gehoben wurden und innerhalb weniger Tage in die untere Stratosphäre gelangten.

Contents

Chapter 1

Introduction

The atmosphere contains numerous trace species, aerosols and trace gases, which have a strong influence on atmospheric chemistry, the Earth´s energy balance and human health. One of the key species influencing chemical reactions in the atmosphere is ozone. In the stratosphere, where ozone mixing ratios are highest, it shields the biosphere from harmful UV radiation of the sun. In the troposphere, ozone strongly influences the self-cleansing capacity of the atmosphere and acts as a greenhouse gas. At the surface, ozone damages plants and may lead to serious health problems by affecting lung tissues or aggravating the effects of asthma. Another example for important trace species are aerosol particles: They influence the transmission of radiation in the troposphere, directly by absorbing and scattering light, and indirectly by acting as cloud condensation nuclei hereby influencing clouds and precipitation. Due to their short-lived nature in the troposphere, their impact is highly variable both in the temporal and spatial domain. Trace gases such as carbon dioxide or methane also interact with solar and terrestrial radiation, but due to their long atmospheric lifetime they influence the energy balance more globally, because they become well distributed within the troposphere. Their continuous increase during the last decades because of rising anthropogenic emissions has led to a modification of the radiation-energy balance of the earth-atmosphere system, known as global warming. In general, the abundance of an atmospheric trace species and its residence or lifetime are a consequence of the interplay between its source strength and sinks. Sinks can be manifold: chemical reactions, deposition to the surface or particles, removal in clouds or precipitation.

The present work adresses the topic of nitrogen oxides in the polar atmosphere. Nitrogen oxides also belong to the key species affecting atmospheric chemistry, both in the trosposphere and stratosphere, and have major anthropogenic and natural sources. Nitrogen oxides govern the cycling processes between the very important OH and HO_2 radicals and as a result, directly influence the oxidation capacity of the atmosphere. They are also critical catalysts in the photochemical production of tropospheric ozone and therefore have a strong impact on ozone and thus, the radiative budget of the atmosphere.

Nitrogen oxides are emitted into the atmosphere mainly in the form of nitrogen monoxide (NO), which is released by different sources such as industrial (combustion) processes, traffic, biomass burning and lightning. Under daylight conditions, NO is rapidly oxidized by ozone to NO_2 (typically

within minutes). NO_2 in turn underlies almost equally rapid photolysis, forming again NO and ozone. This photochemical cycle closely couples NO and NO_2 on short time-scales, which makes it useful to treat both compounds together in the more conserved form of NO_x ($NO_x = NO + NO_2$). However, on timescales of hours to days, atmospheric oxidation processes lead to the formation of other reactive nitrogen species, which are usually referred to as NO_y compounds ($NO_y = NO_x + HNO_3 + PAN + HONO + NO_3 + N_2O_5$..).

The major oxidation products of NO_x in the troposphere are nitric acid (HNO_3) and the organic nitrogen compound PAN (**P**eroxy**a**cetyl **n**itrate, $CH_3C(O)O_2NO_2$), which both have rather different fates in the atmosphere. HNO_3 is a polar molecule and therefore highly water-soluble. It can be efficiently removed by cloud processes and is also readily deposited on surfaces. In the presence of NH_3, nitric acid may form ammonium nitrate aerosol particles (NH_4NO_3). HNO_3 therefore acts as a terminal sink for nitrogen oxides. In contrast, PAN is only a temporary reservoir for NO_x.

PAN is not emitted directly into the atmosphere. It is produced through the same complex photochemistry that forms tropospheric ozone, which is the photochemical oxidation of VOCs (volatile organic compounds) in the presence of nitrogen oxides. PAN was first noted by Haagen-Smit (1950), who assumed the presence of a so far unknown compound "X" in the photochemical Los Angeles smog in the 1940s, being 10 to 50 times more phytotoxic than ozone. The exact chemical structure of this compound, PAN, however was identified only years later by using long-path infra-red techniques (Stephens et al., 1956a,b). Since then PAN has been observed throughout the troposphere at mixing ratios ranging from several pmol mol^{-1} in remote regions to several nmol mol^{-1} close to pollution sources (Roberts et al., 2002, 2004; Singh et al., 2007). Also higher PAN homologues, e.g. PPN (peroxypropionyl nitrate, $CH_3CH_2C(O)O_2NO_2$) and MPAN (peroxymethacryloyl nitrate, $CH_3CCH_2C(O)O_2NO_2$), have been observed in the atmosphere, often at mixing ratios of roughly an order of magnitude lower than that of PAN (Roberts et al., 2004, 2007; Wolfe et al., 2007; LaFranchi et al., 2009). These homologues are formed through similar chemistry, but have different parent VOCs. **Figure 1.1** shows the molecular structure of PAN, the simplest and most abundant member of the PAN family. It contains both an organic ($CH_3C(O)O_2$) and a nitrogen group (NO_2).

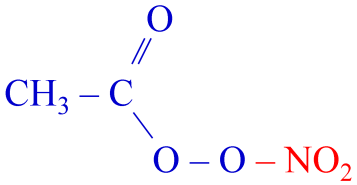

Figure 1.1: *Molecular structure of PAN (Peroxyacetyl nitrate).*

PAN is not very soluble in water and does not act as a precursor for aerosol particles (Roberts, 2005). Since photolysis of PAN is slow, it has a long lifetime of several weeks to months in the cold mid- and upper troposphere (Talukdar et al., 1995). However, it underlies rapid thermolysis at the warmer temperatures of the lower troposphere, hereby releasing NO_2 again ($CH_3C(O)O_2NO_2 \rightarrow CH_3C(O)O_2 + NO_2$). The temperature-dependent lifetime of PAN leads to the most important atmospheric implication of PAN formation: the temporary conservation of NO_x in PAN may delay and, as a result, dislocate ozone production in pollution plumes to regions further downstream. Singh and

Hanst (1981) were the first to propose that NO_x released from PAN thermolysis in subsiding air masses may promote ozone production in remote regions, probably hundreds of kilometers away from the location where PAN originally was formed. Ozone formation induced by PAN dissociation now is a well-accepted mechanism, and was observed in-situ in a number of aircraft and surface-based measurements (Real et al., 2007; Pfister et al., 2006; Lapina et al., 2006; Hudman et al., 2004; Zhang et al., 2008; Val Martín et al., 2006).

The investigation of the atmospheric reactive nitrogen budget and its coupling to other trace gases such as ozone is since many years one of the main research fields of the Institut für Physik der Atmosphäre of the Deutsches Zentrum für Luft- und Raumfahrt (DLR), in short DLR-IPA. Several high precision instruments for the measurement of different nitrogen oxide species were developed and are primarily operated aboard different research aircraft such as the DLR Falcon, the high altitude research aircraft Geophysica, or commercial in-service aircraft (CARIBIC[1]). The nitrogen compounds NO, NO_2, HNO_3 as well as total reactive nitrogen (NO_y) are measured down to very low concentrations using a combination of chemiluminescence detectors with different kind of converters and filters (Feigl, 1998; Ziereis et al., 2004). However, for a detailed investigation of the reactive nitrogen budget, fast and high-accuracy measurements of PAN were so far missing. Also for studying long-range transport of pollutants, PAN measurements are essential. Intercontinental transport of pollutants is a young research field in atmospheric science, and is, in the context of understanding the effects of natural and anthropogenic contributions to the atmospheric nitrogen budget, also a major research topic of the DLR-IPA (Huntrieser et al., 2005; Real et al., 2007, 2008; Fiedler et al., 2009). It was therefore one of the initial aims of this work to establish a suitable measurement method for PAN at DLR-IPA.

The most established technique for measurements of PAN and its homologues is gas chromatography with an electron capture detector (GC-ECD). It benefits from good characterization and provides low detection limits of a few $\mathrm{pmol\,mol^{-1}}$ (Singh and Salas, 1983; Williams et al., 2000; Flocke et al., 2005b). However, the time resolution in the range of several minutes is too low for airborne measurements since time resolution is equivalent to spatial resolution: aircraft cover distances on the order of ten kilometers per minute. A measurement technique which combines a high time resolution ($\sim$1 s) with typically low detection limits (several $\mathrm{pmol\,mol^{-1}}$) is the CIMS technique (Chemical Ionization Mass Spectrometry). CIMS was originally introduced in atmospheric research by Arnold et al. (1978) and is now established as a powerful method for the measurement of a series of different trace gases like SO_2, H_2SO_4, HNO_3, HONO, HO_2NO_2, N_2O_5 (Arnold and Fabian, 1980; Arnold and Hauck, 1985; Neuman et al., 2000; Nowak et al., 2002; Thornton et al., 2002; Hanke et al., 2003; Aufmhoff et al., 2011). CIMS is based on the selective ionization of the desired trace gas in the sample air followed by detection of precursor and characteristic product ions inside a mass spectrometer. The CIMS technique offers high versatility, however, the accuracy might be influenced by cross-sensitivities to other trace gases, such as for example atmospheric water vapor. For this reason, continuous in-flight calibrations are highly desirable. The most elegant way is to use an isotopically labelled standard for an on-line calibration throughout the entire flight.

[1]Civil Aircraft for the Regular Investigation of the atmosphere Based on an Instrument Container

For airborne measurements of PAN, two different CIMS methods have been deployed in recent years. Proton Transfer Mass Spectrometry (PTR-MS) using protonated PAN as product ion (Holzinger et al., 2005), and a thermal dissociation (TD-CIMS) technique using I^- as reagent ions (Slusher et al., 2004). While the PTR-MS technique might suffer from an interference from peroxyacetic acid (de Gouw et al., 2003), the use of the I^- reagent ions has been well established (Flocke et al., 2005a; Neuman et al., 2006; Alvarado et al., 2010). All of these measurements were performed using CIMS instruments equipped with linear quadrupole mass spectrometers (LQMS).

In the last few years, the CIMS technique using an ion trap mass spectrometer (CI-ITMS) was developed and deployed for the measurement of a series of trace gases such as e. g. SO_2, H_2SO_4, CH_3COCH_3 and HNO_3 (Kiendler et al., 2000; Speidel et al., 2007; Fiedler et al., 2009; Aufmhoff et al., 2011) in a close collaboration between the DLR-IPA and the MPI-K (Max-Planck Institut für Kernphysik). Ion trap mass spectrometers (ITMS) offer several advantages compared to often employed linear quadrupole mass spectrometers (LQMS).

Based on these previous developments, it became evident that this work had to pursue the modification of one of the existing CI-ITMS systems for fast and sensitive measurements of PAN. In order to provide measurements with high accuracy, an isotopically labelled PAN calibration source had to be integrated into the new set-up.

This modified CI-ITMS instrument, eventually called FASTPEX (**Fast** Measurement of **Pe**rox**y**acyl nitrates), had the opportunity to be deployed for the first time aboard the Falcon during the POLARCAT - GRACE campaign (**Pol**ar Study using **A**ircraft, **R**emote Sensing, Surface Measurements and Models of **C**limate, Chemistry, **A**erosols, and **T**ransport - **Gr**eenland **A**erosol and **C**hemistry **E**xperiment). POLARCAT was one of the core projects of the International Polar Year 2007 - 2008, to which the GRACE campaign was a major contribution by DLR. The GRACE field activity was conducted in July 2008 with the DLR Falcon operating out of Kangerlussuaq at the west coast of Greenland. The project aimed to study the effects of pollution transport on the chemical composition of the troposphere and lowermost stratosphere in the summer time Arctic.

This topic is of particular interest since atmospheric research has recently returned its focus to the Arctic. Climate change was observed to proceed fastest at high latitudes (Trenberth et al., 2007), while global-circulation-models (GCMs) predict especially strong 21st-century warming in the Arctic (Christensen et al., 2007). Air pollution may accelerate Arctic warming due to changes in local radiative forcing induced by tropospheric ozone and aerosols (Law and Stohl, 2007). There are only a few local pollution sources at high northern altitudes, but it is well-known that the Arctic is perturbed by the inflow from the industrialized mid-latitudes. Long-range transport of anthropogenic pollutants into the Arctic is known to be most efficient in winter, especially in the lower troposphere (Klonecki et al., 2003; Stohl, 2006; Shindell et al., 2008). Low temperatures lead to a strong stratification, which reduces removal processes such as wet and dry deposition. The resulting long aerosol lifetimes lead to the formation of haze layers and decreasing visibility, known as the "Arctic haze" phenomenon, which occurs often in winter/spring (Law and Stohl, 2007; Quinn et al., 2007).

In the mid- and especially the upper troposphere however, models suggest that the anthropogenic influence is stronger during summer (Shindell et al., 2008). In addition, summer is also the boreal fire season, and emissions released by biomass burning provide a large additional source of pollutants, which at least partly will underly transport to even higher latitudes. Forest fires are in general episodic in nature. Timing, location and duration of fires underly strong inter-annual variability (Kasischke et al., 2005; van der Werf et al., 2010). However, a general increase in burning areas is observed, which is attributed to global warming (Stocks et al., 1998; Lavoué et al., 2000; Soja et al., 2007) and which is expected to continue in future. The composition of the emissions vary with fuel type and burning conditions (Yokelson et al., 1996; Andreae and Merlet, 2001), but observations indicate that the typically high VOC/NO_x emission ratios of boreal fires promote rapid conversion of NO_x into PAN (Jacob et al., 1992; Alvarado et al., 2010). Subsequent transport of PAN into remote regions such as the Arctic may strongly impact the reactive nitrogen and ozone budget downstream of the fire regions.

It is striking that although the Arctic is a particular vulnerable region for climate change, the chemical composition of the Arctic atmosphere is not well documented. Present knowledge of Arctic air chemistry has mostly evolved from surface observations, whereas measurements in the troposphere are sparse, especially during summer (Jacob et al., 2010). The ABLE 3-A[2] and B campaigns in summer 1988 showed that the Arctic atmospheric composition was strongly modified by forest fires, industrial emissions and stratospheric inputs (Wofsy et al., 1992). Interestingly, most nitrogen was tied up in the form of PAN (Singh et al., 1992b), and ozone formation in polluted air masses was found to be moderate to low (Sandholm et al., 1992). However, the ABLE measurements were limited both by a small scientific payload and by the maximum flight altitude of ~ 6 km.

The POLARCAT-GRACE project provided an unprecedented opportunity to investigate chemical processes and pollution transport into the Arctic during summer season. Using the aircraft measurements of PAN, NO, NO_y and other tracers (CO, O_3, CO_2), this thesis aims to address some of the main objectives of the campaign: One primary goal of GRACE was to analyze transport patterns of biomass burning and anthropogenic emissions into the Arctic using in-situ observations, and to evaluate analyses from transport models. A further objective was to study the chemical evolution of pollution plumes during their transport to Greenland. Of special interest is the potential for photochemical ozone production in polluted air masses, in order to understand the pollution influence on the radiative budget of the Arctic troposphere. For this, measurements of PAN are essential, because PAN acts as a temporary reservoir for nitrogen oxides, which are catalysts in the formation of ozone. Furthermore, the measurements during GRACE are also highly valuable for the validation of chemistry-transport models (CTMs). Recent model assessments indicate poor agreement between CTMs and surface observations, and a large spread between different models (Shindell et al., 2008). This in turn suggests limited ability to predict Arctic climate responses to emission changes, which already are on-going in the industrialized mid-latitudes and in the boreal fire regions.

The GRACE field campaign provided also the opportunity to study the influence of pollution transport into the extra-tropical tropopause or UTLS (upper troposphere/lower stratosphere) region.

[2] **A**tmospheric **B**oundary **L**ayer **E**xperiments

Chemical processes controlling the budget of ozone and radical species in the UTLS are not yet well understood, but it is clear that perturbations to the trace gas distribution in this region can lead to direct forcing of climate. Of particular interest therefore are processes which may efficiently transport surface emissions into the tropopause region, especially if they act on such short timescales that atmospheric removal processes are not fully efficient. In recent years, synoptic scale up-lift of pollutants within warm conveyor belts (WCBs) has gained increasing scientific attention (Stohl and Trickl, 1999; Cooper et al., 2002, 2004). Transport climatologies suggest that polluted air masses from the industrialized eastern seaboards of North America and Asia show an enhanced probability to reach the tropopause region, and most important, a few percent of the WCB trajectories even enter the lowermost stratosphere (Stohl, 2001; Wild and Akimoto, 2001; Wernli and Bourqui, 2002). These results however have not yet been verified by in-situ measurements. Therefore, another main objective of this work was to look for possible observational evidence wether pollution plumes lifted within WCBs may enter the lower stratosphere.

In summary, this work aims to answer the following scientific questions:

- Is the CI-ITMS technique well suited to accurately measure PAN in the Arctic troposphere and lower stratosphere?
- How strong is the summer time Arctic atmosphere perturbed by long-range transport of pollutants, and what are the main source regions of Arctic air pollution in summer?
- Which is the dominant influence on the chemical composition of the Arctic troposphere during the summer season - biomass burning or anthropogenic pollution?
- How is the reactive nitrogen budget of the Arctic atmosphere affected by the imported emissions?
- Does strong photochemical ozone production take place in pollution plumes, and what is the role of PAN?
- And finally, is there observational evidence that a polluted warm conveyor belt may reach the polar lowermost stratosphere within a few days?

The present work is structured as follows: **Chapter 2** summarizes theoretical background to tropospheric NO_x-O_3 chemistry and discusses present knowledge of long-range transport of pollutants. The CIMS technique is introduced in **Chapter 3**. **Chapter 4** describes the set-up and characterization of the new FASTPEX instrument, as a result of this work. This part is followed by a discussion of the performance of the FASTPEX instrument during GRACE campaign. **Chapter 5** addresses scientific results from the GRACE project. Special focus is paid on the distribution of PAN in the Arctic and its influence of the ozone production potential in pollution plumes. **Chapter 6** focuses on a case study which describes the efficient up-ward transport of Asian surface emission within a warm conveyor belt using in-situ observations and trajectory calculations.

Parts of this work are published in:

Roiger, A., Aufmhoff, H., Stock, P., Arnold, F., and Schlager, H.: An aircraft-borne chemical ionization - ion trap mass spectrometer (CI-ITMS) for fast PAN and PPN measurements, Atmos. Meas. Tech., 4, 173-188, doi:10.5194/amt-4-173-2011, 2011.

Roiger, A., Schlager, H., Schäfler, A., Huntrieser, H., Scheibe, M., Aufmhoff, H., Cooper, O. R., Sodemann, H., Stohl, A., Burkhart, J., Lazzara, M., Schiller, C., Law, K. S., and Arnold, F.: In-situ observation of Asian pollution transported into the Arctic lowermost stratosphere, Atmos. Chem. Phys. Discuss., 11, 16265-16310, doi:10.5194/acpd-11-16265-2011, 2011.

Chapter 2

Tropospheric chemistry and transport

This chapter provides theoretical background on chemical and dynamical processes relevant for the present thesis. The focus of this work is to study the impact of imported pollution on chemical processes in the Arctic summer atmosphere. One main aspect is to better understand the tropospheric ozone budget of the Arctic, which is closely coupled to the presence of nitrogen oxides. In order to understand the interplay between ozone and nitrogen oxides, the chapter starts with an introduction to tropospheric NO_x-O_3 chemistry in the remote atmosphere (2.1). It follows a presentation of the reactive nitrogen cycle (2.2.1) to illustrate photochemical processing of primary emitted NO_x in the troposphere. Special focus is paid to secondary formed PAN, which may serve as an temporary NO_x reservoir and influence chemistry far away from the region where it was formed (2.2.2). The second part of this chapter 2 focuses on the phenomenon of Arctic pollution. First of all main source regions are identified, which have the potential to influence the Arctic troposphere (2.3.1). During summer, these mainly include boreal forest fire emissions but also anthropogenic pollution from the industrial mid-latitudes. It follows a discussion about meteorological processes facilitating long-range transport (LRT) of pollutants (2.3.2) and a presentation of special meteorological conditions driving transport into the Arctic (2.3.3). During one GRACE (**Gr**eenland **A**erosol and **C**hemistry **E**xperiment) flight, relatively fresh surface emissions from Asia were sampled in the polar lowermost stratosphere. This chapter therefore closes with a short introduction to Stratosphere-Troposphere-Exchange (STE) processes (2.4).

2.1 Tropospheric NO_x-O_3 chemistry

Ozone is an important surface pollutant since it is toxic to human beings as well as to many species of plants. Tropospheric O_3 is a greenhouse gas with a radiative forcing RF[1] comparable to that of halocarbons. Due to the short-lived nature of O_3 in the troposphere, its effect on RF however may be much stronger on regional scales (Forster et al., 2007). Model studies suggest that an increase in tropospheric ozone has contributed to one third of the Arctic warming during winter and spring (Shindell et al., 2006). Ozone also plays a pivotal role in tropospheric chemistry. As an oxidizing agent and direct precursor of the extremely important OH radical, it largely controls the

[1] Radiative forcing is a measure of the influence a factor has in altering the balance of incoming and outgoing energy in the Earth-atmosphere system.

self-cleansing capacity of the atmosphere. The tropospheric ozone budget is influenced by several processes: input from the stratosphere, loss due to dry deposition as well as in-situ photochemical O_3 production/destruction. As will be discussed in the following, in-situ ozone formation and loss reactions are largely governed by the presence of nitrogen oxides (for more details see e. g. Seinfeld and Pandis (1998)).

After being emitted into the atmosphere, nitrogen monoxide (NO) rapidly reacts with O_3 to form NO_2:

$$NO + O_3 \rightarrow NO_2 + O_2 \,. \tag{2.1}$$

During daylight hours, the formed NO_2 underlies rapid photolysis:

$$NO_2 + h\nu \rightarrow NO + O(^3P) \quad \lambda \leq 410\,\text{nm} \tag{2.2}$$

The hereby produced $O(^3P)$ reacts with abundant oxygen reforming ozone again:

$$O_2 + O(^3P) \rightarrow O_3 \,. \tag{2.3}$$

If there were no other reactions taking place in the atmosphere, the reaction sequence 2.1 to 2.3 would have no net effect on the ozone concentration, i. e. O_3 would neither be formed nor destroyed. Ozone however is photolyzed at wavelengths of $\lambda \leq 320\,\text{nm}$, which is not only a sink for O_3, but initiates complex and widely branched oxidation cycles involving a series of radicals (Levy, 1971). In the presence of water vapor, photolysis of ozone is followed by the formation of the OH radical:

$$O_3 + h\nu \rightarrow O(^1D) + O_2 \quad \lambda \leq 320\,\text{nm} \tag{2.4a}$$

$$O(^1D) + M \rightarrow O(^3P) + M \,, \tag{2.4b}$$

$$O(^3P) + O_2 + M \rightarrow O_3 + M \,, \tag{2.4c}$$

$$O(^1D) + H_2O \rightarrow 2\ OH \,. \tag{2.4d}$$

The main part of the highly reactive photofragment $O(^1D)$ is collisionally deactivated by molecules M such as N_2 or O_2. $O(^3P)$ then rapidly recombines with molecular oxygen reforming ozone again. A small portion however ($\sim$1 - 10 % depending on e. g. water vapor) reacts with H_2O hereby producing OH.

The presence of the OH radical in the troposphere varies strongly on temporal and spatial scales. The globally weighted 24 h-average OH concentration is only in the range of $\sim 1 \times 10^6$ molecules cm^{-3} (e. g. Lawrence et al. (2001)), however, the OH radical is highly reactive and initializes the oxidation of nearly all species such as for example hydrocarbons, SO_2 or NO_2. The oxidation products subsequently can be removed from the atmosphere via dry or wet deposition. For this reason, OH often is termed as "cleaning agent" of the atmosphere. The degradation of hydrocarbons in turn influences the ozone concentration, and it is the concentration of nitrogen oxides which determines whether ozone hereby is photochemically formed or destroyed. This is exemplary illustrated in the following for the simplest carbon-containing species, carbon monoxide (CO).

In the remote troposphere NO mixing ratios are quite low (i. e. in the range of several few pmol mol^{-1}). The oxidation of CO to carbon dioxide (CO_2) thus leads to net ozone destruction:

$$\mathrm{CO + OH \rightarrow CO_2 + H\,,} \tag{2.5a}$$
$$\mathrm{H + O_2 \rightarrow HO_2\,,} \tag{2.5b}$$
$$\mathrm{HO_2 + O_3 \rightarrow OH + 2\,O_2\,,} \tag{2.5c}$$
$$\mathrm{net:\ CO + O_3 \rightarrow CO_2 + O_2\,.} \tag{2.5d}$$

The hydroperoxy radical HO_2 formed in reaction 2.5b is the second, less reactive member of the important HO_x family ($HO_x = OH + HO_2$). HO_2 reacts much faster with NO than with ozone (by a factor of $\sim$4400), which makes this reaction to become more important at sufficiently high NO levels. The subsequent photolysis of hereby formed NO_2 then leads to formation of O_3:

$$\begin{aligned}\mathrm{CO + OH} &\rightarrow \mathrm{CO_2 + H\,,}\\ \mathrm{H + O_2} &\rightarrow \mathrm{HO_2\,,}\\ \mathrm{HO_2 + NO} &\rightarrow \mathrm{OH + NO_2\,,} \qquad (2.6a)\\ \mathrm{NO_2 + h}\upsilon &\rightarrow \mathrm{NO + O\,,}\\ \mathrm{O + O_2} &\rightarrow \mathrm{O_3 + M\,,}\\ \mathrm{net:\ CO + 2\,O_2} &\rightarrow \mathrm{CO_2 + O_3\,.} \qquad (2.6b)\end{aligned}$$

The oxidation of methane (CH_4) follows a similar but more complex mechanism than the degradation of CO (e. g. Seinfeld and Pandis (1998)). Methane is the simplest alkane, and the principal hydrocarbon species in the background troposphere. Oxidation by OH will convert CH_4 via several reactions into formaldehyde (HCHO), which constitutes the first stable product in the oxidation sequence (having a lifetime of more than a few seconds). In this case, the concentration of NO decides whether O_3 photochemically is produced or not. At first, methane reacts with OH leading to the formation of methylperoxy radicals (CH_3O_2). At low NO_x conditions, CH_3O_2 will react with HO_2 hereby forming methylhydro peroxide (CH_3OOH). CH_3OOH may be processed via two different pathways, which are photolysis (2.7d to 2.7e), or reaction with OH (2.8a):

$$\mathrm{CH_4 + OH \rightarrow CH_3 + H_2O\,,} \tag{2.7a}$$
$$\mathrm{CH_3 + O_2 + M \rightarrow CH_3O_2 + M\,,} \tag{2.7b}$$
$$\mathrm{CH_3O_2 + HO_2 \rightarrow CH_3OOH + O_2\,,} \tag{2.7c}$$
$$\mathrm{CH_3OOH + h}\upsilon \mathrm{\rightarrow CH_3O + OH\,,} \tag{2.7d}$$
$$\mathrm{CH_3O + O_2 \rightarrow HCHO + HO_2\,,} \tag{2.7e}$$
$$\mathrm{net:\ CH_4 + O_2 \rightarrow HCHO + H_2O\,.} \tag{2.7f}$$

$$\begin{aligned}
\mathrm{CH_4 + OH \rightarrow CH_3 + H_2O}\,, \\
\mathrm{CH_3 + O_2 + M \rightarrow CH_3O_2 + M}\,, \\
\mathrm{CH_3O_2 + HO_2 \rightarrow CH_3OOH + O_2}\,, \\
\mathrm{CH_3OOH + OH \rightarrow HCHO + H_2O + OH}\,, \qquad (2.8a) \\
\text{net: } \mathrm{CH_4 + OH + HO_2 \rightarrow HCHO + 2H_2O}\,. \qquad (2.8b)
\end{aligned}$$

If NO however is present at large enough amounts (see also discussion below), the methylperoxy radicals may efficiently convert NO to NO_2, which finally will result in net ozone formation:

$$\begin{aligned}
\mathrm{CH_4 + OH \rightarrow CH_3 + H_2O}\,, \\
\mathrm{CH_3 + O_2 + M \rightarrow CH_3O_2 + M}\,, \\
\mathrm{CH_3O_2 + NO \rightarrow CH_3O + NO_2}\,, \qquad (2.9a) \\
\mathrm{CH_3O + O_2 \rightarrow HCHO + HO_2}\,, \\
\mathrm{HO_2 + NO \rightarrow OH + NO_2}\,, \\
\mathrm{NO_2 + h\nu \rightarrow NO + O(x2)}\,, \\
\mathrm{O + O_2 \rightarrow O_3 + M}\,, \\
\text{net: } \mathrm{CH_4 + 4O_2 \rightarrow HCHO + H_2O + 2\,O_3}\,. \qquad (2.9b)
\end{aligned}$$

HCHO has a photochemical lifetime of a few hours, and again may be photolyzed or react with OH. The subsequent reactions of the hereby produced CO and/or HO_2 again will either form or destroy O_3. Similar to the reaction sequences discussed above, nitrogen oxides will work as catalysts that facilitate the formation of ozone. **Figure 2.1** summarizes the catalytic cycles which lead to O_3 formation.

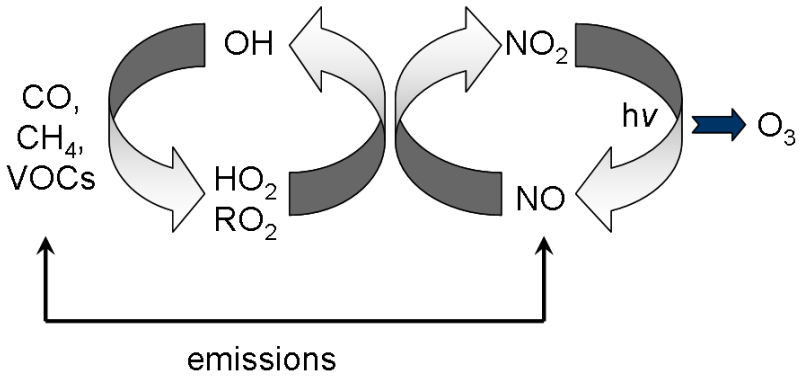

Figure 2.1: *Simplified schematic of chemical ozone formation in the troposphere. The ozone precursors CO, CH_4, VOCs and NO_x which are emitted by natural and anthropogenic sources, react in a catalytic cycle to form ozone.*

The critical NO concentration NO_{crit}

Ozone is not only produced by photochemical processes, but has also several in-situ sinks. Photochemical destruction of ozone occurs via its photolysis in the presence of water vapor (reaction 2.4d), whereas its oxidation by OH only is important at high mixing ratios of OH, as for example in the humid boundary layer (O_3 + OH $\rightarrow$ O_2 + HO_2). As discussed in detail above, degradation of hydrocarbons may either form or destroy ozone, which is largely controlled by the presence of nitrogen oxides. The NO mixing ratio at which photolytical ozone production compensates in-situ loss processes is often termed NO_{crit}. NO_{crit} depends on several parameters such as e. g. water vapor and ozone itself. It ranges between $\sim$5 - 30 pmol mol^{-1} and generally shows a decrease with increasing altitude (Davis et al., 1996; Klonecki and Levy, 1997; Reeves et al., 2002). Although this is a function of a number of competing factors, the decrease in NO_{crit} mainly is driven by less efficient destruction processes at higher altitudes. The large decrease in water vapor lowers removal of ozone via reaction 2.4d, and as a result of less OH also via its oxidation by the OH radical. In addition, the reaction of O_3 with HO_2 (reaction 2.5c) shows a stronger temperature-dependency than the reaction of NO with HO_2 (reaction 2.6a), and thus becomes less important at the cold temperatures prevalent at higher altitudes. **Figure 2.2** illustrates exemplary the net O_3 production in dependency of the NOX mixing ratio (NOX = NO_x + NO_3 + N_2O_5 + HNO_4) for typical conditions in the upper troposphere (200 hPa) at northern mid-latitudes (50°N) (Grooß et al., 1998). During daylight-hours NOX approximately equals NO_x.

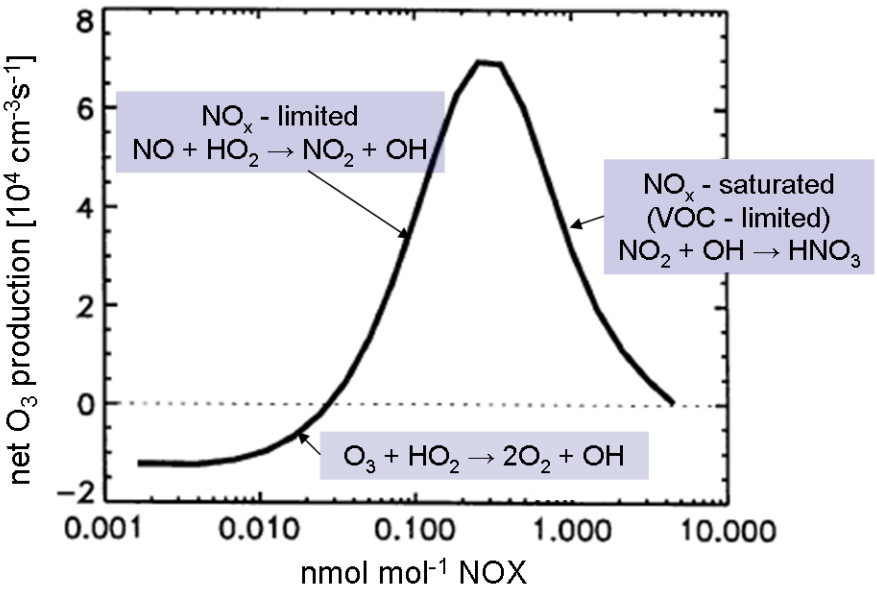

Figure 2.2: *Net ozone production rate as a function of the NOX mixing ratio ($NOX = NO_x + NO_3 + N_2O_5 + HNO_4$). Results from a steady-state calculation for 200 hPa at 50° N latitude and 60° solar zenith angle. At low NOX mixing ratios, an increase in NOX leads to an increase in ozone formation (NO_x - limited regime). At very high NOX conditions, the reaction of NO_2 with OH dominates over the OH oxidation of CO and other VOCs (NO_x - saturated or VOC - limited regime). Adapted from (Grooß et al., 1998)*

At very low NOX conditions, net chemical ozone destruction dominates, in the upper troposphere mainly by the reaction of O_3 with HO_2. With increasing NOX the reaction with NO becomes more important, and a further increase thus leads to more efficient ozone production due to the reaction cycles discussed above (NO_x - limited regime). At very large NOX concentrations, NO_2 however starts to compete with CO and VOCs for OH radicals. Since the reaction of OH with NO_2 will remove NO_x from the active system, photochemical ozone production then decreases with higher NOX mixing ratios (NO_x - saturated or VOC - limited regime). As we will see in the next section, NO_x has a relatively short photochemical lifetime which results in moderate to low concentrations far away from pollution sources. Hence, the main parts throughout the troposphere are in the "NO_x" - limited regime, and input of nitrogen oxides may induce net photochemical ozone formation.

2.2 The reactive nitrogen cycle and PAN (Peroxyacetyl nitrate)

This section will present photochemical cycling processes between primary emitted NO_x and other reactive nitrogen NO_y species ($NO_y = NO_x + HNO_3 + PAN + HONO + HO_2NO_2 + NO_3 + N_2O_5$...). A special focus is then paid on formation and loss processes of peroxyacetyl nitrate.

2.2.1 The reactive nitrogen cycle

Most of the primary emissions of NO_x (NO_x= NO + NO_2) are in the form of NO, which is directly emitted into the atmosphere from high-temperature combustion, lightning and microbial activity in soils (Bradshaw et al., 2000). NO subsequently underlies photochemical processing in the troposphere. Main gas-phase processes involved in the conversion among NO_y species are illustrated in **Fig. 2.3**. Oxidation of NO into nitrogen dioxide (NO_2) takes place within minutes (see equation 2.1), and NO_2 subsequently is photolyzed reforming NO (equation 2.2). As discussed before, the reactions of HO_2 and RO_2 with NO perturb the simple photostationary state between NO, NO_2 and O_3, which results in net formation of ozone. On time-scales of several hours to days, NO and especially NO_2 are however converted to other oxidized inorganic and organic compounds, with the most dominant being HNO_3 and PAN.

One of the most important reactions is the oxidation of nitrogen dioxide which leads to the formation of nitric acid (HNO_3). HNO_3 is thermochemically very stable and highly acidic. It dissolves efficiently in water droplets and therefore is efficiently removed from the atmosphere by either dry deposition or rain-out/wash-out (Logan, 1983). This makes nitric acid a terminal sink for reactive nitrogen. However, in the absence of precipitation it may persist for longer periods in the upper troposphere since photolysis of HNO_3 is quite slow. Other inorganic but much shorter-lived NO_y compounds include HONO (nitrous acid), HO_2NO_2 (peroxynitric acid), NO_3 (nitrate) and N_2O_5 (dinitrogen pentoxide). There are also numerous organic nitrogen species present in the atmosphere (e. g. Roberts (1990)) with the most ubiquitous species being PAN ($CH_3CO(O)_2NO_2$, see next section).

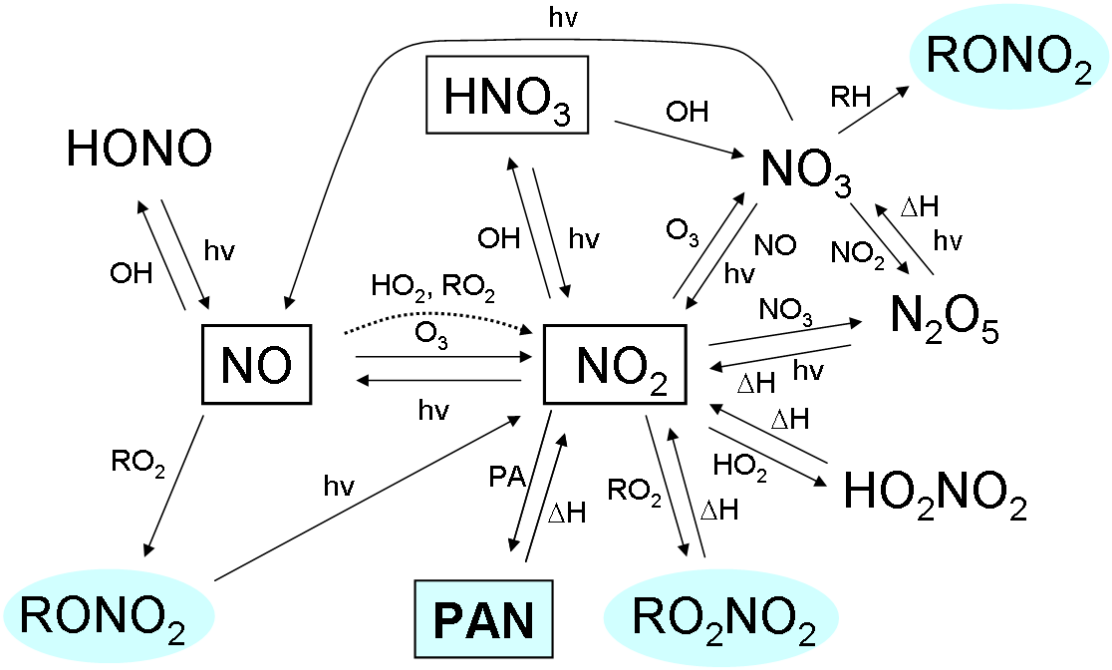

Figure 2.3: *Simplified tropospheric reactive nitrogen cycle (only gas-phase reactions are given). Primary emissions of NO and NO_2 are photochemically processed hereby forming other oxidized nitrogen compounds. The most dominant NO_y species are enclosed in boxes. Blue-shadings highlight organic nitrogen compounds.*

Figure 2.4 shows exemplary the vertical distribution of several nitrogen compounds as observed in the clean background and in the polluted troposphere of North America. The data were obtained in summer 2004 during INTEX-A[2] campaign. The data points are separated according to the pollution tracer carbon monoxide ($CO < 90\,nmol\,mol^{-1}$ for clean air, $CO > 90\,nmol\,mol^{-1}$ for polluted air). Data points influenced by stratospheric air are sorted out with help of the stratospheric tracer ozone ($O_3 > 120\,nmol\,mol^{-1}$). In the lower background troposphere (**Fig. 2.4a**), HNO_3 clearly dominates NO_y, whereas NO_x and PAN mixing ratios are relatively low. PAN values increase with altitude reaching $\sim 120\,nmol\,mol^{-1}$ in the upper troposphere where it is nearly as abundant as HNO_3. PPN (peroxypropionyl nitrate) is the next homologoue of the PANs family (see next section). Its vertical distribution is nearly identical to that of PAN, but PPN mixing ratios are about a factor of ~ 10 lower. NO_x increases strongly in the clean mid- and upper troposphere and dominates NO_y above $\sim$8 km, where it originates mainly from lightning (Singh et al., 2007). Thermally labile peroxynitric acid HO_2NO_2 has a lifetime of only $\sim$20 seconds in the boundary layer up to several hours in the upper troposphere (e. g. Kim et al. (2007)). For this reason, it shows a maximum in the upper troposphere ($\sim 50\,pmol\,mol^{-1}$). The decrease at even higher altitudes is the result of less efficient formation due to less abundant HO_2 (Ren et al., 2008). Similar to the formation of HO_2NO_2, organic nitrates are produced by reversible association reactions of various peroxy radicals (RO_2) with NO_2. Formation of organic nitrates depends on the availability of organic radicals and hence, on the presence of hydrocarbons (Roberts, 1990). For this reason, they are present only in the range

[2] **In**tercontinental Chemical **T**ransport **Ex**periment - North America Phase **A**

of a few pmol mol^{-1} in the background troposphere. Particulate nitrate NO_3^- is formed preferably via the reaction of NH_3 with nitric acid ($NH_3 + HNO_3 \rightarrow NH_4NO_3$, not indicated in **Fig. 2.3**). During INTEX-A, it was always present at moderately low concentrations (<10 % of NO_y, Singh et al. (2007)).

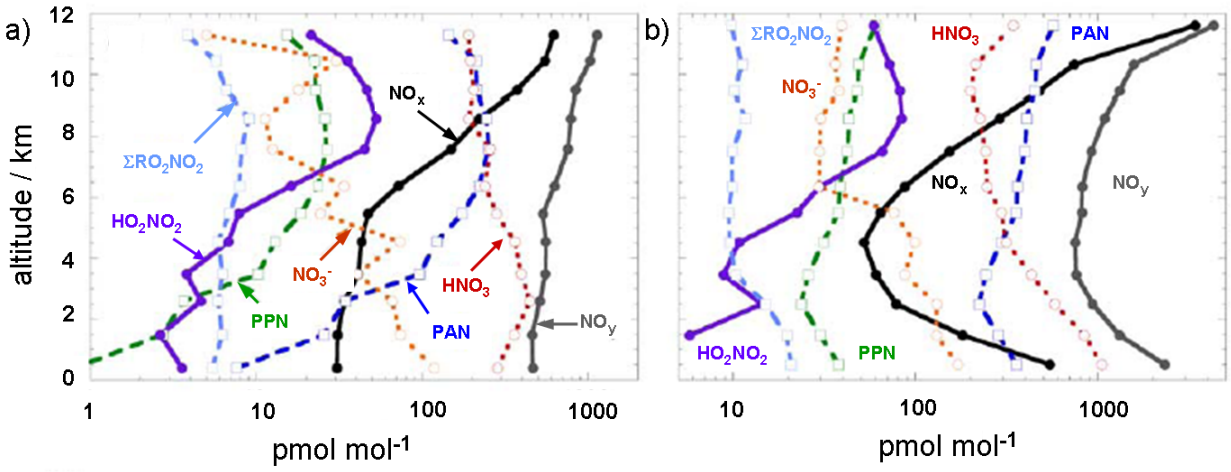

Figure 2.4: *Vertical distribution of several reactive nitrogen species as measured above North America in a) the clean troposphere ($CO < 90\,nmol\,mol^{-1}$, $O_3 < 120\,nmol\,mol^{-1}$) and in b) the polluted troposphere ($CO > 90\,nmol\,mol^{-1}$, $O_3 < 120\,nmol\,mol^{-1}$), adapted from Singh et al. (2007).*

In the polluted troposphere (**Fig. 2.4b**), all reactive nitrogen species are enhanced. Elevated NO_x originates in the lower troposphere from surface emissions and in the upper troposphere mainly from pollution lofted via convection. PAN is abundant now at significant levels also in the lower troposphere, and dominates over HNO_3 in the upper troposphere. Thermally labile HO_2NO_2 again peaks around ∼8 km where it has mixing ratios of nearly 100 pmol mol^{-1} in polluted air masses. Organic nitrates have similar to most other NO_y species their highest values in the lower troposphere (∼20 pmol mol^{-1}).

Not given in **Fig. 2.4** are HONO (nitrous acid) and the night-time species NO_3 and N_2O_5. Nitrous acid plays only a minor role in the remote troposphere but due to its rapid photolysis, HONO may be an important source for OH radicals in urban areas just after sunrise (Platt et al., 1980; Li et al., 2010). The NO_3 radical is formed by the reaction of NO_2 with O_3. It is absent or abundant at very low concentrations during the day due to rapid photolysis, but may during night reach values between a few and several hundreds of pmol mol^{-1} (Brown et al., 2006; Crowley et al., 2010). NO_3 is a powerful oxidant and reacts preferably with a number of unsaturated hydrocarbons, by adding to the double bond. Under certain conditions, this may lead to an efficient production of peroxy radicals at night (Platt et al., 1990). It is worth pointing out that it has its peak-time concentrations when OH concentrations are at minimum levels. Via reaction with NO_2, NO_3 may form also the thermally labile dinitrogen pentoxide N_2O_5. Through heterogeneous processes on cloud drops or aerosols, N_2O_5 will efficiently produce HNO_3 ($N_2O_5 + H_2O \rightarrow 2\,HNO_3$, not indicated in **Fig. 2.3**). This pathway represents an important means of removing NO_x during night (e. g. Crowley et al. (2010)).

2.2.2 PAN - a temporary NO_x reservoir

PAN (peroxyacetyl nitrate, $CH_3CO(O)_2NO_2$) is the most abundant organic nitrate species, and constitutes the simplest and most dominant member of a larger series of PANs (peroxyacyl nitrates, $RCO(O)_2NO_2$). Higher members of the PANs family are for example PPN (peroxypropionyl nitrate, $CH_3CO(O)_2NO_2$) and MPAN (peroxymethacryloyl nitrate, $CH_3CCH_2C(O)O_2NO_2$) which often are present at mixing ratios of roughly an order of magnitude lower than PAN itself (Roberts et al., 2004, 2007; Wolfe et al., 2007; LaFranchi et al., 2009). PANs are not emitted directly into the atmosphere, but are formed through the atmospheric oxidation of organic species in the presence of NO_x. **Figure 2.5** illustrates the formation of peroxyacyl nitrates. All PAN homologues are formed through similar chemistry, but have different parent VOCs. The measured relative abundances of different PANs can therefore be used as indicators for the precursor VOCs (Williams et al., 1997; Roberts et al., 2002).

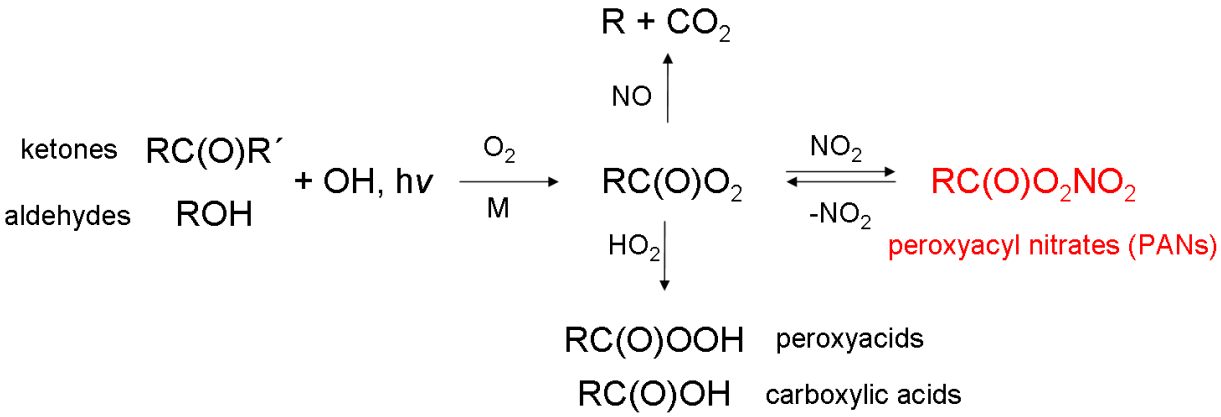

Figure 2.5: *Reaction sequence leading to the formation of members of the PANs family. It is initiated by the photo-oxidation of either ketones or aldehydes which will form peroxyacyl radicals. These subsequently may react either with NO (hereby indirectly producing O_3) or with other radicals (which represents a terminal sink for radicals). The addition of NO_2 to peroxyacyl radicals leads to the reversible formation of PANs.*

The direct precursor of PANs are peroxyacyl radicals ($RC(O)O_2$), which are formed by OH oxidation or photolysis of ketones (RCOR´) and aldehydes (ROH). Ketones and aldehydes may be directly emitted in the atmosphere by motor vehicles and other industrial processes, but originate also from degradation of other organic compounds. The formed peroxyacyl radicals may react further via several pathways. At very low NO_x conditions, the formation of acids or peroxides via radical-radical reactions is favoured. This pathway will efficiently remove radicals from the active system and therefore constitutes an important terminal sink. In the presence of NO, peroxyacyl radicals may similar to many other organic radicals convert it to NO_2, hereby promoting ozone formation. Formation of PANs proceeds by the reversible addition of peroxyacyl (PA) radicals and NO_2:

$$RC(O)O_2 + NO_2 \leftrightarrows RC(O)O_2NO_2\,. \tag{2.10}$$

At planetary boundary layer temperatures, PANs are thermally very labile and may decompose, thereby releasing NO_2 and peroxyacyl radicals again. Other atmospheric dissociation processes of PANs are the reaction with OH and photolysis, which removal rates may slightly differ between various PAN species (Harwood et al., 2003; Orlando et al., 2002).

In the following, the discussion will focus on the simplest and most abundant PAN. According to Roberts (1990), PAN is not very soluble in water, and therefore dry or wet deposition represent only minor removal pathways. Hydrolysis of PAN in n-octanol was studied by Roberts (2005), who concluded that also uptake of PAN on organic aerosol can be neglected throughout the troposphere. The atmospheric lifetime of PAN regarding its reaction with OH, photodissociation and thermal decomposition as a function of altitude is summarized in **Fig. 2.6**.

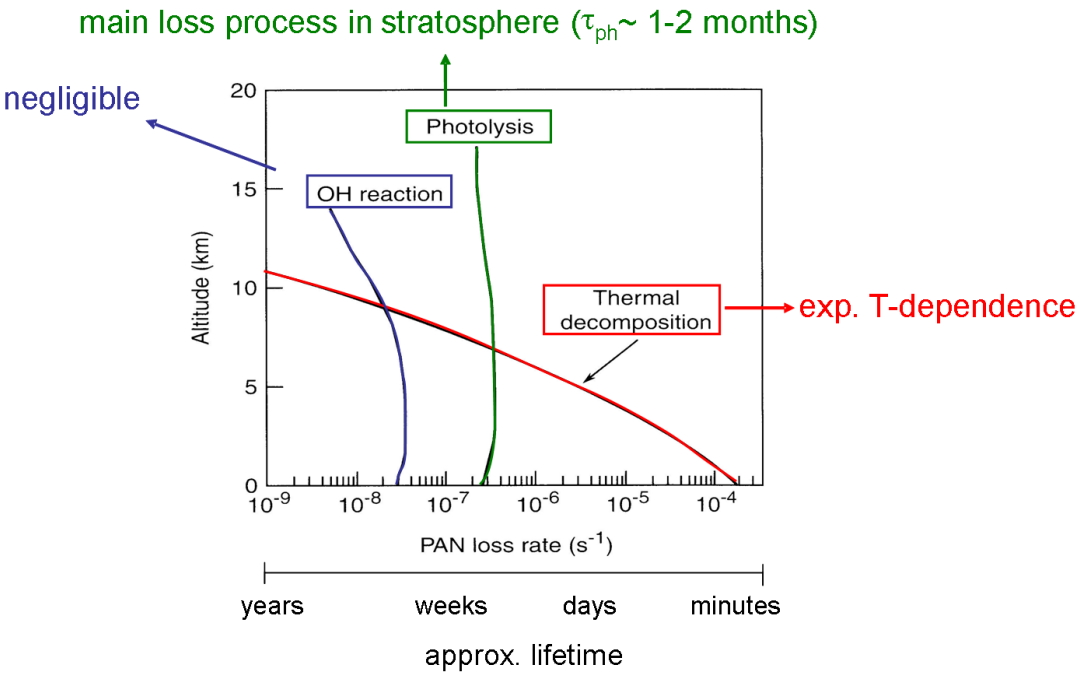

Figure 2.6: *PAN loss rates as a function of altitude (adapted from Talukdar et al. (1995)) calculated using solar actinic flux and OH concentrations from the U. S. standard atmosphere (30°N, 4 July). The lower x-axis gives the corresponding approximate lifetime of PAN. The reaction of PAN with OH is very slow. At altitudes above ~7 km, photolysis limits the lifetime of PAN to several weeks. In the lower and middle troposphere, thermolysis of PAN is the main loss pathway.*

The reaction with OH is very slow throughout the entire troposphere/lowermost stratosphere ($k_{298\,K} < 3\times10^{-14}$ cm^3 s^{-1}), and therefore can be neglected. The absorption cross section of PAN is small at wavelengths above ~290 nm ($\sigma_{PAN} < 10^{-21}$ cm^2), so its photodissociation is expected to be not very efficient in the troposphere/lowermost stratosphere. However, it constitutes the major loss pathway in the upper troposphere and above. In the mid- and lower troposphere, thermal decomposition of PAN is the main removal pathway. Due to the very strong exponential temperature dependence of the thermal decay rate of PAN, the lifetime against thermolysis in the boundary layer is typically less than one hour. In the colder upper troposphere NO_x is conserved in PAN which here will survive

several weeks to months. This makes PAN an important NO_x reservoir species which can undergo long-range transport (LRT) since this occurs mainly in the mid- and upper troposphere where wind velocities are relatively large (see next section). Sooner or later the air mass however will be transported to lower altitudes and thereby experience adiabatic heating. PAN will decompose as the air parcel warm up, hereby releasing NO_2 and peroxyacyl radicals (see back reaction of equation 5.4). Liberated NO_x subsequently may promote ozone production due to the reaction cycles discussed in section 2.1, probably far away from the region where NO_x initially was emitted (Singh and Hanst, 1981). This mechanism is regularly observed in pronounced PAN plumes (Hudman et al., 2004; Real et al., 2007; Zhang et al., 2008), but may also be important if the air mass is advected into remote regions. In these areas, a small amount of additional NO_x may shift NO_x-O_3 chemistry from net ozone destruction to net ozone formation (see **Fig. 2.2**).

2.3 Long-range transport (LRT) of pollutants into the Arctic

Except for a few regions such as upper Siberia and Alaska, the Arctic is sparsely inhabited, and there are only a couple of local pollution sources. These include volcanic emissions in Alaska and Kamchatka, as well as anthropogenic emissions from e. g. the Prudhoe Bay (North Alaska), Norilsk (Siberia), and the Kola Peninsula (North-West Russia) (e.g. Law and Stohl (2007); Bottenheim (2004)). The picture of a truly pristine and clean environment however was first questioned by the observations of strong haze layers by pilots in the 1950s, which led to a strong decrease in visibility (Greenaway, 1950; Mitchell, 1957). The so-called "Arctic haze" phenomenon occurs regularly during winter with a maximum in early spring, and is attributed to poleward transport of aerosol pollution mainly of anthropogenic origin (e.g. Law and Stohl (2007); Quinn et al. (2007)). During summer, boreal forest fires provide an additional, more episodic source of trace gases and aerosols at high northern latitudes. The following sections will give a short introduction to long-range transport. First, source regions of pollution are pointed out, which have the potential to influence the Arctic. It follows a presentation of dynamical processes driving LRT of pollutants in general. Finally, special meteorological conditions of the Arctic will be introduced in order to understand typical transport pathways into the Arctic troposphere.

2.3.1 Source regions of biomass burning and anthropogenic emissions

Major pollution regions at northern mid- and high latitudes are highlighted in **Fig. 2.7**, which shows the geographical distribution of black carbon (BC) emissions in the temperate and boreal regions. Black carbon is used as a tracer for pollution in this case, because it is formed through incomplete combustion processes, and therefore originates both from natural or anthropogenic emissions. The distribution and source strength of emissions certainly varies between different kind of species, however, **Fig. 2.7** is used in a qualitative sense only. **Figure 2.7a** shows the BC emissions originating from fossil fuel/biofuel combustion. Densely populated and/or industrialized regions of North America, Europe and Asia are evident. Maximum BC emissions are observed at the U.S. east coast, in central Europe as well as in south Asia (India) and south-east Asia (China, Korea, Japan).

In general, source regions of pollution in northern Europe/Russia are centered at higher latitudes of up to 60 - 65°N, whereas those in North America and Asia are located typically south of ∼50°N. As will be discussed in the next section, emissions released at the east coasts of both North America and Asia are due to this geographic location especially predestinated to experience LRT. The blue shaded area indicates the approximate coverage of the GRACE flights (see section 5), and shows that no large pollution sources are located in our measurement area.

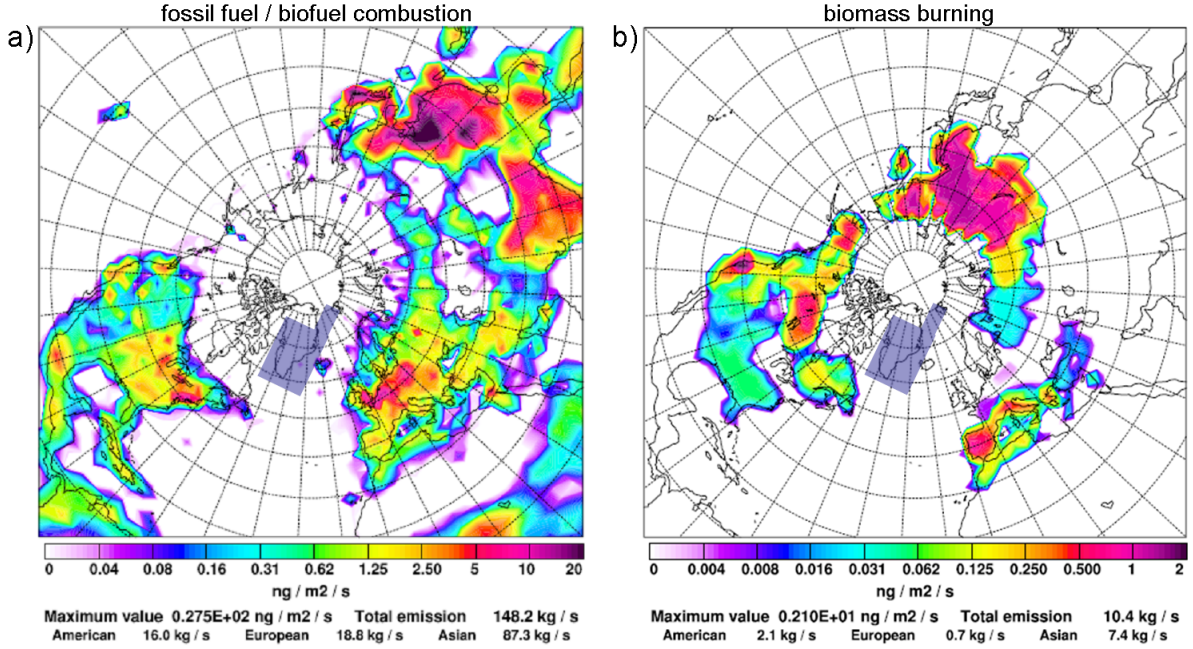

Figure 2.7: *a) Annual mean fossil fuel and biofuel BC emissions (Bond et al., 2004), b) BC emitted by biomass burning in the boreal and temperate region (Lavoué et al., 2000). Figure adapted from (Stohl, 2001). Blue shaded areas around Greenland indicate the approximate coverage of GRACE campaign.*

Figure 2.7b illustrates the source distribution of BC originating from biomass burning, and shows a rather different emission pattern. The by far largest biomass burning region is found in Siberia, which is followed by forest fire areas located in Canada and Alaska. Boreal fire regions are generally centered farther to the north than the industrial zones of the mid-latitudes. Canadian fires may occur at up to ∼60°N, whereas in Siberia and Alaska fires typically take place at even higher latitudes of up to ∼70°N. Due to the large distance, emissions released from biomass burning in the temperate zone (California as well as Spain, Italy and Greece) however play no major role for pollution transport into the Arctic. The numbers at the bottom of both figures indicate that annual mean BC emissions from boreal forest fires are about a magnitude lower than those from anthropogenic activities. However, fire emissions are concentrated basically on the summer season, and the fluxes are therefore temporarily much higher especially in June/July (Lavoué et al., 2000). It is worth pointing out that emissions from wild fires are in general much more difficult to predict than those from industrial activities. Timing, location and duration of fires underly strong inter-annual variability but may underlie also seasonal changes in general (Duncan et al., 2003; Lapina et al., 2008). Fire ignition and burning conditions determine location and strength of fires, and will

be governed by meteorological conditions (e. g. lightning, extreme dryness). Vegetation structure and fire type determine the injection height of emissions, which will in turn influence vertical and thus horizontal distribution of emissions. For example, Canadian fires often are crown fires (∼80%), whereas ∼75% of Siberian fires are surface fires (Val Martin et al., 2010; Lavoué et al., 2000). Rather clear is that there is an increase in burning areas due to a changing climate, which leads to higher temperatures, extended dryness and enhanced convective activity (Lavoué et al., 2000; Stocks et al., 1998; Soja et al., 2007). In turn, more frequent and severe fires are suggested to have a positive feedback on Arctic warming (Stocks et al., 1998; Flannigan et al., 2005).

Also emission ratios of different species strongly depend on vegetation as well as on the type of fire (smoldering vs. flaming combustion, e. g. (Andreae and Merlet, 2001)). The different types of combustion are responsible for the vast diversity of emission products. Whereas smoldering combustion ($400 \leq T \leq 800\,K$) emits mainly reduced substances such as CO, NH_3 and CH_4, flaming combustion ($T \leq 1200\,K$) releases more oxidized molecules such as NO, CO_2 and SO_2 (e. g. Yokelson et al. (1996); Goode et al. (2000); Andreae and Merlet (2001)). Nitrogen oxide emissions in biomass plumes evolve in general only from from fuel nitrogen. Burning temperatures in fires typically are much lower than those prevalent in industrial processes, from which nitrogen oxides arise primarily by the breakdown of air nitrogen (N_2). Early measurements indicated that emissions of nitrogen oxides in boreal biomass burning plumes are even lower than those observed in tropical fire plumes (Wofsy et al., 1992; Jacob et al., 1992), which can be explained by the low nitrogen content of Arctic vegetation (Chapin and Shaver, 1985). This in turn leads to a high VOC/NO_x emission ratio (Jacob et al., 1992; Mauzerall et al., 1996), which influences the distribution of nitrogen compounds by favoring e. g. the production of PAN instead of HNO_3 (see section 2.2.2). Measurements within the framework of ARCTAS-B[3] in summer 2008 confirmed these earlier observations. Alvarado et al. (2010) found rapid conversion of NO_x into PAN with average values of ∼40% within the first few hours after emission. This will on the one hand slow down photochemical ozone production in fresh plumes by removing NO_x. On the other side, exported PAN may strongly influence NO_x-O_3 chemistry in downwind regions, such as for example the Arctic.

2.3.2 Meteorological processes involved in LRT

Most industrial emissions are released close to the surface, in the atmospheric boundary layer (ABL). This is also true for the main part of biomass burning emissions, although as will be discussed shortly, strong heat development in fires will facilitate convective motions. In the lowest few kilometers of the troposphere, wind speeds are low and removal mechanisms efficient. Transport at low levels therefore does not play a major role for LRT. Intercontinental transport however is initiated by upward transport of surface emissions from the ABL into the free troposphere, where relatively strong and persistent winds may carry the polluted air mass over great distances. The necessary up-lift of emissions from the planetary boundary layer to the middle and upper troposphere basically takes place within two different mechanisms, (a) deep convection events (DC) and (b) warm conveyor belts (WCBs).

[3] **A**rctic **R**esearch of the **C**omposition of the **T**roposphere from **A**ircraft and **S**atellites -Phase **B**

Deep convection

Deep convection is one of the most effective mechanisms to transport polluted air into the free troposphere, lifting boundary layer air to the upper troposphere typically within ~ 1 hour. It is mostly effective in summer and is often associated with thunderstorms, which can reach the tropopause region or even the lowermost stratosphere (e. g. (Hauf et al., 1995; Poulida et al., 1996; Fischer et al., 2003)). Thunderstorms can occur within extra-tropical cyclones along or ahead of the cold front, as well as in hot, moist unstable conditions far south of the mid-latitude storm tracks. Biomass burning produces high temperatures and strongly affects radiative processes through e. g. absorption by black carbon. For this reason, forest fires can develop their own dynamics. **Figure 2.8** shows a photograph of fires which were burning in the Canadian province Saskatchewan in summer 2008. The picture was taken on a DC8 flight on 29 June, performed within the framework of ARCTAS-B. Next to the water based white cumuli, so-called pyrocumulus clouds are visible as dark cauliflower shaped clouds. In this case, they extend only up to $\sim$600 m (Fuelberg et al., 2010), but often they are observed to be much higher. Transport within evolving pyrocumulus cloud increases the likelihood that aerosols and trace gases are injected into the free troposphere and even into the UTLS region (Waibel et al., 1999; Fromm et al., 2000; Fromm and Servranckx, 2003; Jost et al., 2004; Damoah et al., 2006; Cammas et al., 2009).

Figure 2.8: *Photograph of a fire burning in the Saskatchewan area of western Canada. Note the dark pyrocumulus clouds at the top of the smoke. The picture was taken from the DC8 cockpit when the aircraft was flying at $\sim$0.5 km. Picture taken from http://fuelberg.met.fsu.edu/gallery/arctas.*

Mid-latitudinal cyclones

Extra-tropical cyclones or low pressure systems are a daily phenomenon of mid-latitudinal weather. They are responsible for large-scale heat and water vapor transfer from the equator to the poles and have a primary role in determining local weather. Cyclones contain several major air streams, which efficiently carry air masses both from low to high altitudes and vice versa. **Figure 2.9** introduces the

four main transport channels within a typical mid-latitude cyclone, the warm conveyor belt (WCB), cold conveyor belt (CCB), dry airstream (DA) and the post cold front airstream (PCF).

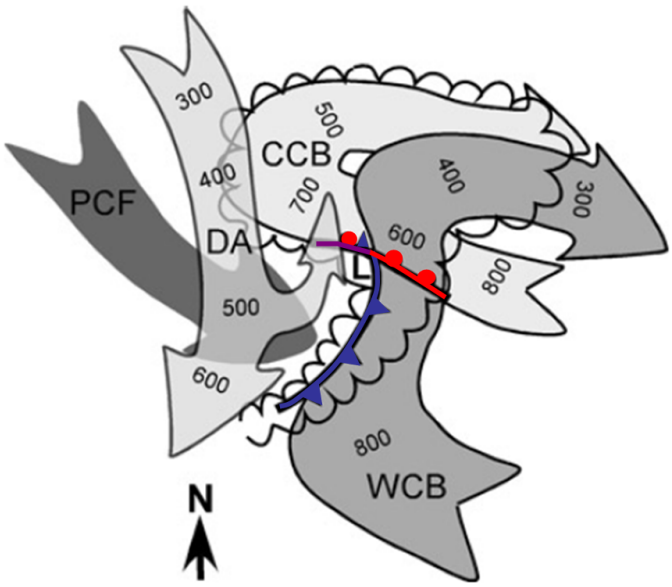

Figure 2.9: *Most important air streams within a mid-latitude cyclone: Warm conveyor belt (WCB), cold conveyor belt (CCB), dry airstream (DA), post cold front airstream (PFA). The center of the cyclone is indicated (L) and the scalloped lines indicate the edges of the typically formed comma-cloud. The numbers on the cold conveyor belts indicate the pressure at the top of these airstreams, while the numbers on the dry airstream indicates the pressure at the bottom of this airstreams. The PCF flows beneath the dry air stream. Also highlighted are the cold (blue) and warm front (blue). Adapted from (Cooper et al., 2002).*

The CCB is located close to the surface and on the northern side of the cyclones warm front. It ascends while moving westwards, having a component heading eastward at higher altitudes (please note the pressure values given along the different air streams in **Fig. 2.9**). The lower portions of the WCB originates in the warm sector, east of the associated cyclone. The air masses are strongly lifted into the mid- and upper troposphere, ahead of the surface cold front. Both the CCB and WCB are ascending moist airstreams, so the ascent is accompanied by an increase of potential temperature due to latent heat release from water vapour condensation, cloud formation, and a loss of moisture by precipitation. The DA descends isentropically from the upper troposphere/lowermost stratosphere into the mid- and lower troposphere, on the polar side of the cold front. Stratospheric intrusions or tropopause folds that occur within DAs always bring ozone and dry air down into the free troposphere, which ultimately will also mix with air masses up-lifted within WCBs/CCBs of the same cyclone. The PCF was introduced to explain the dry air mass in the lower to mid-troposphere that flows behind the cyclone cold front and beneath the DA (Cooper et al., 2002). It is unaffected by wet deposition, and sunny conditions may allow for some photochemical ozone production (Cooper et al., 2004).

The most important air stream for intercontinental transport of pollutants certainly is the WCB (e.g. Stohl and Thomson (1999); Stohl (2001); Cooper et al. (2002, 2004); Stohl et al. (2003)). The warm sector typically develops in regions where conditions allow for the accumulation of photochemically

active trace gases. Ahead of the cold front, air parcels rise on short time-scales of 1 or 2 days from the boundary layer to the upper troposphere (e.g. Wernli and Davies (1997); Eckhardt et al. (2004)). Regions of maximum cyclone occurrence is off the east coasts of North America and Asia, and WCBs therefore frequently incorporate air masses from the industrialized eastern seaboards of North America and Asia (Stohl, 2001; Wernli and Bourqui, 2002), with Asian WCBs experiencing even stronger ascent (Wild and Akimoto, 2001; Stohl et al., 2002).

Intercontinental transport at high altitudes

After being exported from the ABL by deep convection events or within warm conveyor belts, surface emissions are subject to LRT. **Figure 2.10** summarizes typical processes associated with long-range transport in the northern mid-latitudes. In general, mid-latitudinal transport of pollution in the free troposphere is dominated by the prevailing westerly winds. Following this transport pattern, anthropogenic pollution from North America regularly is advected towards Europe (Stohl et al., 2003; Huntrieser et al., 2005). In a similar manner, numerous Asian plumes are transported towards North America (e. g. (Jaffe et al., 1999, 2003; Hudman et al., 2004)), and even Europe (Stohl et al., 2007; Fiedler et al., 2009). Also boreal biomass burning plumes are observed to move over great distances. Alaskan as well as Canadian fire plumes were sampled over Europe (Forster et al., 2001; Real et al., 2007), but may travel even around the world (Damoah et al., 2004).

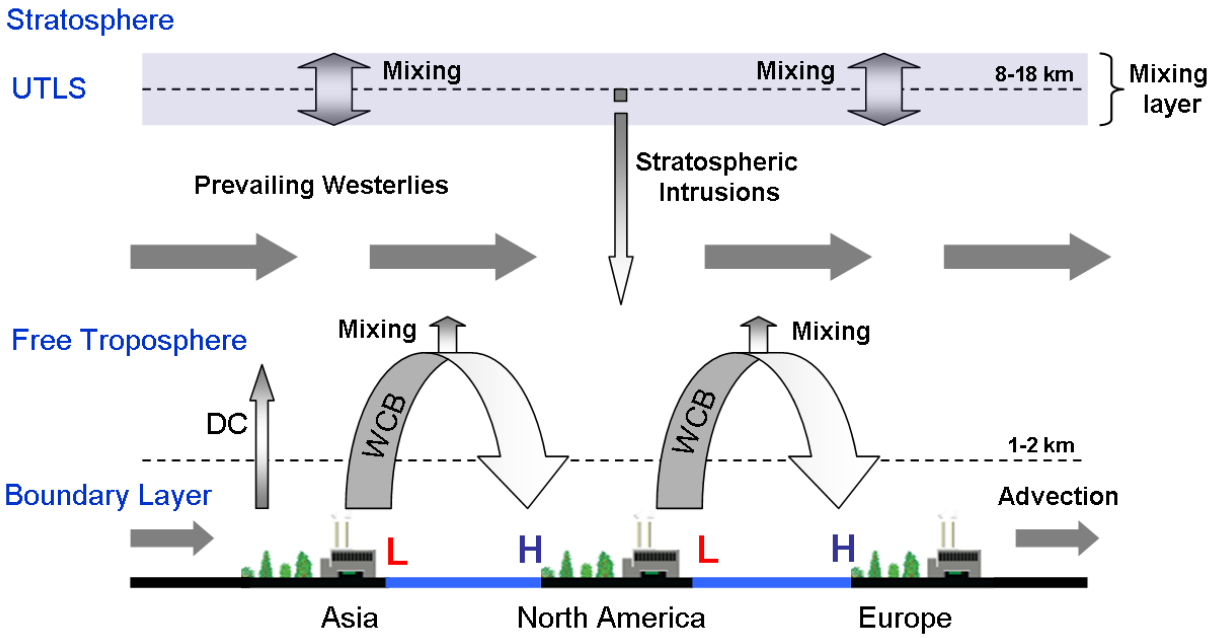

Figure 2.10: *Schematic of dominant dynamical processes involved in long-range transport of pollution in the mid-latitudes. Ground level H and L symbols represent high- and low-pressure systems (after National Research Council (2009)). For more details see text.*

During periods of LRT, chemical composition/concentrations of the polluted air masses are altered through chemical transformation and/or dilution with surrounding air. Mixing processes may take place in the vicinity of fronts or in the WCB outflow region (Esler et al., 2001; Cooper et al., 2002; Mari et al., 2004). Stratospheric intrusions occur frequently within the same mid-latitude cyclone

in which pollution has been vented from the boundary layer, and the different air masses finally will mix also in the free troposphere (Parrish et al., 2000; Brioude et al., 2007). Large-scale mixing in the UTLS region leads to the formation of a mixing layer (see section 2.4).

2.3.3 Transport of pollutants into the Arctic troposphere

The most prominent example of Arctic pollution is the "Arctic haze" phenomenon, which occurs mainly during winter and spring (e. g. Quinn et al. (2007); Law and Stohl (2007)). The Arctic winter is characterized by absence of light and extremely cold temperatures. Low surface temperatures lead to strong surface-based inversions that limit turbulent mixing and vertical transport. Weak mixing processes slow down dry deposition, and the extreme dryness of the Arctic troposphere minimizes also wet deposition. This results in very long aerosol lifetimes in the Arctic troposphere leading to the formation of haze layers and decreasing visibility, the "Arctic haze". However, at the same time transport into the lower Arctic troposphere is hampered since isentropic surfaces (i. e. surfaces of constant potential temperatures) form closed domes over the Arctic (Klonecki et al., 2003). In the absence of diabatic processes (e. g. latent heat release or radiational heating/cooling), an air parcel basically travels along constant isentropic surfaces. Mid-latitudinal air masses originate at higher potential temperatures and therefore will ascend along the upward sloped isentropes, when approaching the Arctic. Pollution from Asia and North America thus enters the Arctic mainly at higher altitudes, as relatively warm and moist mid-latitude air masses ascend over colder, denser Arctic air masses; this may be followed by descent within the Arctic or transport back to the mid-latitudes (Stohl, 2006). Continuous transport at low levels is facilitated for pollution originating from northern Eurasia, if the air masses experience considerable diabatic cooling by passing over snow covered surfaces (Klonecki et al., 2003; Stohl, 2006; Shindell et al., 2008).

Meteorological conditions change significantly in boreal summer. The polar dome is now less stratified since surface inversions are weaker. The upward slopes of isentropes towards the pole are not as strong as during winter. However, meteorological systems generally are weaker than during winter, and slower wind speeds lead to slower transport. Furthermore, removal rates are more efficient during summer due to photo-oxidation, and more intense mixing dilutes polluted plumes. Models and surface observations therefore show clearly, that LRT from the industrial mid-latitudes into the Arctic lower troposphere in general is much less pronounced in summer than during winter/spring (Klonecki et al., 2003; Stohl, 2006; Fuelberg et al., 2010). This seasonal feature however weakens with altitude, and models suggest that in summer, the Arctic upper troposphere is more influenced by LRT of anthropogenic emissions (Klonecki et al., 2003; Shindell et al., 2008). This is illustrated in **Fig. 2.11**, which shows Arctic sensitivities based on simulations of a passive tracer (lifetime = 50 days), as averaged from 8 different models (Shindell et al., 2008). The Arctic here is defined as the region poleward of 68°N, and the source regions were chosen to encompass the bulk of Northern hemisphere emissions (see Shindell et al. (2008) for more details).

As mentioned, the Arctic surface is most sensitive to European emissions, and the influence is largest in winter (**Fig. 2.11a**). During summer, when the polar dome is less intensive, emissions from all four source regions however have a comparable influence. In the middle troposphere, sensitivities

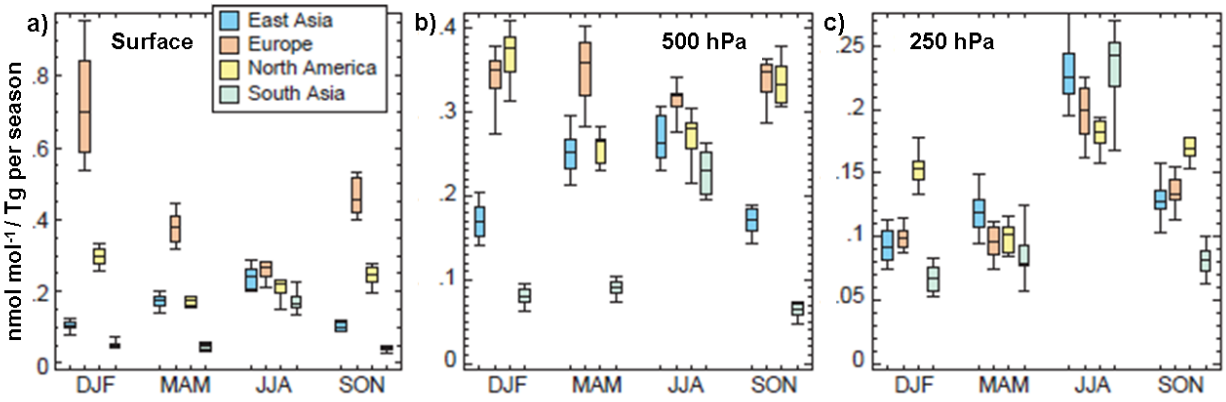

Figure 2.11: *Arctic sensitivity at three atmospheric pressure levels for a passive tracer (lifetime 50 days), as simulated from 8 different models (Shindell et al., 2008). Sensitivities from emissions from four source regions at a) the surface, b) 500 hPa, c) 250 hPa.*

to emissions from North America are similar to those from European emissions (**Fig. 2.11b**). Sensitivities to East Asian pollution are somewhat less, and higher during spring/summer season. South Asian emissions are suggested to play only a minor role at these levels (outside of summer), most probably to the larger distance to the Arctic. Sensitivities in the Arctic upper troposphere are clearly different. According to the model results they are largest during June to August, with a comparable influence from all four source regions. However, measurements in the Arctic troposphere are sparse especially during summer, and in-situ observations have mostly been performed at the surface (Jacob et al., 2010). Earlier measurement campaigns (ABLE3-A and B) showed that the NO_y budget of the Arctic summer troposphere is influenced by input from the stratosphere, emissions from Siberian fires, and probably also by urban input from the mid-latitudes (Sandholm et al., 1992). It is also important to note that model studies investigating Arctic pollution either focused on transport of passive tracers (Stohl, 2001), or transport of anthropogenic emissions only (Klonecki et al., 2003; Shindell et al., 2008). Emissions from boreal biomass burning however constitute a major perturbation to the Arctic troposphere, especially due to their close proximity (see section 2.3.1).

2.4 The tropopause region

The extra-tropical tropopause region or UTLS (upper troposphere/lowermost stratosphere) is the transition region between the convectively dominated, well-mixed troposphere and the stable stratified stratosphere (Holton et al., 1995). Due to the different characteristics of the troposphere and stratosphere (e. g. chemical composition, static stability), understanding of Stratosphere-Troposphere-Exchange (STE) processes are of special interest. **Figure 2.12** summarizes schematically processes involved in STE. Globally, the (Brewer-Dobson) circulation in the upper troposphere and stratosphere can be described by large-scale ascent in the tropics, which is followed by trans-

port into the extra-tropics and downward transport from the stratosphere to the troposphere in the middle and high latitudes. The stratosphere or "overworld" (Hoskins, 1991) is the region above the 380 K isentrope. Transport from here to the troposphere requires diabatic cooling since the air must cross isentropic surfaces, and thus is very slow. The lowermost stratosphere or "middleworld" is the region, where isentropes intersect the tropopause. Here in the middleworld, isentropic surfaces lie partly in the troposphere (in the tropics) and partly in the lowermost stratosphere (at high latitudes).

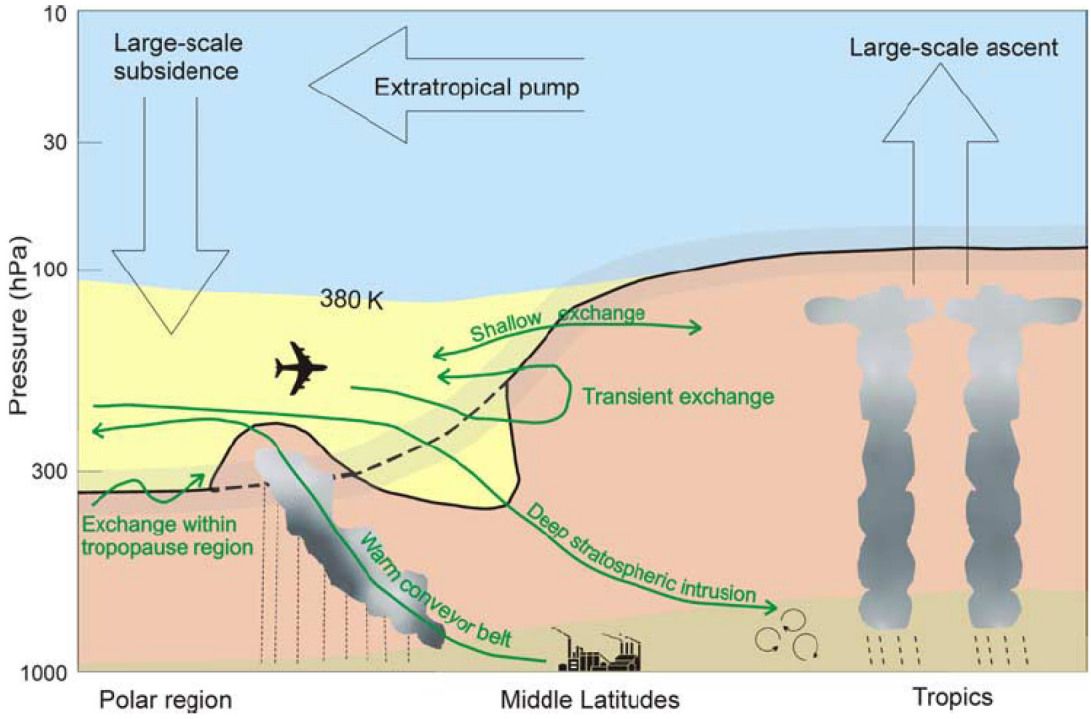

Figure 2.12: *Global aspects of STE (Stohl et al., 2003). The thick black line gives the average position of the tropopause. The atmosphere is divided into several regions: the overworld (blue, above the 380 K isentrope), in which isentropes lie entirely in the stratosphere, the lowermost stratosphere (yellow), where isentropes cross the tropopause, the free troposphere (red), and the atmospheric boundary layer (brown). Bulges near the warm conveyor belt and stratospheric intrusion illustrate strong perturbation of the tropopause from its average position. For more details see text.*

The chemical composition of the lowermost stratosphere thus is a mixture of aged stratospheric air descending slowly from the overworld through the 380 K isentrope and recent injections of tropospheric air. Tropospheric injections can be related to either diabatic processes, e.g. via deep convection, or adiabatic along isentropes across the tropopause. This large-scale mixing and intermingling of air masses leads to the formation of a mixing layer (see top of **Fig. 2.10**) which can be quantified using tracer relationships (Fischer et al., 2000; Zahn et al., 2000; Hoor et al., 2002, 2004; Pan et al., 2004, 2007; Kunz et al., 2009).

The tropopause can be defined using different approaches. According to the World Meteorological Organization (WMO), the tropopause is defined as the lowest level at which the temperature lapse

rate decreases to $2\,\mathrm{K\,km^{-1}}$ or less, and the lapse rate averaged between this and any level within the next 2 km does not exceed to $2\,\mathrm{K\,km^{-1}}$. A dynamic definition relies on potential vorticity (PV, see appendix A1), which for many purposes is more convenient since PV is conserved under adiabatic and frictionless conditions. PV values used range from 1.6 to 3.5 PVU, with 2 PVU used mainly. Since chemical tracers such as O_3 and CO show steep gradients across the tropopause, some studies suggest to use the chemical tropopause (Zahn and Brenninkmeijer, 2003; Pan et al., 2004).

The transport of pollutants from the troposphere into the stratosphere effects the chemical balance in both regions. For this reason, it is especially important to study whether biomass burning and/or anthropogenic emissions have the potential to reach the tropopause region within a few hours or days, when oxidation and removal processes of pollutants have not yet been fully efficient. As mentioned before, biomass burning emissions may enter the lowermost stratosphere through the explosive combination of intense fires and extreme convection (Waibel et al., 1999; Fromm et al., 2000; Fromm and Servranckx, 2003; Jost et al., 2004; Damoah et al., 2006; Cammas et al., 2009). Up-lift within WCBs probably is less rapid, but acts on larger scales and thus may be another important mechanism to bring pollution into the UTLS. Lagrangian transport climatologies show an enhanced potential for WCB trajectories to reach the tropopause region (Stohl, 2001; Wernli and Bourqui, 2002). A few percent are observed to even enter the lowermost stratosphere, not only within active WCBs, but also a few days after the WCBs decay (Eckhardt et al., 2004). Since WCBs often incorporate pollution from the industrialized coastal regions of North America and Asia, this transport pattern possibly presents an important mechanism to bring pollution into the polar lowermost stratosphere (Stohl, 2001; Wernli and Bourqui, 2002). However, up to now observational evidence of this process is lacking. As we will see in chapter 6, this WCB-pathway was for the first time confirmed by in-situ measurements during GRACE campaign.

Chapter 3

Experimental methods

3.1 Chemical ionization mass spectrometry

The Chemical Ionization Mass Spectrometry (CIMS) is a measurement technique which fulfills the requirements of a low detection limit, a high sensitivity and a good time resolution. The use of mass spectrometric techniques for atmospheric chemical studies was pioneered by Arnold et al. (1978) who analyzed ambient ions in the atmosphere with the PACIMS technique (Passive CIMS). Hereafter, the MPI-K group (head: Prof. Frank Arnold) introduced the ACIMS (Active CIMS) technique into airborne atmospheric research using rocket, balloon, and aircraft as carriers of their CIMS instruments (Arnold and Hauck, 1985; Knop and Arnold, 1987; Schlager and Arnold, 1987; Moehler and Arnold, 1991). ACIMS, in the following referred to as CIMS, uses artificially produced reagent ions as precursor ions. Initially, the MPI-K group utilized linear quadrupole mass filters, but in recent years the use of ion trap mass spectrometers (see section 3.3) was introduced (Kiendler et al., 2000; Speidel et al., 2007; Fiedler et al., 2009; Aufmhoff et al., 2011).

CIMS is based on the selective ionization of the desired trace gas in the sample air followed by detection of artificially produced educt ions ($E^{\pm}$) and characteristic product ions ($P^{\pm}$) inside the mass spectrometer. Apart from its high time resolution and low detection limit, the CIMS technique offers high versatility: it provides the possibility of measuring a series of different trace gases if used with different precursor ions. If only one type of product ion is formed, the bimolecular ion-molecule reaction is described by the following equation:

$$E^{\pm} + X \xrightarrow{k} P^{\pm} + Y\,. \tag{3.1}$$

wherein X represents the trace gas molecules to be measured, $E^{\pm}$ the educt ions, and $P^{\pm}$ the formed product ions. Y is a neutral reaction product and k the rate coefficient of the specific ion-molecule reaction. For a bimolecular reaction the reaction rates are given as:

$$\frac{d[P^{\pm}]}{dt} = k[X][E^{\pm}]\,. \tag{3.2}$$

$$\frac{d[E^{\pm}]}{dt} = -k[X][E^{\pm}]\,. \tag{3.3}$$

The bimolecular temperature dependent rate coefficient k is given in $cm^3\,s^{-1}$ and is characteristic for each specific ion-molecule reaction. If assuming a high excess of trace gas molecules X, i. e. $[X] >> [E^{\pm}]$, reactions 3.2 and 3.3 can be treated as pseudo-first order reactions ($[X]_{(t)} \approx [X]_{(t=0)}$). With the introduction of $\tau = (k[X])^{-1}$ and the assumption of charge and mass conservation ($[E_0^{\pm}] = [E^{\pm}] + [P^{\pm}]$), their integration leads to:

$$[\mathrm{P}^{\pm}](t) = [\mathrm{E}_0^{\pm}](1 - e^{-\frac{t_r}{\tau}})\,. \tag{3.4}$$

$$[\mathrm{E}^{\pm}](t) = [\mathrm{E}_0^{\pm}]e^{-\frac{t_r}{\tau}}\quad. \tag{3.5}$$

Educt ($E^{\pm}$) and product ions ($P^{\pm}$) are detected simultaneously within the mass spectrometer. If rate coefficient k and reaction time t_r are known, the trace gas concentration can be calculated using the so-called **ACIMS-formula** (obtained through division of equations 3.4 and 3.5):

$$[\mathrm{X}] = \frac{1}{kt_r}\ln\left(1 + \frac{[\mathrm{P}^{\pm}]}{[\mathrm{E}^{\pm}]}\right)\quad. \tag{3.6}$$

Ion-molecule reactions are more efficient at higher pressures due to a higher collision rate of ions and molecules. Likewise, an increase of t_r results in a higher number of product ions and thus may improve for example the sensitivity of the measurement. On the other hand it has to be considered that the probability of wall losses as well as of undesired associating and backward reactions increases with increasing t_r.

Ideally, the educt ions should react in a high selective manner with the analyte molecules in order to produce only one kind of product ions. This condition is indeed not fulfilled in ambient conditions, but parallel reactions can be neglected for a small ratio of $[P^{\pm}]/[E^{\pm}]$. Otherwise, if a highly reactive educt ion is used or in the case of sampling strongly polluted air, equation 3.1 has to be extended. Instead of equation 3.6 the so-called **Parallel-ACIMS** Formula is obtained:

$$[\mathrm{X}_i] = \frac{1}{k_i t_r}\frac{[\mathrm{P}_i^{\pm}]}{\sum_{j=1}^{n}[\mathrm{P}_j^{\pm}]}\ln\left(1 + \frac{\sum_{j=1}^{n}[\mathrm{P}^{\pm}]}{[\mathrm{E}^{\pm}]}\right)\quad. \tag{3.7}$$

A more detailed theoretical description of ion-molecule gas phase reactions can be found for example in Wollny (1998).

3.2 Isotopic calibration

As discussed above, the concentration of the trace gas can be calculated using the **ACIMS-formula** (equation 3.6), if both rate constant and reaction time are known. However, the accuracy of CIMS-systems might be influenced by several reasons. The major uncertainty is often due to the uncertainty of the rate constants of the used ion-molecule reactions. Especially ambient water vapor variations can cause problems because the rate constants are strongly dependent on the number of water

molecules attached to the reagent ions. Wall losses or memory effects especially of sticky molecules might differ for varying humidity, too. Ion transmission or detector fluctuations of the mass spectrometer can also result in sensitivity variations, and an exact knowledge of the mass discrimination between educt and product ions is necessary. Therefore, continuous in-flight calibrations are essential in order to perform high accuracy measurements.

There are two different ways to perform in-flight calibrations of CIMS instruments. One way is to add a certain, well-known amount of the measured trace gas several times per flight in order to get information on the instrument performance over time and in different kinds of air masses. The most elegant way however is to use an isotopically labelled standard for an on-line calibration. It has the same ion chemical behavior within the measurement uncertainty of most MS systems, and provides calibration throughout the whole flight, because it does not interfere with the product ion of the measured atmospheric trace gas. However, there are some points worthy of attention: 1. The mass spectrometer needs a sufficient mass resolution to be able to separate the adjacent peaks which often lie only one or two mass peaks apart. 2. One has to ensure that no interfering signals contribute either to the mass peak of the measured trace gas or to the mass peak of the isotopic standard. Also the background of both mass peaks has to be determined regularly. 3. The isotopic distribution of both standard and ambient air has to be considered: Depending on the isotopic purity of the calibration gas, the standard may contribute to a minor extent also to the mass peak of the ambient atmospheric gas to be detected. The same argument holds for the ambient air, which may produce a signal also on the calibration mass peak, depending on the terrestrial isotopic distribution. The isotopic compositions of standard and ambient air are considered with the help of constants K_{ij}, where i represents the ambient (a = ambient) and standard mass peak (s = standard) to which the corresponding air j (a = ambient, s = standard) contributes. The ion intensities at both mass peaks I_a and I_s then are given by:

$$I_a = K_{aa} * C_a + K_{as} * C_s \; . \tag{3.8}$$

$$I_s = K_{sa} * C_a + K_{ss} * C_s \; . \tag{3.9}$$

C_a and C_s represent the mole fractions of the ambient and standard air, respectively. Equations 3.8 and 3.9 can be solved for the ambient mixing ratio C_a (Bandy et al., 1993):

$$C_a = C_s * \left(\frac{K_{ss} * R - K_{as}}{K_{aa} - K_{sa} * R} \right) \; . \tag{3.10}$$

Herein, R is the ratio of the signals at the ambient and standard mass peak, $R = I_a/I_s$. The constants K_{aa} and K_{sa} are calculated with the help of terrestrial distributions. K_{ss} and K_{as} reflect the purity of the isotopic standard, and have to be determined experimentally in the laboratory.

3.3 Ion trap mass spectrometers

The invention of the Ion Trap Mass Spectrometer (ITMS) goes back to 1953, when the later Nobel prize winner Paul suggested for the first time a mass filter without magnetic fields which made former MS systems heavy and unwieldy (Paul and Steinwedel, 1953; Paul and Raether, 1955). As mentioned above, the MPI-K group introduced the deployment of ion trap mass spectrometers for airborne measurements of atmospheric trace gases (Kiendler et al., 2000; Speidel et al., 2007; Fiedler et al., 2009; Aufmhoff et al., 2011).
Ion trap mass spectrometers offer certain advantages compared to often used linear quadrupole mass spectrometers: Ion traps have a large mass range (∼15–2000 amu), a high sensitivity also at high mass to charge (m/z) ratios and an excellent duty cycle. The quasi-simultaneous sampling of all ions over the desired mass range is especially helpful if air masses with different atmospheric trace gas concentrations are rapidly intercepted by a research aircraft, as is the case for example during sampled of aircraft exhaust plumes (Jurkat et al., 2011). A whole spectrum can be derived within milliseconds if a high time resolution is needed. On the contrary, at low ion concentrations a higher sensitivity can be obtained by increasing the sampling time (Fiedler et al., 2005; Aufmhoff et al., 2011). A mass resolution of ∼0.3 amu is achieved over the entire mass range which leads to an unambiguous detection of neighboring air masses. This is especially important if an isotopic calibration is used, as in the present study. The calibration peak is, dependent on the isotope used, generally one or two mass units apart from the ambient mass peak. Finally, an ITMS (ion trap mass spectrometer) allows the performance of fragmentation studies of mass selected ions, which may greatly improve ion identification. The ion fragmentation mode of an ITMS can be used in flight or in laboratory test measurements (Kiendler et al., 2000; Schröder et al., 2003).

In a paul ion trap a three-dimensional RF (radio frequency) field is created in order to store ions within defined boundaries. The trap consists of a ring electrode and two hyperbolic electrodes serving as end caps through which the ions can enter and leave the trap. Between these electrodes an electric potential is applied in such a way that ions of a certain mass to charge range (m/z) move on stable trajectories. The field strength disappears in the center of the trap and increases outwards which results in back-driving forces acting onto the ions. **Figure 3.1** shows a schematic of a quadrupole ion trap.
The electrode system is symmetric with respect to the axis of rotation z, thus for the mathematical description it is appropriate to use cylindric coordinates (ρ, φ, z).
The applied potential is a superposition of a constant voltage U and an alternating voltage $V\cos(\omega t)$, generally expressed as:

$$\phi_0 = U - V\cos(\omega t)\,. \tag{3.11}$$

with $\omega = 2\pi f$ and f the frequency of the alternating potential.

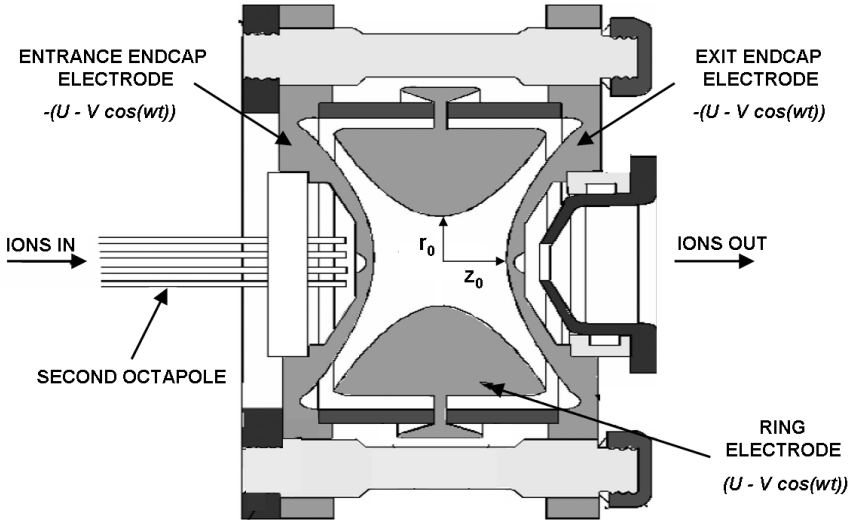

Figure 3.1: *Schematic of a quadrupole ion trap [graphic by Finnigan].*

The distances of the electrodes are designed in a way that the condition $\varphi_0^2 = 2z_0^2$ (in cartesian coordinates $r_0^2 = 2z_0^2$) is fulfilled and the field, which satisfies the Laplace´s equation $\Delta\phi = 0$ can be described as follows (March and Hughes, 1989):

$$\phi(\rho, \varphi, z, t) = \frac{\phi_0}{\rho_0^2}(\rho^2 - 2z^2)\,. \tag{3.12}$$

An ion with charge Q and mass m will experience a force in the electric field described by:

$$F = ma = -Q\,\vec{\nabla}\,\phi. \tag{3.13}$$

Differentiation of 3.12 and applying on 3.13 leads to:

$$\frac{d^2\rho}{dt^2} + \frac{2Q}{m\rho_0^2}(U - V\cos\omega t)\rho = 0\,. \tag{3.14}$$

$$\frac{d^2z}{dt^2} - \frac{4Q}{m\rho_0^2}(U - V\cos\omega t)z = 0\,. \tag{3.15}$$

With introduction of the dimensionless parameters

$$\xi = \omega t/2, \qquad a_z = -2a_\rho = \frac{8QU}{m\rho_0^2\omega^2}, \qquad q_z = -2q_\varphi = \frac{4QV}{m\rho_0^2\omega^2} \tag{3.16}$$

the following **Mathieu-equations** can be derived (which describe the uncoupled motion of an ion in the r- and z-directions):

$$\frac{d^2\rho}{d\xi^2} + (a_\rho - 2q_\rho \cos(2\xi))\rho = 0\,. \tag{3.17}$$

$$\frac{d^2 z}{d\xi^2} + (a_z - 2q_z \cos(2\xi))z = 0\,. \tag{3.18}$$

The solutions of the Mathieu-equations can be found e. g. in Mathieu (1868) or McLachlan (1947). To remain stored in the trap an ion has to be simultaneously stable in both the ρ and z directions. The occurrence of stable ion trajectories depends on the parameters β_ρ and β_z which are determined by the stable solutions of the Mathieu-equations. These solutions can be summarized in a stability diagram, which is in **Figure 3.2** given for a paul ion trap, using cartesian coordinates according to **Fig. 3.1**.

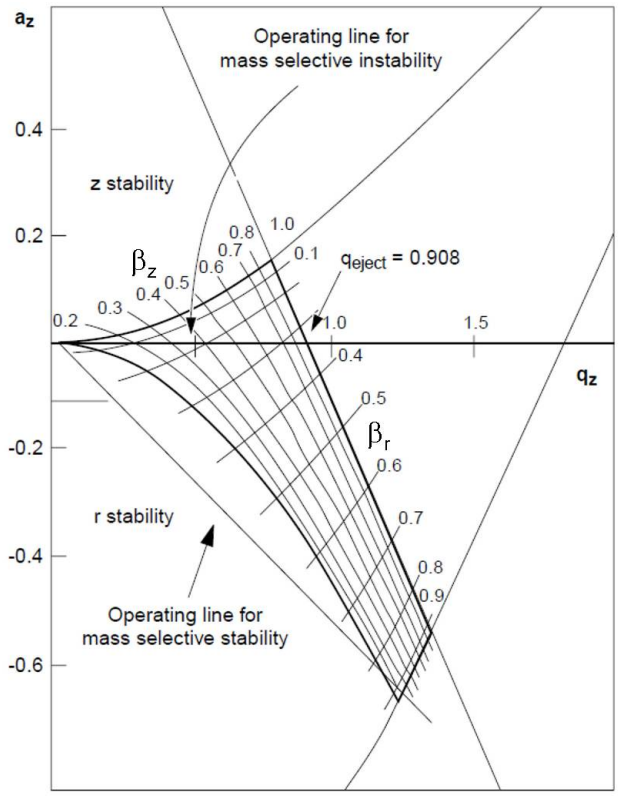

Figure 3.2: *Stability diagram for a paul ion trap, adapted from March and Todd (1995).*

The stability diagram shows a theoretical region where radial and axial stability of the ion motions overlap. Depending upon the amplitude of the voltage applied to the ring electrode, an ion of a given m/z will have β_ρ and β_z values that will fall within the boundaries of the stability diagram, and the ion will be trapped. If the values at that voltage fall outside of the boundaries of the stability diagram, the ion will hit the electrodes and be lost. Ions of different m/z values have stable orbits at the same time.

The Ion Trap Mass Spectrometer (ITMS) used in the present work is commercially available from Finnigan (Finnigan MAX LCQ, Finnigan Company USA). **Figure 3.3** shows a schematic of the manifold of the employed ITMS. The ITMS was initially equipped with an electro spray unit which allows the measurements of liquids. This ionization unit was replaced by a stainless steel adapter to enable the mounting of the flow reactor, a tubing with 40 mm diameter (Kiendler et al., 2000). The originally at the front of the first octapole mounted skimmer was replaced by a critical orifice (front electrode) which permits a higher gas flow.

The manifold comprises two pumping stages, the first pumping stage is pumped down to about 10^{-3} hPa whereas the second is evacuated to $3 \cdot 10^{-5}$ hPa. This is done by a turbomolecular pump (Balzers Pfeiffer TMH 260/130), backed by a membrane pump (MZ D4 vacuum brand). The front electrode is followed by an ion optic in order to increase the ion transmission. The optic focuses the ions onto the entrance cap electrode by means of two octapoles and one inter-octapole lens (see also **Fig. 3.1**). The sign of the applied potential is opposite to the sign of the measured ions. The system can be tuned onto the desired m/z ratio in order to increase the count rate for these ions and thus improve the sensitivity. This is done by appropriate setting of the different voltages of the front electrode, the two octapoles, the inter-octapole lens and also of the radio frequency. It is worth mentioning that tuning results in mass discrimination, especially of lower masses (March and Todd, 1995). This effect has to be considered when the ACIMS-formula (equation 3.6) is used.

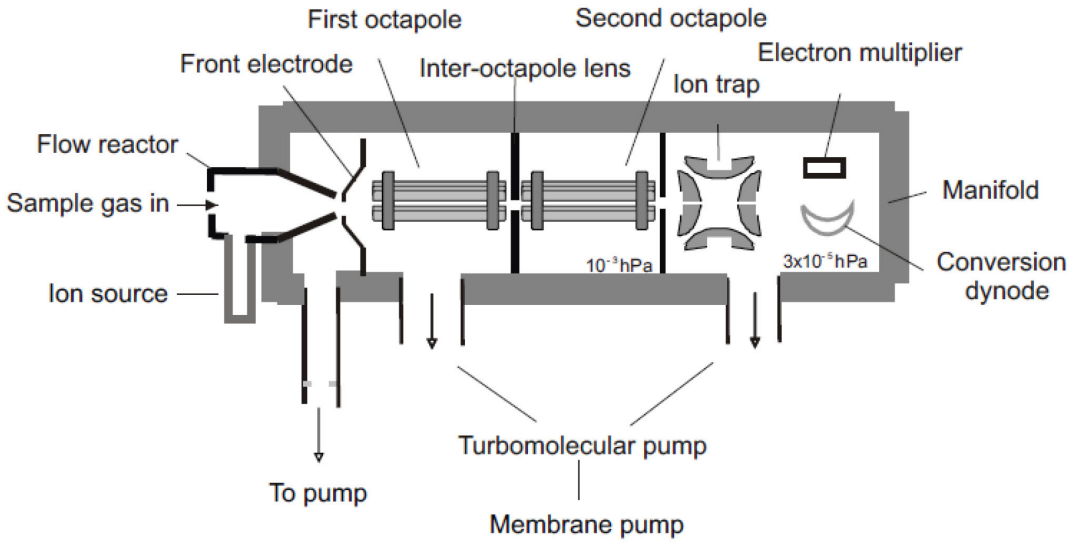

Figure 3.3: *Schematic of the ion trap mass spectrometer. A small part of the ionized sample air enters the first pumping stage via the front electrode. It follows the ion optic which comprises two octapoles and an inter-octapole lens. The ion optic focuses the ions onto the entrance endcap electrode of the ion trap. Ions leaving the trap hit a conversion dynode, and emitted electrons are detected by an electron multiplier.*

The entrance of the ions into the trap is not continuous but pulsed, controlled from the inter-octapole lens which works as electronic gate. For a short time period, the so-called injection time[1], an attractive potential (max. $\pm$ 10V) is applied to the gate carrying the ions into the second octapole

[1] The injection time is typically in a range of 10^{-2} s to 10 s (dependent on e.g. the mole fraction of the trace gas).

region. Afterwards a repulsive potential of $\mp$ 300V applied to the inter-octapole lens prevents the ions to enter the second chamber. The injection time can be fixed by the operator but it is also possible to run the ITMS in the automatic gain control mode (AGC). In this case, a short pre-scan is performed (duration of about 0.2 ms) to obtain the actual ion concentration which varies due to changing humidity and trace gas abundance. The system then automatically adjusts the appropriate injection time for the analytic scan, corresponding to the maximum number of ions allowed in the trap (so-called *MS target*). This is important in order to avoid space-charge effects, which will result in a loss of mass resolution (see section 4.1.4).

The trap contains Helium as buffer gas in order to slow down the incoming ions. As described above, the injected ions of the pre-set m/z range then move inside the trap on stable trajectories. Entering ions loose a part of their kinetic energy through collisions with the He atoms and thus are confined closer to the center increasing the trapping efficiency (Stafford et al., 1984). Additionally, dissociation of ions is induced resulting in the dismantling of associated water clusters which simplifies the obtained spectra (see also section 4.1.2). This process can be used also for fragmentation studies which help to identify formerly unknown product ions (referred to as MS^2 or MS^n mode). In this case an additional RF (radio frequency) at the end cap electrodes is applied and the ions decompose through ion resonance excitation. This may facilitate the identification of the parent ions, since lower mass lines are easier to identify.

The mass scan is performed during the ion read-out process by changing the RF potential (scan-rate = 5500 amu/s). As discussed above, the RF amplitude is ramped up at a constant rate which increases the amplitude of the trajectories of the trapped ions. They become destabilized in the axial direction and are ejected one after another through the end-cap electrode, starting with low m/z ratios. The exit lens (at ground potential) focuses the ions towards a conversion dynode, which is located off-axis at a right angle to the ion beam and generates secondary electrons by ion impact. Thereafter, the electrons are amplified by an electron multiplier and converted into an electric current (15 channels/mass). The current is digitized by an analogue-to-digital converter and finally software-processed.

With the help of a software, all voltages of the ion optics and the trap chamber can be tuned in order to optimize the ion current and thus improve the detection sensitivity of the ions with the desired m/z ratio. The optimized parameters are stored in a so-called *Tune-File*. The system allows software-averaging over the sum of several single mass spectra obtained (so-called micro-scans) to one macro-scan, which may increase the signal-to-noise (S/N) ratio considerably (see section 4.1.4). The micro-scan time comprises the time for the injection of ions (injection time), the time the ions are ejected for the mass scan (read-out time, dependent on the size of the chosen mass range) and several delay times, e.g. for the adjustment of the different voltages. The final time resolution is then given by the micro-scan time multiplied by the selected number of micro-scans. The conversion of the mass spectra obtained into time-series for each single mass peak as well as further data processing is carried out with the help of a custom-written routine in a commercial software (IGOR Pro).

Chapter 4

The new airborne instrument: FASTPEX

In this chapter the new FASTPEX (**Fast** Measurements of **Pe**rox**x**yacyl nitrates) instrument is described. The FASTPEX system uses an ion trap mass spectrometer previously developed and deployed by a DLR/MPIK collaboration (see also previous section 3).
Section 4.1 presents the set-up and discusses the laboratory experiments. It starts with a presentation of the PAN calibration source (PCS), which was built and characterized in the framework of this thesis (4.1.1). The ion-molecule reaction (IMR) for the detection of PAN is introduced, and its dependency on several parameters is described (4.1.2). The IMR uses a dissociation product of PAN, which is generated in the thermal decomposition region (4.1.3). Subsequently, the optimization of the utilized ion trap mass spectrometer is presented (4.1.4). The first field deployment of FASTPEX took place aboard the DLR Falcon in summer 2008 during GRACE campaign[1] (see section 5). The instrument performance during this field experiment is discussed in section 4.2. After the presentation of typical mass spectra (4.2.1), the importance of the in-flight calibration (4.2.2) as well as the influence of ambient water vapor is described (4.2.3). Some examples of atmospheric PAN and PPN measurements are given (4.2.4 and 4.2.5). Finally, the results of a PAN in-flight intercomparison are presented (4.2.6).

4.1 Set-up and laboratory experiments

4.1.1 PAN calibration source (PCS)

Due to its thermal instability, PAN cannot be stored for example in gas bottles but it has to be produced in-situ with the help of a photochemical method (Warneck and Zerbach, 1992). The formation of PAN is initiated by the photolysis of acetone ($CH_3C(O)CH_3$) in the presence of oxygen. The generated radicals then oxidize a small, well-defined amount of nitric oxide (NO) first to NO_2, and in a second step, PAN is formed. A schematic of the PAN calibration source (PCS) is given in **Fig. 4.1**. The main gas stream is synthetic air containing acetone (~200 μmol mol^{-1}, Air Liquide) which streams through a reaction chamber made of quartz glass. A small flow of a NO calibration gas is added upstream of the reaction vessel (NO/N_2, 3 μmol mol^{-1}, Air Liquide).

[1] **Gr**eenland **A**erosol and **C**hemistry **E**xperiment

The gas flows are controlled using mass flow controllers (MFC, Bronckhorst). The reaction chamber is externally covered with an aluminium foil. A phosphorous coated pen-ray lamp (Jelight Corp.) is bordered pressure-tight into the center of the chamber cap. The reaction vessel is temperature-stabilized (∼15°C) in order to minimize thermal losses of the produced PAN. A fore-pressure controller (FPC) regulates the chamber pressure and keeps it constant at 1050 hPa.

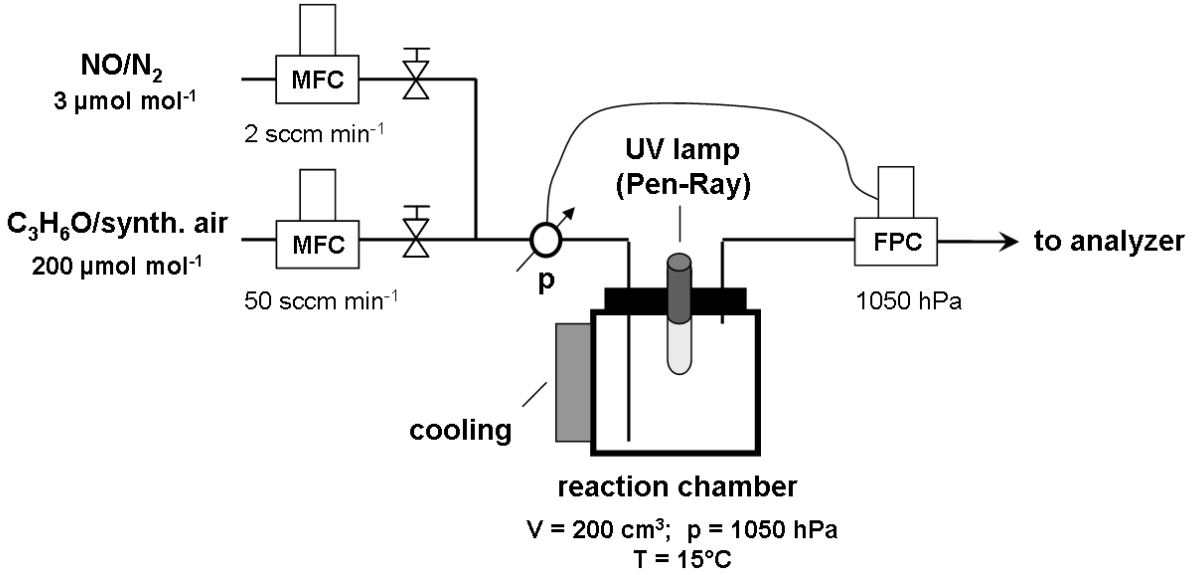

Figure 4.1: *Schematic of the PAN calibration source (PCS). The reactions take place in a temperature- and pressure-stabilized reaction vessel (quartz glass). A small amount of NO calibration gas is added to the main gas flow of a $CH_3C(O)CH_3$/synthetic air mixture. All tubings (1/8" or 1/4") are made of Teflon (PTFE, polytetrafluoroethylene) or PFA (perfluoro alkoxy). UV light with a wavelength of ∼285 nm photolyzes $(CH_3)_2CO$, hereby initializing photochemical reactions. All given mass flows, pressure, and temperatures represent values optimized in a series of laboratory experiments.*

The first step in the PAN formation is the photolysis of acetone. Acetone is the most suitable hydrocarbon precursor for the efficient production of PAN. Photolysis of acetone leads to the formation of the direct PAN precursor, the peroxyacetyl radical ($CH_3C(O)O_2$). The photodissociation rate of a molecule is given by the product of the spectral actinic flux and the absorption cross section. **Fig.** 4.2 shows the absorption cross sections of acetone, PAN and NO_2 between 240 nm to 340 nm (Atkinson et al., 2004, 2006). In this wavelength region, acetone has a maximum absorption cross section around 270 to 280 nm. PAN is photolyzed in the UV spectral range with absorption cross sections of several 10^{-18} cm^2 at wavelengths around 200 nm, but as evident in **Fig. 4.2**, it absorbs much less towards higher wavelengths. NO_2 is a strong absorber in the entire ultraviolet and visible range of the solar spectrum, but has a local absorption minimum in the region around ∼250 nm. Ideally, acetone is photolyzed with high efficiency, whereas NO_2 and PAN should not absorb significantly. As shown in **Fig.** 4.2, the used UV lamp Typ "285" (Jelight-Corp.) has its maximum emission intensity around 285 nm, and therefore is well-suited for our application.

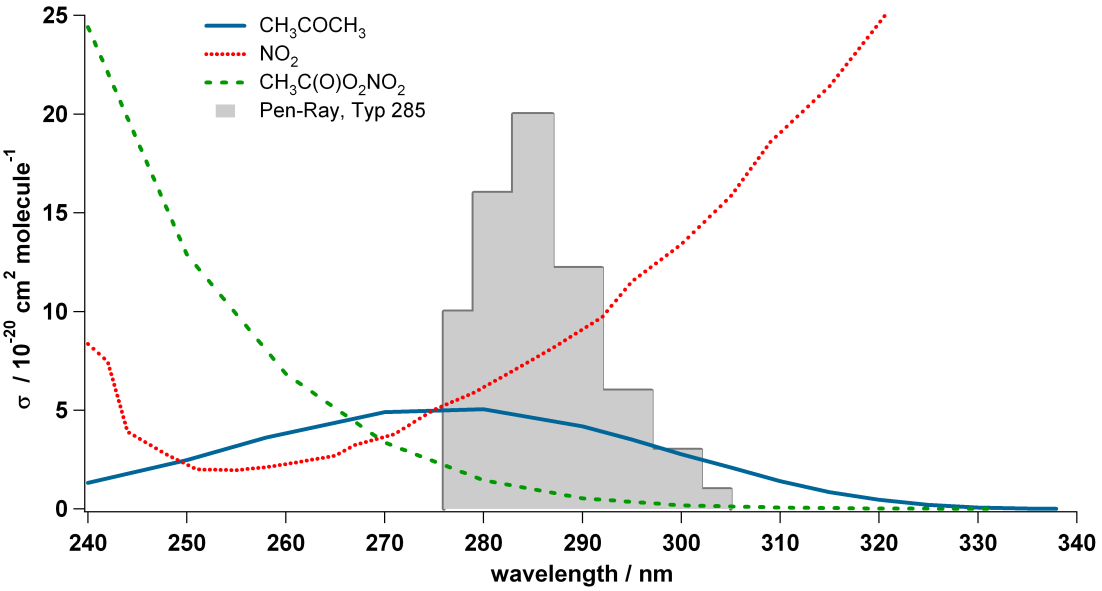

Figure 4.2: *Absorption cross sections between 240 nm and 340 nm: Acetone (blue solid line), NO_2 (red dotted line) and PAN (green dashed line). The emission spectrum of the utilized Pen-Ray UV lamp has a maximum around ∼285 nm (grey pattern, intensity in arbitrary units).*

The reactions relevant for the PAN formation are given in equations 4.1a to 4.1g (Volz-Thomas et al., 2002).

$$\mathrm{CH_3C(O)CH_3} + h\nu + \mathrm{O_2} \rightarrow \mathrm{CH_3C(O)OO} \qquad \varphi_{CH_3CO} \sim 0.3\,, \tag{4.1a}$$

$$\rightarrow \mathrm{CH_3OO} \qquad \varphi_{CH_3} \sim 0.3\,, \tag{4.1b}$$

$$\mathrm{CH_3C(O)OO + NO} \rightarrow \mathrm{CH_3C(O)O + NO_2}\,, \tag{4.1c}$$

$$\mathrm{CH_3OO + NO} \rightarrow \mathrm{CH_3O + NO_2}\,, \tag{4.1d}$$

$$\mathrm{CH_3C(O)OO + NO_2} \rightleftharpoons \mathrm{CH_3C(O)OONO_2}\,, \tag{4.1e}$$

$$\mathrm{CH_3O + NO_2} \rightleftharpoons \mathrm{CH_3ONO_2}\,, \tag{4.1f}$$

$$\mathrm{CH_3OO + NO_2 + M} \rightleftharpoons \mathrm{CH_3OONO_2 + M}\,. \tag{4.1g}$$

The photolysis products of acetone (CH_3CO and CH_3) react quasi-instantaneously with abundant oxygen hereby forming peroxy radicals $CH_3C(O)O_2$ and $CH_3(O)O$ (reactions 4.1a - 4.1b). For this reason, a mixture of acetone in synthetic air (N_2/O_2) instead of pure N_2 is used. The quantum yields φ_{CH_3CO} and φ_{CH_3} depend on the exact wavelength, the given values represent only average values for this wavelength region (Atkinson et al., 2006). The peroxy radicals oxidize the added nitric oxide in a first step to NO_2 (reactions 4.1c - 4.1d). NO_2 is not used directly as precursor gas, because it is observed to be lost on stainless steel surfaces whereas NO has a much better stability. Finally, PAN is formed via reaction 4.1e. Also other peroxy nitrates are produced (reactions 4.1f - 4.1g). However, these are thermally even less stable than PAN and readily decompose again (Atkinson et al., 2004).

Optimization of the PCS

The PAN mixing ratio produced in the PCS (C_{PAN}) is given by the product of the NO mixing ratio and the conversion efficiency CE_{PCS}:

$$C_{PAN} = \frac{Q_{NO} \times NO_b}{(Q_{acetone} + Q_{NO})} \times CE_{PCS} \,. \tag{4.2}$$

Herein, $Q_{acetone}$ and Q_{NO} represent the respective mass flows and NO_b the NO mixing ratio of the used calibration gas bottle. The conversion efficiency CE_{PCS} reflects the factor by which the added NO is converted into PAN. If acetone is added in great excess to ensure sufficient radical production, the conversion of NO into PAN is close to 100%. CE_{PCS} was analyzed and optimized in the laboratory. For these experiments, a chemiluminescence detector (CLD) for the measurement system of nitrogen monoxide (NO) was coupled with different converters in order to detect NO, NO_2, HNO_3 and total NO_y ($NO_y = NO + NO_2 + NO_3 + HNO_3 + N_2O_5 + PAN...$) (Fahey et al., 1985; Feigl, 1998). Although PAN is not directly measured with the utilized instrument combination, this kind of set-up is often used for the characterization of photolytic PAN calibration sources (e. g. Flocke et al. (2005b)). It allows for the detection of the precursor gas NO, the intermediate product NO_2, and the possible formed impurity HNO_3. PAN itself is quantified indirectly, by assuming that $PAN \approx NO_y$ - NO - NO_2 - HNO_3. The laboratory set-up for the PCS characterization studies is presented in **Fig. 4.3**.

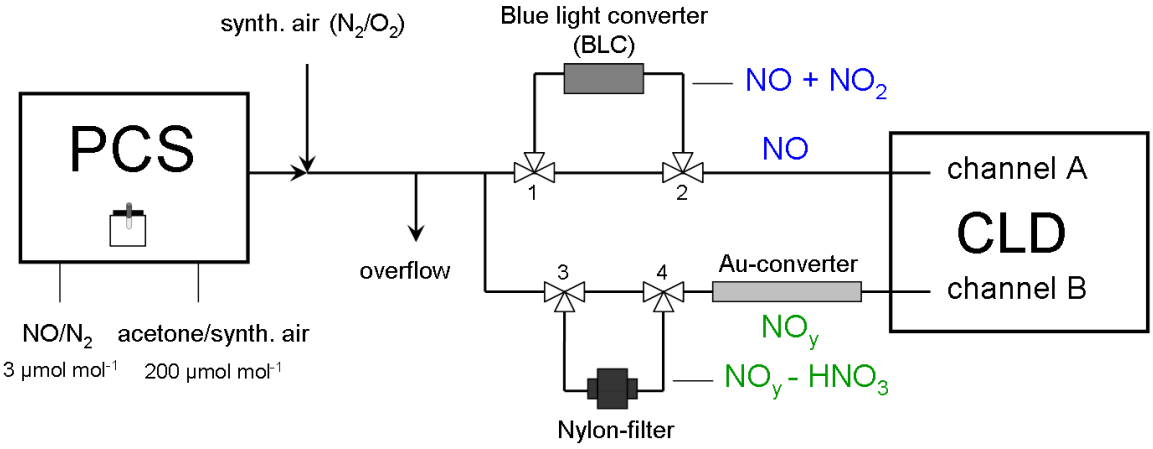

Figure 4.3: *Experimental set-up for the characterization of the PAN calibration source. The output of the PCS was measured using a chemiluminescence instrument (CLD). The CLD measures NO in two independent channels. Depending on the configuration in front of the CLD, also the sum of ($NO+NO_2$), NO_y, and the difference of (NO_y-HNO_3) can be detected. All sampling lines were made of Teflon® or PFA (1/4").*

The CLD instrument uses the chemiluminescence technique for the measurement of NO and has two independent channels A and B (Feigl, 1998). It needs a mass flow of ~1.5 slm per channel, therefore the output of the PCS was first diluted with synthetic air (5 slm, Air Liquide, purity 5.0). Depending

on the configuration in front of the CLD, further oxidized nitrogen compounds can be detected. The sum of NO and NO_2 is measured, if the sample air is passed first through an UV blue light converter (BLC). Herein, NO_2 is selectively photolyzed to NO by using ultraviolet light emitting diodes with a narrow spectral output around 385 nm. The photolysis takes place in a region where only NO_2 has an absorption band, but no other NO_y compounds as for example HONO, NO_3 and PAN (see **Fig. A.2**). The NO formed in the BLC subsequently is detected in channel A. The sum of all NO_y compounds is measured when the sample gas first is drawn through a heated Au converter (300 °C). Herein, oxidized nitrogen compounds as for example NO_2, HNO_3 and PAN are reduced to NO by adding carbon monoxide (CO) as reducing agent (Fahey et al., 1985; Feigl, 1998). Finally, the converted NO_y species are detected as NO in channel B. Nitric acid (HNO_3) can be measured using an indirect method. HNO_3 is a sticky molecule and adsorbs readily to surfaces. The adsorption is especially efficient on nylon surfaces (e. g. Talbot et al. (1990)). For the PCS experiments, HNO_3 was removed from the sample gas with the help of a Nylon membrane filter (Nylasorb^{TM}, pore size 1 μm) from which three are stacked in a PTFE filter pack. Since all other NO_y compounds pass the filter without being lost, HNO_3 can be determined by taking the difference between the NO_y and (NO_y - HNO_3) measurement mode. **Figure 4.4** shows exemplary a time sequence of a laboratory experiment carried out for the characterization of the PCS.

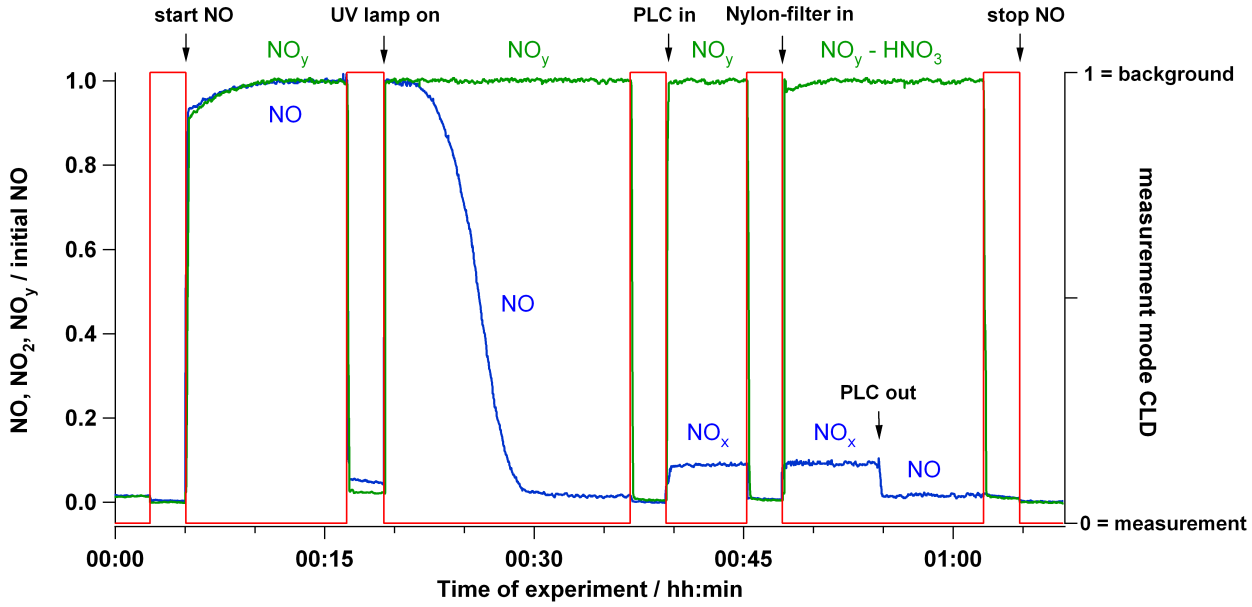

Figure 4.4: *Time-series of a laboratory experiment carried out for the characterization of the PCS output. Depending on the measurement configuration, the blue line shows either NO or NO_x ($NO + NO_2$), whereas the green line gives either NO_y or (NO_y - HNO_3) (please note also the remarks at the top). All mixing ratios are given relative to the initial NO mixing ratio. The red line gives the CLD measurement mode. Mode "0" corresponds to the normal NO measurement mode, whereas Mode "1" denotes a background measurement (see scaling at the right axis).*

The output of the PCS was analyzed by measuring NO, NO_2, HNO_3 and NO_y. The NO sensitivities of both channels A and B were determined before and after each experiment. The conversion

efficiency of the BLC (~70%) and of the gold tube converter (~100%) was calibrated using a known amount of NO_2, generated by gas phase titration of a NO standard with O_3, described in detail in (Feigl, 1998). Conversion efficiency for PAN and other NO_y compounds is assumed to be similar to that of NO_2 (Fahey et al., 1985; Feigl, 1998). In **Fig. 4.4** all mixing ratios are given relative to the initial mixing ratio of NO. The blue line corresponds to the measurements obtained from channel A. Depending on the position of the hand valves 1 and 2, either NO or NO_x ($NO_x = NO + NO_2$) was detected (see **Fig. 4.3**). The green line corresponds to the mixing ratios derived from channel B, which measures either NO_y or the difference of (NO_y - HNO_3), by switching of hand valves 3 and 4. The red line gives the measurement mode of the CLD instrument (axis on the right). Mode "0" corresponds to the normal NO measurement mode, whereas Mode "1" denotes a background measurement, which was performed several times predominantly at the end of a certain measurement configuration.

At the beginning of the experiment, channel A was in the NO measurement configuration whereas channel B measured NO_y. During the first few minutes, the PCS was fed only with the acetone/synthetic air mixture, diluted with 5 slm synthetic air (N_2/O_2). After ~5 min., the NO calibration gas was added to the acetone/synthetic air flow, upstream of the reaction vessel (see **Fig. 4.1**). The residence time in the reaction chamber is several minutes, therefore it takes a certain time until a constant mixing ratio is established and measured by the CLD instrument. Both the NO and the NO_y channel detect similar mixing ratios since the sample flow only contains NO and not yet higher oxidized nitrogen compounds. After ~19 min., the UV lamp was switched on. As a result, the NO signal in channel A decreased to values close to zero within ~10 min., because NO now is efficiently oxidized by the radicals generated by the photolysis of acetone (see reaction 4.1b to 4.1c). The decrease of the NO concentration is delayed since it takes a few minutes until the reaction chamber is completely flushed (and because of the burn-in time of the UV lamp). Inside the Au converter in channel B, all oxidized nitrogen compounds including NO_2 and PAN are reduced to NO. Therefore the signal in channel B remains constant. After ~39 min., the photolysis converter was switched into the sampling line in front of channel A using hand valves 1 and 2. In this configuration, channel A measures not only NO but NO_2 in addition, and shows a clear signal increase due to the abundance of NO_2. This indicates that not all produced NO_2 is further oxidized to PAN or other peroxymethyl nitrates. After 48 min., the Nylon-filter was switched into channel B. In this configuration, HNO_3 should be efficiently removed, however, the signal in channel B does not show a decrease[2]. HNO_3 is produced in the gas phase by the reaction of NO_2 with OH ($NO_2 + OH \rightarrow HNO_3$). This reaction however is sufficiently suppressed by the use of dry calibration gases. The concentration of H_2O, the precursor of OH, seems to be too small to produce traceable amounts of HNO_3.

The NO to PAN conversion efficiency of the PCS (CE_{PCS}) was optimized by using different mass flows of the acetone/synthetic air carrier gas (20 to 100 sscm min^{-1}) as well as several $CH_3C(O)CH_3$ mixing ratios (50, 100 and 200 μmol mol^{-1}). Also different reaction chamber sizes (V = 100, 200 and 500 cm^{-3}) have been used in order to study e. g. the influence of the reaction time. Best results were found with the parameters given in **Fig. 4.1**. Under these conditions, a maximum NO to

[2]The lower HNO_3 values at the very beginning of this measurement mode are due to pressure variations.

PAN conversion efficiency CE_{PCS} of 92($\pm$5%) was reached, with the remainder mainly in form of NO_2 (see discussion below). These results are comparable with similar PAN sources described in the literature (Volz-Thomas et al., 2002; Flocke et al., 2005b). For ambient measurements, isotopically labelled $^{13}C_3$-acetone is used (see section 4.1.2.1).

Figure 4.5 shows a photograph of the built PAN calibration source. The 19"-chassis contains all components of the PCS, as for example the reaction chamber and the cooling device. In addition, all mass flow, pressure and temperature controllers for the operation of the FASTPEX instrument are integrated into the PCS chassis. In order to save space and weight, the NO and acetone calibration gases are stored in stainless steel tanks (Swagelok). These are refilled from 10 L calibration bottles a few hours prior each flight.

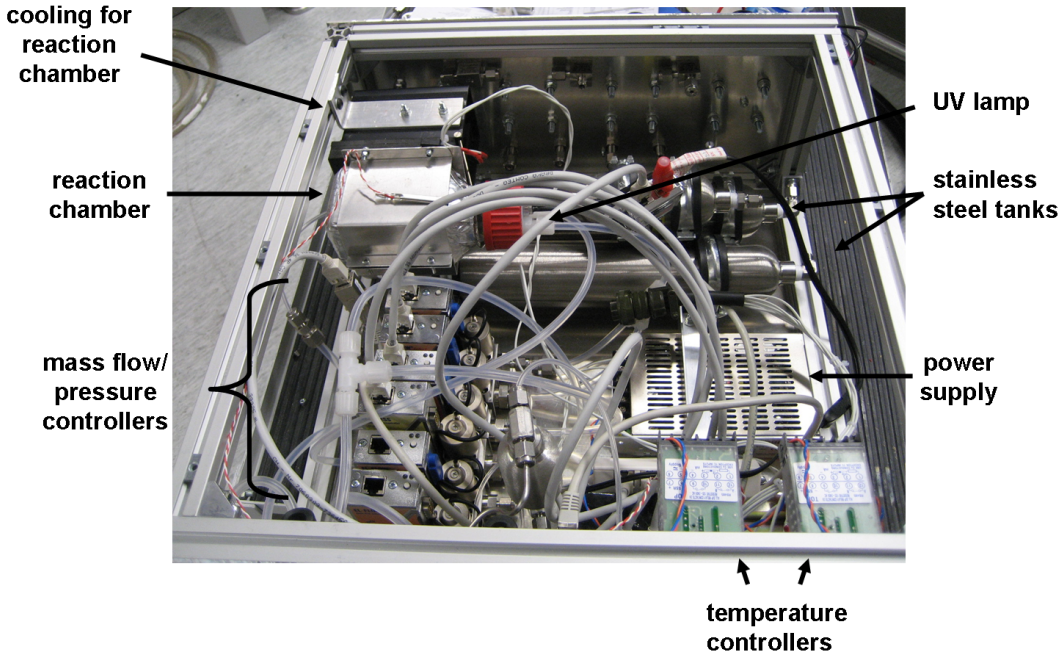

Figure 4.5: *Photograph of the PAN calibration source (PCS). The 19" chassis houses the reaction chamber, the chamber cooling, a series mass flow and pressure controllers as well as several stainless steel tanks for the calibration gases.*

Accuracy of the PCS

The PAN mixing ratio produced with the help of the PCS is calculated by equation 4.2. The accuracy of the PAN concentration depends on the uncertainties of several parameters, such as those of the different mass flows and of the NO calibration gas. The highest uncertainty however is given by the accuracy of the NO to PAN conversion efficiency of the PCS (CE_{PCS}). For identical conditions, CE_{PCS} was found to be highly reproducible ($\pm$1% after a burn-in time of the UV lamp of $\sim$15 min). The laboratory studies for the determination of CE_{PCS} were conducted as relative experiments since the conversion efficiency was determined relative to initial NO. Therefore, $\triangle CE_{PCS}$ is independent from the absolute accuracy of the CLD instrument itself. However, the uncertainty of the BLC photolysis efficiency has to be considered which is estimated to $\pm$3%, given by the uncertainty of the calibration using gas phase titration of NO. The accuracy of the conversion efficiency of

the NO_y converter can be neglected: All initial NO was found again in the NO_y mode hereby confirming the 100% conversion efficiency determined by the calibrations. A small uncertainty of CE_{PCS} remains because we were not able to measure higher oxidized methyl nitrates which possibly are also formed (see equations 4.1f - 4.1g). Certainly these are also measured in the NO_y mode and therefore cannot be distinguished from PAN. The thermal lifetime of methyl nitrates is only a few seconds at room temperature (Atkinson et al., 2006). However, the abundance of NO_2 may lead to a steadily production of methyl nitrates meaning that they might be abundant at trace amounts. To account for these inaccuracies, the total uncertainty of CE_{PCS} is estimated to $\pm 5\%$.

4.1.2 Ion chemistry for PAN detection

The CIMS method is based on an ion-molecule reaction between artificially produced educt ions and the trace gas to be measured (see chapter 3.1). The product ions hereby formed subsequently are detected by the mass spectrometer. For the measurement of PAN, the ion-molecule reaction of I^- with the thermal decomposition product of PAN, the PA radical is used ($k = 9^{+7}_{-5} \times 10^{-10}\,cm^3\,s^{-1}$ in He at 67 Pa (Villalta and Howard, 1996)):

$$CH_3C(O)O_2 + I^-(H_2O)_n \rightarrow CH_3C(O)O^-(H_2O)_n + IO\,. \tag{4.3}$$

Figure 4.6 shows a schematic of the processes taking place in front and inside the flow reactor (FR).

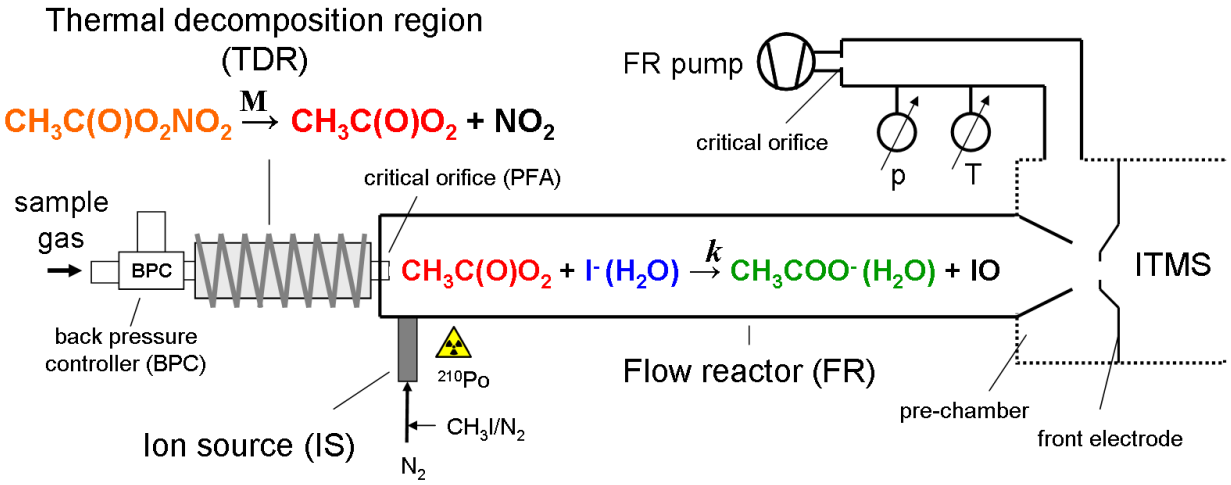

Figure 4.6: *Schematic of the ion-molecule reaction used for the detection of PAN. The sample gas first is drawn through a heated inlet, the thermal decomposition region (TDR). Inside the flow reactor (FR), the PA radicals generated in the TDR react with the reagent ions $I^-(H_2O)_{n=0,1,2...}$, coming from the ion source (IS). A small amount of the ionized air then is analyzed in the ITMS.*

The ion-molecule reaction involves not PAN itself, but the PA radical ($CH_3C(O)O_2$). The sample gas therefore is drawn first through the thermal decomposition region (TDR). In the heated PFA tube (∼180° C) the PA radicals are generated through the breakup of the PAN molecules (see next section 4.1.3). The total sample mass flow is regulated by the combination of the back-pressure controller (BPC) with a PFA critical orifice. The latter separates the TDR from the flow reactor (FR). The sampling gas is then introduced into the FR (stainless steel, 40 mm OD) where it mixes with the reagent gas coming from the ion source.

The reagent ions I^- are produced in a radioactive ion source (Polonium 210, $\tau_{1/2}$=138.4 d) by dissociative electron attachment to CH_3I molecules. A small amount of a CH_3I/N_2 gas mixture (1000 μmol mol^{-1} CH_3I) is added to the N_2 carrier gas which subsequently passes through the ^{210}Po inline-ionizer (740 mBq, NRD, Model P-2031). The α-particles emitted by the ion source fragment the CH_3I molecules and free electrons attach to the electronegative iodine I ($EN_{Pauling} = 2.88$ eV). The I^- ions react very rapidly with atmospheric water vapor molecules, leading to hydrated $I^-(H_2O)_n$ cluster ions. These serve as effective reagent ions for the detection of PA-radicals formed in the TDR leading to product ions $CH_3C(O)O^-(H_2O)_n$ (see equation 4.3). Ion-molecule reactions take place along the whole length of the FR. The FR pressure is controlled by a second critical orifice in front of the flow reactor pump. **Figure 4.7** shows a photograph of the laboratory set-up in front of the ion trap mass spectrometer (IT-MS).

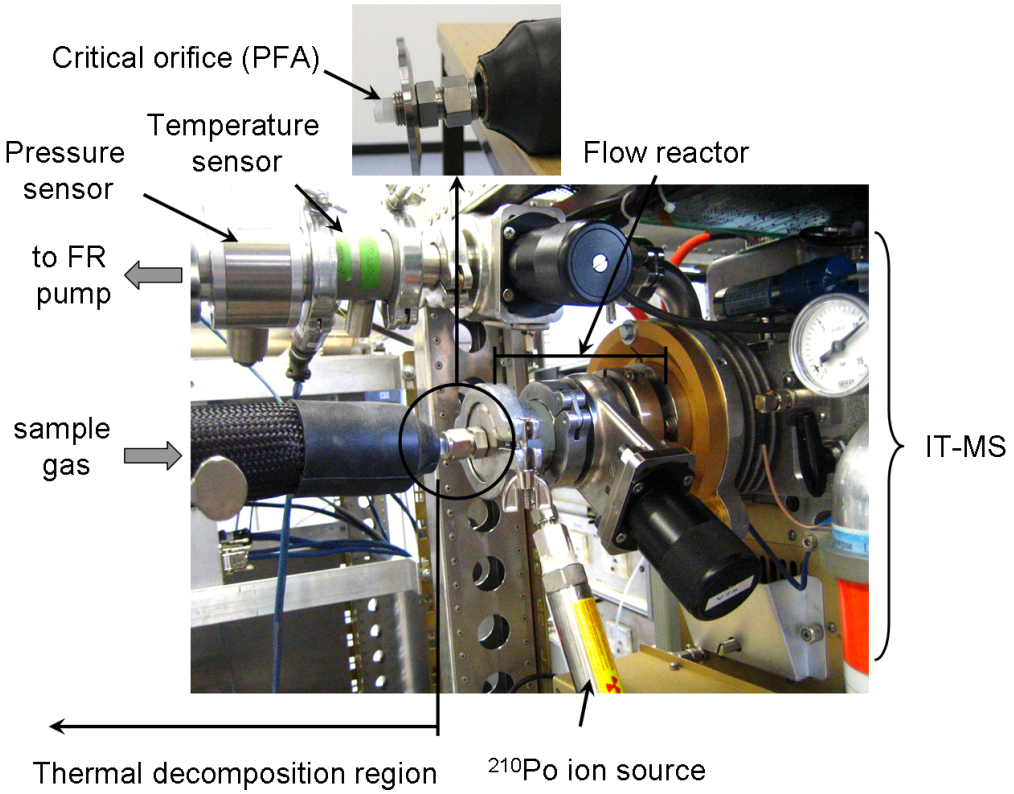

Figure 4.7: *Photograph of the laboratory set-up of the inlet part in the front of the ion trap mass spectrometer. The protection cover of the radioactive ion source is removed for demonstration purposes.*

In order to avoid contact of the sample air with stainless steel, the PFA tube is fed through the small flange adapter and is mounted outside with a stainless steel fitting (see small inset at the top of **Fig. 4.7**). The custom-made PFA critical orifice is pressed into the PFA tube which extends into the flow reactor FR. The FR itself reaches into the pre-chamber of the ITMS, which is evacuated by the flow reactor pump (see also **Fig. 4.6**).

The acetate ion CH_3COO^- clusters stronger with water molecules than I^- ($\triangle G_0 = 39\,kJ\,mole^{-1}$ compared to $\triangle G_0 = 23\,kJ\,mole^{-1}$). The formed product ions therefore normally are distributed in several mass peaks due to the formation of hydrates ($CH_3C(O)O^-(H_2O)_{n=0,1,2..}$). This would reduce the signal on the mass peak of the dehydrated product ion $CH_3C(O)O^-$ and as a result, the signal-to-noise ratio (S/N). To minimize this effect, LQMS (linear quadrupole mass spectrometer) systems are often employed together with a collision dissociation chamber (CDC) in which hydrated ions undergo dehydration before the ions enter the quadrupole. Inside the ion trap, ions are efficiently dehydrated through collisions with the damping gas helium (see section 3.3). Therefore, apart from measurements at high water vapor mixing ratios as e.g. in the humid boundary layer, essentially only the dehydrated product ion is present in the mass spectra (see also section 4.2.1).

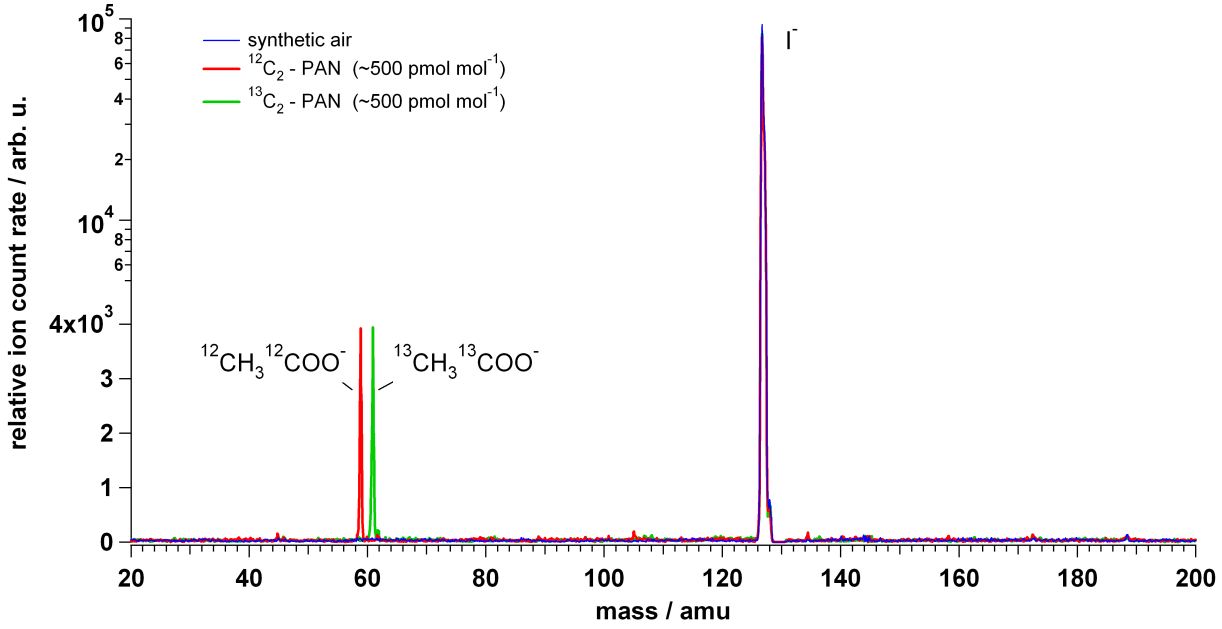

Figure 4.8: *Three mass spectra merged into one figure. Mass spectrum as obtained with zero air only (blue), and after the addition of ambient $^{12}C_2$ PAN (red) and of isotopically labelled $^{13}C_2$ PAN (green), respectively. Note the logarithmic scale above 4000 arb.u.*

4.1.2.1 Isotopic calibration

For atmospheric measurements, isotopically labelled acetone ($^{13}CH_3^{13}CO^{13}CH_3$, $^{13}C_3$-acetone) is used in order to have a permanent online calibration (see section 3.2). **Figure 4.8** shows exemplary some mass spectra as obtained in the laboratory. The blue line represents a background spectrum,

which is obtained when the FASTPEX instrument samples pure synthetic air. Only one mass peak at 127 amu is present corresponding to the I^- educt ions. The red and green spectrum were obtained by addition of PAN with the help of the PAN calibration source. If ambient acetone ($^{12}C_3$) is used for the synthesis of PAN (in the following referred to as $^{12}C_2$-PAN), the corresponding mass peak of the product ion is present at 59 amu (red spectrum). If the PCS is fed with isotopically labelled $^{13}C_3$ acetone to produce $^{13}C_2$-PAN, the corresponding product ion appears at 61 amu (green spectrum). It is only two amu apart since one $^{13}CH_3$-group is lost during the photolysis of acetone (see equation 4.1a). Apart from these mass lines, no other peaks are present in the spectra. It is well known that I^- reacts very selectively with peroxyacyl radicals $RC(O)O_2$ (Huey et al., 1995; Slusher et al., 2004; Zheng et al., 2011). This results in relatively simple and clear spectra with only a few dominant mass peaks. However, it has to be noted that the spectra in **Fig. 4.8** are remarkably clean, since the ion trap mass spectrometer was disassembled and cleaned right before this experiment.

The NO to PAN conversion efficiency was found to be similar for both acetone isotopomers ($^{12}C_3$ and $^{13}C_3$). **Fig. 4.9** shows a time-series of the ion signals at mass peak 59 amu (red) and mass peak 61 amu (green) detected with the FASTPEX instrument, when the PCS was supplied with the two different acetone isotopomers. At the beginning of the experiment, the PCS source was fed with $^{12}C_3$-acetone. Therefore a signal at mass peak 59 amu is present, whereas the ion intensity at mass peak 61 amu is close to zero. The acetone/synthetic air mixture is taken from a stainless steel tank with a volume of 500 cm^3, which is regularly filled from a bigger 10 l gas bottle. Around 16:30h UTC, the stainless steel tank was newly filled with $^{13}C_3$-acetone, which during the next few minutes replaced the $^{12}C_3$-acetone. For this reason, the signal at 59 amu decreased while at the same time the ion intensity at mass peak 61 amu increased. Finally, the ion intensity at 61 amu reached similar values as those from mass peak 59 amu (see also statistics given in **Fig. 4.9**). As a conclusion, we can assume that the NO to PAN conversion efficiency is equivalent for both isotopomers. This experiment also confirms that the mass discrimination between the two mass peaks can be neglected (due to their close proximity). The $^{13}C_3$-acetone gas used for this laboratory study however was not isotopically pure, indicated by the slightly higher signal noise at mass 59 amu. This increase is undesired because it adds a background on the ambient mass which adversely affects the detection limit. A second $^{13}C_3$-acetone gas from the same manufacturer however was found to be isotopically pure.

With the help of the isotopic standard, the ambient PAN mixing ratio C_a can be calculated via (see section 3.2):

$$C_a = C_{ILS} \times \left(\frac{K_{ss} \times R - K_{as}}{K_{aa} - K_{sa} \times R}\right). \tag{4.4}$$

Herein, C_{ILS} represents the $^{13}C_2$-PAN standard mixing ratio (already diluted with the sample gas). R gives the ratio of the signals at mass 59 and 61 amu, corrected with the corresponding instrument background (BG):

$$R = \frac{(S_{59} - BG_{59})}{(S_{61} - BG_{61})}. \tag{4.5}$$

K_{aa} and K_{sa} are calculated with the help of the terrestrial abundances of ^{12}C (98.9%), ^{13}C (1.1%), ^{16}O (99.762%) and ^{18}O (0.2%) while contributions of less abundant isotopes ^{17}O and ^{2}H can be neglected. Taking all the possible permutations into account, K_{aa} and K_{sa} are calculated to 0.9731 and 2.1×10^{-3}, respectively. The latter only becomes important for a high ratio R, hence for ambient PAN mixing ratios much higher than the added standard PAN mole fraction. K_{ss} and K_{as} were determined experimentally in the laboratory, since each calibration gas may have a different isotopic composition. As mentioned above, the standard used for the POLARCAT-GRACE campaign (Air Liquide) was found to be isotopically pure within the measurement uncertainty because no significant signal at the mass corresponding to $^{12}C_2$-PAN was observed. As a result, the values for this standard were set to $K_{ss} = 1$ and $K_{as} = 0$, respectively.

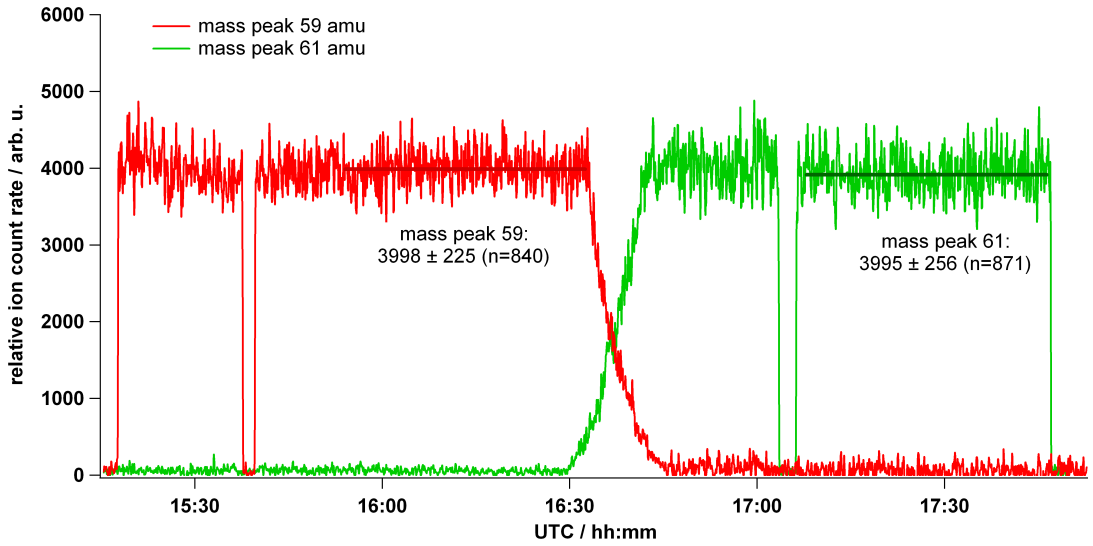

Figure 4.9: *Time-series of ion signals at mass 59 (red) and 61 amu (green) reflecting $^{12}C_2$ and $^{13}C_2$-PAN, respectively. At around 16:30h UTC, the $^{12}C_3$-acetone was exchanged in the PCS by $^{13}C_3$-acetone.*

4.1.2.2 Flow reactor conditions

In an ideal case without backward and subsequent reactions, the amount of formed product ions depends on the number density of both educt ions and the trace gas to be measured, the reaction time and the temperature-dependent rate coefficient (see equation 3.1). The yield of product ions determines the sensitivity of the PAN measurement. It was studied in the laboratory with respect to certain flow reactor conditions, as for example flow reactor pressure, reaction time, and different source gas flows.

Dependence on flow reactor pressure

The flow reactor pressure controls the yield of product ions due to several reasons. It determines the number density of gas molecules in the FR, and therefore the collision rate of the ions and molecules. Furthermore, at a constant sample mass flow it controls the flow velocity and hence, the residence

time in the FR. Finally, a higher FR pressure increases the flow into the ion trap mass spectrometer itself, which in turn means that more ions enter the ion trap through the front electrode (see section 3.3). The dependence on the FR pressure is illustrated in **Figure 4.10**, which shows the ion intensity measured at 59 and 127 amu, as obtained at different flow reactor pressures.

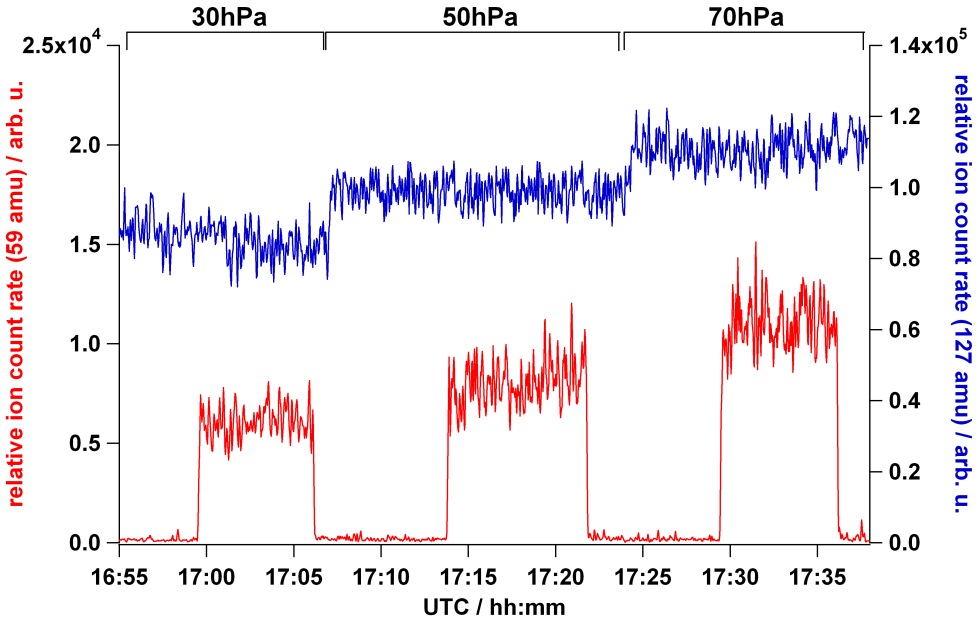

Figure 4.10: *Ion signals at mass 59 amu and mass 127 amu as a function of the pressure in the flow reactor. At higher pressures, the signal increases at the mass peaks of both educt and product ions.*

During the course of this experiment, the system was supplied with a constant $^{12}C_2$-PAN mixing ratio from the PCS. The pressure in the FR was varied by reducing the pump performance of the FR pump, with the help of a hand valve in front of the pump. The pressure in front of the PFA critical orifice was controlled by the BPC (150 hPa) and ensured a constant sample mass flow[3]. As illustrated in **Fig. 4.10**, the ion intensities both at 127 amu (I^-) and 59 amu ($CH_3CO(O)^-$) rise with higher pressures. The increase of I^- certainly is the result of a higher flow into the mass spectrometer, whereas the increase of $CH_3CO(O)^-$ can be attributed also to the longer reaction time as well as the higher collision rate. The FR pressure however has an upper limit, which is dictated both by the lowest expected ambient pressure at the highest flight level and by the maximum pressure allowed inside the ion trap. Note that the possibility of backward and/or consecutive reactions may increase likewise at higher FR pressures, depending on the respective ion chemistry. The influence of cross-sensitivities therefore has to be carefully evaluated for the prevailing conditions.

Dependence on N_2 carrier source gas flow

Nitrogen N_2 (purity 5.0, Air Liquide) is used as carrier gas for the CH_3I/N_2 mixture. A flow of ~2 slm N_2 is flushed through the ^{210}Po ion source (see **Fig. 4.6**). It was found that a higher carrier gas flow resulted in higher signals both at the educt and product masses. **Figure 4.11** shows

[3]The PFA critical orifice always was operated under "sonic state" conditions (see appendix A2).

the measured ion intensities as a function of the N_2 gas flow. The total sample gas flow was held constant during this study, since the pressure in front of the PFA critical orifice remained the same (controlled by the BPC). The increase in the FR pressure due to the higher N_2 carrier gas flow was balanced by the use of the hand valve in front of the FR pump. Thus FR pressure and reaction time remained the same during the course of the experiment. The sample gas flow however was more diluted at higher N_2 mass flows which reduces the trace gas concentration, and therefore should diminish the sensitivity. On the other hand, the higher N_2 flow carries the ionized air faster into the FR, and finally also into the ion trap. This might explain the higher signal at 127 amu. The signal enhancement at the product ion mass is attributed to the abundance of more educt ions inside the FR which in turn leads to the formation of more product ions.

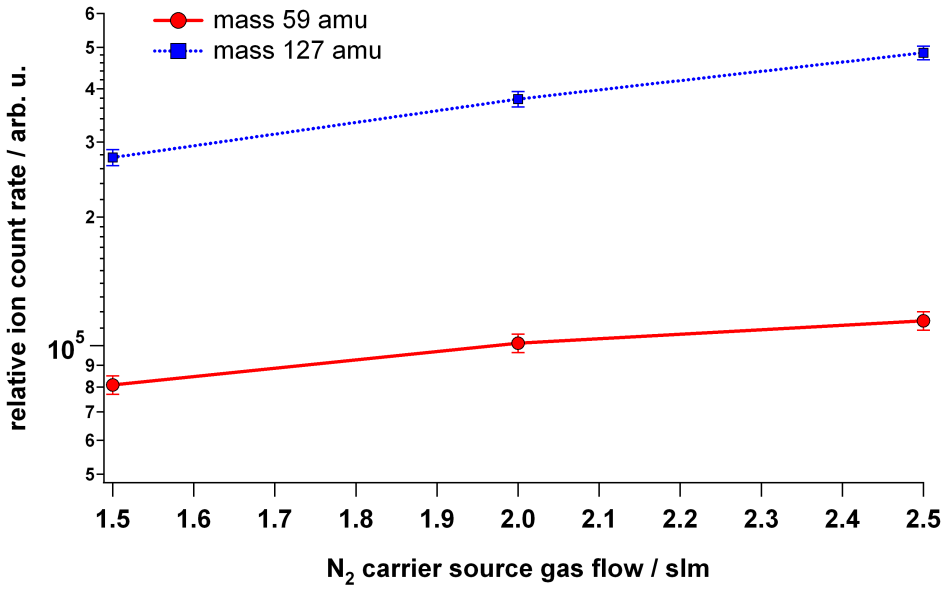

Figure 4.11: *Ion signals at mass 59 (red) and 127 amu (blue) as a function of the N_2 carrier source gas flow. A higher N_2 mass flow increases the ion intensities both at the educt (127 amu) and product (59 amu) ion mass.*

Dependence on CH_3I source gas

As mentioned at the beginning of section 4.1.2, the reagent ions I^- are produced by the ionization of a CH_3I/N_2 gas ($\sim$1000 μmol mol^{-1} CH_3I in N_2 5.0) which is added to the main N_2 carrier gas. In a series of experiments, the mass flow of the used CH_3I/N_2 source gas was found to have a great impact on the yield of product ions, which is illustrated exemplary in **Fig. 4.12**. Using a 5 sccm min^{-1} MFC, the CH_3I/N_2 mass flow was varied between 0.05 to 3 sccm min^{-1}. During the course of this experiment, the instrument was supplied with a constant $^{12}C_2$-PAN mixing ratio. At each single mass flow, the PAN standard was switched out of the sampling line in order to monitor also the corresponding background signal at mass 59 amu, which however was found to be independent of the CH_3I/N_2 mass flow (not shown).

The ion intensity at the mass corresponding to I^- (127 amu) increases between 0.05 and 0.5 sccm min^{-1}, but stays relatively constant for mass flows ≥ 0.5 sccm min^{-1}. The decrease at lowest CH_3I/N_2 mass flows might be attributed to a less efficient I^- production in the ion source due to less abundant CH_3I molecules. It is very likely much more pronounced as it seems from **Fig. 4.12**, but is masked by the mass discrimination of the ion trap mass spectrometer[4].

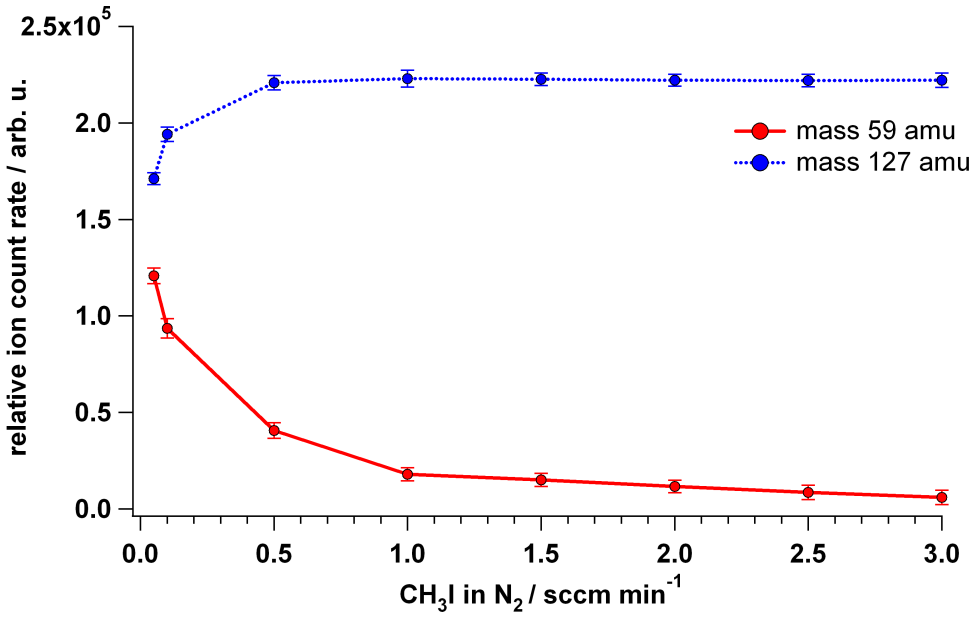

Figure 4.12: *Ion signals at mass 59 (×10, red) and mass 127 amu (blue) as a function of the CH_3I mass flow. A lower CH_3I/N_2 mass flow results in significantly higher ion intensities at the product ion (59 amu). The signal of the educt ion (127 amu) is constant at mass flows ≥ 0.5 sccm min^{-1}, but decreases at the lowest mass flows 0.1 and 0.05 sccm min^{-1}. For more details see text.*

The signal at the product ion CH_3COO^- is observed to continuously decrease at higher CH_3I/N_2 flows, and shows the strongest decline at lowest mass flows. This negative relationship between the product ion yield and the CH_3I/N_2 mass flow is counterintuitive, but was found to be consistent through all conducted laboratory studies. It was observed for a series of different CH_3I/N_2 source gases (i. e. different CH_3I mixing ratios and/or manufacturers). Also different source gas feedings were tested, but had no impact on the negative dependency. The reason for this behavior is unclear. It disagrees with gas phase kinetics, which would suggest a more efficient formation of product ions at a higher educt ion concentration (at least if side or subsequent reactions can be neglected). One explanation might be that ion-ion self reactions play a role, which very likely take place already in the ion source itself. Actually, this effect seems to be unique to our special set-up. Another group working with the same ion chemistry does not find such a strong dependence on the educt and product ion yield on different CH_3I/N_2 mass flows (Frank Flocke, NCAR, personal communication).

[4]The tuning of the voltages for the product ions leads to a lower sensitivity for the heavier educt ions.

4.1.2.3 Cross-sensitivity tests

I^- ions are known to react very selectively with peroxyacyl radicals and are found to react very slowly with most other abundant trace gases as for example NO_3, O_3 and NO_2 (Huey et al., 1995; Slusher et al., 2004). Nevertheless, cross-sensitivity tests were performed for several abundant trace gases by means of calibration gases (Air Liquide) or permeation devices (VICI Metronics). The influence of NO, NO_2, HNO_3, HNO_3, O_3, HCl and SO_2 was determined at mixing ratios typical for tropospheric/stratospheric air masses. Some of these gases gave a (small) signal on different mass peaks. For example NO_2 contributed to mass 62 (NO_3^-) and HCl to mass 163 (I^-HCl). The addition of HNO_3 increased the signal at mass 190 (I^-HNO_3) and also at mass 62, but no cross sensitivities for the relevant masses at 59 or 61 amu were found.

Acetic acid (CH_3COOH) certainly is a favorite candidate for interferences, since the PAN product ion is the acetate ion CH_3COO^-. However, no significant signal is induced at mass 59 amu by the addition of CH_3COOH. Obviously the reaction of I^- with acetic acid is too slow. This is consistent with the results reported by (Slusher et al., 2004), who did not find cross sensitivities for typical ambient levels of acetic acid either. However, on the contrary to I^- the product ion $CH_3C(O)O^-$ is very reactive, and thus may be depleted due to consecutive reactions. Due to their low gas phase acidity, acetate ions $CH_3C(O)O^-$ react rapidly with a series of organic and inorganic acids (Veres et al., 2008). As a result, these may interfere due to an isotope exchange reaction with the isotopically labelled product ions. The $^{13}CH_3^{13}COO^-$-ions can abstract a proton from e. g. CH_3COOH, and generate $^{12}CH_3^{12}COO^-$-ions:

$$^{13}CH_3^{13}COO^- + ^{12}CH_3^{12}COOH \rightarrow ^{13}CH_3^{13}COOH + ^{12}CH_3^{12}COO^- . \quad (4.6)$$

Reaction 4.6 shows that per acetic acid molecule one $^{12}CH_3^{12}COO^-$ (product of ambient PAN) is formed while one $^{13}CH_3^{13}COO^-$ (product of the PAN standard) is consumed. As a result the mass peak 59 increases while that at mass peak 61 will decrease in the same way, which finally even doubles the effect on the calculated PAN concentration. It has to be noted that the $^{12}C_2$-PA radicals created by the decomposition of ambient PAN might react in the same way with $^{12}CH_3^{12}COOH$. However, this can not be distinguished and therefore has no influence on the PAN detection. The effect of the isotope exchange reaction was studied in the laboratory and is illustrated in **Fig. 4.13**. It shows a mass segment of spectra between 50 and 80 amu. CH_3COOH and the next homologue acid, propionic acid (CH_3CH_2COOH) were injected with the help of permeation sources (VICI Metronics) at concentrations of $\sim$20 nmol mol^{-1}.

The blue line shows the reference spectrum when the instrument is supplied with $\sim$1 nmol mol^{-1} isotopically labelled PAN from the PCS, and only the product ion $^{13}CH_3^{13}COO^-$ is present. If additionally CH_3COOH (^{12}C) is injected, reaction 4.6 induces a signal at mass 59 amu, which may be misinterpreted as ambient PAN (red spectrum). At the same time, the signal at mass 61 amu declines in the same way. By a similar mechanism, adding of propionic acid (^{12}C) in the presence of $^{13}C_2$ PAN induces a signal at mass 73 amu. This pretends the existence of PPN (peroxypropionic acid), the next higher homologoue of the PANs family. Reaction 4.6 indicates that the higher the

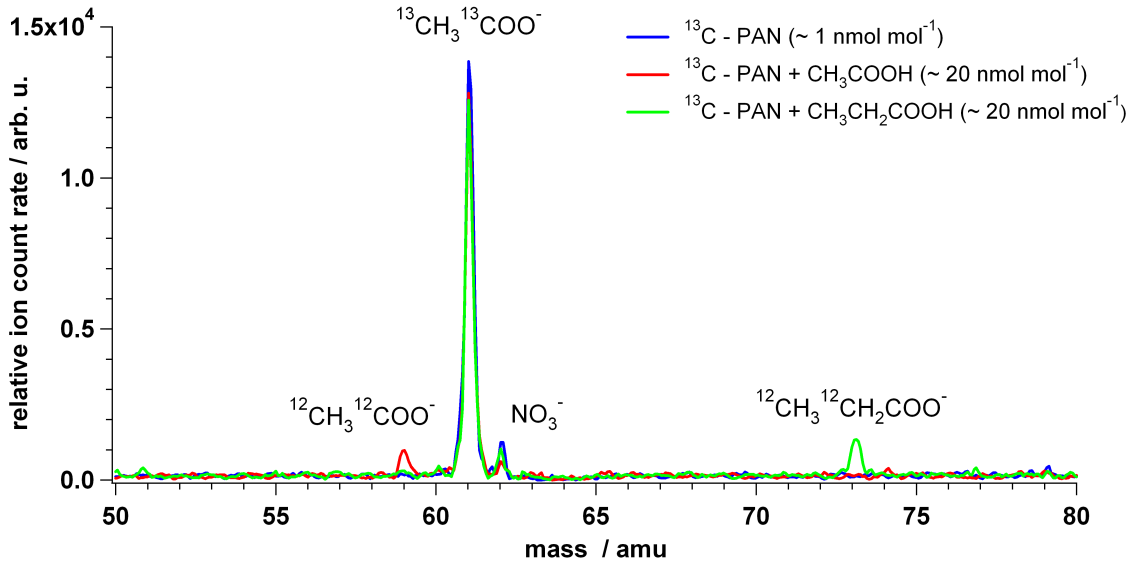

Figure 4.13: *Mass spectra obtained when the instrument is supplied with $^{13}C_2$-PAN only (blue spectrum). The additional injection of a large amount of CH_3COOH induces a signal at mass 59 amu, while that of mass 61 amu decreases at the same time (red spectrum). In case of adding a high mixing ratio of propionic acid CH_3CH_2COOH, the intensity at mass 73 amu shows an increase. Again, this leads to a depletion of $^{13}CH_3^{13}COO^-$ ions and therefore a lower signal at mass 61 amu (green spectrum).*

$^{13}CH_3^{13}COO^-$ abundance, the higher the cross-sensitivity. Therefore it becomes more important at high isotopic standard concentrations as well as at longer ion residence times, because in each case more $^{13}CH_3^{13}COO^-$ is available. For the present set-up, the influence is calculated to be less than 2% at atmospheric acetic acid mixing ratios of 2 nmol mol^{-1}. Typical ambient mixing ratios of CH_3COOH are 1 nmol mol^{-1} or even lower (Reiner et al. (1998)), which means that this cross-sensitivity normally can be neglected. However, in order to exclude potential artifacts due to proton transfer ionization, the isotopically labelled standard regularly has to be switched off (see section 4.2.2).

4.1.3 Thermal decomposition region

The thermal instability of PAN and the resulting implications for the atmospheric chemistry was already discussed in section 2.2.2. The controlled thermal breakup of PAN molecules into PA radicals and NO_2 is used for the measurement of PAN, since the ion-molecule reaction is based on the detection of the PA radical (see previous section 4.1.2). As predominant decomposition pathway of PAN, the O-N homolysis was identified (Roberts and Bertman, 1992):

$$CH_3C(O)OONO_2 + M \longrightarrow CH_3C(O)OO + NO_2 + M\,. \tag{4.7}$$

Figure 4.14 depicts the half-life of PAN as a function of the temperature between 270 and 425 K (at 150 hPa). The half-life $\tau_{1/2}$ is $\sim$35 min. at 298 K, but decreases rapidly with higher temperatures. Around 423 K, PAN survives only for a few ms.

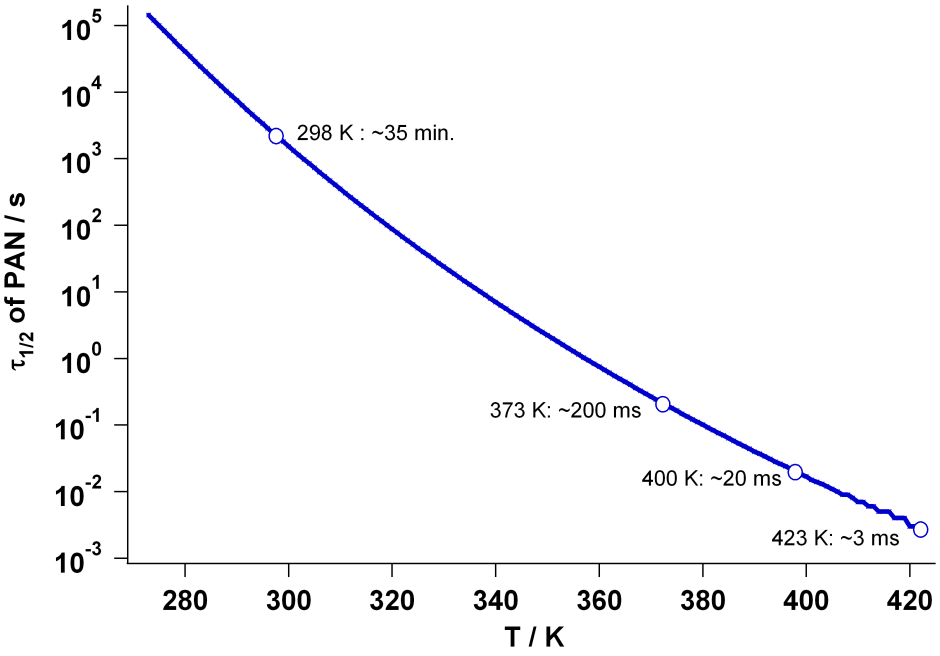

Figure 4.14: *Thermal decomposition half-life of PAN in dependency of the temperature (at 150 hPa), calculated with data taken from Atkinson et al. (2006).*

In order to obtain a high sensitivity of PAN, the conversion of PAN to PA radicals has to be as efficient as possible. The thermal decomposition region (TDR) is located in front of the flow reactor (see **Fig. 4.6**). PA radicals are readily lost on metallic surfaces (Slusher et al., 2004). Although the flow through the heated inlet is assumed to be laminar ($Re < 1000$ for typical conditions), the thermal breakup for this reason takes place in a heated 3/8" o. d. tube made of PFA. Every time a tube was heated for the first time, a series of signals (e. g. at mass 85 amu) was observed from outgassing of the heated PFA material. This in turn led to a diminished sensitivity for PAN due to a lower abundance of educt ions, but the effect always decreased after several hours of operation. Several studies were carried out in order to optimize length, temperature and pressure of the TDR. **Figure 4.15** shows exemplary the ion count rate at mass 59 amu (avg $\pm$ std) as a function of the temperature of the TDR, measured at the outside of the PFA tube. The gas temperature in the inlet certainly is much lower, and depends on the residence time τ_{TDR} in the TDR. With the configuration used for this experiment ($p_{TDR} = 150$ hPa, $V_m = 5.2$ slm, $l_{TDR} = 50$ cm), τ_{TDR} is calculated as ~ 20 ms by assuming a laminar flow. **Figure 4.15** shows clearly that the higher the temperature, the larger the signal at mass 59 amu due to a more efficient thermal dissociation of PAN into PA radicals and NO_2. The increase is stronger between 160°C and 190°C, and plateaus around 200 to 220°C. The maximum operating temperature of PFA is 260°C, however, already at temperatures around 200°C the PFA tube was observed to start yielding. Therefore a temperature of ~190°C was chosen as best compromise.

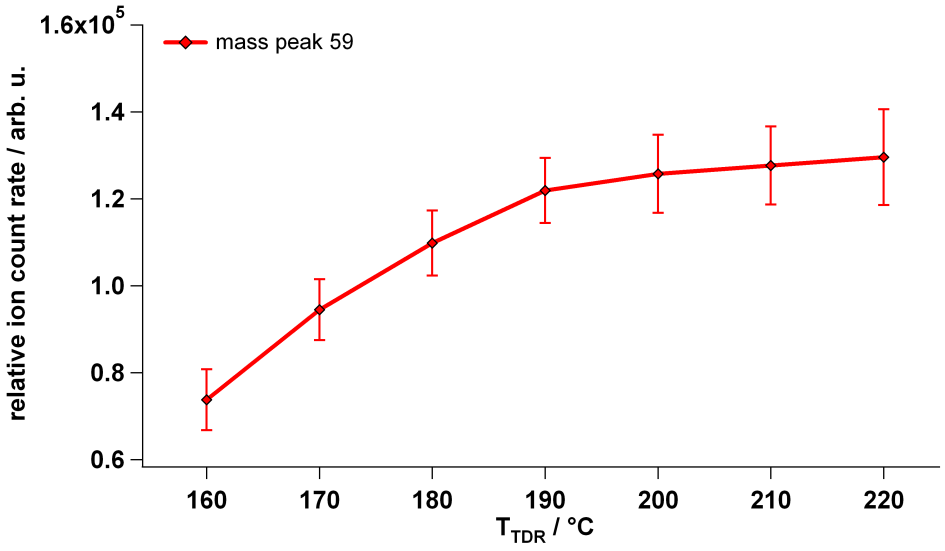

Figure 4.15: *Ion signals (avg ± std) at mass 59 amu as a function of the TDR temperature. At higher temperatures, the signal increases due to a more efficient production of PA radicals in the TDR.*

The breakup of PAN in the thermal decomposition region may be followed by several chemical reactions of the PA radical. It may be titrated by nitric oxide NO (see equation 4.8a), which becomes a significant reaction if strongly polluted air is sampled. Also recombination processes with NO_2 (equation 4.8b) and $CH_3C(O)O_2$-$CH_3C(O)O_2$ radical self reactions may lead to losses of PA radicals (equation 4.8c and 4.8d).

$$CH_3C(O)OO + NO \rightarrow CH_3C(O)O + NO_2\,, \tag{4.8a}$$

$$CH_3C(O)OO + NO_2 \rightarrow CH_3C(O)OONO_2\,, \tag{4.8b}$$

$$CH_3C(O)OO + CH_3C(O)OO \rightarrow O_2 + CH_3C(O)O + CH_3C\,, \tag{4.8c}$$

$$\rightarrow CH_3OCOCOOCH_3 + O_2\,. \tag{4.8d}$$

The influence of subsequent reactions is minimized if the thermal breakup occurs closer to the end of the TDR, which could be achieved by using a hotter and shorter inlet. Other radicals such as RO_2 and HO_2 may also interfere, but certainly they do not make it through the inlet system without special care. Therefore their concentrations can be expected to be low. It is worth noting that these reactions are accounted for if an online isotopic calibration is used. This however is not true for the measurement of higher PANs (see section 2.2.2). (Zheng et al., 2011) presents a careful evaluation of the complex dissociation pathways of PANs with a charbon chain length of 4 and more.

Background determination by NO titration

The reaction of the PA radical with nitric oxide (NO) is relatively fast ($k=2.4\times10^{-11}\,cm^3\,s^{-1}$ at 298 K). Slusher et al. (2004) suggested to use the NO titration also for the determination of the instrument background at mass peak 59 amu. This was tested also in the framework of this work

and is illustrated in **Fig. 4.16**. It shows two mass spectra as obtained by measurements of ambient air. Both spectra show several peaks, including signals which can be attributed to the cluster-ions $I^-(H_2O)$, $I^-(HCOOH)$ and $I^-(HNO_3)$. The red spectrum shows also a signal at mass 59 amu (CH_3COO^-) and 77 amu ($CH_3COO^-(H_2O)$) reflecting an ambient PAN mixing ratio of $\sim$230 pmol mol^{-1}. Adding $\sim$300 pmol mol^{-1} NO upstream of the TDR resulted in a signal removal at both of these masses (blue spectrum). All other apparent mass peaks however are not influenced. NO obviously reacts highly selective with the PA radical, but does not change the matrix of the sample air. This makes the NO titration an elegant way to determine the instrument background at mass peak 59 amu. If isotopically labelled $^{13}C_2$-PAN is added, the background at mass peak 61 amu is obtained in the same way.

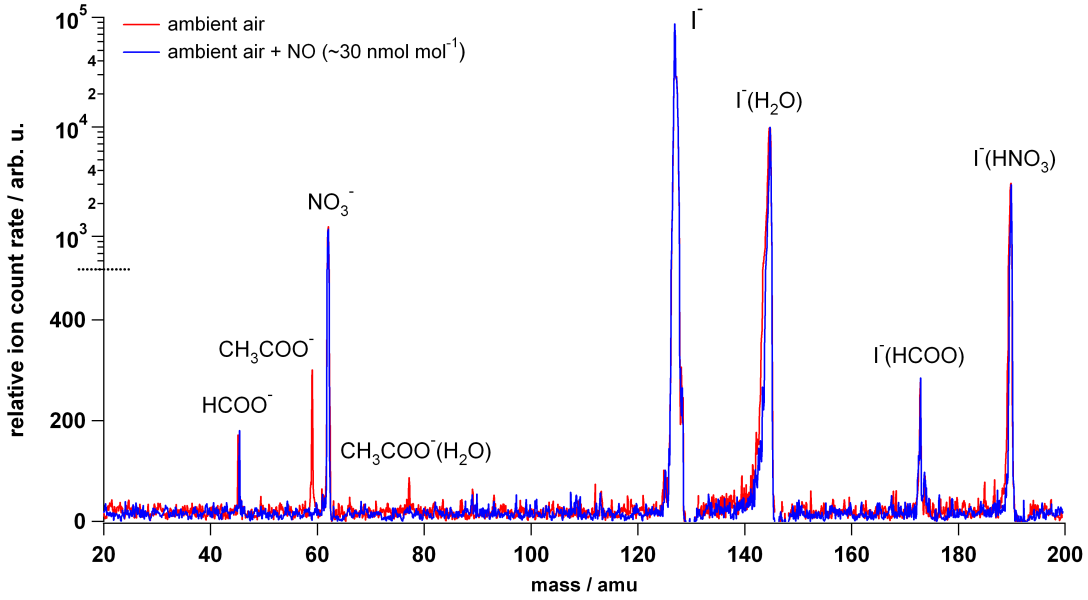

Figure 4.16: *Mass spectra as obtained by sampling ambient air at ground levels (red spectrum). The blue spectrum was derived by the additional injection of NO. Please note the logarithmic scale above 500.*

Titration by NO presents an ideal solution because no additional components are needed. The NO calibration gas itself is normally already available since it is also used for the PAN formation in the PCS (see section 4.1.1). However, it has to be noted that the mass spectra shown in **Fig. 4.16** were obtained while having a relatively high pressure in the TDR, which was close to the ambient pressure of $\sim$950 hPa. This resulted in fairly long residence times of $\sim$180 ms and additionally a high number density inside the TDR. Further tests conducted at typical flight conditions (i. e. at $p_{TDR} = 150$ hPa and $\tau_{TDR} \sim 20$ ms) showed that the NO titration under these conditions is not fully efficient[5]. A much higher NO mixing ratio has to be present in the TDR in order to reach a complete titration of the PA radicals. Using the same NO calibration gas (NO $\sim$3 μmol mol^{-1}), several hundreds of sccm min^{-1} had to be added, hereby diluting the sample stream too much. The

[5]Note that the reaction time of reaction 4.8a is shorter than the total residence time τ_{TDR} in the TDR, since it is a subsequent reaction of the thermal decomposition of PAN.

deployment of a higher concentrated NO calibration gas is unpracticable. This would require further components (e. g. stainless steel canister) and complicate the safety analysis for the airworthiness certification. For this reason it was decided to use another kind of in-flight background calibration: The PAN present in the sample stream is thermally destroyed already before the sample gas enters the TDR. For this, the sample gas is passed first through the BCU (background calibration unit, 30 cm, 300 °C). The PA radicals hereby generated are rapidly lost by surface catalysis and therefore do not reach the flow reactor (see section 4.2).

4.1.4 Settings of the ion trap mass spectrometer

The ion trap mass spectrometer (ITMS) was already successfully deployed on the Falcon for the measurement of SO_2 (Speidel et al., 2007; Fiedler et al., 2009) as well as for ground-based measurements of OH and H_2SO_4 (Fiedler et al., 2005; Aufmhoff et al., 2011). The influence of the parameters described in section 3.3, i. e. the trapping time, the maximum number of ions allowed in the trap (MS target) and the number of micro-scans have been studied in the laboratory, and were optimized for a high time resolution and a sufficiently low detection limit.

Trapping time

The ions are injected into the trap for a certain time period, the so-called injection or trapping time. The injection time can be varied from ~1 ms up to several seconds. It is chosen dependent on several parameters, as for example the expected ion signals and/or the needed time resolution. **Figure 4.17** shows exemplary the signals at mass 127 amu and 59 amu in dependency of trapping times between 1 and 200 ms.

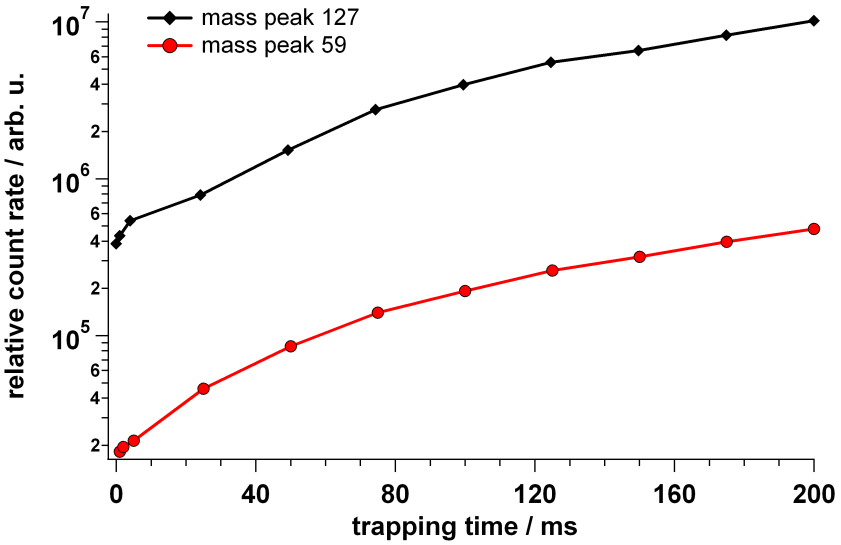

Figure 4.17: *Ion signals at mass 59 amu (CH_3COO^-) and 127 amu (I^-) as a function of the trapping time.*

During this experiment, a constant PAN concentration was established in the FR. Higher trapping times generally lead to higher ion signals, thus greater sensitivity. On the other hand, a large

amount of ions will induce space-charge effects, and therefore a distortion of the mass scans. For the prevalent conditions, trapping times longer than ~200 ms (corresponding to ~1×10^8 ions) resulted in a peak shape broadening due to overloading of the trap. The resulting decline in mass resolution is illustrated in **Fig. 4.18**. It shows a small mass segment of spectra recorded at different sampling times. For a sampling time of 200 ms (red solid line), the two mass peaks at 61 ($^{13}CH_3{}^{13}COO^-$) and 62 amu (NO_3^-) are clearly separated. The minimum peak separation $\triangle M_{FWHM}$[6] is ~0.35. At longer injection times, the trajectories of the trapped ions are disturbed due to columbic repulsion. The green dashed line shows a spectrum recorded when the sampling time was increased to 300 ms. Both mass peaks are broadened, which leads to a signal decrease at the peak maximum (the peak area approximately stays the same), and a loss of mass resolution ($\triangle M_{FWHM} \sim 0.55$). These effects are even stronger if the sampling time is increased to 400 ms (blue dotted line). In this case, the two mass peaks are not longer clearly separated ($\triangle M_{FWHM} \sim 0.9$).

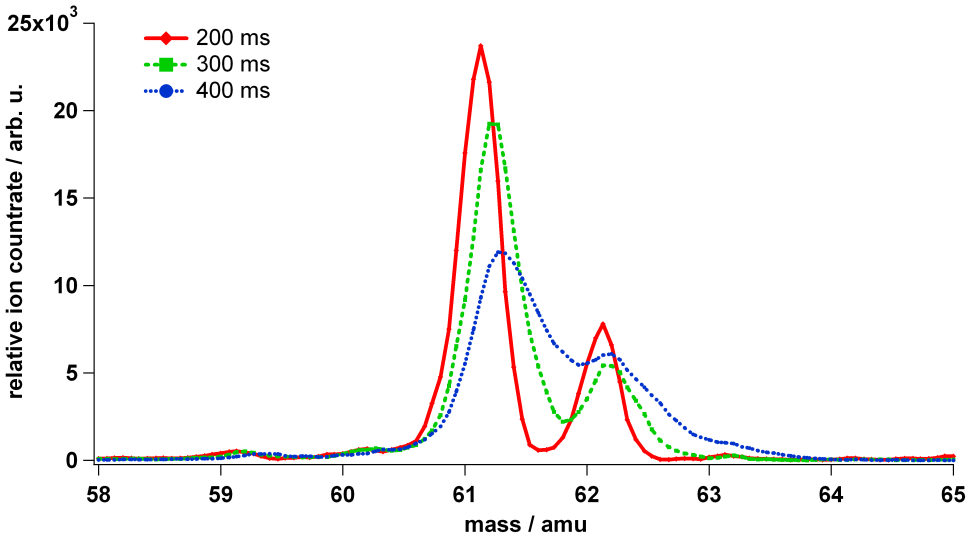

Figure 4.18: *Mass spectra as obtained using different trapping times: 200 ms (red solid line), 300 ms (green dashed line), and 400 ms (blue dotted line). During all experiments a constant mixing ratio of isotopically labelled PAN was established in the FR. At sampling times greater than 200 ms, a clear loss of mass resolution is observed due to space-charge effects inside the trap.*

It is important to note that it is not the trapping time itself, but essentially the number of ions in the trap which determines the strength of space charge effects. This means that the used ion chemistry and the kind of sample air determines whether space-charge effects play a role since depending on humidity and pollutant load of the ambient air, more or less ions enter the ion trap. In order to prevent overloading of the trap, the ion trap mass spectrometer can be operated in the AGC (automatic gain control) mode. In this case, a short pre-scan is performed (duration of about 0.2 ms) to obtain the actual ion concentration which varies due to changing humidity and trace gas abundance. The system then automatically adjusts the appropriate injection time for the analytic

[6]The minimum peak separation is defined by the width of the peak measured at 50% of the peak height - full width at half maximum (FWHM).

scan, corresponding to the maximum number of ions allowed in the trap, termed "MS target". The MS target is set by the operator and should ensure that space-charge effects are negligible.

Number of micro-scans

The detection limit is a linear function of the standard deviation σ at instrumental background conditions (i. e. measuring PAN-free air). As mentioned in section 3.3, the system software allows averaging over several single mass spectra (μ-scans). For constant trapping times, the standard deviation decreases strongly with a increasing number of μ-scans, as illustrated in **Fig. 4.19**. It shows the standard deviation σ at mass 59 amu as a function of the number of micro-scans. The trapping time for this experiment was held constant at 100 ms. The top axis gives the corresponding scan-time and hence, the obtainable time resolution. Please note that the read-out time has to be accounted for each micro-scan (see section 3.3).

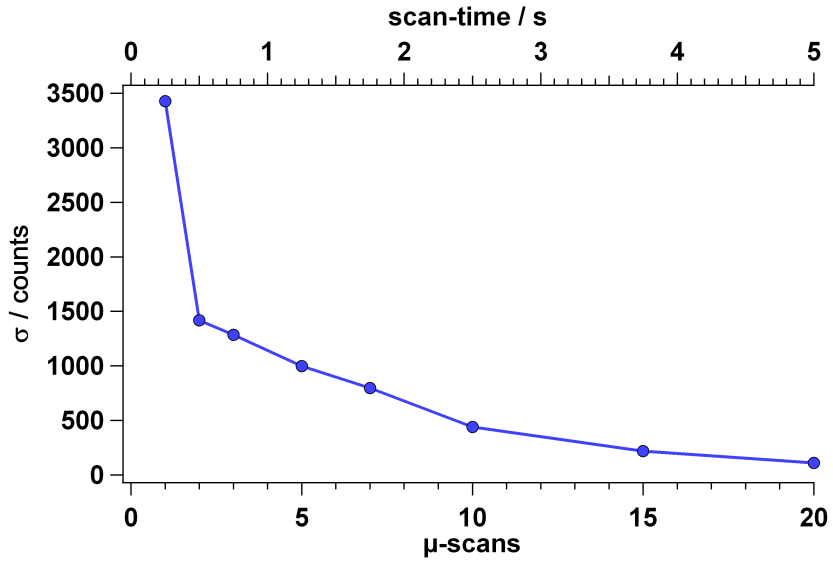

Figure 4.19: *Standard deviation of the ion signal at instrumental background conditions as a function of the number of μ-scans (trapping time: 100 ms). The corresponding scan-time is plotted on the top axis.*

Time resolution versus detection limit

Airborne measurements need a high time resolution since this is equivalent to spatial resolution. At the same time, the detection limit has to be low due to the small abundance of trace gases. A better time resolution generally leads to a higher detection limit and vice versa, thus one has to find a reasonable compromise for the required application. The detection limit (DL) is given by the mixing ratio corresponding to the 2σ-standard deviation at instrumental background conditions:

$$\mathrm{DL} = \frac{2 \times \sigma_{\mathrm{BG}_{59}}}{\mathrm{Sens}_{\mathrm{PAN}}} \,. \tag{4.9}$$

Herein, $Sens_{PAN}$ represents the sensitivity for PAN, given by the signal at mass peak 59 (or 61 amu) per pmol mol^{-1}, respectively. The relation between DL and time resolution was studied in the laboratory and is illustrated in **Fig. 4.20**.

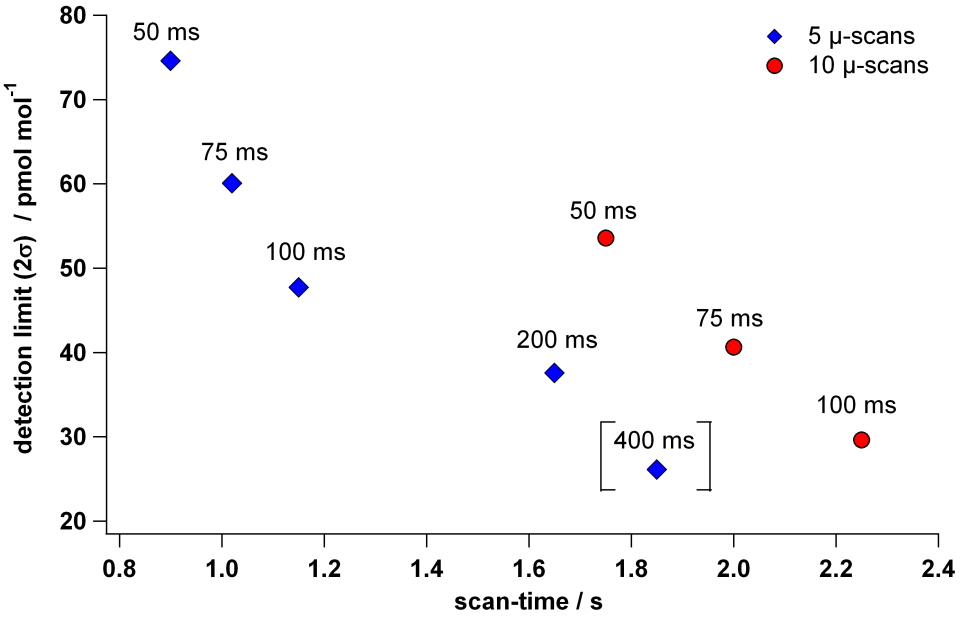

Figure 4.20: *Detection limit for PAN as a function of the scan-time. The 2σ detection limits are given for several trapping times and 5 (blue diamonds) and 10 (red circles) µ-scans, respectively*

Several trapping times between 50 and 400 ms were tested in combination with either 5 (blue squares) or 10 μ-scans (red circles). In general, a higher number of μ-scans improves the DL but decreases the time resolution. For an injection time of 50 ms, the 2σ-DL is e. g. $\sim$75 pmol mol^{-1} for 5 μ-scans, but improves to $\sim$52 pmol mol^{-1} if 10 μ-scans are used. The time resolution however is diminished by a factor of two. The detection limit can be improved also by increasing the sampling time. The lowest detection limit was reached with the highest sampling time of 400 ms. However, as discussed before, the mass resolution is declined at these high sampling times, therefore the corresponding marker is denoted by the parenthesis. Note that during the GRACE field campaign, the sensitivity for PAN was nearly twice as high as during this experiment. Therefore an even lower detection limit of 22 pmol mol^{-1} could be achieved (see section 4.1.5).

4.1.5 Measurement uncertainty

Table 4.1 lists all uncertainties which have to be considered in the calculation of the total uncertainty. These include the error of the nitrogen oxide calibration gas ($\pm$1%, Air Liquide), the gas flows of NO and acetone regulated by commercially available mass flow controllers ($\pm$0.5%, Bronckhorst), the sample gas flow controlled by a PFA critical orifice calibrated with a DryCal (D2) ($\pm$1%), and finally of the uncertainty of the NO to PAN conversion efficiency of our custom-made photolytic PAN source ($\pm$5%). For the uncertainty of the backgrounds δBG_{59} and δBG_{61}, the 1σ deviation of all in-flight background calibrations (BCU-mode) is used (see appendix A3).

Table 4.1: *Uncertainties which have to be considered for the calculation of the total uncertainty of FASTPEX.*

parameter	value	uncertainty
NO_{calgas}	3 μmol^{-1}	$\pm$1%
Q_{NO}	2 sccm min^{-1}	$\pm$0.5%
Q_{aceton}	50 sccm min^{-1}	$\pm$0.5%
Q_{sample}	5.05 sLm	$\pm$1%
CE_{PCS}	92%	$\pm$5%
S_{59}, S_{61}	variable	$\sqrt{S_{59}}$, $\sqrt{S_{61}}$
BG_{59}, BG_{61}	variable	1σ
K_{aa}, K_{sa}	0.9731, 2.1$\times$10^{-3}	negligible
K_{as}, K_{ss}	0, 1	negligible

Figure 4.21 presents the calculated relative error as a function of the ambient PAN volume mixing ratio, as obtained for the GRACE conditions (i. e. a time resolution of 2 s). A detailed error calculation is given in appendix A4. **Figure 4.21** shows that at PAN mixing ratios greater than $\sim$200 pmol mol^{-1}, the accuracy of FASTPEX is about $\pm$10%. At lower PAN mixing ratios the uncertainty of the instrumental background BG_{59} becomes more dominant and the uncertainty therefore increases rapidly towards smaller mixing ratios. At 50 and 100 pmol mol^{-1}, the overall uncertainty is calculated to $\pm$30 and $\pm$20% at 50 and 100 pmol mol^{-1}, respectively.

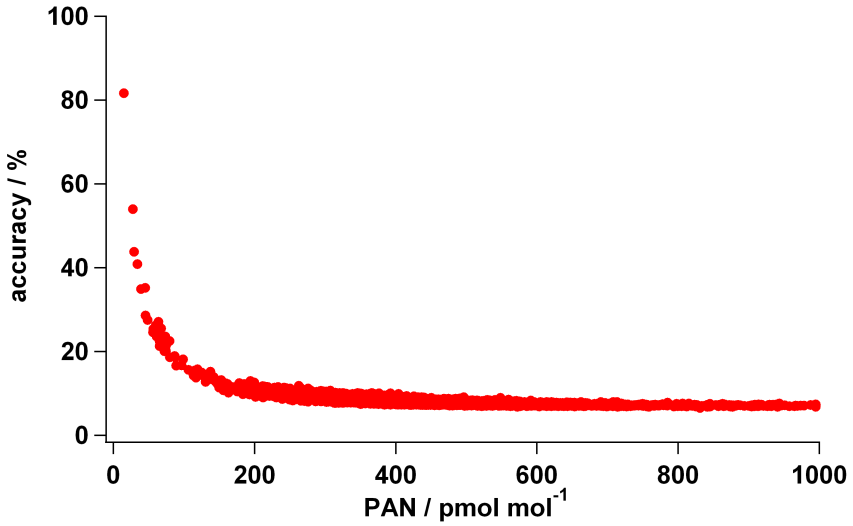

Figure 4.21: *Relative error of FASTPEX as a function of the PAN mixing ratio. At low PAN mole fractions, the total uncertainty is dominated by the uncertainty of the instrumental background, whereas at PAN mole fractions of 200 pmol mol^{-1} and more, the uncertainty of the PAN standard becomes more important.*

4.2 Atmospheric deployment

The FASTPEX instrument was deployed for the first time on the DLR Falcon during the POLARCAT-GRACE campaign in summer 2008. The scientific results are discussed in chapter 5. In this section, the set-up of FASTPEX during the GRACE field experiment is presented, and the performance of the instrument is discussed. **Figure 4.22** shows a schematic of the FASTPEX instrument as operated during GRACE. Atmospheric air is drawn in by a rotary vane pump (Alcatel 9014) through the backward-oriented air inlet (AI) sticking out of the aircraft top fuselage and the aircraft boundary layer. Thereupon the air passes through the sampling line (SL) via the back pressure controller (BPC) into the thermal decomposition region TDR (see section 4.1.3). Subsequently the air enters the flow reactor (FR), where also reagent ions I^- generated by the ion source (IS) are introduced (section 4.1.2). After passage through the FR, the air is pumped out by the rotary vane pump and exits the instrument via an air exhaust. A small fraction of the atmospheric air containing reagent and product ions enters the ITMS via a small circular entrance orifice (drilled into the front electrode) where it is analyzed (section 3.3). Online calibration is carried out by using isotopically labelled PAN (containing ^{13}C atoms), which is generated by the PAN calibration source (see section 4.1.1).

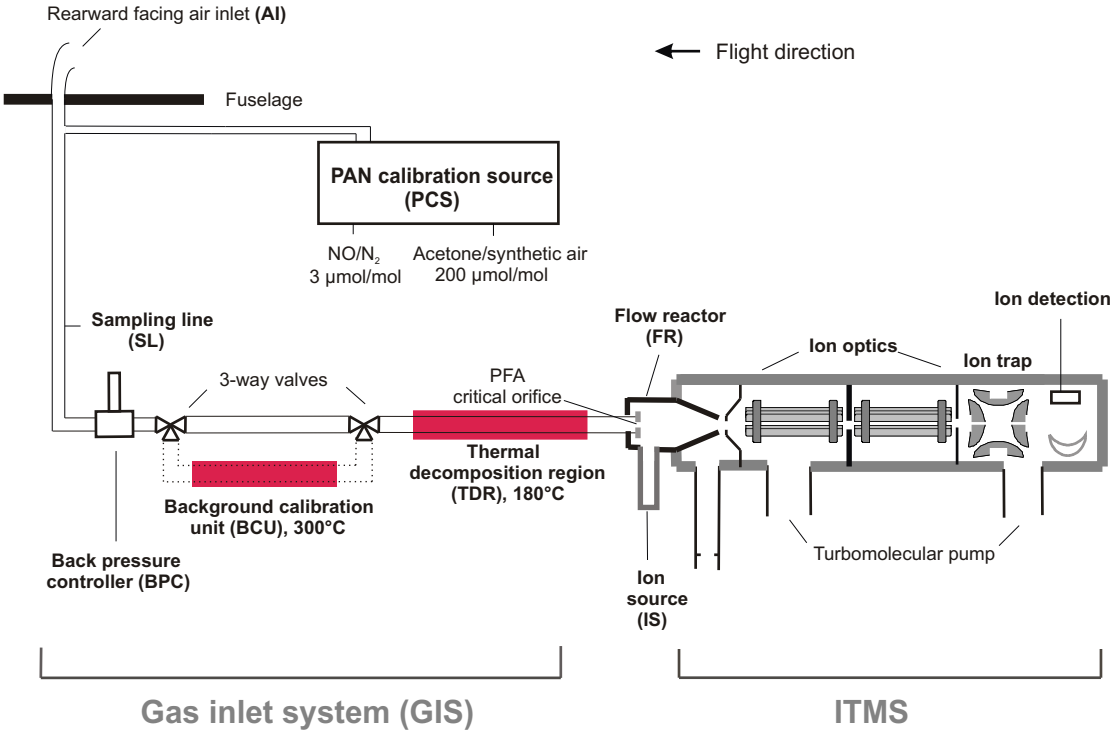

Figure 4.22: *Experimental set-up of the FASTPEX instrument as deployed on the DLR Falcon during the POLARCAT-GRACE campaign 2008. The main components of FASTPEX are a gas inlet system (GIS), a PAN calibration source (PCS), a tubular flow reactor (FR), an ion source (IS) and an ion trap mass spectrometer (ITMS). For more details see text.*

Table 4.2: *Parameters of the FASTPEX instrument during GRACE campaign 2008.*

parameter	**description**	**value**
p_{FR}	flow reactor pressure	70 hPa
l_{FR}	length of flow reactor	20 cm
p_{TDR}	TDR pressure	150 hPa
T_{TDR}	TDR temperature	190 °C
l_{TDR}	length of TDR	50 cm
N_2	source gas carrier flow	2.2 slm
CH_3I/N_2	source gas flow	0.1 sccm min^{-1}
Q_s	sample gas flow	5.05 slm
Q_{PCS}	PCS calibration gas flow ($Q_{NO} + Q_{acetone}$)	52 sccm min^{-1}
C_{ILS}	Mixing ratio of PAN standard	1.09 nmol mol^{-1}
T_{BCU}	BCU temperature	300 °C
l_{BCU}	length of BCU	50 cm
MS target	Max. number of ions allowed in trap	5×10^7
μ-scans	Number of μ-scans for each spectrum	7

For instrumental background measurements a hot Au tube (BCU) is integrated into the FASTPEX instrument in a bypass line of the SL. All temperatures as well as mass flow and pressure controllers/sensors (Wagner Mess- und Regeltechnik) are controlled by a custom-written LabView program. As described in section 4.1, the settings of the ITMS as well as of the FR conditions were optimized in the laboratory. Space, weight and gas supply limitations, as well as low ambient pressure at high altitudes, and finally the need for a high time resolution had to be taken into consideration. Table 4.2 summarizes all parameters of the FASTPEX instrument, as chosen for the GRACE campaign.

The sensitivity for PAN was found to be much higher at lower CH_3I/N_2 source gas flows (see section 4.1.2.2). For this reason the corresponding MFC was replaced by a smaller one (0 - 1 sccm min^{-1}) in order to be able to accurately regulate the low mass flow of 0.1 sccm min^{-1}. The ion residence time in the FR for the GRACE set-up was $\sim$60 ms. The MS target was set to 5×10^7 in order to prevent a loss of mass resolution, resulting in trapping times of $\sim$60 - 80 ms on average. A maximum trapping time of 100 ms was chosen in order to keep the time resolution reasonable, hence, at low ion concentrations the trap was closed after 100 ms.

4.2.1 Atmospheric mass spectra

A representative atmospheric mass spectrum (averaged over 20 single spectra) is plotted in **Fig. 4.23**. It illustrates the difference to the comparatively simple mass spectra which were sampled under controlled laboratory conditions (see e. g. **Fig. 4.8**). The shown spectrum was obtained at an altitude of 6.9 km in the upper troposphere. Note the logarithmic scale above 5×10^4. The by far largest mass peak is the reagent ion I^-. Besides bare I^--ions, also some $I^-(H_2O)$ at mass peak

145 amu is present (ratio ~70:1), but no $I^-(H_2O)_2$. As intended, the collisional ion dehydration in the trap is very efficient. The second largest mass peak at 61 amu is due to the isotopically labelled PAN calibration ion $^{13}CH_3^{13}COO^-$, which corresponds to a PAN mole fraction of 1062 pmol mol^{-1}. A trace of its hydrated form is also present (79 amu). The third largest mass peak at 62 amu is due to the impurity ion NO_3^-, which may originate from ion-molecule reactions with HNO_3, NO_2 or N_2O_5. Next in abundance is the ambient CH_3COO^- (59 amu), reflecting a PAN mole fraction of 281 pmol mol^{-1}. Mass peak 73 amu ($C_2H_5COO^-$) is equivalent to a PPN mole fraction of 36 pmol mol^{-1}. Always present in the spectra are enhanced signals at mass peak 45 and 46 amu, probably due to $HCOO^-$ (Veres et al., 2008) and HONO (Roberts et al., 2010). A blow-up of the mass-segment for 57 to 64 amu is given in the lower panel of **Fig. 4.23**. Additionally, an instrumental background spectrum is shown (BCU-mode). Herein, the signals at mass peak 59 and 61 amu are close to zero and the ion intensity at mass peak 62 amu has decreased but is still high.

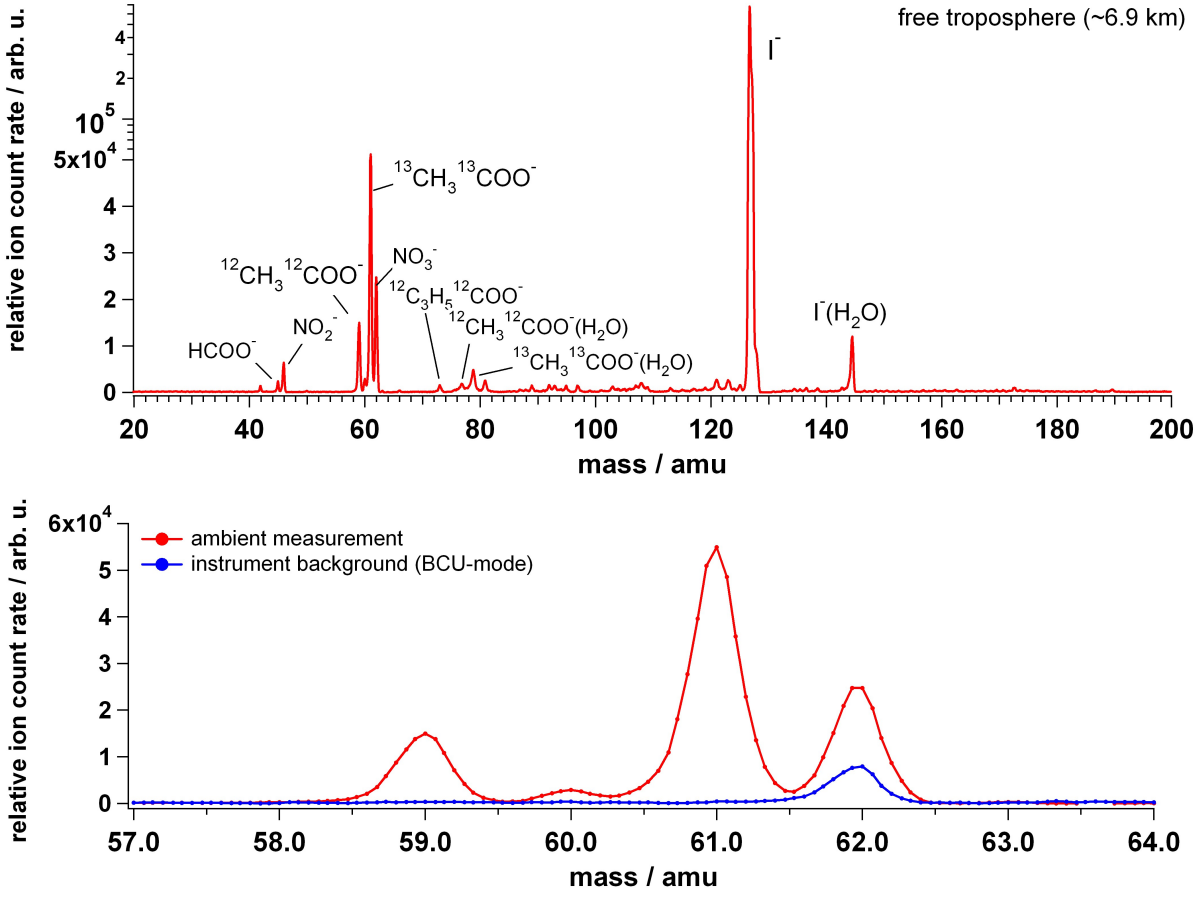

Figure 4.23: *The upper panel shows a representative mass spectrum obtained during atmospheric measurements in the upper troposphere (6.9 km). Note the logarithmic scale above 5×10^4. The main peaks correspond to the reagent ions I^- (127), the isotopic calibration ions $^{13}CH_3{}^{13}COO^-$ (61), the impurity ions NO_3^- (62) and finally to $^{12}CH_3{}^{12}COO^-$ (59), reflecting the ambient PAN mixing ratio (~280 pmol mol^{-1}). A blow-up of the mass-segment 57 to 64 is shown in the lower panel, together with a spectrum obtained during a background determination (via BCU). For more details see text.*

A zoom into spectra obtained during measurements in the polluted boundary layer over southern Germany (upper panel) and in the lowermost stratosphere (lower panel) is given in **Fig. 4.24** (each averaged over 20 single spectra). Due to the much higher humidity in the lower troposphere (altitude 1.5 km), the ratios of the dehydrated to hydrated ions are greatly reduced. The $I^-/I^-(H_2O)$ ratio is now only about ~3:1 (cut in the upper panel of **Fig. 4.24**). The abundance ratio of $CH_3COO^-/CH_3COO^-(H_2O)$ is close to 1 since CH_3COO^- clusters stronger with water than I^- (see section 4.1.2). The measured PAN signal is equivalent to an ambient atmospheric PAN mole fraction of 648 pmol mol^{-1}. It is worth noting that the isotopic calibration peak can still be used, because both ambient and standard ions experience the same water association and subsequently also the same dehydration within the ion trap. However, the PPN peak now sits on the rising edge of the ions corresponding to the hydrated forms of ambient and standard PAN ions (77 and 79 amu). Although the ion trap has an excellent mass resolution of ~0.3 amu, cluster ions like $I^-(H_2O)$ are observed to have a rising edge. As a result, the PPN background depends on water vapor mixing ratios (see section 4.2.3.2).

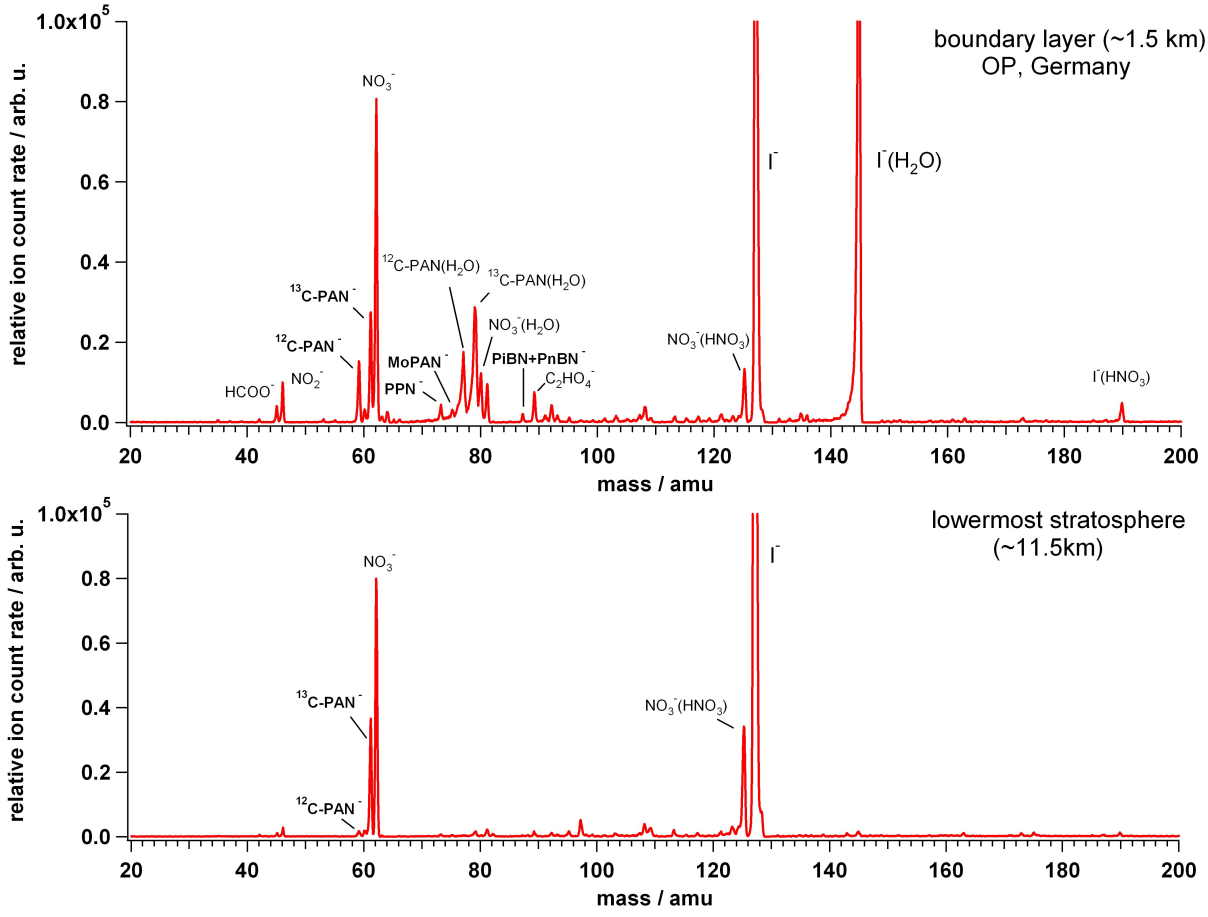

Figure 4.24: *Mass spectra obtained in the polluted boundary layer (BL) over southern Germany (upper panel) and in the lowermost Arctic stratosphere (lower panel). The high humidity in the BL is reflected in the abundance of hydrated ions whereas the spectrum obtained in the lowermost stratosphere shows nearly no hydrated forms.*

The measurements in the polluted boundary layer over Germany are the only case in which also potential signatures of other higher PAN homologues were observed, namely at mass peaks 75 and 87 amu. These might correspond to MoPAN ($CH_3OC(O)OONO_2$) and the sum of PBNs ($(CH_3)_2CHC(O)OONO_2$, peroxyisobutyryl nitrate and $CH_3(CH_2)_2C(O)OONO_2$, peroxybutyryl nitrate), respectively (Zheng et al., 2011). At mass peak 85 amu corresponding to MPAN (peroxymethacryloyl nitrate, $CH_3CH_2CC(O)O_2NO_2$), which was often measured during earlier studies at mixing ratios of several 10 to 100 pmol mol^{-1} (Williams et al., 1997; Roberts et al., 2002, 2004), no significant signal during any of the POLARCAT-GRACE flights was observed. Actually we expected to see low MPAN mixing ratios since our measurement area was mainly influenced by aged pollution and not by local emissions. MPAN is, however, exclusively derived from isoprene chemistry, and has a short lifetime of only one or two days with respect to OH oxidation (Orlando et al., 2002). In the boundary layer, the higher HNO_3 concentration is reflected in the enhanced signals at mass peaks 125 ($NO_3^-HNO_3$) and 190 amu (I^-HNO_3) and to some extent also at the impurity ion (62 amu) which is now more abundant than the calibration ion. The mass peak at 89 amu might correspond to oxalic acid ($C_2H_2O_4$), the simplest di-carboxylic acid.

The lower panel of **Fig. 4.24** shows a typical stratospheric spectrum. No more hydrated forms of the abundant ions are visible because of the low water vapor content. The PAN mixing ratio is here only 34 pmol mol^{-1}. The higher HNO_3 mixing ratio in the stratosphere is reflected at mass 125 amu ($NO_3^-HNO_3$) but not at 190 amu (I^-HNO_3), probably because the latter is formed primarily in a cluster exchange reaction with $I^-(H_2O)$.

4.2.2 In-flight calibration and background determinations

For in-flight calibrations isotopically labelled acetone ($^{13}CH_3^{13}C(O)^{13}C$) is used (see section 4.1.1). The resulting PAN calibration peak is then shifted from mass 59 amu ($^{12}CH_3^{12}COO^-$) to mass 61 amu ($^{13}CH_3^{13}COO^-$). A time sequence of signals at masses 59, 61 and 127 amu is shown in **Fig. 4.25** as measured during part of the flight on 9 July 2008. While the calibration peak ($^{13}CH_3^{13}COO^-$) remains nearly constant, the signal at mass 59 amu ($^{12}CH_3^{12}COO^-$) changes, reflecting atmospheric PAN variability. At about 19:45 UTC, the ion intensity at mass 59 amu reaches a pronounced maximum, and hereafter decreases abruptly. Here, the Falcon encountered a pollution plume which was rich in PAN. The maximum at mass 59 amu is accompanied by a weak minimum of mass peak 61 amu, which reflects losses of the highly reactive CH_3COO^- due to reactions with other trace gases having elevated concentrations in the biomass burning plume. On the other hand, the mass peak at 127 amu remains relatively constant, since I^- reacts almost exclusively with peroxyacyl radicals and is in great abundance. This example underlines the importance of the isotopic calibration: The ambient PAN product ion obviously will be lost in the same way, therefore the assumption of a constant sensitivity would in this case result in an underestimation of the ambient PAN mixing ratio.

Figure 4.25 also shows 3 background measurement phases at about 18:37, 19:15, and 19:55 UTC. The background signals at masses 59 and 61 amu were obtained several times on each flight by passing the sample gas first through the BCU (BCU-mode, 18:37 UTC and 19:55 UTC). Additionally, the

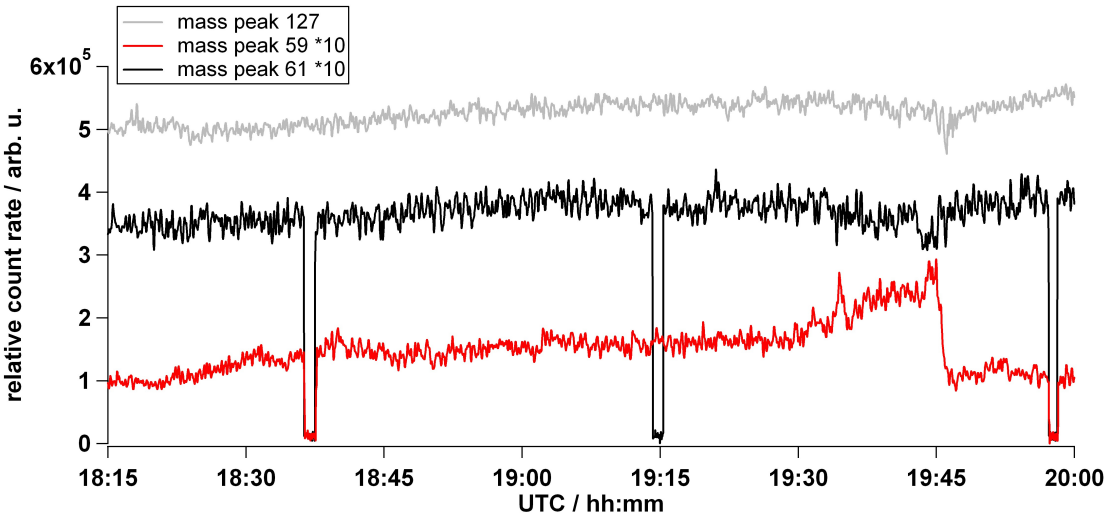

Figure 4.25: *Time-series of the ion signals at masses 59 ($^{12}CH_3{}^{12}COO^-$), 61 ($^{13}CH_3{}^{13}COO^-$) and 127 (I^-) for part of the flight on 9th July. Signals at masses 59 and 61 are multiplied by a factor of 10. Three background determinations are noticeable, two with the help of the BCU at about 18:37h and 19:55h and one without isotopic standard at 19:15h. See text for more details.*

isotopically labelled standard was switched off regularly in order to obtain a zero signal only at mass 61 amu (noILS-mode, 19:15 UTC), and to monitor potential artifact signals due to acetic acid (see section 4.1.2.3). The signal at mass 59 never showed a decrease as it would be expected for a significant cross-sensitivity induced by CH_3COOH. No significant changes in the average background signals of both BCU- and noILS-mode were observed over time, and for mass 61 amu no difference between both background modes (see also appendix A3). Also no trends connected with polluted or stratospheric air masses were found. As a conclusion, only electronic noise variations but no chemical interferences were responsible for fluctuations of the instrumental background.

4.2.3 Influence of water vapor

4.2.3.1 Sensitivity

During all the GRACE flights an isotopic PAN standard was added, producing a signal at mass 61 ($^{13}CH_3^{13}C(O)O^-$) and, dependent on water vapor, also at mass 79 amu ($^{13}CH_3^{13}C(O)O^-(H_2O)$). The mixing ratio of the PAN standard was kept constant, which allows to discuss the sensitivity variations of the system in dependency on several parameters, as, for example, on ambient water vapor concentration. This is particularly interesting, since a water-vapor dependent sensitivity is reported for the PAN measurement using I^--chemistry, most probably due to a faster reaction of $CH_3C(O)O_2$ with $I^-(H_2O)$ than with I^- (Slusher et al., 2004; Zheng et al., 2011). **Figure 4.26** shows the ion signals at mass peak 61 amu and the sum at mass peaks 61 and 79 amu in dependency on the ambient water vapor mixing ratio, as derived from all GRACE flights (note the logarithmic scale). Humidity was measured with the standard Falcon meteorological measurement system including a combination of three instruments: a commercial aircraft dew point hygrometer (GE 1011B, General

Eastern), a slightly modified capacitive sensor (Humicap-H,Vaisala) and a Lyman-alpha absorption instrument (Buck Research, Boulder). The average signals (vertical markers show the standard deviation) are calculated for several bins of water vapor concentrations (indicated by the horizontal markers), the number of data points for each bin is given below.
Obviously, the signal at mass 61 amu is highest for ambient water vapor mixing ratios of about 200–1000 μmol mol^{-1}. At lower humidities the ion intensity is less, probably due to the reported slower reaction with bare I^-. However, the signal decreases with humidities greater than ~1000 μmol mol^{-1} even more strongly. This is a result of the higher abundance of hydrated forms of ions inside the flow reactor $(^{13}CH_3^{13}C(O)O^-)(H_2O)_{n=0,1,2,...}$. These are not longer completely dehydrated inside the trap, and therefore the signal is partly shifted to mass 79 amu. This shift is confirmed by looking at the sum of the signals at both masses, which shows, if any, only a small decrease at the highest water vapor mixing ratios. At the mass of the next hydrate (97 amuamu, $^{13}CH_3^{13}C(O)O^-(H_2O)_2$), no significant increase was observed, even at the highest encountered humidities.

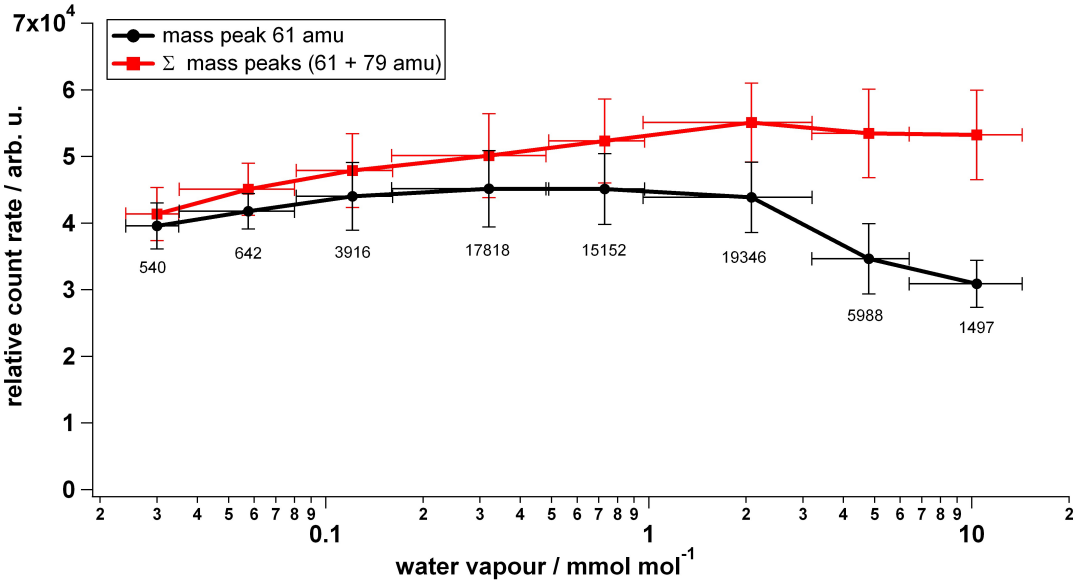

Figure 4.26: *Ion signals at mass peaks 61 amu ($^{13}CH_3{}^{13}COO^-$) and the sum of the signals at masses 61 and 79 amu ($^{13}CH_3{}^{13}COO^-(H_2O)$) as a function of ambient humidity. At high humidities, the mass peak 61 decreases due to shifting to higher hydrates, whereas the sum of 61 and 79 remains relatively constant. At low humidity, both signals decrease, mainly due to a slower reaction of CH_3COO_2 with bare I^- compared to $I^-(H_2O)$.*

It is worth noting that the observed water vapor dependency is accounted for by the online calibration. However, the detection limit is increased in the atmospheric boundary layer due to the lower sensitivity at the mass peak at 61 amu (by a maximum of ~30%).

4.2.3.2 Instrumental background of PPN

The instrumental PPN background has an interfering water vapor-dependent component at high ambient humidities (> 1000 μmol mol^{-1}), because the corresponding mass peak (73 amu) sits on

the rising edge of the hydrated forms of the PAN product ions (see section 4.2.1). In humid but clean air this artificial signal may become even higher than the ambient PPN signal. The in-flight background determinations (see section 4.2.2) cannot be used for a correction, because the major responsible mass peaks at 77 and 79 amu (hydrated form of the ambient and the isotopic calibration ion) disappear here as well.

The water vapor dependency was corrected by adopting the following approach: The mass peak at 73 amu sits on the rising edge of mass peaks at higher m/z ratios. Hence, the signals at mass peaks before and after the mass peak at 73 amu increase as well, approximately with a linear function towards higher mass peaks. No atmospheric signal is expected at the two mass peaks at 72 and 74 amu. This justifies taking the average of the signal at the two mass peaks as an instrumental background signal for mass peak 73 amu, easily calculable for each spectrum. The background values derived with this approach and their water vapor dependency were highly reproducible for all flights. For low-humidity conditions as prevalent in the upper troposphere/lowermost stratosphere, the calculated background signals show a good agreement with the values obtained with the help of the BCU-mode. Finally, some cross-checks were performed for several cases per flight with the following method: A linear curve was fitted to the bottom of the PPN peak at different humidities and hence, different peak heights of mass peak 79 amu, as illustrated in **Fig. 4.27**.

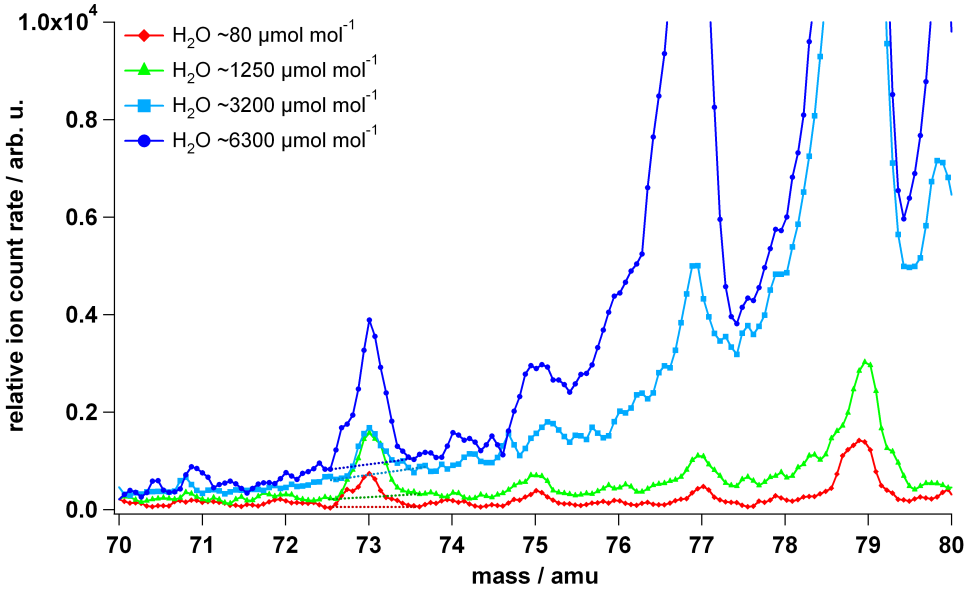

Figure 4.27: *Linear curve fit to the bottom of the signal at mass peak 73 amu (PPN) at different ambient water vapor mixing ratios. The PPN peak sits on the rising edge of the hydrated PAN product ions (mass peak 77 and 79 amu, respectively). The resulting increase in the background signal is estimated by taking the value of the linear curve fit at 73 amu.*

The maximum discrepancy between these 3 different PPN instrumental background determinations was, translated into mixing ratios, $\sim$9 pmol mol^{-1}. As a result, the PPN detection limit is likewise increased at high humidities $>$1000 μmol mol^{-1}.

4.2.4 Time-series of PAN and CO: Flight on 7 July 2008

To give an example of atmospheric PAN measurements, **Fig. 4.28** shows a time-series of PAN together with carbon monoxide (CO) for part of the flight on 7 July 2008 (13:45–15:10 UTC). CO was detected by a system using vacuum-UV fluorescence (see section 5). The altitude of the Falcon is given at the y-axis on the left hand side. The top of **Fig. 4.28** shows additionally a zoom into two parts of the time-series.

The Falcon was guided into a biomass burning plume originating from Saskatchewan, Canada. The plume extended over several hundreds of kilometres, and was intercepted several times at slightly different altitudes, as indicated by higher concentrations of both PAN and CO. As discussed in more detail in section 5.3, CO is produced during incomplete combustion processes and has a relatively long lifetime of several weeks in the free troposphere. This makes CO an excellent pollution tracer for combustion processes. PAN is expected to have elevated concentrations in biomass burning plumes because fires emit both precursor gases needed for PAN formation: VOCs and NO_x (see section 2.2.2). Inside the plume, the CO mixing ratio was ~150–180 nmol mol^{-1} compared to ~120 nmol mol^{-1} outside of it. PAN mole fractions were on average about 350 pmol mol^{-1} when the Falcon sampled the biomass burning pollution, atmospheric background mixing ratios of PAN were ~200 pmol mol^{-1}. The two blow-ups in the upper part of **Fig. 4.28** show that as expected, PAN and CO correlate very well, not only in gross, but also in fine structures.

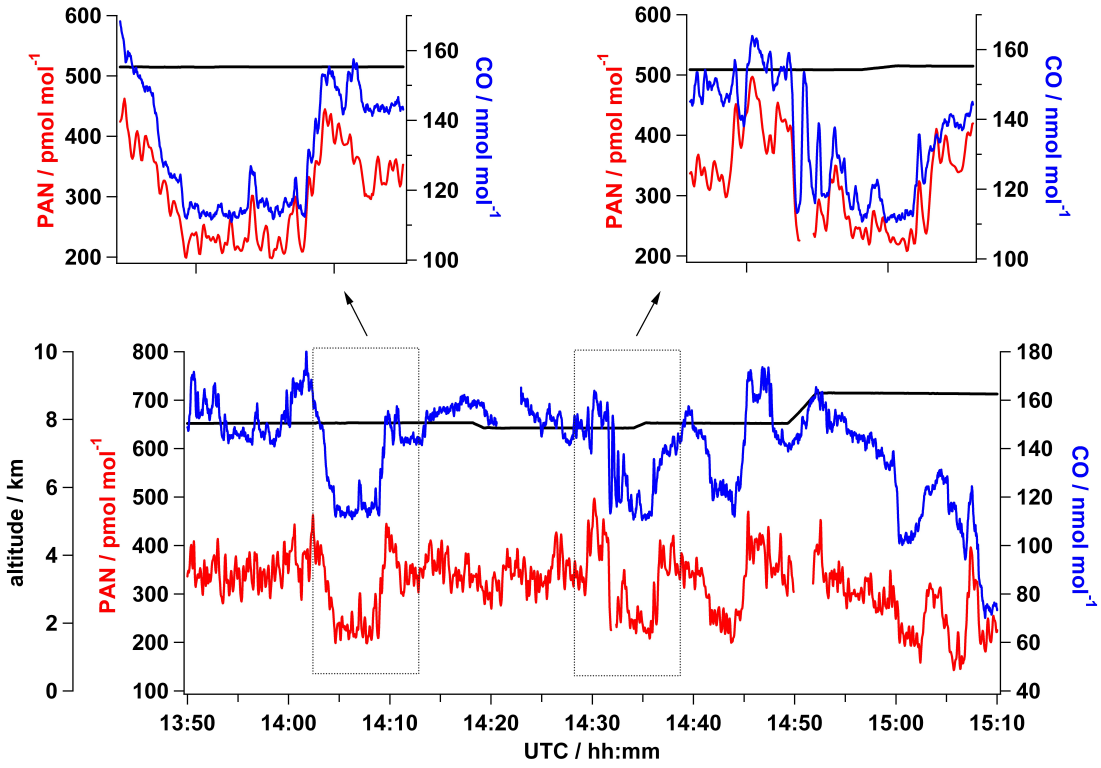

Figure 4.28: *Time-series of PAN (2 s) and CO (1 s) for part of the flight on 7 July (13:50–15:10 UTC). An aged Canadian biomass burning plume was intercepted several times at slightly different altitudes, as indicated by elevated PAN and CO concentrations (PAN > 300 pmol mol^{-1}, CO > 150 nmol mol^{-1}). A blow-up for two parts of the time-series is shown at the top.*

4.2.5 PPN/PAN ratios

As mentioned in section 4.1.2, higher homologues of PAN can be detected simultaneously using the I^--chemistry. The second most abundant PAN-type compound is PPN (peroxypropionyl nitrate): reported PPN/PAN ratios vary from less than 2% up to more than 25% (Roberts et al., 2002, 2004; Flocke et al., 2005a; Wolfe et al., 2007). The sensitivity for both PAN and PPN can be assumed to be identical (Slusher et al., 2004; Flocke et al., 2005a; LaFranchi et al., 2009). For the calculation of PPN, in equation 4.5 the signal at mass 59 amu is replaced by the signal at mass peak 73 amu (for calculation of ratio R). Due to the proximity of the two mass peaks ($\triangle$m/z = 12), the relative mass discrimination of the ion trap can be neglected. The constant K_{aa} in this case is set to 0.9662, as calculated from the terrestrial isotopic distribution, whereas the constant K_{as} (contribution from ambient PPN on the PAN calibration peak) is negligible.

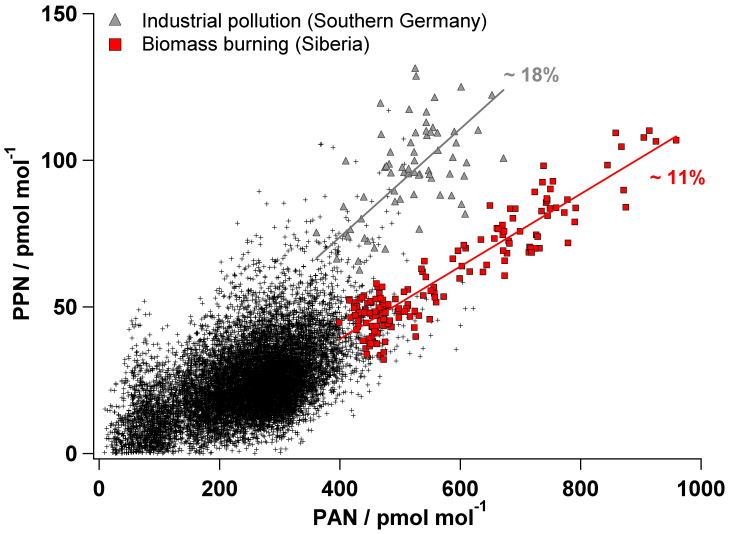

Figure 4.29: *Correlation of PPN versus PAN for all POLARCAT-GRACE data (10 s). Dark grey triangles represent data from measurements in fresh anthropogenic pollution above southern Germany, red squares data obtained during the interception of an aged Siberian biomass burning plume. See text for more details.*

The derived PPN mole fractions were most of the time below ~50 pmol mol^{-1}, as illustrated in **Fig. 4.29**. The correlation plot of PPN versus PAN contains 10 s values for all POLARCAT-GRACE flights. The bulk of the data (black crosses) lies within 0.03 to 0.3 which is in the range of values observed before.

For polluted situations precise PPN/PAN ratios can be determined. PPN mixing ratios measured during the descent to Oberpfaffenhofen on the 18 July 2008 (grey triangles in **Fig. 4.29**) belong to the highest observed values and are up to ~130 pmol mol^{-1}, the corresponding PPN/PAN ratio clusters around 0.18. Another main event was the interception of a Siberian biomass burning plume on 9 July, in which the highest PAN mixing ratios of almost 1 nmol mol^{-1} have been measured. The PPN mixing ratios in this plume were up to ~110 pmol mol^{-1}, which results in a significant lower PPN/PAN ratio of about 0.11 compared to the 0.18 measured in anthropogenic pollution.

This observation is in agreement with previous measurements (Williams et al., 1997; Roberts et al., 1998, 2002). PPN is known to be formed mainly from anthropogenic hydrocarbons (e.g. propanal) whereas PAN derives from almost all non-methane hydrocarbon species, see e.g. Altshuller (1993).

4.2.6 Intercomparison flight with the NASA DC8

The best evaluation of airborne measurement systems is an in-flight intercomparison. An intercomparison between two aircraft reveals insight into the instrument performance during ambient measurements which might differ significantly from observations made under controlled laboratory conditions. In the framework of the GRACE campaign, a wing-by-wing intercomparison flight between the NASA DC8 and the DLR Falcon was conducted. The comparison results were reviewed by the Tropospheric Airborne Measurement Evaluation Panel (TAbMEP) in July 2009 (http://www-air.larc.nasa.gov/TAbMEP.html).

The intercomparison flight took place on 09 July, 2008 above Greenland, when the DC8 aircraft left their POLARCAT base in Cold Lake (Canada) for an overnight stay in Thule (Greenland). The two aircraft met close to Summit (72°35´46"N, 38°25´19"W), a scientific research station located at 3200 m altitude a. s. l. In the framework of POLARCAT, continous measurements of NO, NO_2, PAN, NO_y and non-methane hydrocarbons (NMHC) have been performed at the Summit station from summer 2008 to winter 2009, along with observations of O_3. Therefore, also an intercomparison of measurements aboard the Falcon and the Summit station was planned on 09 July, but had to be skipped at short hand notice due to bad visibility conditions above the Summit station. After the rendezvous of the Falcon and the DC8 above Summit, the two aircraft flew jointly together towards the south-west. **Figure 4.30** shows the flight paths of the DLR Falcon and the NASA DC8 on 09 July, 2008.

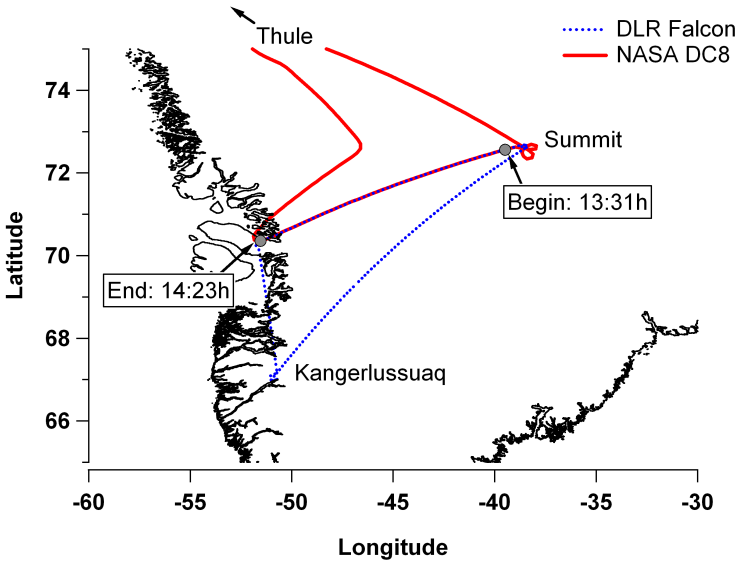

Figure 4.30: *Flight-path of the DLR Falcon (blue) and the NASA DC8 (red) on July, 9th, 2008. The wing-by-wing intercomparison period is indicated by the start and end times.*

Figure 4.31 shows the PAN time-series of both instruments. The altitude of both aircrafts as well as the start and end time of the intercomparison period is indicated. The intercomparison period was ∼52 min. and covered an altitude range from ∼4300 m to ∼7300 m. The original plan was to climb to even higher flight altitudes of ∼10000 m. However, due to instructions from ATC (air traffic control) the ascent had to be stopped (∼14:10 UTC). Both aircrafts then had to descent again to ∼5800 m. During the intercomparison period, the aircraft separation was less than ∼10 m in the horizontal, and less than ∼200 m in the vertical, allowing for a detailed intercomparison of all measurement systems. The time-series is extended towards the beginning and the end in order to illustrate the high variability of ambient PAN at different locations and altitudes, respectively.
PAN and its homologues was measured aboard the DC8 by a similar TD-CIMS instrument (Slusher et al., 2004), operated by Greg Huey and co-workers from the university of Georgia (GIT). Similar to the FASTPEX instrument, the DC8 instrument was calibrated with an isotopically labelled standard produced by a photolytic PAN source. The DC8 PAN mixing ratios were reported at a time interval of 30 s. The PAN values from the FASTPEX instrument have a time resolution of ∼2 s and were therefore merged into the 30 s time intervals.

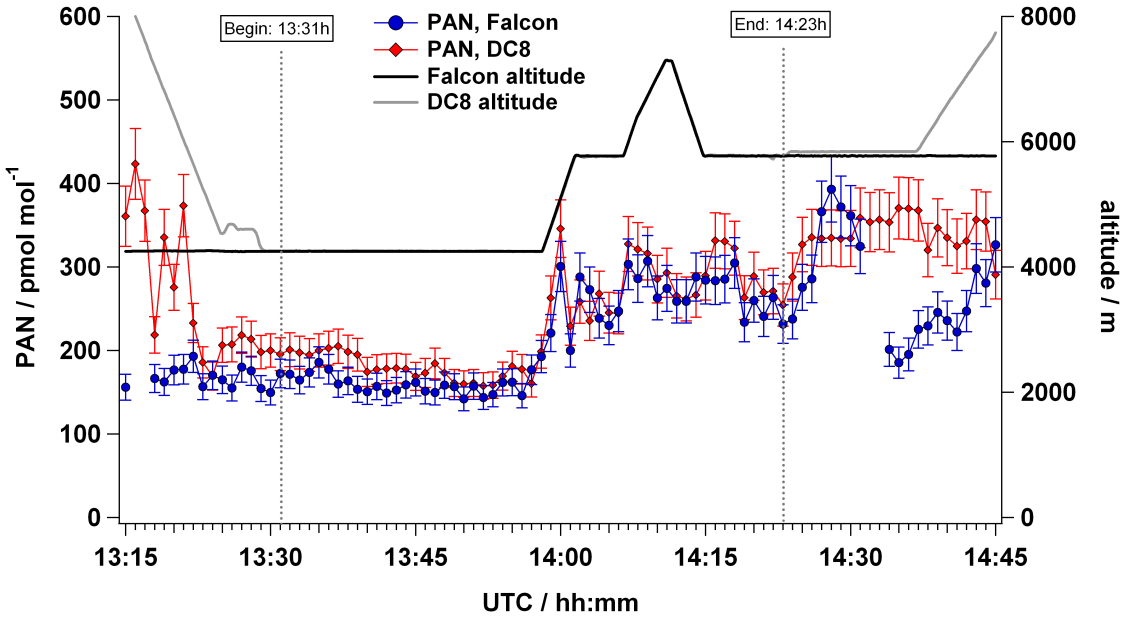

Figure 4.31: *Time-series of PAN (30 s values) as measured by the two instruments aboard the DLR Falcon and aboard the NASA DC8, for the intercomparison period on 09 July, 2008. On the Falcon, PAN data were obtained using the FASTPEX instrument (blue). Aboard the DC8, PAN was measured with a similar CIMS instrument using a quadrupole mass filter (red).*

The PI of the DC8 PAN measurements (Greg Huey) reports an uncertainty of ±10% for their PAN values, as indicated by the vertical error bars. The uncertainty of the FASTPEX instrument was also assumed to be ±10%, although PAN mixing ratios lower than ∼200 pmol mol^{-1} were encountered during the intercomparison. The relative error generally is assumed to be higher at these low PAN mixing ratios (see **Fig. 4.21**). However, the averaging to a time period of 30 s improves the accuracy and shifts the strong increase of the relative error towards lower mixing ratios.

Throughout the whole intercomparison period, the PAN time-series of the two instruments show a good agreement. In general, the Falcon PAN values are found to be slightly lower than the DC8 mixing ratios. Interestingly, the deviation is a bit higher at the beginning of the intercomparison period. It is worth noting that exactly in this phase, also other measurement systems (e. g. CO_2) showed a higher disagreement than during the remaining intercomparison period. For this reason, the TAbMEP panel discussed to shift the start time of the comparison. The final decision will depend on the results of a recap of meteorological parameters (e. g. wind direction). However and most important, the error bars generally overlap (except for two points in the mentioned earlier part of the comparison around ~13:38 UTC). This means that the PAN measurements agree within the combined measurement uncertainty of both instruments. A scatter plot of Falcon vs. DC8 PAN mixing ratios is given in **Fig. 4.32**.

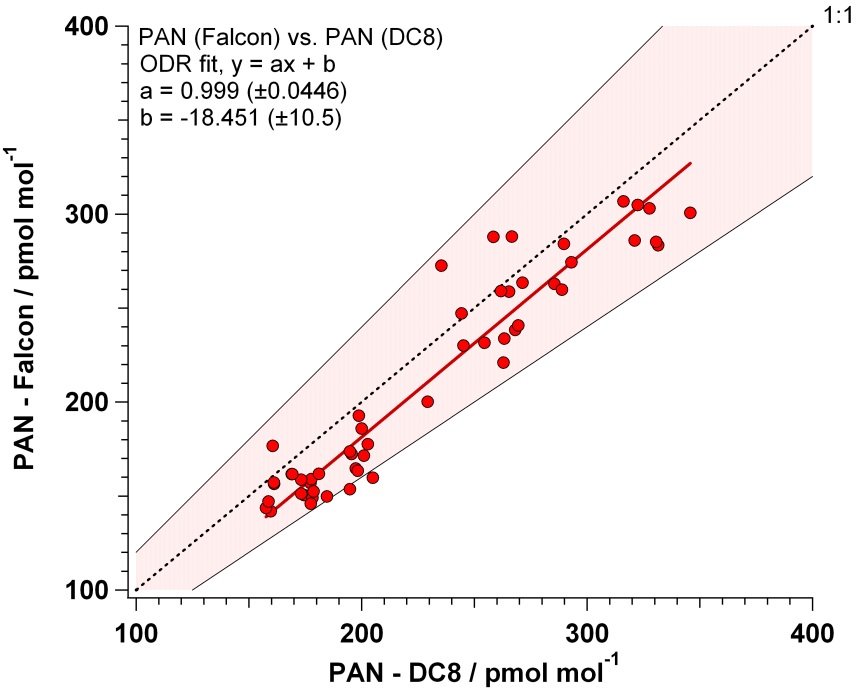

Figure 4.32: *Scatter plot of Falcon PAN vs. DC8 PAN measurements for data sampled during the intercomparison period (red circles). A linear fit using the orthogonal distance regression (ODR) was performed (red solid line). Values within the red shaded area agree within the combined measurement uncertainty of both instruments (limited by the thin black lines).*

Since in this case both x and y are independent variables having errors, a linear fit was performed using the Orthogonal Distance Regression (ODR) technique. The ODR technique minimizes the orthogonal distance of both x and y data to the fitting curve rather than minimizing the sum of squared errors only in the dependent variable y. As already mentioned, a slight bias is observed between both instruments, with only some exceptions. This bias is also reflected in the fitting parameters which suggest a slope close to one (0.999±0.046) but an offset of -18.451±10.5. Reason for this bias could be e. g. a difference in the background signals or between the two standards.

A cross-check between both standards was not possible because of the different home bases of the two aircraft. However, due to the general agreement of both PAN instruments within the combined measurement uncertainty, the intercomparison was evaluated as "successfull" at the 2009 TAbMEP meeting.

Chapter 5

Chemical composition of the summer Arctic atmosphere

This chapter discusses the main scientific results of GRACE (**Gr**eenland **A**erosol and **C**hemistry **E**xperiment) campaign. It starts with a short presentation of the scientific objectives (5.1) and of the tools used for the analysis (5.2). Subsequently, the influence of forest fire and anthropogenic emissions on the Arctic troposphere during GRACE is analyzed (5.3). It follows a discussion of the vertical distribution of PAN in the Arctic summer and its correlation with carbon monoxide CO and reactive nitrogen NO_y (5.4). The vertical distribution of other important trace gases during GRACE campaign is also presented (5.5). Sampled biomass burning plumes were often found in close proximity to air masses associated with stratosphere-troposphere-exchange (STE). This is illustrated by means of two selected case studies, which are also used to evaluate photochemical ozone production in biomass burning plumes (5.6). Finally, the O_3 formation potential as a result of PAN decomposition downstream of Greenland is analyzed by using a lagrangian photochemical model, CiTTyCAT (5.7).

5.1 Objectives of POLARCAT-GRACE Campaign

The POLARCAT project

As discussed in chapter 2.3, it is a well-known phenomenon that the Arctic is polluted both by industrial pollution from the mid-latitudes and by boreal forest fire emissions (e. g. Law and Stohl (2007)). Anthropogenic pollution is believed to enter the Arctic predominantly during winter and spring (Eckhardt et al., 2003; Klonecki et al., 2003; Stohl, 2006; Shindell et al., 2008). During boreal summer, emissions from forest fires have long been recognized to be the dominant source of trace gases and aerosols in the Arctic (Jacob et al., 2010; Shindell et al., 2008). However, large uncertainties remain regarding the transport pathways, and the relative contributions of different source regions. Within the framework of the 2007 - 2009 International Polar Year activities (http://www.ipy.org), a series of field campaigns were conducted as part of the POLARCAT (**POL**ar study using **A**ircraft, **R**emote sensing, surface measurements and modeling of **C**limate, chemistry, **A**erosols and **T**ransport) project

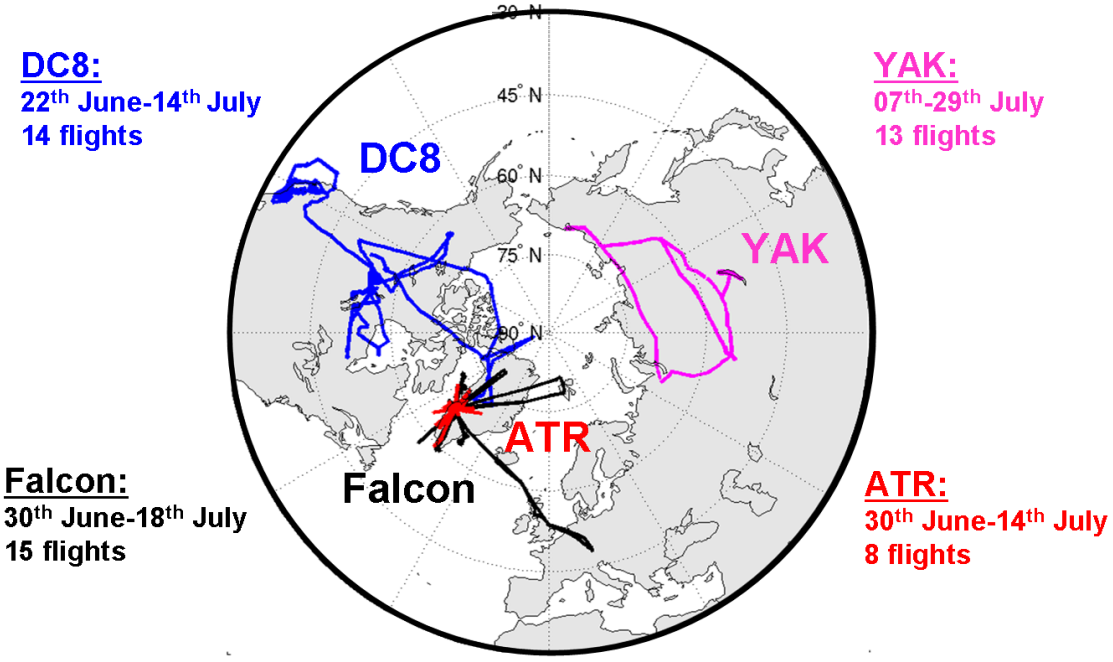

Figure 5.1: *Flight pattern of 4 POLARCAT campaigns which were carried out in summer 2008. The NASA DC8 (ARCTAS-B) as well as the YAK (AEROSIB) field campaigns took place close to the fire regions in Canada and Siberia, respectively. The DLR Falcon (POLARCAT-GRACE) and the ATR (POLARCAT-France) were based in Kangerlussuaq, Greenland, downwind of these fire regions.*

(http://www.polarcat.no). One main objective of POLARCAT was to combine both aircraft and satellite observations with models in order to study the influence of long-range poleward transport of trace gases and aerosols on composition, chemistry and climate in the Arctic. Several aircraft campaigns were conducted at different times of the year in order to follow pollution plumes of different origin and from different source regions into the Arctic, and to analyze chemical and aerosol processing of these plumes.

Figure 5.1 gives an overview over the main POLARCAT flight activities during summer 2008. Two field deployments were carried out close to the main fire regions in the boreal zone, Canada and Siberia. In the framework of ARCTAS-B (**A**rctic **R**esearch of the **C**omposition of the **T**roposphere from **A**ircraft and **S**atellites), the NASA DC8 was based in Cold Lake, Canada (54°N, 110°W), and performed several measurement flights close to the fires burning in the province Saskatchewan (Singh et al., 2010). The objective of the YAK-AEROSIB campaign (**A**irborne **E**xtensive **R**egional **O**bservations in **Sib**eria) was to document the distribution of CO_2, CO, ozone as well as aerosols in the Siberian troposphere impacted by forest fires (Paris et al., 2009). The french ATR as well as the DLR Falcon were based in Greenland, and focused on sampling the polluted outflow from North America and Siberia.

POLARCAT-GRACE

The GRACE (**GR**eenland **A**erosol and **C**hemistry **E**xperiment) campaign was a German contribution to POLARCAT, and took place from 30 June to 18 July 2008. The DLR Falcon was based in Kangerlussuaq, Greenland (67.01°N, 50.7°W), and performed a total of 15 local flights. Latitudes from 57°N to 81.5°N, longitudes from 66°W to 16°E and altitudes up to 11.8 km were covered by the Falcon. The main objectives of the GRACE field campaign were:

- to determine trace gas and aerosol distribution in the summer time Arctic;
- to study transport pathways of emissions from boreal forest fires and urban pollution into high northern latitudes;
- to examine processing (chemistry, aerosol ageing) in pollution plumes during transport (using POLARCAT-GRACE, ARCTAS, and YAK data);
- to analyze dispersion and mixing of pollution plumes during long-range transport using ambient and artificial tracer;
- to study the effects of boreal forest fire emissions injected into the lower stratosphere by pyro-convection;
- to investigate the distribution and impact of reactive halogen compounds in the Arctic to validate space-borne observations of trace gases and aerosol properties.

Figure 5.2 shows the coverage of the Falcon flights. The flight tracks are color-coded according to the flight altitude and labelled by their mission ID. Most data were sampled in the free troposphere between ∼4 to 9 km, in the region around southern Greenland. Generally, all missions started and ended at the home base in Kangerlussuaq, apart from one day when the Falcon did a stop-over in Spitsbergen (F15a + F15b). Those flights as well as one further mission (F10) were carried out in order to cover also the high northern latitudes.
The overall scientific objective of all flights was to sample distinct pollution plumes originating from the fire regions both in Canada and Siberia. For this, forecasts from the FLEXPART model (see chapter 5.2.2) were used to plan the flights. Several flights were conducted as so-called Lagrangian experiments: The Falcon tried to re-sample pollution plumes, which were already encountered by the NASA DC8 aircraft several days before (F07, F08, F09a, F12, F17). In case of a successful match, such experiments allow to study the chemical evolution in a plume by using a trajectory based box model (Real et al., 2007, 2008). Several flights were especially designed for a TRACER experiment (F07, F08, F12, F13a, F13b, F14b). This experiment enables to analyze mixing and dispersion of air masses by releasing different artificial and chemically inert tracers in a certain air mass, ideally inside a pollution plume (Auby et al., 2010; Schlager, 2011). With the help of FLEXPART forecasts, the released tracer was then re-sampled again by the Falcon on the following days. The flight routes for two missions (F02, F10) were adjusted in order to match with a fly-over of IASI (Infrared Atmospheric Sounding Interferometer) in order to perform a validation (Pommier

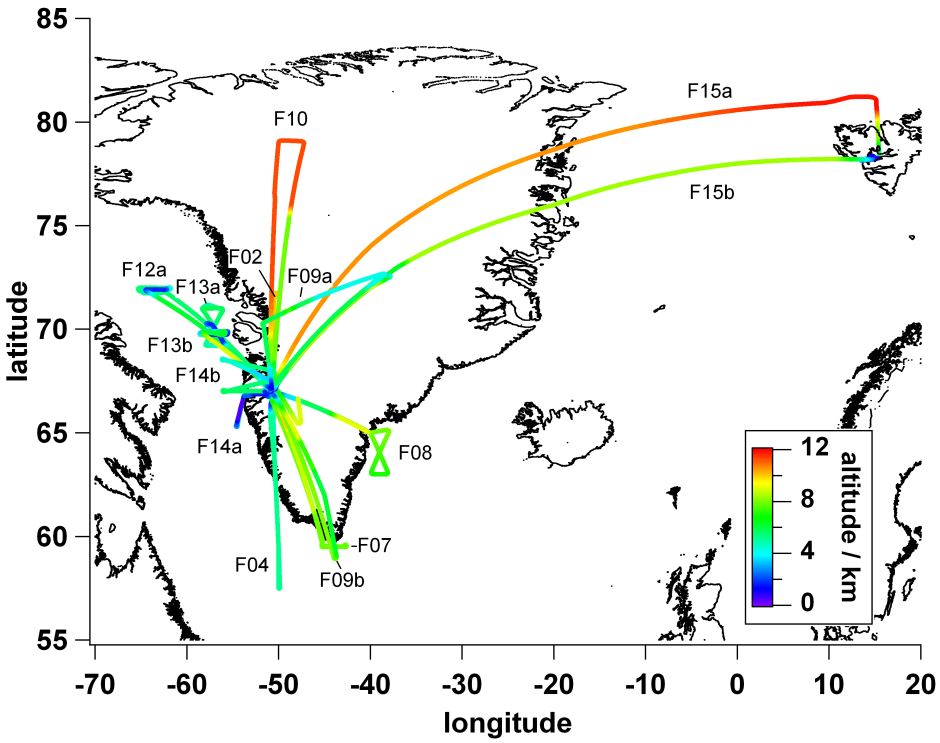

Figure 5.2: *Flight pattern of all 15 local Falcon missions carried out during GRACE campaign. Campaign base was Kangerlussuaq (67.01° N, 50.7° E). The flight tracks are color-coded according to their flight altitude (see color-scale at the right bottom). The flight tracks are labelled by their corresponding mission ID.*

et al., 2010). The composition of the Arctic UTLS (upper troposphere/lowermost stratosphere) region was studied during two missions (F10, F15a). Table 5.1 summarizes the objectives of all flights.

5.2 Measurements and methods

5.2.1 In-situ trace gas instruments on the Falcon

The Falcon was equipped with a series of instruments to measure trace gases, aerosol microphysical properties as well as meteorological parameters. The present work focuses on the trace gas instruments operated by the DLR-IPA group, which are shortly presented in the following and summarized in table 5.2.

PAN

Peroxyacetyl nitrate (PAN) measurements were performed with the Chemical Ionization - Ion Trap Mass Spectrometer which was built and characterized in the framework of the present thesis (see chapter 4).

CO

The CO measurements are based on a system using vacuum-UV fluorescence (AL-5001, Aero-Laser).

Table 5.1: *Date and scientific objectives of all 15 local GRACE flights.*

Mission ID	Date	Objective
F02	02 July	Test flight, SCIA/IASI validation
F04	04 July	Sampling of Canadian BB emissions mixed with anthropogenic pollution
F07	07 July	SCIA/IASI validation, sampling of Canadian BB emissions
F08	08 July	Lagrangian re-sampling of Canadian BB emissions
F09a	09 July	Intercomparison flight with NASA DC8, sampling of Canadian BB emissions
F09b	09 July	Sampling of Canadian and Asian BB emissions
F10	10 July	Arctic survey in UTLS, sampling of Canadian and Asian BB/FFC emissions SCIA/IASI validation
F12	12 July	Sampling of Asian BB/FFC emissions, Tracer release (PMCP)
F13a	13 July	Re-sampling of PMCP tracer
F13b	13 July	Release of i-PPCH tracer
F14a	14 July	Intercomparison flight with French ATR
F14b	14 July	Re-sampling of i-PPCH tracer
F15a	15 July	Arctic survey in UTLS
F15b	15 July	Sampling of Siberian BB emissions
F17	17 July	Sampling of Siberian BB emissions

Carbon monoxide (CO) is excited by means of a gas-discharge lamp (0.25% CO_2 in Argon, Air Liquide), which emits light by the dissociation of CO_2^* to CO and O between $\lambda \sim 145$-175 nm. The CO excitation wavelength ($\lambda \sim$150 nm) is selected by means of an optical filter. Part of the excited CO^* emits light due to resonance fluorescence ($\sim$160-190 nm) which is detected by a photomultiplier. Since CO^* may be deactivated also by collisions with other molecules such as N_2, the fluorescence cell is maintained at a low pressure of typically $\sim$5 hPa. The sample gas continuously is dried by means of a PermaPure drier system, because water vapor is a possible interferant due to its strong absorption at $\lambda < 190$ nm. Both instrument background and span are determined regularly during the flights by means of a Hopcalite filter and a CO calibration gas, respectively.

O_3

Ozone was measured using a TE49C system (Thermo Scientific). The measurement principle is based on the UV absorption at 254 nm. A mercury vapor lamp emitting at 253.7 nm is utilized as light source. The sample gas is drawn either directly through the absorption cuvette, or it is flushed via an ozone-scrubber to a reference cell. This ensures that UV absorption by species other than ozone are cancelled out. The ozone-scrubber is switched every 5 s between both cells in order to minimize disturbances due to differences between the two cuvettes. The sensitivity of the TE49C instrument is characterized by long-term stability. Nevertheless, it was calibrated regularly between the flights using an O_3-calibrator from Ansyco ($O_3$41M).

Table 5.2: *In-situ trace gas instruments (DLR-IPA) aboard the Falcon during GRACE 2008.*

species	measurement technique	accuracy, detection limit	reference
CO	VUV fluorescence	5%, 2 nmol mol^{-1}	Gerbig et al. (1999)
O_3	UV absorption	5%, 1 nmol mol^{-1}	Schlager et al. (1997)
CO_2	IR absorption	5%, 5 nmol mol^{-1}	Gurk et al. (2008)
NO, NO_y	chemiluminescence+Au converter	10, 15%, 10, 15 pmol mol^{-1}	Feigl (1998)
PAN	CI-ITMS	10%, 25 pmol mol^{-1}	Roiger et al. (2011a)

CO_2

CO_2 is detected by using a commercial analyzer (LI-COR 7000). The measurement principle relies on differential non-dispersive infra-red (IR) absorption spectroscopy. An infra-red light beam is directed through two geometrically identical cells, one measurement cuvette and one reference cell. The reference cuvette is purged with a small flow of a reference gas, which has a CO_2 mixing ratio close to the expected ambient value ($CO_2 \sim 390\,\mu$mol mol^{-1}, Air Liquide). The sample gas is drawn through the measurement cell, which for in-flight calibrations regularly is flushed also with the reference gas. A second calibration gas is used for in-flight calibrations in order to derive the span of the instrument ($CO_2 \sim 400\,\mu$mol mol^{-1}, Air Liquide). Pre- and post campaign calibrations were performed using 4 calibration standards from NOAA (National Oceanic and Atmospheric Administration).

NO, NO_y

NO and the sum of reactive nitrogen compounds, NO_y, were measured by a 2-channel chemiluminescence detector (CLD-790 SR, ECO-Physics, Feigl (1998)). The CLD instrument uses the luminescence of excited NO_2, which is produced by the chemical reaction of NO with O_3. The excited NO_2^* emits light in the infra-red ($\lambda \sim 500$ - 3100 nm), which is detected by a photo-multiplier. To avoid cross-sensitivities from fluorescent unsaturated hydrocarbons, a zeroing volume is integrated into both channels. Quenching of NO_2^* is suppressed by maintaining the reaction chamber at low pressure ($\sim$4 - 5 hPa). Reactive nitrogen NO_y (NO_y = NO, NO_2, NO_3, N_2O_5, HNO_3, PAN...) is first converted to NO at the surface of a gold converter by adding CO as reducing agent, and subsequently is detected as NO (Feigl, 1998; Fahey et al., 1985). Calibration of the NO-NO_y-system was performed at the ground before/after each flight. Sensitivity of the NO system was checked by calibration with a NO calibration bottle (3 μmol mol^{-1} NO in N_2, Air Liquide). The NO_y conversion efficiency was determined by using the gas-phase titration of NO with O_3 (Feigl, 1998). Conversion efficiencies of other NO_y species than NO_2 was assumed to be equivalent to that of NO_2 (Fahey et al., 1985).

5.2.2 The FLEXPART transport model

For the analysis of all GRACE flights, the FLEXPART model was used in order to attribute anthropogenic and biomass burning pollution sources to the in-situ observations. FLEXPART is a

Lagrangian particle dispersion model (Stohl et al. (2005) and references herein). For this study, it was driven with meteorological analyses from the European Centre for Medium-Range Weather Forecasting (ECMWF) with a 0.5° x 0.5° resolution. FLEXPART includes a sub-grid scale convective transport scheme. Stochastic fluctuations are obtained by solving Langevin equations (Stohl and Thomson, 1999) and are superimposed on the grid-scale winds to represent transport by turbulent eddies. For CO, NO_2 and SO_2, the EDGAR (Emissions Database for Global Atmospheric Research) version 3.2 emission inventory for the year 2000 (fast track) on a $1° \times 1°$ grid was used outside North America and Europe. Over Europe, the EMEP (European Monitoring and Evaluation Programme) emission inventory for the year 2005 with a resolution of $0.5° \times 0.5°$ was used and over most of North America, the inventory of Frost et al. (2006). For the input of biomass burning emissions, hot spot locations are obtained daily from measurements made with MODIS (**Mod**erate Resolution **I**maging **S**pectroradiometer) onboard the Aqua and Terra satellites and are compared to a land-use inventory with 1-km resolution. The emissions are estimated assuming an area burned of 180 ha per fire detection. They depend on a parameterization based on biomass available for burning, the fraction actually burned, and emission factors, all dependent on land-use. Fire emissions were only distributed within the lowest 150 m of the boundary layer and fires burned for 24 h (Stohl et al., 2007). In the framework of this thesis, only CO is used as a tracer, which is considered separately for both anthropogenic and biomass burning pollution, and is further separated according to the different source regions Asia, North America or Europe. Previous experience with the 1995 EDGAR inventory has shown that Asian CO emissions are underestimated (probably by a factor of 2 or more), while American CO emissions may be overestimated. Please note that the modelled FLEXPART CO only represents the CO emitted by pollution sources during the last 20 days. In order to compare it with mixing ratios of in-situ measured CO, the FLEXPART CO has to be added to the (unpolluted) background atmosphere, which itself differs for example between the troposphere and stratosphere. To be clear, CO from the FLEXPART model is therefore is referred to as "excess-CO" in this work. Another point worth noting is that the modelled excess-CO underlies passive transport without involving removal processes, as for example the oxidation by the hydroxyl radical OH. After a lifetime of 20 days, it is removed under the assumption that it becomes incorporated into the so-called atmospheric background (Sodemann et al., 2011). The present thesis uses mainly FLEXPART backward simulations. These were started along the flight track every time the Falcon moved by 0.15 degrees in either longitude or latitude, or whenever the altitude changed by 10 hPa. For each release 60000 particles were followed backward in time for 20 days. The model output of such backward simulations consists of fields of emission sensitivities which can be multiplied with emission fields to yield maps of source contributions for passive tracers (Stohl et al., 2003). When spatially integrated, tracer mixing ratios are obtained which allow to construct tracer time-series (e. g. of "excess-CO") along the flight path. Further information used herein is the fraction of particles remaining in the stratosphere during the last 20 days. For this, troposphere and stratosphere are separated based on a threshold of 2 PVU (potential vorticity units).

5.3 Pollution transport into the Arctic during GRACE

The summer time Arctic is perturbed by emissions of boreal forest fires which are located primarily in Canada, Russia, and Alaska. The mean area annual burned is ∼2.2 and ∼6.8 Mha for boreal North America and boreal Siberia, respectively (Giglio et al., 2010). However, there is great inter-annual variability dependent on continental climate, extreme weather and ignition conditions (Kasischke et al., 2005; Giglio et al., 2010; van der Werf et al., 2010). The fire activity during the GRACE field deployment is illustrated in **Fig. 5.3** for a 10-day period. It shows a map depicting forest fires as derived from the MODIS thermal anomalies product (Justice et al., 2002). The summer 2008 showed in general low to moderate biomass burning activity in Canada (van der Werf et al., 2010; Singh et al., 2010). However, fire activity in the northern part of the province Saskatchewan was unusually high, approximately four times the 20-year average (Soja et al., 2008). In Siberia, boreal fires burned mainly in the eastern regions, and were the most intense ones since the record-breaking year in 2003 (van der Werf et al., 2010).

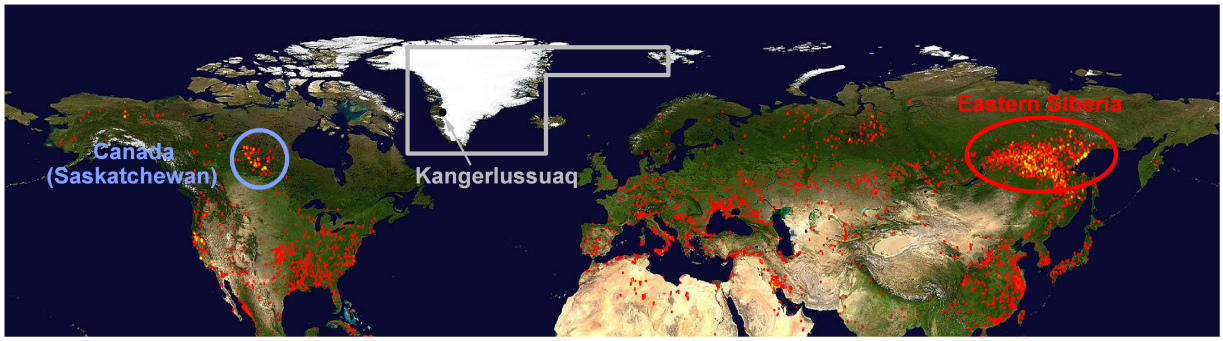

Figure 5.3: *MODIS fire map for the time period 30.06. to 07.07.2008 (http://rapidfire.sci.gsfc.nasa.gov/). Each colored dot indicates a location where MODIS detected at least one fire. Color ranges from red where the fire count is low to yellow where number of fires is large. The grey marked area indicates approximately the region covered by the Falcon during GRACE campaign. The main boreal fire regions in summer 2008 were in the province Saskatchewan (Canada) and in eastern Siberia, as marked by the blue and red circles, respectively.*

During GRACE, the Arctic troposphere was impacted by emissions imported from both fire regions in Canada and Siberia. According to prevailing meteorological conditions, the field campaign can be separated into two phases. During the first half of the GRACE field campaign (∼02 to 09 July), mainly pollution from the North American continent was advected into our measurement area. Responsible for this were several low-pressure systems moving from North America towards Greenland (Fuelberg et al., 2010). In the second half of the campaign (∼10 to 17 July), the Arctic troposphere was predominantly impacted by emissions from Siberian fires which often were mixed with Asian fossil fuel combustion (FFC). Interestingly, the main part of the pollution from the Asian continent was transported directly across the North Pole into the European sector of the Arctic (Fuelberg et al., 2010; Sodemann et al., 2011).

Forest fires emit a variety of different trace and aerosol species (see also section 2.3.1), including carbon monoxide (CO). CO is formed during in-complete combustion processes from human activities

or biomass burning. It is an excellent tracer to study the transport of pollution since it has a relatively long lifetime of several weeks in the free troposphere. This allows CO to be transported for long distances before being removed from the atmosphere. Carbon monoxide however is also present in the background atmosphere, formed by oxidation processes of methane (CH_4). Its major sink is the reaction with OH radicals, which results in generally lower CO background values in the summer troposphere compared to winter. For the same reason, lower CO background values are observed in the tropics compared to the middle and polar latitudes (Novelli et al., 1992, 2003).

Figure 5.4a shows an average CO profile as calculated from all 15 local GRACE flights (median and lower/higher quartiles). For comparison, also an average CO profile sampled during the CONTRACE campaign is given (avg $\pm$ std). The CONTRACE[1] field campaign was carried out in fall 2001 from southern Germany, and focused on the long-range transport of North American pollution to Europe. The CONTRACE profile reflects a quite typical vertical CO distribution for the industrial mid-latitudes. CO mixing ratios roughly follow a L-shape because CO is emitted mainly at the ground and experiences dilution at higher altitudes. The GRACE CO profile however looks rather different. In the lowest few kilometers of the Arctic, CO is present at mixing ratios of $\sim$90 nmol mol^{-1}, which is a quite typical value for Arctic summer background conditions (Fischer et al., 2006; Paris et al., 2009). In the free troposphere, CO however reaches median values between $\sim$120 and 140 nmol mol^{-1}, being even higher than in the industrial mid-latitudes above Europe. In the tropopause region (above $\sim$9 to 10 km), CO strongly decreases down to values of $\sim$40 to 50 nmol mol^{-1}. This is attributed to a less efficient CO production from methane oxidation in the lowermost stratosphere. The shift of the higher CO quartile in the highest altitude bin (11 to 12 km) is dominated by the sampling of an Asian pollution plume in the lowermost stratosphere (see chapter 6).

As discussed in section 5.2.2, the FLEXPART model was used to assign the polluted air masses to their origin. The excess-CO values from different source types and regions were interpolated on the Falcon flight tracks[2]. **Figures 5.4b** and **c** show averaged FLEXPART excess-CO profiles as calculated from all 15 local GRACE flights. Excess-CO originating from biomass burning (BB) is illustrated in **Fig. 5.4b**, whereas **Fig. 5.4c** highlights the contribution from anthropogenic sources (AS). Similar to in-situ measured carbon monoxide, also both FLEXPART profiles show enhanced values of excess-CO in the free troposphere, but with a different extent. For biomass burning, FLEXPART suggests excess-CO of $\sim$ 20 to 50 nmol mol^{-1} in the altitude region between $\sim$ 4 to 9 km whereas pollution from anthropogenic sources (AS) only adds median excess-CO values of $\sim$ 5 to 10 nmol mol^{-1}. The sampling of the Asian anthropogenic plume above 11 km is reproduced also in the FLEXPART model, indicated by the shift of the higher quartile in the AS-CO. The present study uses FLEXPART excess-CO more qualitatively and not in a quantitative way. Nevertheless, average values are found to be in relatively good agreement with our in-situ measured CO. Assuming a tropospheric CO background of $\sim$ 90 nmol mol^{-1}, adding FLEXPART excess-CO of $\sim$ 20 to 50 nmol mol^{-1} fits quite well with the observed $\sim$ 110 to 130 nmol mol^{-1}.

[1] **Con**vective Transport of **Trac**e Gases into the Middle and Upper Troposphere over **E**urope: Budget and Impact on Chemistry

[2] all FLEXPART data are available under http://transport.nilu.no/flexpart-cmp-products?cmp=GRACE

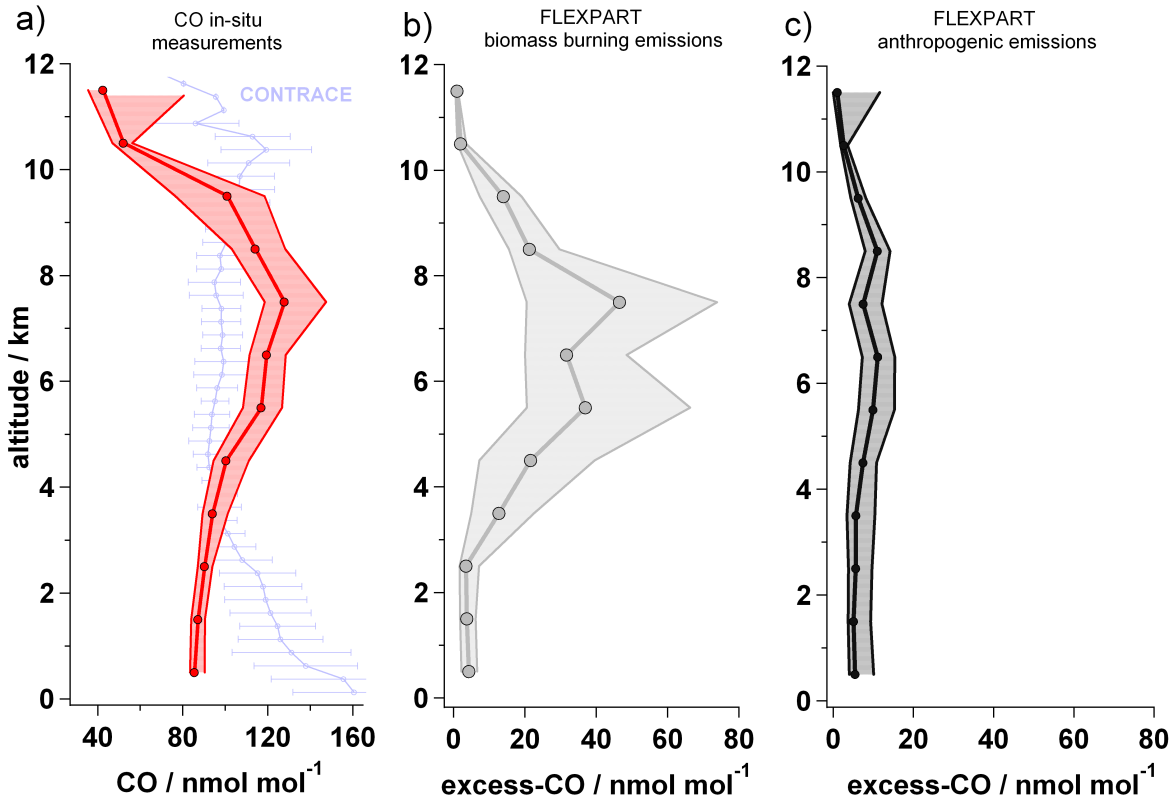

Figure 5.4: *Comparison of in-situ measured CO with modelled FLEXPART excess-CO profiles, interpolated on the Falcon flight tracks. a) In-situ CO profile from GRACE (red, median and lower/higher quartiles) and CONTRACE (light purple, avg ± std), b) FLEXPART excess-CO originating from biomass burning (median and lower/higher quartiles) and c) FLEXPART excess-CO emitted by anthropogenic sources (median and lower/higher quartiles). For more details see text.*

The shown FLEXPART profiles are separated only by fuel type, but not according to the various source regions. As will be discussed also in section 5.6, the BB-CO was transported approximately in equal amounts from Canada and Siberia into our measurement area. On the contrary, the anthropogenic CO mainly originated from Asia, and these emission were often observed to be mixed with BB emissions advected from Siberia. Transport times for the pollution plumes to Greenland was ∼5 - 10 days for emissions originating from North America, whereas pollution from Siberia/Asia reached our measurement area on average ∼10 - 20 days after emission.

The question wether the GRACE in-situ CO profile is representative for the Arctic summer is difficult to answer. Our sampling strategy certainly has biased the vertical CO distribution towards higher mixing ratios. Most flight plans were especially designed to probe distinct pollution plumes originating from different source regions. On the other hand, also during flights dedicated to study the Arctic background troposphere, sampling of aged pollution plumes was unavoidable. Imported emissions were observed on large scales, and were found to be more or less mixed into the Arctic background. This large-scale influence is reflected in the lowest CO percentiles (see also **Fig. 5.8a**), which show a bias towards higher CO mixing ratios in the free troposphere compared to the boundary layer.

5.4 PAN in the Arctic summer atmosphere

As discussed above, the Arctic summer troposphere during GRACE was impacted mainly by imported biomass burning pollution. PAN formation is relatively efficient in forest fire plumes (see section 2.2.2) meaning that PAN values are expected to be enhanced in those air masses. This section presents the vertical distribution of PAN and compares it with earlier measurements: Singh et al. (1992b) deduced from ABLE-3A[3] measurements in summer 1988, that at the cold temperatures of the Arctic troposphere, the main part of reactive nitrogen is stored in organic forms such as PAN. It follows a discussion about the correlation of PAN with CO in different layers of the atmosphere. PAN/CO ratios of distinct biomass burning plumes are compared with values reported in the literature. Finally, the relation of PAN to NO_y in different kinds of air masses is discussed.

5.4.1 Vertical distribution of PAN

The vertical distribution of PAN is illustrated in **Figure 5.5a**. It shows all PAN data which were sampled during the local GRACE flights. For comparison with the industrial mid-latitudes, also PAN measurements from the ferry flight Reykjavik - Oberpfaffenhofen are given (F18b). The vertical PAN profiles look very similar for all local flights. Similar to CO, highest PAN mixing ratios are found between ∼4 and 9 km. As a result of the pollution import from biomass burning and anthropogenic sources, PAN here reaches median values of ∼300 pmol mol^{-1} (see also later **Fig. 5.8b**). The most prominent pollution plumes sampled by the Falcon stand out from the remaining data, and are labelled by their origin. The observed PAN values are relatively high and comparable with mixing ratios measured in the industrial mid-latitudes. Singh et al. (2007) report for example PAN median values of ∼330 pmol mol^{-1} which were sampled in the summer free troposphere above North America during INTEX-A. At the west coast of North America, Roberts et al. (2004) found even slightly lower PAN median values of 180 pmol mol^{-1} for altitudes above 4 km, observed during a field campaign in spring 2002 (ITCT-2K2).

In the Arctic summer time troposphere, PAN measurements are sparse. The only data available in the literature have been sampled within the framework of the ABLE-3A campaign in July-August 1988. Similar to our observations, Singh et al. (1992b) found a systematic increase of PAN with height, but their measurements were limited to an altitude of ∼6 km. Their reported PAN median values are also indicated in **Fig. 5.5a** (white diamonds). Interestingly, the ABLE-3B measurements are quite close to our observations, in spite of the large temporal difference of 20 years between both field campaigns, and a certainly different sampling strategy.

Due to start-up and shut-down procedures after take-off and before landing, PAN mixing ratios from GRACE are available only above ∼1 km, exceptional for one flight (F14a), when the lowest intercomparison leg with the ATR was performed in the marine boundary layer at FL 15 (∼460 m). The main reason for the decrease of PAN towards lower levels is its shorter thermal lifetime. **Figure 5.5b** gives the thermal decomposition lifetime of PAN as a function of height, calculated from the average temperatures measured during all local GRACE flights. In our measurement area, the lifetime of

[3] Atmospheric Boundary Layer Expeditions-3A

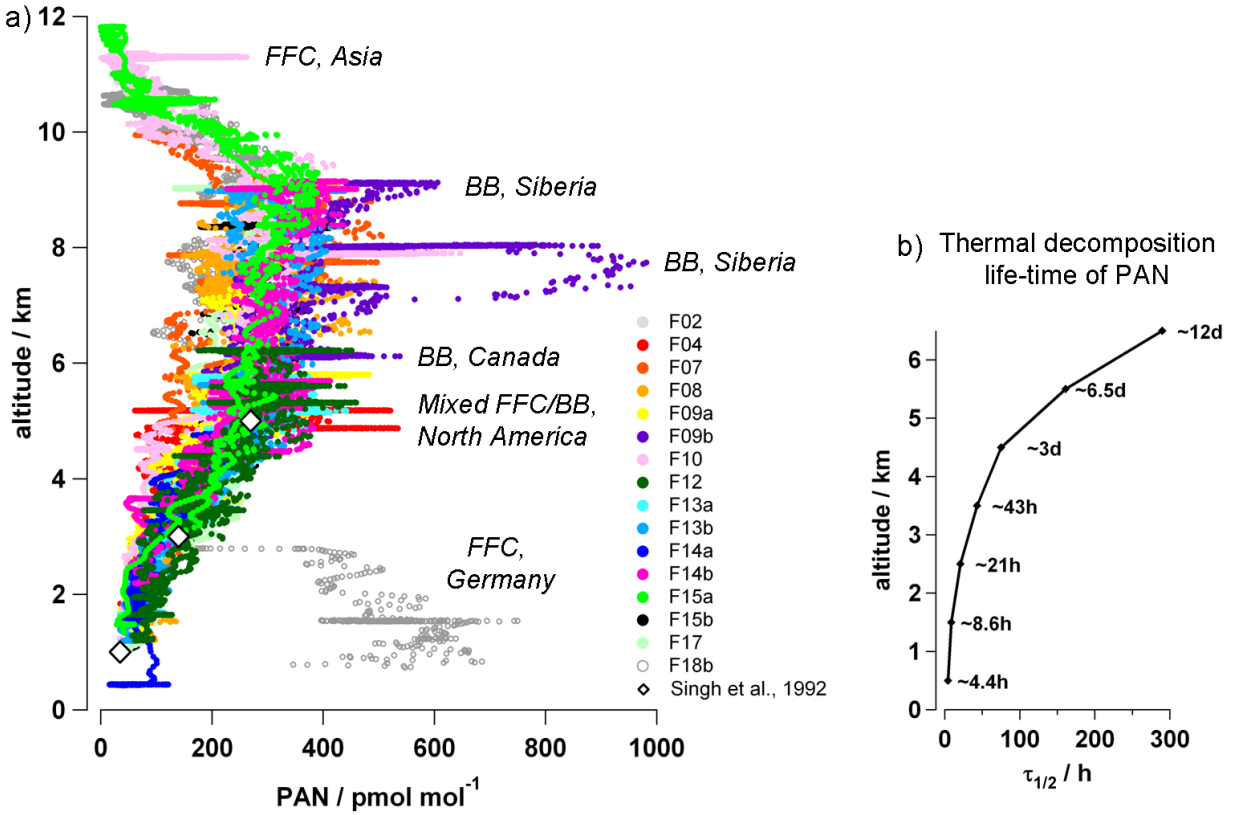

Figure 5.5: *a) PAN vertical profiles from the 15 local POLARCAT-GRACE flights. For comparison, also PAN data from the transfer flight Reykjavik - Oberpfaffenhofen are given (F18b). The source regions of the most prominent PAN plumes are labelled. White diamonds indicate median values reported by (Singh et al., 1992b), who performed measurements above Greenland in summer 1988. b) PAN thermal decomposition lifetime as a function of height, calculated by using average ambient temperatures during the GRACE field campaign.*

PAN is several days or more for altitudes above 4 km. In the lowest few kilometers, PAN is supposed to survive only several hours. Note however, that the abundance of PAN in the warm boundary layer is a question of both sources and sinks. In other words, PAN may also accumulate at low altitudes, if its precursors are continuously emitted and photochemically processed. During the ARCTAS-B campaign, Singh et al. (2010) found for example PAN average values of $\sim$400 pmol mol^{-1} in the lowest few kilometers of the troposphere, biased by their sampling strategy which focused on probing fresh Canadian biomass burning emissions. Also the Falcon measured high PAN mixing ratios during one flight at low altitudes. The profile F18b in **Fig. 5.5a** shows that up to $\sim$800 pmol mol^{-1} PAN was observed in the polluted continental boundary layer in the vicinity of Oberpfaffenhofen (close to Munich, Germany).

Above $\sim$9 km, PAN mixing ratios drop to values close to the detection limit (25 pmol mol^{-1}). This again is a combined effect of small local sources and a a significant large sink: PAN formation in this altitude region is negligible due to a lack of hydrocarbon precursors. Additionally, the PAN lifetime is comparatively low in the tropopause region ($\sim$1 month), limited by photolysis (Talukdar et al., 1995). This prevents the substantial accumulation of PAN in the UTLS region.

5.4.2 Correlation with CO and NO_y

PAN versus CO

Figure 5.6 shows a scatter plot of PAN versus CO (10 s values) for all GRACE data up to 200 nmol mol^{-1} CO. The color-code represents the potential temperature Theta (Θ). Theta often is used as vertical coordinate instead of atmospheric pressure. It is a good meteorological tracer since in the absence of diabatic processes (latent heat release, sensible heating, or the absorption/emission of long and short wave radiation), an air parcel will be transported along constant isentropic surfaces. Theta therefore helps to differentiate between various layers of the atmosphere. A mean vertical Θ profile from all local GRACE measurements is given in **Fig. A.3**.

PAN and CO show a positive relationship throughout the whole troposphere, as well as in the lowermost stratosphere. However, depending on the altitude region, the data can be separated into several branches. Most of the measurements were performed in the free troposphere. Θ-values between 310 and 330 K represent the mid- and upper troposphere ($\sim$6 - 10 km). In this region, PAN shows a quite compact correlation with CO. A linear regression yields a slope of $\sim$2.8 (R^2=0.84). PAN values at potential temperatures between $\sim$300 and 310 K ($\sim$3 - 6 km) however are less well correlated with CO. For CO mixing ratios of $\sim$ 120 nmol mol^{-1} and more, they show a much higher scattering having a partial trend to lower values. This indicates that PAN to some extent is depleted due to thermal dissociation at these altitudes. A main part of PAN loss processes certainly took place already during advection towards Greenland. At even lower altitudes ($\Theta < 300$ K), thermolysis of PAN is much more pronounced: Whereas CO is still present at background concentrations between $\sim$80 to 100 nmol mol^{-1} (originating from methane oxidation), PAN in this region rapidly drops down.

Air sampled in the UTLS (upper troposphere/lowermost stratosphere) region contains low PAN and CO mixing ratios. Like in the mid- and upper troposphere, a quite compact correlation between both trace gases is observed in the lowermost stratosphere. Due to missing local sources, PAN sharply decreases to values around the detection limit, CO here is still abundant at mixing ratios of $\sim$30 nmol mol^{-1}, arising from methane oxidation. The shorter lifetime of PAN ($\sim$ 1 month) compared to CO ($\sim$ 3 months) in the lowermost stratosphere leads to a rather steep slope observed between PAN and CO ($\sim$4.04 for Θ>330 K, R^2=0.82).

PAN/CO enhancement ratios in BB plumes

During GRACE, 29 distinct biomass burning plumes have been sampled (see overview table A.1). Table 5.3 compares the average of observed PAN/CO enhancement ratios (ERs) with values reported in the literature. Obviously, the derived mean ER[4] ΔPAN/ΔCO of 2.61 ($\pm$ 0.36) is significantly lower than those from all the other observations, independently also from fuel type. The main difference between our and earlier measurements is the plume age, which possibly might be the explanation of this discrepancy. Pollution sampled during POLARCAT arrived after a minimum travel time of

[4]The ERs were determined for each plume by taking the difference between the average PAN values inside the plume and those of the surrounding background air ($\Delta PAN = PAN_{plume} - PAN_{background}$), and then normalizing it to ΔCO ($CO_{plume} - CO_{background}$).

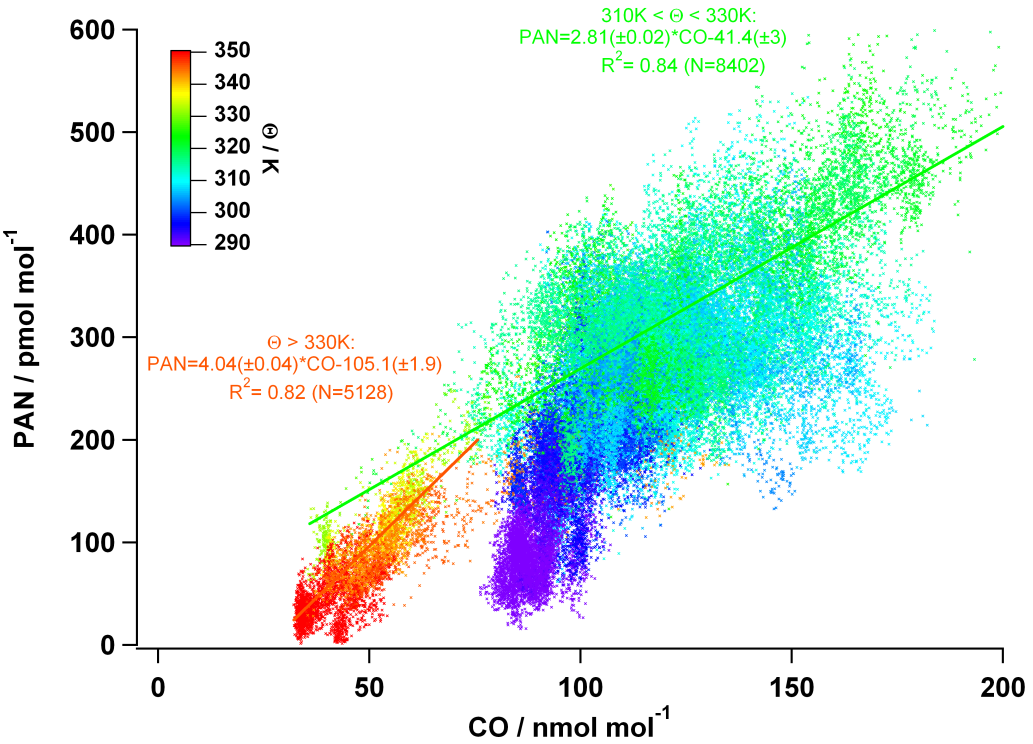

Figure 5.6: *Scatter plot of PAN vs. CO using all data from the 15 local GRACE flights. Color-code represents potential temperature Θ (see color-scale at the left top). Fore more details see text.*

5 days in the Arctic, whereas all other studies focused on generally younger plumes with a maximum plume age of 5 days. If we assume a comparable PAN/CO emission ratio, chemical and/or mixing processes during the long-range transport may have altered PAN and CO concentrations differently, in such a way that PAN decreases stronger than CO. Most likely, dilution with surrounding air masses explains the lower ERs: Apart from aged pollution, all other air masses (e. g. clean tropospheric air or lowermost stratospheric air) typically contain much lower PAN than CO.

Table 5.3: *In-situ observations of mean PAN/CO enhancement ratios in biomass burning plumes.*

	Source region	**Experiment (aircraft, measurement area)**	**PAN/CO mmol/mol**	**No. of plumes (age)**
This study	boreal forest	POLARCAT (DLR Falcon, Greenland)	2.61 (±0.36)	30 plumes (∼5-20 days)
Flocke et al. (2005a)	boreal forest	NEAQS (P3, West Pacific)	4.3 - 6.1	n.s. (CO > 200 nmol mol^{-1})
Holzinger et al. (2005)	not identified	MINOS (DLR Falcon, East Mediterranean)	6.5	10 plumes (∼ 2 - 3 days)
Singh et al. (2004)	Southern China, South East Asia	TRACE P (DC8, West Pacific)	3.8 (±2.1)	12 plumes (∼ 2 - 5 days)
Mauzerall et al. (1998)	Southern Africa, Brazil	TRACE A (DC8, South Atlantic)	5.3 - 7.5	≈50 plumes (∼ 0.2 to > 6 days)

PAN versus NO_y

Reactive nitrogen (NO_y) contains all oxidized nitrogen compounds, as for example NO, NO_2, NO_3, HNO_3, PAN, N_2O_5 etc. In the troposphere, the exact composition of NO_y might differ considerably depending on sources/sinks as well as region and altitude, e. g. (Bradshaw et al., 2000). PAN/NO_y ratios are observed therefore in a wide range. In the free troposphere above North America, average PAN/NO_y ratios between ~18 to 40 % were measured for example by Singh et al. (2007). Roberts et al. (2004) report PAN/NO_y ratios of nearly 60 %, observed in tropospheric air masses at the U.S. west coast. The highest PAN/NO_y ratios were attributed to Asian pollution plumes, probed after long-range transport across the Pacific.

Figure 5.7 shows a scatter plot of PAN versus NO_y as obtained from all GRACE flights (10 s values). Like in the PAN-CO scatter plot, the data are color-coded according to Θ and can be separated into several branches. The highest NO_y values are found in the lowermost stratosphere ($\Theta > 335$ K). Here, NO_y is composed primarily of HNO_3 and NO_x ($NO_x = NO + NO_2$), produced mainly in the tropics by the photolysis of N_2O followed by oxidation (Murphy et al., 1993). The small abundance of PAN leads to small PAN/NO_y ratios of 2 - 3%. The increase of PAN in the tropopause region is accompanied by a strong decrease of NO_y. In the free troposphere as well as in the atmospheric boundary layer, PAN shows a positive correlation with NO_y. Most PAN/NO_y ratios range between 30 and 90%. Between ~4 to 8 km, PAN is found to be the dominant NO_y compound (see also later **Fig. 5.8f**). The high fraction of PAN is consistent with former observations in this part of the Arctic, and is attributed to its long lifetime due to relatively cold temperatures at high latitudes (Singh et al., 1992a; Wofsy et al., 1992). During the 2008 ARCTAS-B campaign, sampled PAN/NO_y ratios were on average 60% at the high latitudes above North America, whereas over California PAN accounted only for 20% of total NO_y (Singh et al., 2010).

The dominance of PAN during GRACE indeed can be explained by several reasons. First of all, the sampled air masses were influenced mainly by aged boreal fire emissions (see section 5.3). Boreal biomass burning plumes are found to have a high PAN content (up to 90%), due to rapid conversion of emitted NO_x into PAN in fresh plumes (Jacob et al., 1992; Alvarado et al., 2010). The polluted outflow sampled above Greenland then experienced long-range transport which often is initiated by lifting within warm conveyor belts (see section 2.3.2). Whereas HNO_3 is efficiently washed-out during these kind of ascends, PAN survives the lifting process, which increases the PAN/NO_y ratio significantly. Fresh pollution might still contain considerable amounts of NO_x, which is exported from the boundary layer without loss. In the free troposphere, NO_x might be converted into both HNO_3 and PAN, where the dominant pathway will depend on the availability of hydrocarbons (Liang et al., 2011). During transport in the upper troposphere, the ratio of PAN/NO_y will stay rather constant or slightly decrease due to HNO_3 photolysis or further wash-out. However, transport in the mid-to lower troposphere may reduce the PAN/NO_y ratio due to thermal loss of PAN, as observed during GRACE.

For comparison, the average ($\pm$ std) PAN/NO_y ratio measured in the polluted atmospheric boundary layer over southern Germany is also indicated in **Fig. 5.7**. Although PAN is observed at rather high values of several hundred pmol mol^{-1}, the PAN/NO_y ratio is found to be quite low ($\sim$18%).

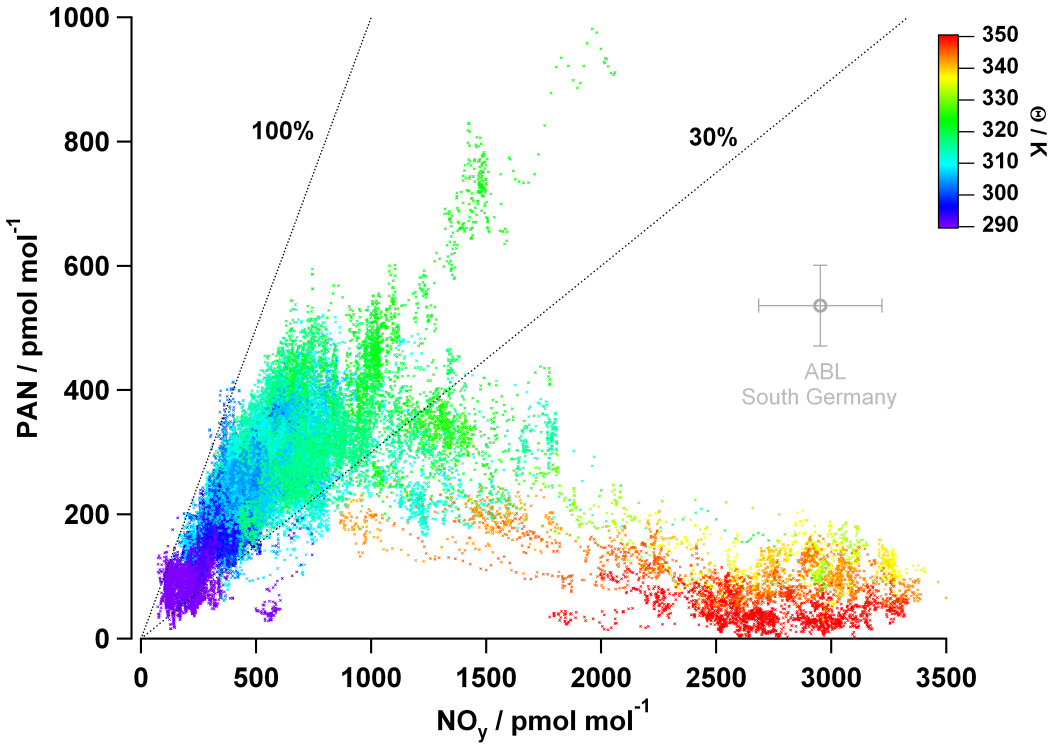

Figure 5.7: *Scatter plot of PAN vs. NO_y using all data from the 15 local GRACE flights. Color-coded according to the potential temperature Θ (see color-scale at the right top). Fore more details see text.*

This can be explained by a generally lower PAN formation in anthropogenic pollution due to a much higher NO_x/hydrocarbon emission ratio (Neuman et al., 2009). In addition, thermolysis in the warm boundary layer suppresses the accumulation of PAN. The remaining NO_y comprises NO ($\sim 600\,\mathrm{pmol\,mol^{-1}}$) which was not yet chemically processed, as well as HNO_3: The fresh surface emission did not experience wash-out processes as did the air masses sampled above Greenland.

5.5 Vertical distribution of other trace gases

Figures 5.8a and **b** present the mean vertical distribution including several percentiles for the trace gases CO and PAN, as calculated from all 15 local GRACE flights. As discussed in detail in the previous sections, both CO and PAN show elevated levels in the free troposphere, and lower mixing ratios below and above. The upper quartiles reach values of more than $140\,\mathrm{nmol\,mol^{-1}}$ (CO) and $350\,\mathrm{pmol\,mol^{-1}}$ (PAN), which is attributed to the sampling of a series of distinct pollution plumes. Additionally, also the lower percentiles (10th/25th) show elevated levels in the free troposphere, if compared e. g. with mixing ratios in the atmospheric boundary layer. This reflects continuous import of aged pollution, which more or less already was diluted into the Arctic background. Beside CO, forest fires and industrial processes emit a large amount of different trace gases such as for example carbon dioxide and nitrogen oxides. Photochemical processing not only leads to the formation of PAN, but may result in in-situ ozone production (see section 2.1). For this reason it is interesting to discuss how the aged pollution does influence the vertical distribution of different trace gases.

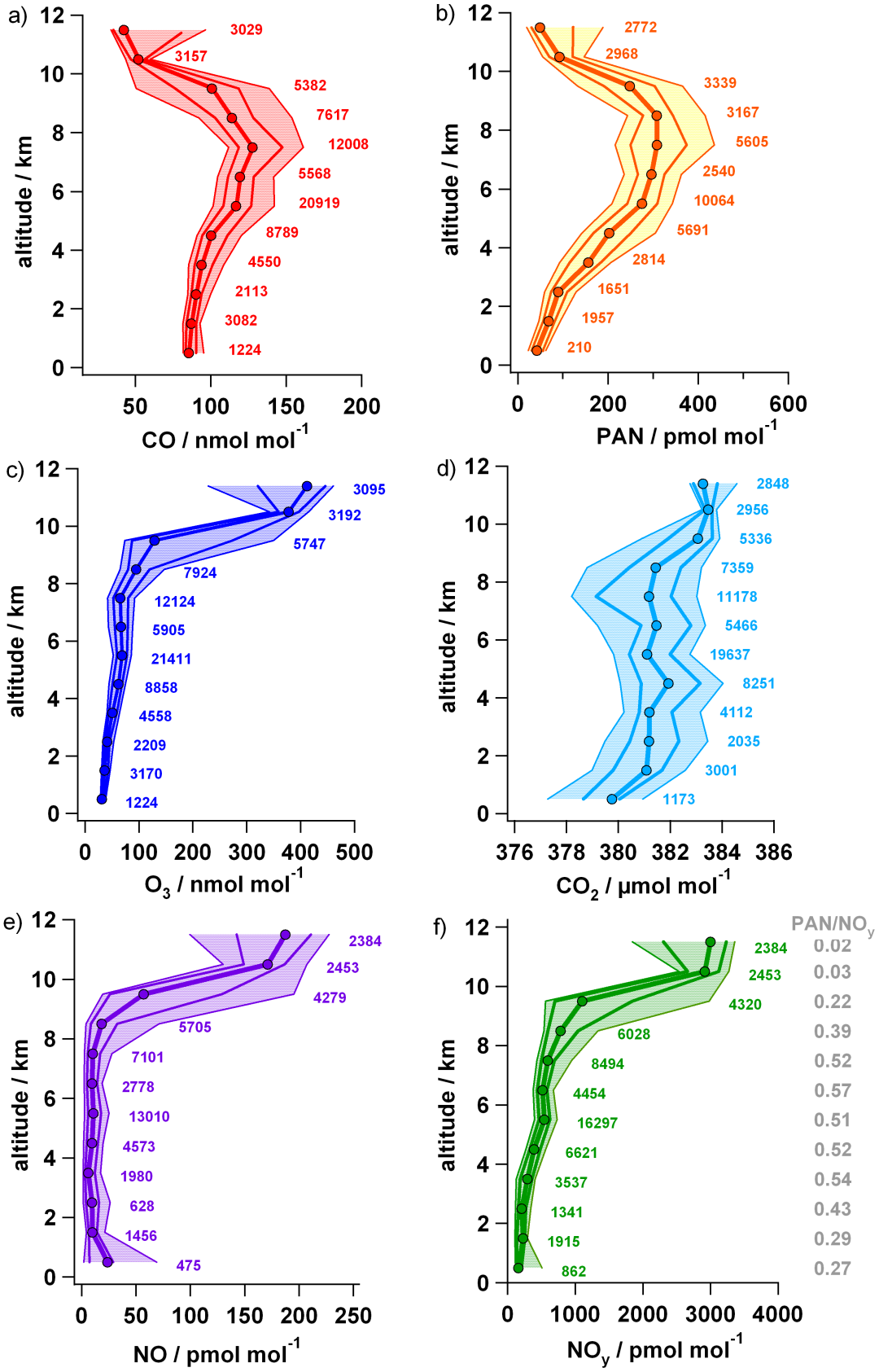

Figure 5.8: *Vertical distribution of a) CO, b) PAN, c) O_3, d) CO_2, e) NO and f) NO_y. Given are median values (thick black lines with markers), upper/lower quartiles (thick lines) as well as 10th/90th percentiles (thin lines). The profiles were calculated from data of all 15 GRACE flights, each for 1-km altitude bins. The numbers represent number of data points available for each bin.*

Figures 5.8c to f presents mean vertical GRACE profiles of O_3, CO_2, NO and NO_y. The median O_3 profile is given in **Fig. 5.8c**. Understanding the tropospheric ozone budget of the Arctic was one of the main objectives of the POLARCAT project, since tropospheric ozone acts as a greenhouse gas and therefore also may contribute to Arctic warming (Law and Stohl, 2007). The GRACE profile shows a rather constant increase of ozone with altitude. In the atmospheric boundary layer, ozone has lowest values around 30 to 50 $\mathrm{nmol\,mol^{-1}}$, which is attributed to net photochemical destruction in the humid and NO_x-poor boundary layer and dry deposition at the surface. In the mid- to upper troposphere, ozone ranges between 60 and 70 $\mathrm{nmol\,mol^{-1}}$ as a result of less photochemical destruction and increasing input from the stratosphere. One important aspect of POLARCAT was to study photochemical ozone production which has frequently been observed in forest fire plumes (Wotawa and Trainer, 2000; Forster et al., 2001; Pfister et al., 2006; Lapina et al., 2006; Val Martín et al., 2006; Real et al., 2007). As will be discussed in more detail in section 5.6, ozone formation in biomass burning plumes was found to be only of minor importance during GRACE. This is also indicated in the mean ozone profile: The steady increase of O_3 with height even seems to be slightly interrupted in the region of enhanced CO and PAN, and thus, in the region where most plumes were sampled.

Figure 5.8d shows the mean CO_2 profile obtained from the GRACE measurements. Carbon dioxide is highly variable in the atmosphere. Apart from an increasing trend during the last decades due to industrialization, CO_2 has seasonal, diurnal, and spatial variations. It is, for example, depleted during summertime in the lower troposphere by plant uptake. The seasonal cycle related to photosynthesis and respiration typically ranges from $\pm 1\,\mu\mathrm{mol\,mol^{-1}}$ in the southern hemisphere up to $\sim 15\,\mu\mathrm{mol\,mol^{-1}}$ in the northern boreal forest zone (Wigley and Schimel, 2000). This is reflected also in the GRACE vertical profile, which shows the lowest median CO_2 value of $\sim 380\,\mu\mathrm{mol\,mol^{-1}}$ in the boundary layer. In the free troposphere, mean carbon dioxide values are rather constant ($\sim$381 - 381.5 $\mu\mathrm{mol\,mol^{-1}}$), but span a quite high range. The vertical profile gives no indication for enhanced CO_2 values due to imported pollution, although carbon dioxide is a product of combustion. Forest fires however have low combustion efficiencies, which leads to rather small initial CO_2/CO emission ratios (e. g. Andreae and Merlet (2001); Suntharalingam et al. (2004)). Furthermore, background CO_2 in boreal forests may be depleted due to plant assimilation. The higher carbon dioxide values above the tropopause reflect the propagation of the seasonal cycle into the lowermost stratosphere (e.g. Bönisch et al. (2009); Sawa et al. (2008)). Observed CO_2 mixing ratios were on average $\sim 2\,\mu\mathrm{mol\,mol^{-1}}$ higher in the lowermost stratosphere than in the troposphere: Median CO_2 for $O_3 < 100$ $\mathrm{nmol\,mol^{-1}}$ was $381.4 \pm 0.4\,\mu\mathrm{mol\,mol^{-1}}$ compared to $383.3 \pm 0.2\,\mu\mathrm{mol\,mol^{-1}}$ for ozone values $> 100\,\mathrm{nmol\,mol^{-1}}$.

Figure 5.8e shows the median profiles for nitrogen monoxide (NO) which is a tracer for fresh pollution. NO is emitted directly into the atmosphere by high-temperature combustion, lightning and by microbiological soil activities (e. g. Bradshaw et al. (2000)). Once released into the atmosphere, it is rapidly oxidized by O_3 to nitrogen dioxide (NO_2) which is recycled back again to NO by photolysis. NO and NO_2 however are further oxidized forming other reactive nitrogen compounds compounds such as e. g. NO_3, HNO_2, HNO_3 and PAN (see section 2.2.1). In the boundary layer of industrialized

regions or areas affected by forest fires, NO may be present at values of several hundreds pmol mol^{-1} up to several nmol mol^{-1}. This applies not to the GRACE profile, which shows median NO values close to the detection limit of $\sim$10 to 15 pmol mol^{-1} which is attributed to missing local pollution sources. Interestingly, also in the free troposphere NO mixing ratios are close to the detection limit, although probed air masses often were impacted by forest fire or anthropogenic emissions. This reflects sampling of aged, photochemically processed air masses, in which initially emitted NO was already completely converted to other NO_y compounds. This is confirmed by FLEXPART analyses. These suggest that the youngest plumes sampled were about 5 to 6 days old, but most of the times pollution was even more aged (see also section 5.6). The main stratospheric source of NO is N_2O photolysis ($N_2O + O \rightarrow 2\,NO$) which explains the higher NO median values of $\sim$150 to 200 pmol mol^{-1} in the UTLS region.

The median NO_y-profile is presented in **Fig. 5.8f**. Similar to NO, NO_y shows low values in the boundary layer ($\sim$180 pmol mol^{-1}) which is consistent with the low mixing ratios observed for CO and PAN. The mean PAN/NO_y fraction is given for each bin at the right. Although PAN is strongly affected by thermolysis, it makes nearly up to a third of total NO_y. Reactive nitrogen continuously increases with height, also because of the higher mixing ratios of PAN, which dominates total NO_y between 4 and 8 km. Since there is almost no NO_x, the remaining NO_y fraction certainly is dominated by HNO_3. In the upper troposphere, NO_y rapidly increases because of the more dominant stratospheric influence (increase of NO, NO_2 and HNO_3).

5.6 Case studies of selected biomass burning (BB) plumes

During the GRACE field campaign, 29 distinct biomass burning plumes have been probed by the Falcon. By means of the FLEXPART model, source region, plume age and anthropogenic contribution were determined for each single pollution plume. Chemical properties were derived from the in-situ measurements and are summarized in table A.1. This section discusses typical characteristics of sampled pollution plumes with the help of two case studies. From both main source regions in Canada and Siberia, one plume was selected in order to present typical transport patterns and to analyze chemical and dynamical processes which took place during advection to Greenland.

5.6.1 F080707: Canadian BB plume

Figure 5.9 shows a 40-min. time-series ($\sim$450 km) of several parameters, when the Falcon probed a biomass burning plume originating from Saskatchewan, Canada. The polluted air was found to be partially mixed with air from the UTLS region. The plume was encountered on the mission on 07 July, 2008 at a constant flight level of $\sim$8 km. On this day, the Falcon flew southeast, before turning to the east at the most southern point ($\sim$59.5°N, see **Fig. 5.2** and flight path indicated in **Fig. 5.10a**). The Falcon then returned along the same route. **Figure 5.9a** shows the FLEXPART parameters fire excess-CO and stratospheric contribution.

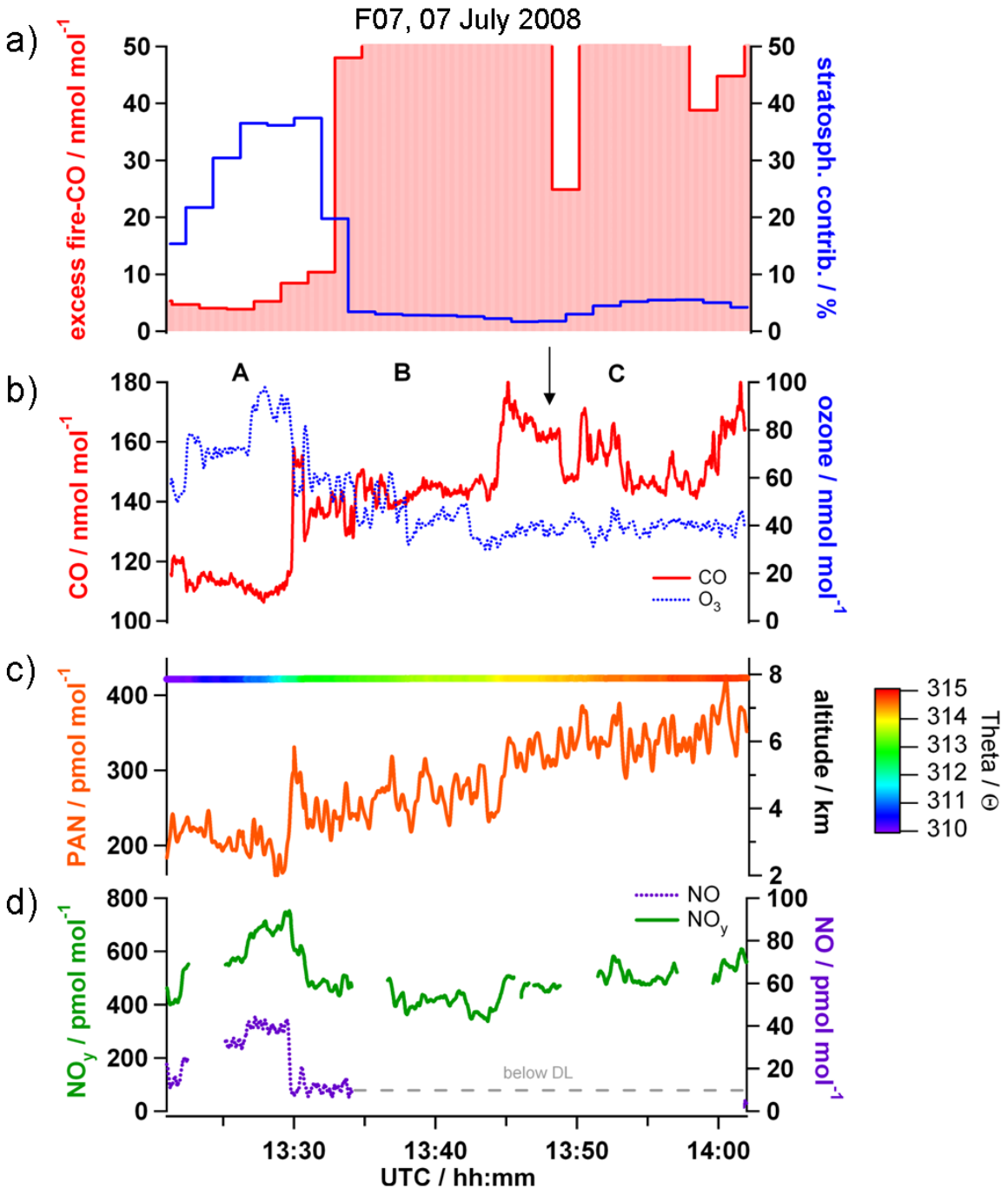

Figure 5.9: *Interception of a Canadian biomass burning plume which partially was mixed with UTLS air (F07, 07 July 2008). a) FLEXPART fire excess-CO (red pattern) and stratospheric contribution (blue line), b) CO (red) and O_3 (blue dotted), c) PAN (orange) and altitude (color-coded by potential temperature Θ), d) NO (purple dotted) and NO_y (green). Black arrow in panel b) indicates time of FLEXPART CO source contribution (see* ***Fig. 5.10****)*

.

The stratospheric contribution indicates what fraction of the sampled air stayed above the 2 PVU dynamic tropopause during the last 20 days. The FLEXPART tracers indicate a transition between air masses associated with stratosphere-troposphere exchange (stratospheric contribution of ∼35-40%), as well as air influenced by forest fire emissions (fire excess-CO up to ∼200 nmol mol^{-1}, cut in **Fig. 5.9a**). **Figure 5.9b** shows in-situ ozone and carbon monoxide for the same time period. The time-series can be divided into three parts, as indicated by the labels "A" to "C". In the beginning, O_3 and CO were present at mixing ratios of ∼70 and ∼115 nmol mol^{-1}. Ozone then increased to ∼100 nmol mol^{-1} which was accompanied by a slight decline of CO (region "A"). The pollution was entered at the outbound leg at ∼63.2°N. CO first climbed to moderate values of ∼140 nmol mol^{-1} (region "B"), before it increased further to nearly 160 to 180 nmol mol^{-1} (region "C"). O_3 showed a continuous decrease from ∼100nmol mol^{-1} down to ∼40 nmol mol^{-1} as the plume was traversed. High fire excess-CO should be related to high in-situ CO whereas a higher stratospheric fraction generally is accompanied by enhanced levels of in-situ ozone. In conclusion, FLEXPART reproduces the in-situ observations quite well. However, the FLEXPART tracers change rather stepwise than continuously which means that the partial mixing between these two different air pools (region "B") is not resolved by the model.

The flight altitude is given in **Figure 5.9c**. It is color-coded by the potential temperature Θ which slightly increases from 310 to 315 K along the flight path. PAN is well correlated with CO and continuously increases from ∼200 pmol mol^{-1} outside of the plume up to values of 350 pmol mol^{-1} inside. On the contrary, NO and NO_y show their highest values of ∼40 and 700 pmol mol^{-1} right before the plume was entered (**Figure 5.9d**), similar to O_3. The positive relationship with ozone as well as the negative correlation with CO indicate that the higher NO and NO_y values can be attributed to the influence from the UTLS air. Inside the plume, NO values are below the detection limit. This suggests that the main part of the NO initially emitted by the fires was already oxidized to other NO_y species such as e. g. PAN and HNO_3. NO_y shows moderate values of ∼500 to 600 pmol mol^{-1} inside the plume.

The transport pathway of the sampled fire emissions is illustrated in **Fig. 5.10a** and **Fig. 5.10b**, which show the results of a backward simulation started along the Falcon flight track. The "column integrated emission sensitivity" plot is given for 13:48h UTC (see arrow in **Figure 5.9b**). The vertically integrated emission sensitivity is proportional to the residence time of the released particles over a unit area, but gives no altitude information (Stohl et al., 2005). According to this, the sampled air mass was advected across the fire regions in Saskatchewan. The red highlighted MODIS hot spots indicate where the entrainment of the BB emissions took place. The numbers superimposed on the colored shading give the number of days back in time for the centroid of the released particles. According to this, the pollution was incorporated ∼5 days before it was sampled by the Falcon. The upper panel of **Figure 5.10b** shows the mean altitude (black line) of the sampled air mass for the last 20 days. The circles represent groups of particles using a clustering algorithm (the size is representative for the fraction of sampled air, see Stohl et al. (2002)). The polluted air mass was strongly up-lifted ∼3 days before it was probed over southern Greenland. The ascend took place in a warm conveyor belt as indicated also by the cyclonal pathway evident in **Fig. 5.10a**. The middle

panel of **Fig. 5.10b** illustrates the contribution of boundary layer air to the probed air mass. It shows a maximum of ∼60 % approximately 3 to 5 days before the air mass was sampled when a part of it was advected across the fires. The lower panel of **Fig. 5.10b** gives the fraction of particles which stayed above the tropopause during the last days, which at least for this part of the plume is negligible.

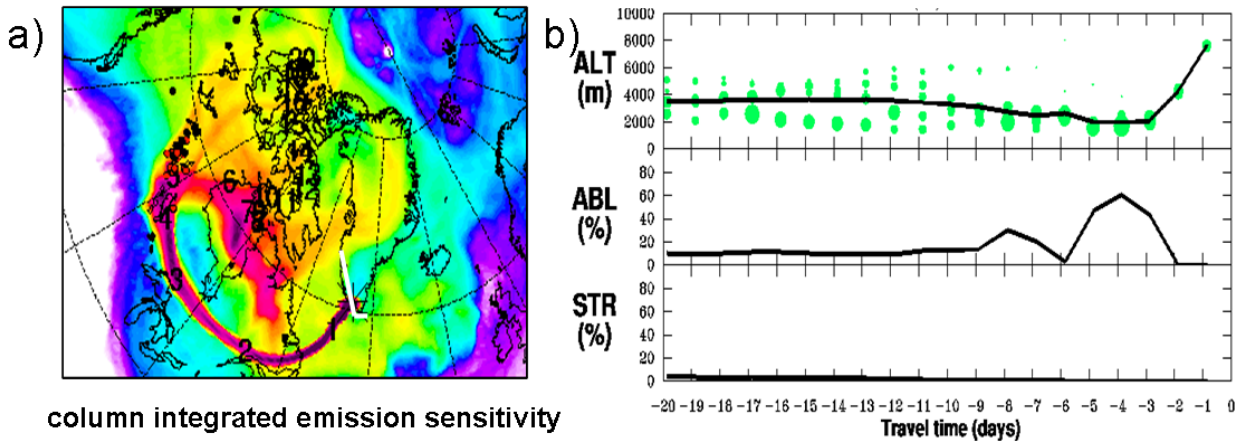

Figure 5.10: *Results from FLEXPART analysis for the Canadian biomass burning plume. a) FLEXPART column integrated emission sensitivity plot for the air mass sampled at 13:48h. Red dots indicate MODIS fire spots on forested land. b) Temporal evolution of altitude (upper panel), contribution from the atmospheric boundary layer (middle panel) and stratospheric air (lower panel) for the same air parcel, as suggested by the FLEXPART model.*

Scatter plots of O_3 vs. CO and PAN/NO_y vs. CO are given in **Fig. 5.11**. The colored circles belong to the data shown in **Fig. 5.9** and the color-code represents Θ (same scaling as in **Fig. 5.9c**). The grey dots belong to all remaining GRACE data. The relationship between O_3 and CO provides an effective diagnostic tool in order to study both chemical and mixing processes. The data of the sampled Canadian BB plume are split into the three groups which were already introduced in **Fig. 5.9b**. Ozone is highest outside of the plume (region "A"), where it has a negative correlation with CO, as typically observed in the UTLS region. The biomass burning emissions are characterized by highest CO and lowest ozone (region "C"). The data of group "B" obviously result from incomplete mixing processes between these different air masses. Both O_3 and CO have moderate values and show a less steep correlation than in the UTLS air. The meteorological tracer Θ also indicates partial mixing, as obvious from the color-code. Tropospheric mixing of pollution with UTLS air masses is a quite regular phenomenon. Parrish et al. (2000) presents a case study where anthropogenic pollution was adjacent to elevated O_3 of stratospheric origin. Brioude et al. (2007) reports from a quite similar case like the one discussed herein, when biomass burning emissions where mixed with a stratospheric intrusion. Such mixing events bring together air masses having rather different chemical characteristics hereby influencing tropospheric chemistry. O_3-rich stratospheric air mixed with H_2O-rich tropospheric air may result in enhanced OH mixing ratios and hence, a higher atmospheric oxidation capacity (Esler et al., 2001). However it remains unclear to what extent this will result in a more efficient degradation of pollutants.

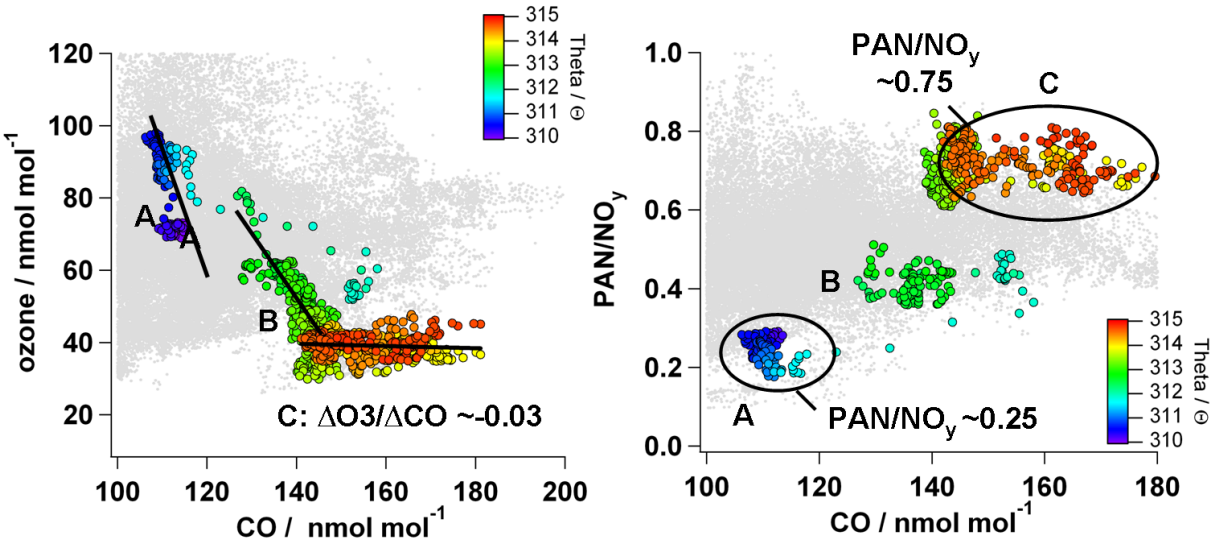

Figure 5.11: *Scatter plots of a) O_3 vs. CO and b) PAN/NO_y vs. CO. Colored circles represent data from the Canadian biomass burning plume which was probed by the Falcon on 07 July, 2008 (F07). The color-code gives the corresponding potential temperature Θ. Grey dots represent all other GRACE data.*

Photochemical O_3 production

The relationship between ozone and CO also can be used as an estimate for the net photochemical ozone production in polluted air masses. The enhancement ratio $\Delta O_3/\Delta CO$ gives the difference between ozone concentrations in the pollution plume and in the surrounding background air (ΔO_3), which is normalized by the corresponding difference in CO (ΔCO). It is worth noting that generally smaller slopes are found in air masses impacted by fire emissions compared to those observed in anthropogenic plumes. This largely can be explained by a lower NO_x/VOC emission ratio of biomass burning (Wofsy et al., 1992; Pfister et al., 2006), which is even more pronounced for boreal compared to tropical fires, due to the low nitrogen content of boreal vegetation (Wofsy et al., 1992). Reported slopes from aged boreal biomass burning plumes vary widely, and range from slightly negative (Real et al., 2007; Val Martín et al., 2006) to positive (Wotawa and Trainer, 2000; Forster et al., 2001; Pfister et al., 2006; Lapina et al., 2006; Val Martín et al., 2006; Real et al., 2007). In the case discussed herein, a linear fit to the data sampled inside the biomass burning plume ("C") yields a slightly negative slope of ∼-0.03. Such negative slopes arise from titration of background ozone by fire-emitted NO, and often are observed in fresh biomass burning plumes (Mauzerall et al., 1998; Real et al., 2007; Alvarado et al., 2010). Thereafter, photochemical O_3 production during plume evolution generally shifts the slopes from initially negative to positive values. The observed slope in this case however is still negative, although our observations were made several days downwind of the source region. This suggests that if any, only small net O_3 production took place during transport. There are several reasons which might explain low ozone production in biomass burning plumes. de Gouw et al. (2006) found large enhancements of VOCS in forest fire plumes, which resulted in depressed levels of OH, the main driver of photochemistry. Optically thick aerosols emitted by fires may also

substantially reduce photochemical O_3 production (Verma et al., 2009). Val Martín et al. (2006) suggested that ozone losses on organic aerosol will counteract O_3 production. Ozone destruction as a result of nighttime chemistry (Brown et al., 2006) however certainly plays no role during boreal summer. The most reasonable explanation is the already mentioned limited availability of NO_x. As discussed in section 5.4.2, PAN dominates NO_y in the free troposphere. In a Canadian biomass burning plume, Alvarado et al. (2010) observed rapid conversion of NO into PAN within the first hours ($\sim$90%) which reduces photochemical ozone production in fresh plumes. During transport in the cold mid- and upper troposphere to Greenland, PAN conserves NO_x which therefore is not available for ozone production during long-range transport. The high PAN/NO_y ratio observed in the polluted air mass is also reflected in **Fig. 5.11b**, which presents a PAN/NO_y-CO scatter plot. As expected, PAN accounts only for a small fraction of NO_y inside the UTLS air masses. The remaining NO_y certainly constitutes NO (see **Fig. 5.9d**), NO_2 and HNO_3. Inside the plume however, total NO_y comprises $\sim$75% of PAN whereas NO (and as a result also NO_2), is abundant only at very low mixing ratios.

5.6.2 F080713a: Siberian BB plume

As mentioned above, a series of biomass burning plumes arriving from eastern Siberia have been intercepted during GRACE campaign. Due to the much larger distance to our measurement area, Siberian plumes were much more aged than those originating in Canada (see also table A.1). In addition, Siberian BB plumes often were found to be less homogenous. This is very likely the result of the larger travelling time meaning that dispersion and shear forces had more time to act on the plume. This section discusses the probing of a Siberian biomass burning plume on 13 July, 2008, and shall illustrate the often observed "patchy" structure of sampled emissions. The 13 July flight especially was designed for the re-sampling of an artificial tracer. The tracer was released inside the Siberian plume on the flight one day before (F12, see also section 5.1). Note that according to forward trajectories released along the 13 July flight track, the plume subsequently descended towards Europe. This plume therefore will be exemplary used to evaluate the ozone production potential in subsiding pollution plumes (see next section 5.7).

The 13 July flight track of the Falcon followed a "8"-pattern which was flown in the region where the released tracer position was predicted by the FLEXPART forecasts (see **Fig. 5.2**). **Figure 5.12** shows a 40-min. time-series of several parameters, but only along one of these legs (from north-east to south-west). The FLEXPART tracers "fire excess-CO" and "anthropogenic excess-CO" are given in **Fig. 5.12a**, along with the stratospheric fraction. According to the model, the biomass burning plume in this case was influenced also by emissions from Asian fossil fuel combustion (10 - 20%), as it was typically observed for plumes originating from Siberia. In-situ CO and O_3 values are given in **Fig. 5.12b**, and show mixing ratios between $\sim$100 - 160 nmol mol^{-1} (CO) and 50 - 90 nmol mol^{-1} (O_3). Both trace gases vary considerably on horizontal scales of only $\sim$10 to 40 km, and are clearly negatively correlated. Note that the Falcon slightly changed the altitude by a few hundred meters (see **Fig. 5.12c**).

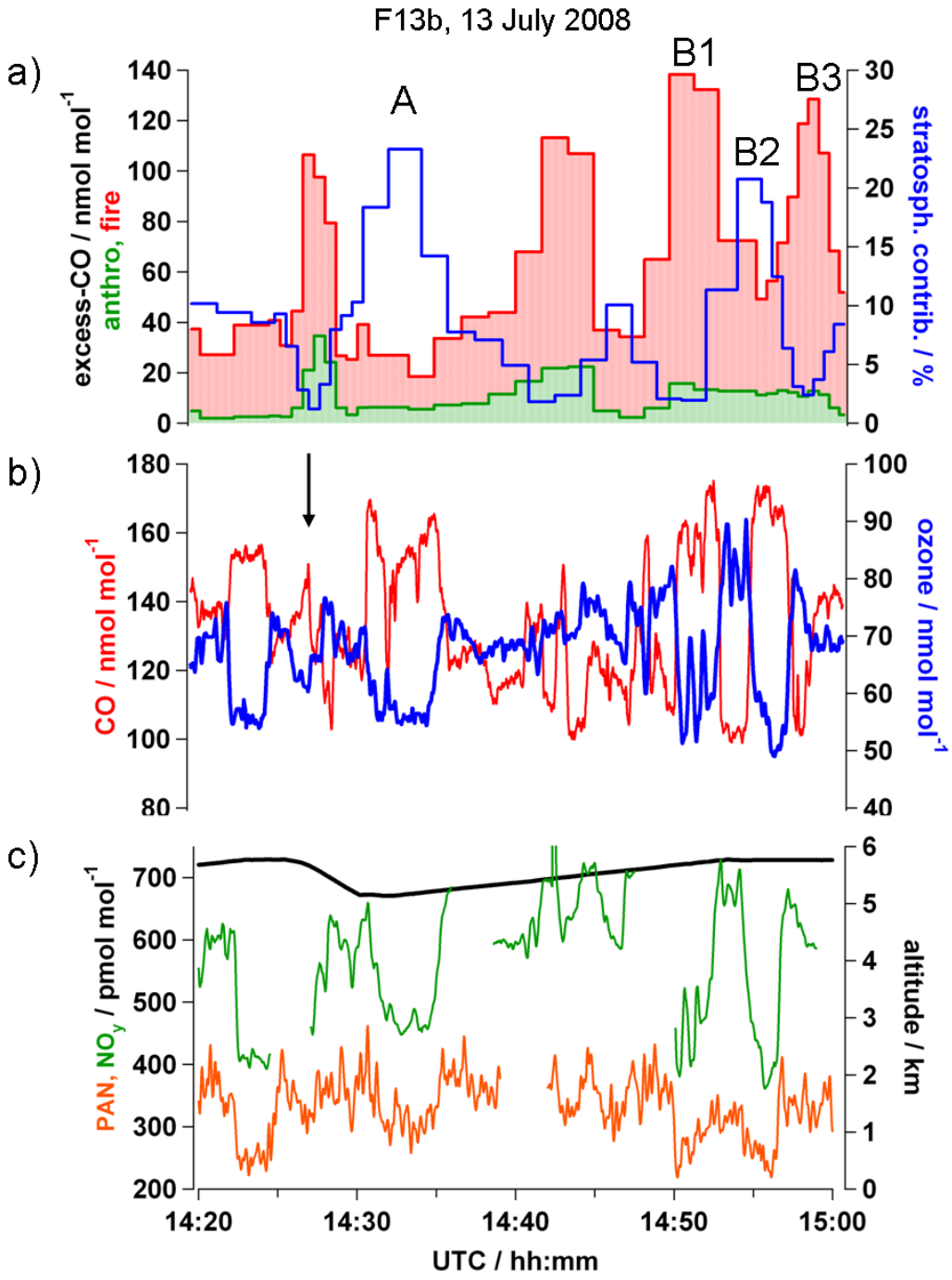

Figure 5.12: *Interception of a Siberian biomass burning carrying also anthropogenic pollution from East Asia (F13b, 13 July 2008). a) FLEXPART excess-CO from BB (red pattern) and AS (green pattern), as well as stratospheric contribution (blue line). b) O_3 (blue) and CO (red), c) PAN (orange), NO_y (green) and altitude (black). Black arrow in panel b) indicates time point of the FLEXPART CO source contribution plot (see* ***Fig. 5.13****)*

The high variability of in-situ CO and O_3 reflects strong layering/interleaving of air masses having rather different chemical signatures. The FLEXPART model generally reproduces the observed filamentary structures. It shows alternating high fire and anthropogenic excess-CO values along with low stratospheric contributions and vice versa. A comparison of in-situ O_3 and CO mixing ratios with the FLEXPART tracers however indicates that the model does not capture the exact positions of the different air mass types. Almost no agreement is observed for example in region A. Here, the model suggests high stratospheric contribution together with low fire and anthropogenic CO, whereas the in-situ measurements show low ozone and high CO mixing ratios. By contrast, the agreement is reasonable well in Region B: a region of high fire-CO (B1) is followed by a region with high stratospheric contribution (B2), which again is followed by peak values of FLEXPART fire-CO (B3). The in-situ observations follow a similar sequence (B1-high CO, B2-high ozone, B3-high CO), although the in-situ structures appear on somewhat smaller scales.

PAN and NO_y show similar to CO and O_3 strong variability on comparatively small spatial scales. NO_y follows O_3 meaning that NO_y is higher in the upper tropospheric air masses than in the polluted air. Surprisingly, PAN is also well correlated with O_3 and NO_y and has higher values outside of the plume than inside (where CO is high). As will be discussed shortly, the observed PAN values of only 250 pmol mol^{-1} inside the plume are quite low, whereas mixing ratios of 300 to 400 pmol mol^{-1} in the surrounding air masses represent more typical values.

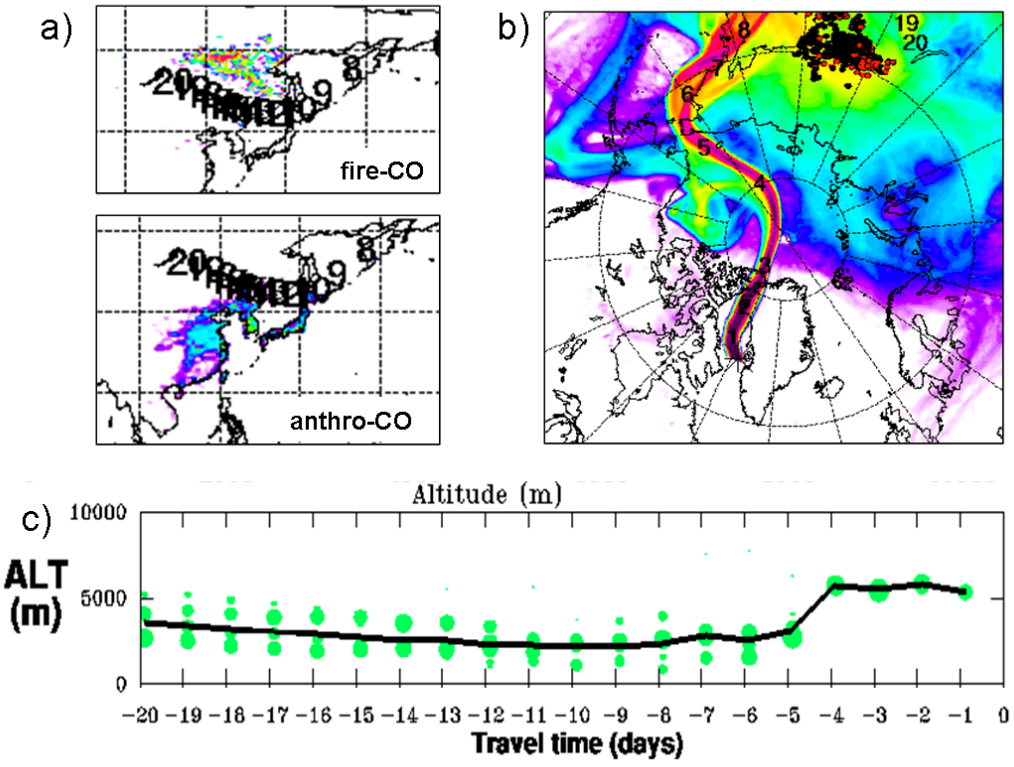

Figure 5.13: *Results from FLEXPART analysis for the Siberian biomass burning plume. a) FLEXPART CO source contribution plot for BB and AS (14:27h), b) FLEXPART column integrated emission sensitivity, c) mean altitude of the sampled air mass during last 20 days (FLEXPART).*

Figure 5.13a shows the source contribution plots of both biomass burning (upper panel) and anthropogenic CO (lower panel) for 14:27h (see arrow in **Fig. 5.12b**). According to the model, anthropogenic emissions originated in the North China Plain as well as from Korea, and Japan. However, it has to be pointed out that this result from the FLEXPART model cannot be validated by our in-situ measurements. The Falcon measured neither a direct tracer for anthropogenic emissions (e. g. SF_6), nor for biomass burning pollution (e. g. HCN, CH_3CN). **Figure 5.13b** illustrates the transport pathway of the polluted air mass into the European sector of the Arctic. The column integrated emission sensitivity shows that the emissions reached our measurement area directly across the pole, which was the dominant transport pathway into the Arctic between ~10 to 18th July, 2008 (Fuelberg et al., 2010). The mean altitude of the sampled air mass is given in **Fig. 5.13c**. According to this, the plume was up-lifted to its sampling altitude of ~5 km roughly 6 to 4 days before our measurements. The air mass started to ascend approximately at the north-eastern edge of Eurasia, at the same time when it was advected towards northern latitudes. The FLEXPART model suggests that the pollution was entrained ~10 to 15 days before (not shown). The air mass was then transported at ~2 to 3 km before it was up-lifted to 5 km. This indicates that the emissions remained at low levels for a few days, which might explain the low PAN values inside the plume. Thermolysis of PAN in the warmer lower troposphere will release NO_x, observed NO values however were below the detection limit. A reasonable explanation for the low NO levels is fast photochemical processing during the subsequent low-level transport across the pole (see also discussion of reactive nitrogen cycling in section 5.7.2).

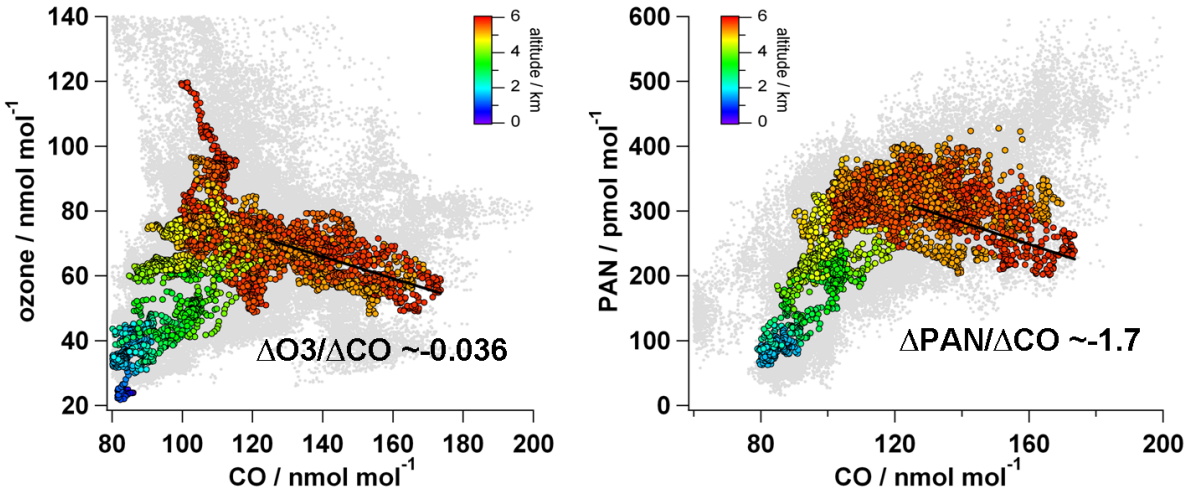

Figure 5.14: *Scatter plots of a) O_3 vs. CO and b) PAN vs. CO. Colored circles represent data obtained in the Siberian biomass burning plume, which was sampled by the Falcon on 13 July, 2008 (F13b). The color-code gives the corresponding potential temperature Θ. Grey dots belong to all other GRACE data.*

Figure 5.14 depicts scatter plots of O_3 and PAN vs. CO. Colored circles represent data from the entire flight on 13 July whereas grey dots show all local GRACE data. Similar to the Canadian biomass burning plume, the O_3-CO correlation inside the plume is slightly negative. As discussed in the previous section, this again indicates low photochemical ozone production. If we assume that

as usual PAN was formed in the fire and/or industrial pollution plumes, the NO_x release from the thermal dissociation of PAN obviously was not sufficient to stimulate O_3 production. As will be discussed in detail in the following section, photochemical O_3 formation in the humid boundary layer is counteracted by efficient photochemical O_3 destruction, which might explain these observations.

5.7 Potential for photochemical O_3 formation in subsiding plumes

As discussed in detail in the previous section, there was no indication that strong photochemical O_3 production took place in the biomass burning plumes which were advected to Greenland. Ozone formation was NO_x-limited, since nitrogen oxides were conserved in PAN during long-range transport in the mid- and upper troposphere. PAN however is not a terminal sink for NO_x and may release NO_2 under warmer low-altitude conditions. Singh and Hanst (1981) were the first to propose that NO_x input from PAN thermolysis may promote ozone production in remote regions, far away from the region were NO_x initially was emitted. Meanwhile, a series of observational studies report on O_3 formation related to PAN dissociation. By the combined analysis using aircraft measurements and a global chemistry-transport model, Hudman et al. (2004) suggested that PAN decomposition represents a major component of O_3 formation in transpacific Asian pollution plumes. Zhang et al. (2008) showed that sustained O_3 production driven by PAN dissociation in Asian plumes roughly doubles the transpacific influence from ozone produced in the Asian boundary layer. Real et al. (2007) studied the transport of an Alaskan biomass burning plume on its way to Europe by using a Lagrangian approach. Airborne measurements up- and downwind were analyzed and compared with a trajectory based box model. The observed strong O_3 production ($17\,\mathrm{nmol\,mol^{-1}}$ in 5 days) was attributed primarily to PAN decomposition. Biomass burning plumes probed during GRACE generally contained low NO_x, but several hundreds $\mathrm{pmol\,mol^{-1}}$ of PAN. In this context the question arises: May PAN decomposition trigger O_3 formation in polluted air masses subsiding downstream of Greenland? For this reason, the potential for O_3 production was studied exemplary for one GRACE biomass burning plume using the same trajectory based box model as in the study by Real et al. (2007), the CiTTyCaT model.

5.7.1 The CiTTyCaT chemistry and transport model

The Cambridge Tropospheric Trajectory model of Chemistry and Transport (CiTTyCaT) model is a Lagrangian air parcel trajectory model originally developed by Wild et al. (1996) and validated e. g. by Evans et al. (2000). An isolated air parcel is run along trajectories calculated using large-scale meteorological analyzes (ECMWF - European Centre for Medium-Range Weather Forecasts). The model includes schemes in order to consider the following processes: photochemistry, uptake of emissions, wet/dry deposition and mixing processes. In the present work, chemistry-only simulations are performed in order to study the influence of PAN decomposition on tropospheric ozone chemistry. The chemical composition is updated every 5 min. along the trajectory. The chemistry model includes a full description of tropospheric gas phase chemistry. All reactions relevant for O_x, HO_x and NO_x as well as the complete methane oxidation are included. A hydrocarbon scheme considers

the degradation of 12 VOCs (volatile organic compounds). Reaction rates are taken from JPL (http://jpldataeval.jpl.nasa.gov/), and updates discussed in Arnold et al. (2007). Photolysis is treated using a 2-stream multiple scattering scheme. As mentioned before, the model is run along a trajectory, which is calculated by the FLEXTRA model using ECMWF wind fields.

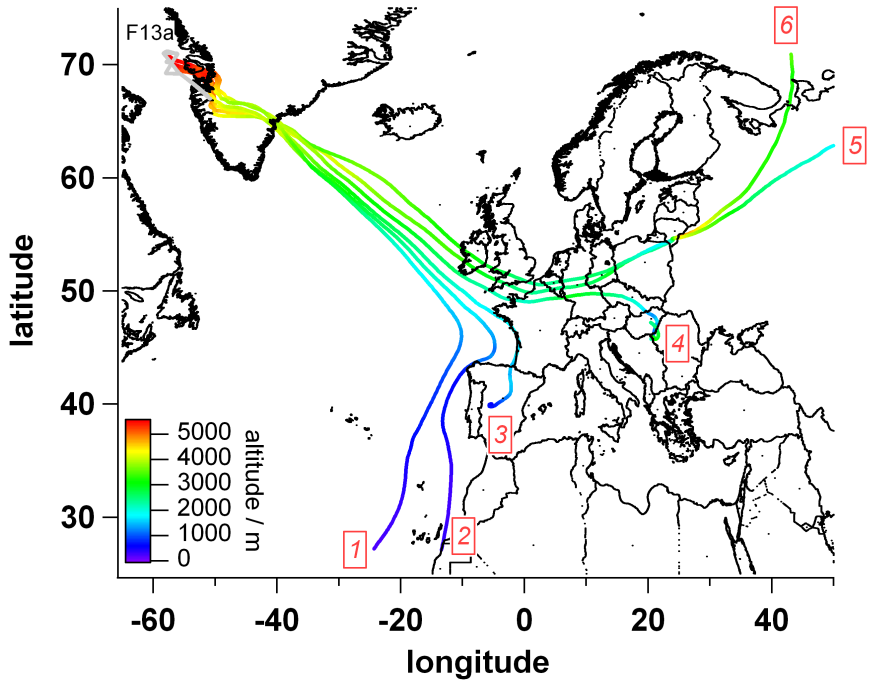

Figure 5.15: *FLEXTRA forward trajectories initialized along the Falcon flight path during the interception of the Siberian pollution plume on 13th July, 2008 (see also* ***Fig. 5.12****). The flight pattern from the 13th July flight is indicated as a grey line. The trajectories are color-coded according to their corresponding altitude.*

5.7.2 Case study: The Siberian biomass burning plume

Forward trajectories initialized along the 13th July Falcon flight path indicate that the sampled Siberian plume (see section 5.6.2) descended on its way to Europe. To illustrate the general transport pattern, **Figure 5.15** shows exemplary six FLEXTRA forward trajectories, started every ∼5 min. between 14:30h and 15:00h UTC. During the first two to three days the trajectories stay close together but start to diverge above the North Atlantic. Air parcels initiated at the northern part of the flight leg descended faster while being advected across the Atlantic (trajectories 1 to 3). Trajectories 1 and 2 then entered the marine boundary layer west of the European continent, followed by low-level transport to the south (1 and 2). Trajectory No. 3 travelled along the French west coast and subsided into the continental boundary layer above Spain. Forward trajectories started in the southern part of the flight leg (4 to 6) show that after a slight descend, the air masses remained most of the time at altitudes around ∼3 km. The air masses were further advected east (No. 4) or north-eastward (No. 5 and 6) and reached different parts of eastern Europe. In the following, photochemical processes controlling O_3 levels are discussed in detail for trajectory 3. Finally, also the temporal evolution of ozone along the other trajectories shown in **Fig. 5.15** will be discussed.

Table 5.4: *Mixing ratios of several trace gases as used for the CiTTyCaT initialization.*

species	average (±std)	species	average (±std)
CO / nmol mol^{-1}	161 (9.6)	C_3H_8 / pmol mol^{-1}	163 (23)
O_3 / nmol mol^{-1}	55.2 (2.2)	C_4H_{10} / pmol mol^{-1}	28 (7)
NO[a] / pmol mol^{-1}	5 (5)	C_5H_{12} / pmol mol^{-1}	9 (2)
NO_2[b] / pmol mol^{-1}	5 (5)	C_6H_6 / pmol mol^{-1}	59 (13)
HNO_3[c] / pmol mol^{-1}	120 (12)	C_2H_6CO / nmol mol^{-1}	2 (1)
PAN / pmol mol^{-1}	273 (45)	HCOH / nmol mol^{-1}	2 (2)
C_2H_6 / pmol mol^{-1}	1030 (211)	CH_3OH / nmol mol^{-1}	4 (2)
C_2H_4 / pmol mol^{-1}	6 (2)	CH_3COH / pmol mol^{-1}	60 (13)
C_2H_2 / pmol mol^{-1}	206 (22)		

[a] NO was close to or below the detection limit (DL) of 10 pmol mol^{-1} and therefore is estimated to be 5(±5) pmol mol^{-1}.
[b] At these altitudes, NO_2 is approximately as abundant as NO due to the stationary equilibrium (Bradshaw et al., 2000).
[c] HNO_3 is estimated by HNO_3 = NO_y-NO_x-PAN.

Initialization

For the initialization of the model run, average values of the plume interception were used for all species measured by the Falcon. The Falcon was not equipped with a system for the measurements of hydrocarbons. For this reason, hydrocarbon values were initialized with mixing ratios measured by the DC8 on 9th July, 2008, which in this days performed a measurement flight above Greenland. Hydrocarbon mixing ratios were determined by normalization with CO, as illustrated exemplary for ethane (C_2H_6) in **Fig. 5.16**. Table 5.4 summarizes mean (±std) values of the species measured by the Falcon and DC8, which were used for the model run. Temperature and water vapor were interpolated on the trajectory from large-scale ECMWF analysis.

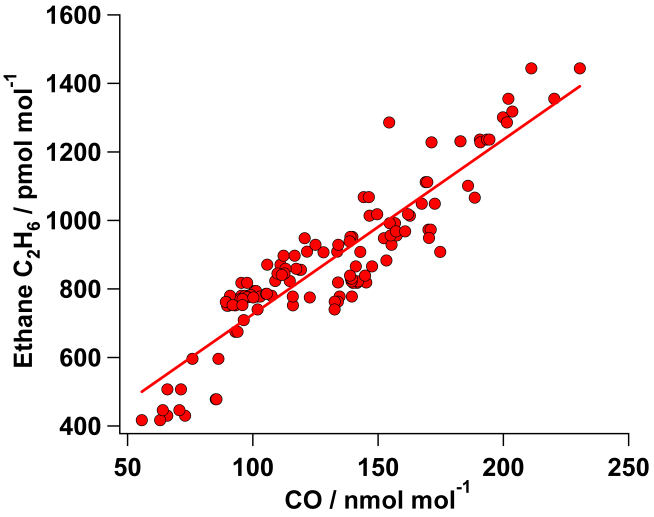

Figure 5.16: *Correlation of ethane (C_2H_6) vs. CO as measured by the DC8 on 9th July, 2008 above Greenland (Hydrocarbon data are taken from http://www-air.larc.nasa.gov/cgi-bin/arcstat-c).*

Results

The simulation starts on 13th July (14:49 UTC) and is run for a period of 9 days. **Figure 5.17a** shows a time-series of altitude and corresponding air mass temperature along the trajectory path.

Simulated PAN and NO_x ($NO_x = NO + NO_2$) for the same time period are given in **Fig. 5.17b**. As expected, the air mass warms up while it descended on its way to Europe. After its probing west of Greenland, the polluted air mass first remained at nearly constant altitude before it started to descend down to ∼4 km (∼15th - 16th July). The temperature increase from ∼250 K to ∼260 K results in only marginal PAN losses at the beginning, and a very small increase in NO_x.

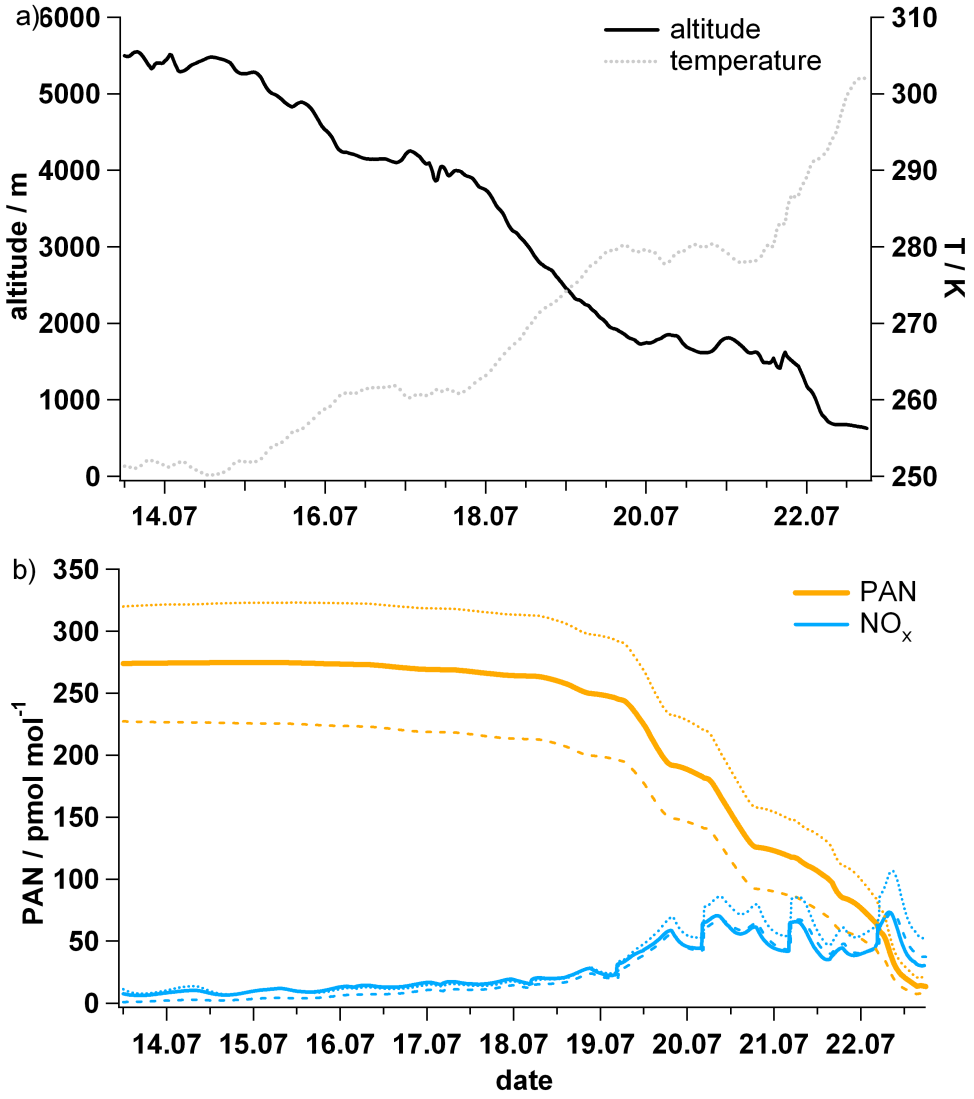

Figure 5.17: *a) Temporal evolution of altitude (black solid) and temperature (grey dotted) along the forward trajectory 3 (see* ***Fig. 5.15****). b) PAN (orange) and NO_x (light blue) along the trajectory, as simulated by the CiTTyCaT model. Simulations were initialized with mean plus/minus standard deviation mixing ratios, and results are presented as solid (mean), dotted (mean plus std) and dashed lines (mean minus std).*

From ∼18th to 20th July, the air parcel subsided down to ∼1800 m hereby warming up to ∼280 K. The resulting thermal dissociation of PAN is accompanied by an increase of NO_x to values of ∼50 pmol mol^{-1}. PAN may reform again slowing down its loss rate especially at night, when NO_2 photolysis rates are close to zero. On 22th July, the air mass entered the boundary layer (∼600 m) hereby reaching temperatures of ∼300 K. Although finally only a small amount of initial

PAN ($\sim$20 pmol mol^{-1}) is left, average NO_x values have not further increased during the last days of the simulation. As we will see shortly, this is because of rapid cycling of nitrogen compounds in the photochemically active boundary layer.

Photochemical O_3 production/destruction

Figure 5.18a presents the temporal evolution of ozone and water vapor for the same time period as shown in **Fig. 5.17**. According to the simulation, ozone values continuously decrease during daylight hours in the first five to six days. Net photochemical O_3 destruction lowers ozone mixing ratios from $\sim$55.2 nmol mol^{-1} down to $\sim$53.2 nmol mol^{-1}. Water vapor is abundant at mixing ratios of $\sim$1.5 μmol mol^{-1} at the beginning of the simulation, but continuously increases during subsidence. The ozone concentration stays rather constant on 19th July, followed by a slight increase of $\sim$0.5 nmol mol^{-1} (20th July). During the last 2 days of the simulation O_3 values show an even stronger decline down to mixing ratios of $\sim$51.2 nmol mol^{-1}. This coincides with a sharp increase in water vapor which finally reaches values between $\sim$9 to 13 μmol mol^{-1} in the humid boundary layer.

Photochemical reactions both form and destroy ozone (see also section 2.1), and the difference describes the net photochemical ozone formation. In summary, all reactions which oxidize NO to NO_2 contribute to the production of O_3:

$$P(O_3) = k_1[NO]\ [HO_2] + \sum k_{2i}[NO]\ [RO_2]_i\phi_i\ . \tag{5.1}$$

Herein, RO_2 represent organic peroxy radicals and ϕ gives the corresponding NO_2 yield from each reaction. Major loss processes for ozone are its photolysis in the presence of water vapor, and the reaction with OH and HO_2:

$$L(O_3) = k_3[O(^1D)]\ [H_2O] + k_4[O_3]\ [OH] + k_5[O_3]\ [HO_2] + \sum k_{6j}[O_3][RO_2]_j\ . \tag{5.2}$$

Net photochemical ozone formation $nP(O_3)$ is given by the difference of $P(O_3)$ and $L(O_3)$:

$$nP(O_3) = P(O_3)\ \text{-}\ L(O_3)\ . \tag{5.3}$$

For the case discussed herein, photochemical O_3 production and destruction terms are illustrated in **Fig. 5.18b** and **c**. The HO_2 radical reacts both with NO and O_3, resulting in either O_3 formation or destruction (see section 2.1). Although NO generally is abundant at much lower mixing ratios than ozone, the much larger rate coefficient for the reaction of HO_2 with NO makes it a very important pathway for ozone production. In our case, the low abundance of NO_x during the first five to six days however results in only very small ozone formation terms. Maximum values do not exceed $\sim$50 pmol mol^{-1} per hour whereas O_3 production terms of 1 to 2 nmol mol^{-1} per hour have been reported for other biomass burning plumes (e. g. Real et al. (2007, 2008)). Photolytic O_3 loss is slightly larger than ozone formation during the first days and is dominated by the reaction of O_3 with HO_2, closely followed by O_3 photolysis in the presence of water vapor. Reaction with OH is only of minor importance due to moderate OH levels at these altitudes ([OH] $\sim$0.5 - 1 $\times$ 10^6 cm^{-3}).

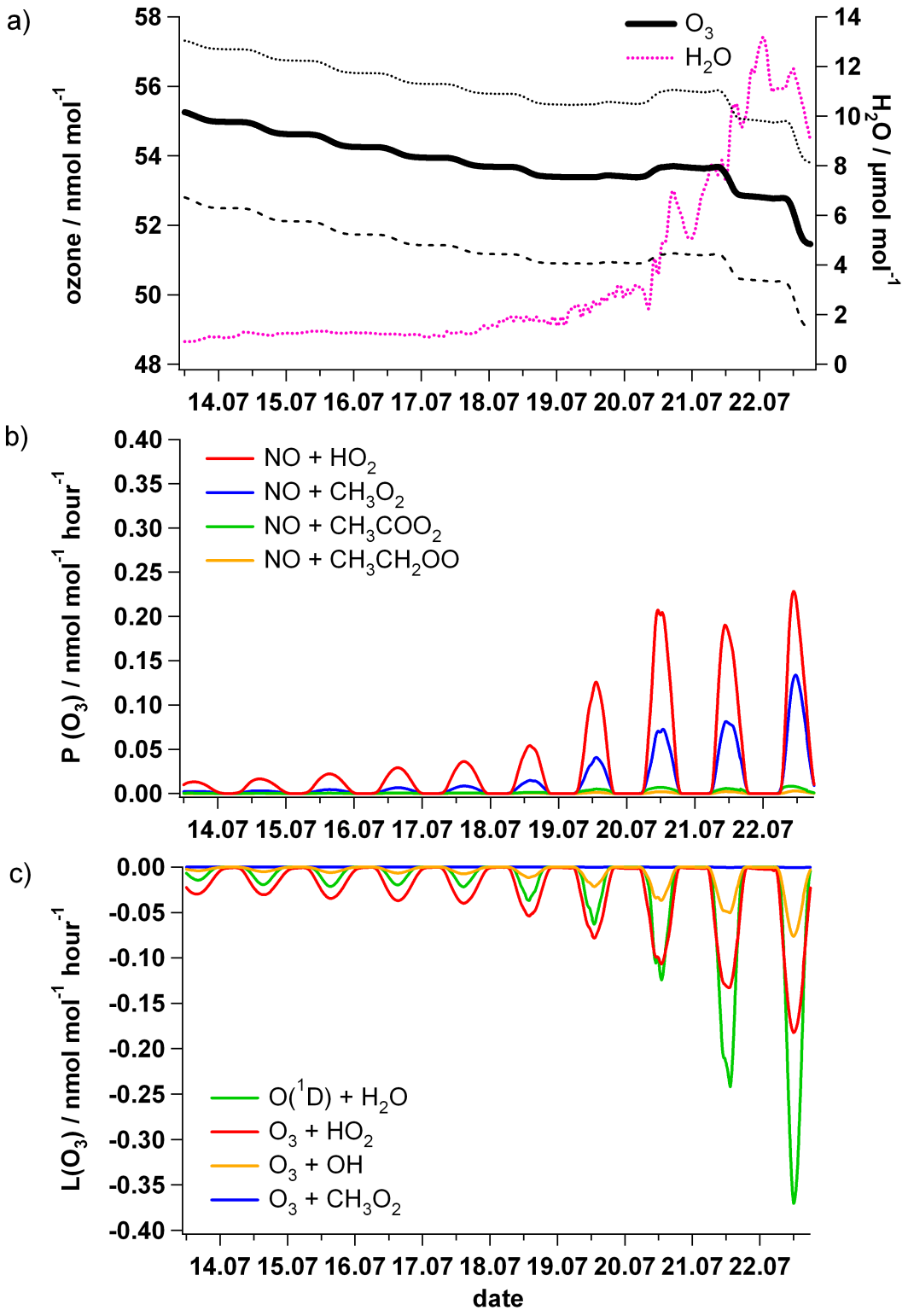

Figure 5.18: *Temporal evolution of several parameters as obtained from the CiTTyCaT simulation. a) O_3, initialized with mean (solid black line) and plus/minus std (dotted/dashed black line) and H_2O (dark pink), b) dominant photolytical O_3 production and c) dominant photochemical O_3 loss terms.*

On 19th July, ozone formation approximately equals O_3 destruction, since NO_2 liberated from PAN decomposition enhances O_3 production terms by about a factor of 2. This is followed by net ozone formation on 20th July, promoted by the on-going NO_2 input from PAN decomposition. Ozone production still is dominated by reaction of NO with HO_2 which contributes ~60 % to the total ozone formation, whereas the remainder mainly arises from reaction of NO with RO_2. The increase of water vapor at the lower levels however makes O_3 photolysis to become a more and more important ozone loss pathway. This reaction sequence leads to formation of much more OH radicals ([OH] $\sim 5\times 10^6$ cm^{-3}) which in turn may react with ozone acting as a further O_3 sink. Total photochemical O_3 destruction increases dramatically on 21th and 22th July reaching values of ~0.4 to 0.6 nmol mol^{-1} per hour during the day. Ozone formation is still going on and is slightly higher in the humid boundary layer (~0.4nmol mol^{-1} per hour), supported also by elevated levels of HO_2 and CH_3CO_2 (due to more OH). However, in summary wet chemical processing leads to significant ozone destruction during the last two days.

Reactive nitrogen cycling

The small net-O_3 production nP(O_3) following subsidence of the air mass basically is the result of very efficient ozone destruction in the warm and humid lower troposphere. Additionally, rapid conversion of NO_2 into HNO_3 limits the ozone production efficiency of NO_x released by PAN. **Figure 5.19** illustrates the cycling between the most dominant NO_y species, as simulated by the CiTTyCaT model (please compare with reactive nitrogen cycle given in **Fig. 2.2.1**). The reactive nitrogen compounds NO, NO_2, NO_3 and N_2O_5 are given in **Fig. 5.19a**, whereas PAN and HNO_3 are presented in **Fig. 5.19b**.

At the beginning of the simulation, NO and NO_2 values are present only at their low initialization values (~5 pmol mol^{-1}). The photostationary state equilibrium between NO and NO_2 is evident. NO and NO_2 are abundant at similar mixing ratios during daylight hours. At night when photolytic rates are close to zero, NO_2 is the dominant form. In the absence of light, NO_2 may react further with O_3 hereby forming the nitrate radical NO_3 (see e. g. marker A). This reaction has a strong-temperature dependency and becomes more important in the lower troposphere. The nitrate radical is a strong oxidant which preferably reacts with unsaturated hydrocarbons (see section 2.2.1). Formation of NO_3 is also followed by the production of N_2O_5 ($NO_3 + NO_2 \rightarrow N_2O_5$). Both of these two species however are rapidly photolyzed at sunrise, which leads to a spontaneous increase of NO_2 (see e. g. marker B). Note that heterogeneous processes are not taken into account in this simulation. These would lead to a possible formation of nitric acid HNO_3 in water droplets ($N_2O_5 + H_2O \rightarrow 2\,HNO_3$).

Dissociation of PAN on 19th July adds a relatively high amount of NO_2 (marker C). Liberated NO_2 is either photolyzed, hereby forming NO, or it is further oxidized by OH producing HNO_3. Whereas photolysis of NO_2 will trigger O_3 formation, conversion into HNO_3 will efficiently remove NO_2 from the active system, since photolysis of HNO_3 is comparatively slow. The simulations shows that the conversion of NO_2 to HNO_3 accelerates when the air mass enters the humid boundary layer (~20th July, see e. g. marker D). Rapid cycling into HNO_3 counteracts the NO_x input from PAN decomposition and hence, limits present NO_x available for ozone production. Nearly all PAN has

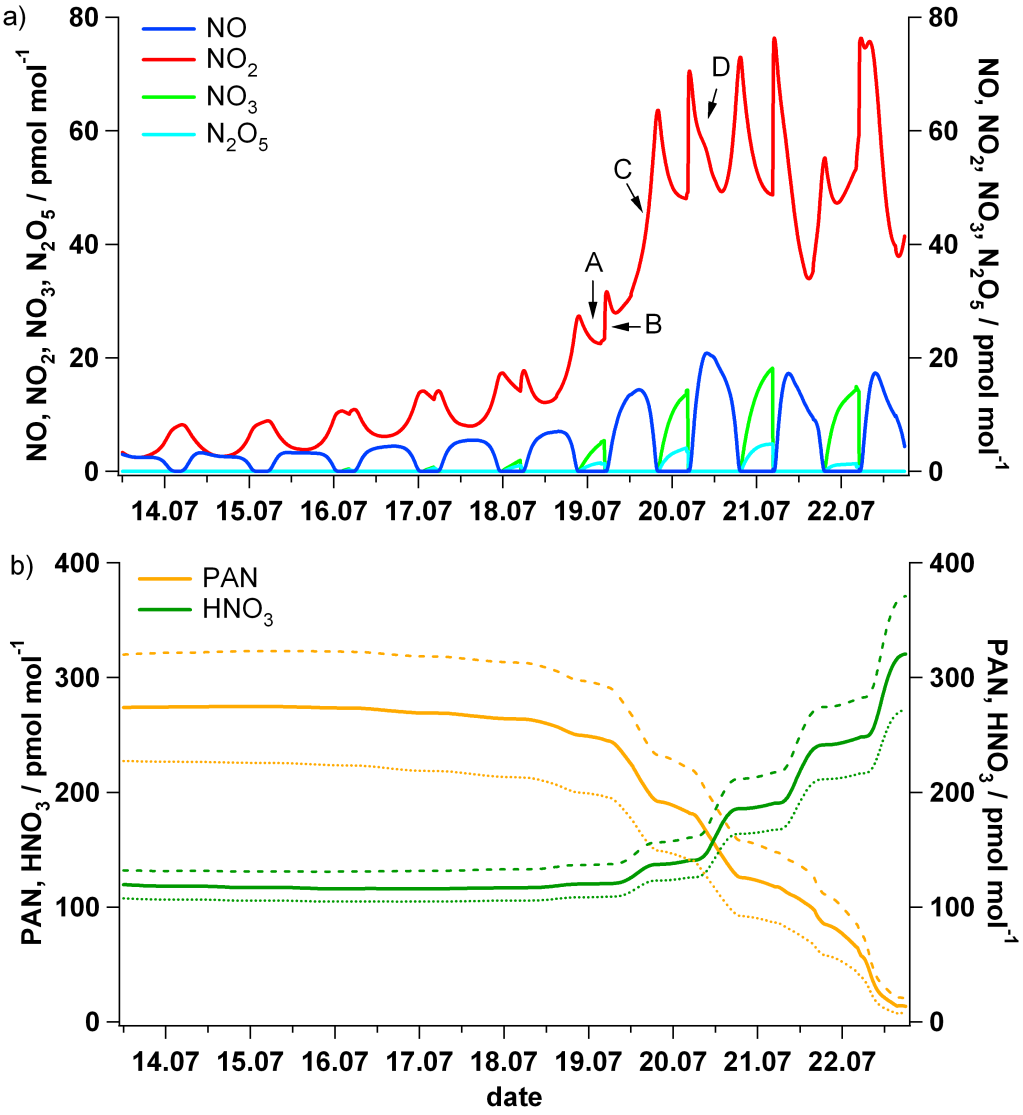

Figure 5.19: *Temporal evolution of several NO_y compounds along trajectory 3, as simulated by the CiTTyCaT model, starting on 13 July, 2008. a) NO (dark blue), NO_2 (red), NO_3 (light green) and N_2O_5 (light blue), b) PAN (orange) and HNO_3 (dark green).*

decomposed at the end of the simulation, and the main part of released NO_2 (∼90%) efficiently has been converted into HNO_3, as illustrated in **Fig. 5.19b**. The remaining part is partitioned in other NO_y forms such as NO, NO_2, but also e. g. HONO (not shown).

Finally, the temporal evolution of ozone along three different forward trajectories is compared in **Figure 5.20**. In addition to the ozone time-series discussed in detail above (trajectory 3), the evolution of O_3 along trajectory 1 and 6 is given (see **Fig. 5.15**). In comparison to trajectory 3, trajectory 1 descended faster, ultimately reaching the marine boundary layer (MBL) where it was advected to the south. Similar to trajectory 3, decomposition of PAN counteracts ozone destruction resulting in small net O_3 production on 19th July. However, the high humidity in the MBL (15 to 20 μmol mol^{-1} H_2O) in combination with high photolysis rates at southern latitudes leads to

much more efficient O_3 destruction at the end of the simulation (up 3 to 4 nmol mol^{-1} per day). In comparison, ozone mixing ratios simulated along trajectory 6 show slight ozone destruction along the whole simulation. Trajectory 6 descends only to altitudes around $\sim$3 km which results in less efficient PAN decomposition ($\sim$180 pmol mol^{-1} PAN is left at the end of the simulation - compared to $\sim$20 pmol mol^{-1} PAN remains at the end of the run along trajectory 3). However, due to the lower humidity at these levels, ozone destruction does not increase. Finally, ozone is present at similar values as in the run along trajectory 3.

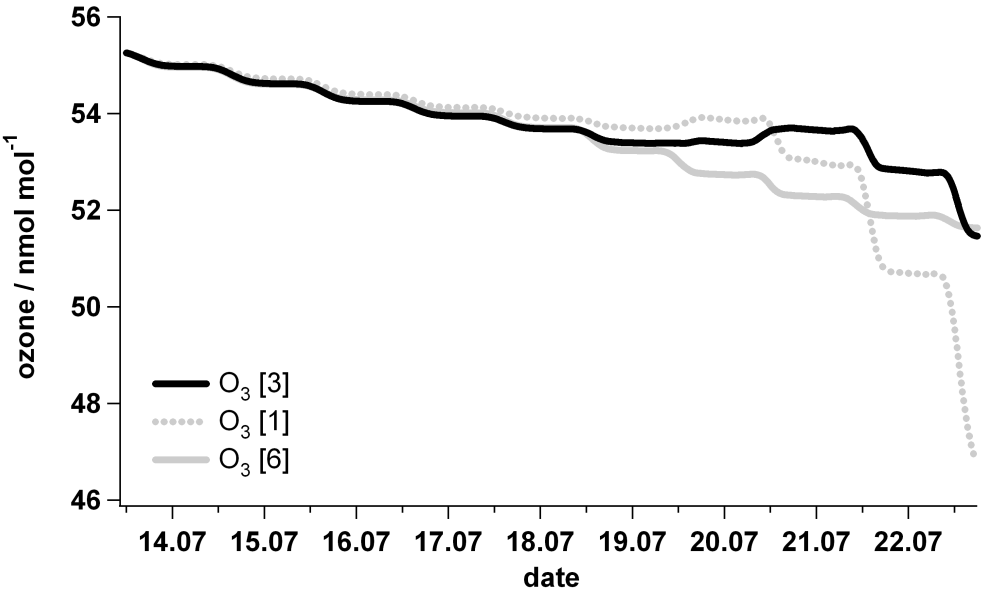

Figure 5.20: *Temporal evolution of ozone mixing ratios along three different trajectories No. 1 (grey dotted line), 3 (black solid) and 6 (grey solid).*

Note that the results discussed herein were obtained by chemistry-only simulations, whereas important atmospheric processes have been disregarded. First of all, only gas-phase reactions were considered. Including heterogeneous processes certainly would have accelerated shifting of NO_x into the HNO_3 reservoir during night-time, further limiting photolytic O_3 production. Accounting for wet and dry deposition would have removed HNO_3 efficiently from the system, especially at lower levels at the end of the simulation. However, photolysis of HNO_3 which might cycle NO_2 back into the active system did not play a significant role in this simulation. The highest uncertainty certainly arises from mixing processes which have not been considered in these model runs. It is almost clear that including mixing processes would have enhanced O_3 levels significantly, since the Siberian biomass burning plume was embedded in upper tropospheric air masses (like most of the other plumes sampled by the Falcon, see section 5.6). Since ozone as OH precursor drives photochemistry, this will in turn influence photochemical processes: The amount of ozone loss is directly and positively correlated to the O_3 concentration itself. This was evaluated in a comparison run along trajectory 3: O_3 was initialized with a 20 nmol mol^{-1} higher O_3 value (75.2 nmol mol^{-1} instead of 55.2 nmol mol^{-1} as in the run discussed above). This resulted in a total net O_3 loss of

$\sim$8.5 nmol mol^{-1} instead of 3.5 nmol mol^{-1}. On the other hand, mixing with air masses of UTLS origin might provide more NO_x, both directly or indirectly by photolysis of HNO_3. Resulting O_3 formation induced by NO_x input will counteract the enhanced photochemical O_3 destruction. However, exact values will critically depend on several parameters, as for example mixing rates which in turn will depend on e. g. meteorological conditions. It is also important to note that the disregard of mixing becomes more important in the turbulent boundary layer.

In summary, the model results suggest that ozone formation due to PAN decomposition does not play a dominant role, if the air mass descends into the warm and humid boundary layer. Therefore the question arises: what is the difference between our study and those who report on substantial ozone production due to PAN decomposition? In general, the biomass burning plumes observed during GRACE were much more aged and diluted, and therefore contained much less PAN than other plumes (by a factor of $\sim$10). Furthermore, temperature and humidity conditions play a dominant role in governing whether strong O_3 production takes place during subsidence or not. Real et al. (2007) examines a case when the air mass descends down to only 5 km where PAN decomposition already took place. However, due to much smaller water vapour mixing ratios at this altitude the photochemical lifetime of released NO_x is much longer, which in turn leads to more efficient ozone formation. In addition, photochemical destruction is not as efficient as in the boundary layer (see also section 2.1). Hudman et al. (2004) emphasize that the ozone production potential is especially high for plumes subsiding over the northeast Pacific, due to intense radiation and low humidity.

Chapter 6

Case Study: Transport of Asian pollution into the Arctic lower stratosphere

This chapter describes a more exceptional case observed during the GRACE field campaign, when the Falcon sampled Asian anthropogenic pollution in the Arctic lowermost stratosphere. On the local flight on 10 July, 2008, an air mass with unusually high carbon monoxide (CO), peroxyacetyl nitrate (PAN) and water vapor (H_2O) mixing ratios was sampled above the Arctic tropopause. The description of the case study begins with a presentation of the meteorological situation at the time of our measurements (6.1) and a discussion of the in-situ observations (6.2). Subsequently, the source region of the encountered air mass is identified by using a Lagrangian particle dispersion model and a backward trajectory model (6.3). The analysis of the meteorological situation in the source region (6.4) as well as during transport to Greenland (6.5) is followed by a discussion of tracer correlations (6.6.1) and mixing processes that have occurred during the cross-polar transport (6.6.2). The case study is described in detail also in Roiger et al. (2011b).

6.1 Meteorological situation at upper levels

The weather situation close to the time of observation (10 July 2008, 18:00 UTC) is presented in **Fig. 6.1a** using 300 hPa geopotential height (black isolines) and pressure altitude p_{2PVU} of the dynamical tropopause, defined as the 2 potential vorticity units (PVU) surface (color-coded). The red line gives the Falcon flight path. The geopotential height shows a large-scale trough over north-eastern Canada with a discrete low over the Davis Strait. The entire trough region is characterized by a low dynamical tropopause (equivalent to high values of p_{2PVU}, up to $\sim$400 hPa within the closed contour line of the low). On its leading edge, the low has southerly flow at 300 hPa (see geopotential isolines) and the dynamical tropopause is situated at $\sim$300 hPa. Above northern Greenland, north of a nearly east-west oriented narrow filament with a lower tropopause ($p_{2PVU} > 400$ hPa), the dynamical tropopause is at higher levels ($p_{2PVU} \sim 230$ hPa). The connected air mass is located in the diffluent exit region of a jet. At this time the jet was located right over the pole, as shown by the widening spacing of geopotential isolines from the North Pole towards the most northern part of the 10 July flight.

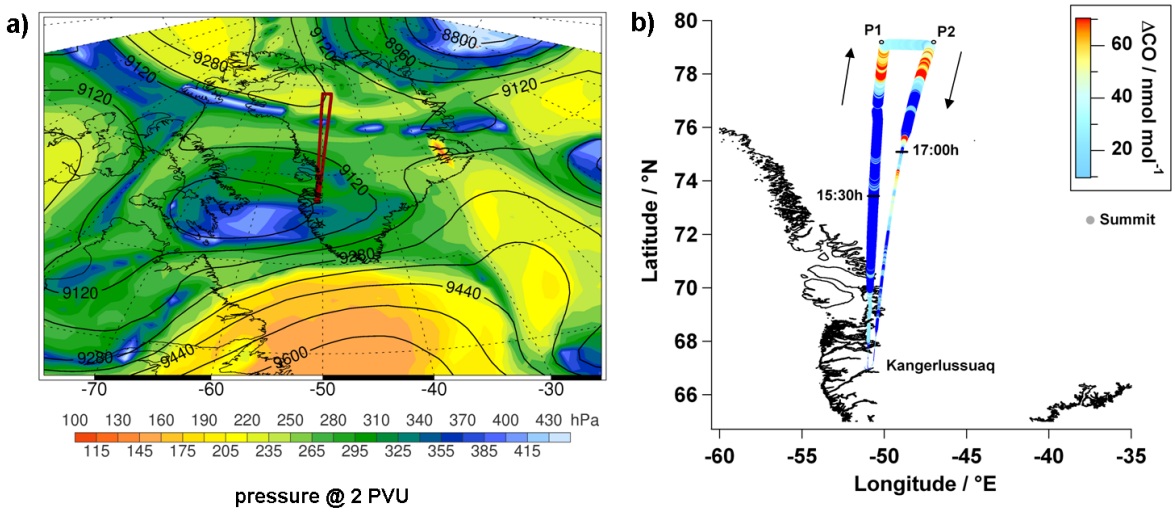

Figure 6.1: *a) Flight path of the DLR Falcon on 10 July 2008 between ∼14:30 UTC and 18:30 UTC (red line) superimposed on ECMWF analysis data at 18 UTC of pressure (color shaded, hPa) at the 2 PVU (dynamical tropopause) surface and geopotential height at 300 hPa (black lines, m). b) Flight path, color-coded by CO above altitude-dependent background values as derived from all GRACE data. Areas with CO < 10 nmol mol^{-1} are shown in dark blue. North of approx. 77.5°N, an air mass with enhanced CO mixing ratios was entered by the Falcon, both on the outbound and return leg at a constant flight level (11.3 km). The thickness of the line indicates the altitude (larger markers represent higher altitudes). For more details see text.*

6.2 In-situ observations

On the flight on 10 July 2008, CO values up to 138 nmol mol^{-1} were observed at 11.3 km altitude, whereas during GRACE typical CO mixing ratios at this altitude were ∼40 to 50 nmol mol^{-1}(see **Fig. 5.8a**). **Figure 6.1b** shows the Falcon flight-path, for illustration purposes it is color-coded by the measured CO above the altitude-dependent CO background (see color-scale on the right). The CO background here is defined as the 30th percentile of all POLARCAT-GRACE measurements, calculated separately for altitude bins of 1 km. CO values of < 10 nmol mol^{-1} are shown in dark blue. The marker size represents the flight altitude (larger markers indicate higher altitudes). After take-off in Kangerlussuaq, the Falcon climbed up to 11.3 km altitude while flying north (up to point P1), and then ∼60 km to the east (towards point P2).

On the way back to the south, the Falcon descended at ∼75.5°N to 7.9,km before landing again in Kangerlussuaq. The layer with enhanced CO was traversed twice, both on the outbound and the return leg, right before point P1 and after point P2. The maximum horizontal separation is 60 km (P1 to P2). Comparison with **Fig. 6.1a** shows that the layer with enhanced CO agrees well with the region of elevated tropopause, as indicated by the lower atmospheric pressure at the 2 PVU surface. **Fig. 6.2** presents the time-series for several trace gases for a part of the flight between 15:30 and 17:00 UTC (see time markers in **Fig. 6.1b**). It shows CO and O_3 (a), NO and NO_y (b) together with PAN and CO_2 (c). Also given are the potential temperature and the water vapor mixing ratio (d). The time resolution is 1 s, except for PAN, which is reported every 2 s.

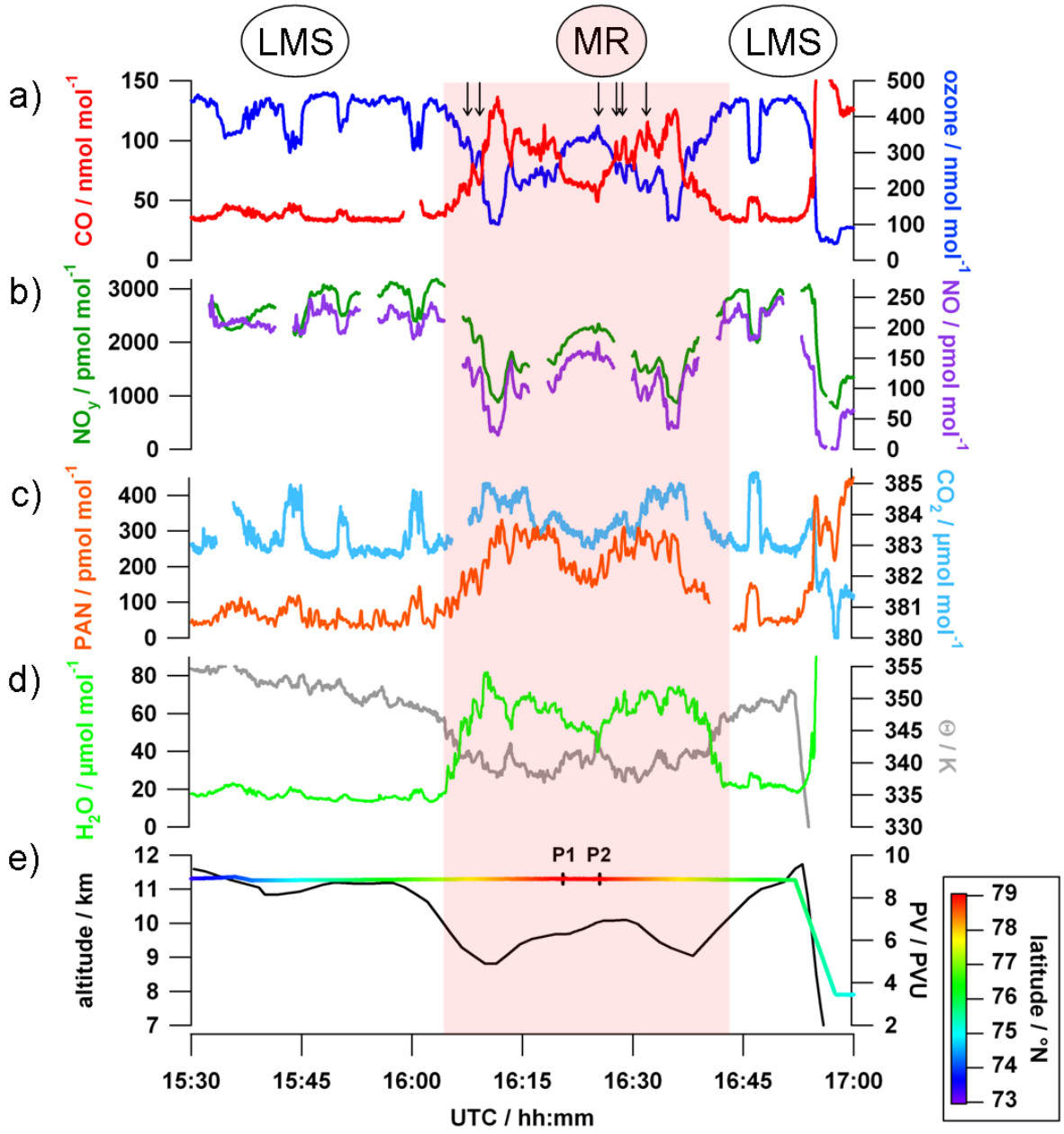

Figure 6.2: *Time-series of measured trace gases for the GRACE flight on 10 July 2008, between 15:30 and 17:00 UTC. a) O_3 (blue) and CO (red), b) NO_y (green) and NO (purple), c) PAN (orange) and CO_2 (light blue), d) H_2O (light green) and potential temperature (grey). Missing data correspond to internal calibration periods. e) Flight altitude (latitude is color-coded) and potential vorticity (black), as interpolated from the ECMWF analysis at 18 UTC. The flight segment discussed in the present study is highlighted in light red (mixing region, "MR"), whereas the remaining data at this flight altitude are denoted by "LMS" (lowermost stratosphere). Black arrows indicate smaller scale filaments.*

Panel e) shows the flight altitude (color-coded by the latitude of the Falcon), and potential vorticity as interpolated from the ECMWF analysis fields. The two way points P1 and P2 are marked as vertical lines (see **Fig. 6.1b**). The red shaded area in **Fig. 6.2** highlights the flight segment with enhanced CO. In the following this segment is referred to as mixing region "MR". The remaining data sampled at the same altitude, i.e. further south of "MR", are denoted by "LMS" (lowermost stratosphere). When the Falcon entered the "MR", CO increased from about 40 nmol mol^{-1} up to ∼140 nmol mol^{-1} over a time span of ∼7 min. (corresponding to ∼80 km). The Falcon then observed a sharp decrease down to ∼80 nmol mol^{-1}, and a region of moderate CO values of 100 nmol mol^{-1} (∼65 km). At the most northern point, CO did not completely drop to mixing ratio values observed further south in the lowermost stratosphere ("LMS"), which indicates that the aircraft possibly did not traverse the entire mixing region.

The time-series of the trace gases inside the "MR" is nearly symmetric due twice penetrating this air mass. The CO enhancement in the "MR" was accompanied by an increase of the tropospheric pollutant PAN (up to 330 pmol mol^{-1} compared to ∼40 pmol mol^{-1} in the "LMS"), and of water vapor (∼80 μmol mol^{-1} compared to ∼20 μmol mol^{-1} in the "LMS"). The trace gases with generally higher values in the stratosphere than in the unpolluted regions of the troposphere (i. e. O_3, NO and NO_y) showed smaller mixing ratios within the "MR" of down to 100 nmol mol^{-1}, 30 pmol mol^{-1} and 900 pmol mol^{-1}, respectively. The anticorrelation of the different trace gases indicates that the Falcon sampled an air mass of both tropospheric and stratospheric origin. The interpretation of the chemically inert greenhouse gas CO_2 (atmospheric lifetime of ∼100 years) however is more complicated, due to underlying temporal and spatial variations (see Sect. 3.6). In some parts of the "MR" some smaller scale filaments are observed (indicated by black arrows). Thermodynamic parameters also vary within the "MR". Potential temperature and potential vorticity both decrease, pointing to a less stable stratification in the "MR". Potential vorticity during this part of the flight had a minimum value of ∼5 PVU, and the minimum vertical distance between flight altitude and the 2 PVU tropopause was ∼800 m (see Sect. 6.5).

6.3 Identification of source region

6.3.1 FLEXPART Backward Analysis

The results of the FLEXPART backward runs initialised along the flight track are shown in **Fig. 6.3b**. To allow an easier comparison, the in-situ O_3 and CO time-series are repeated in **Fig. 6.3a**. Generally, the structure of the "MR" is very well captured by the FLEXPART model. The blue line in the middle panel gives the fraction of air with a stratospheric origin which decreases inside the "MR" to a minimum of ∼50%. The red pattern in **Fig. 6.3b** represents the Asian excess-CO, indicating that the tropospheric part of the encountered air mass was polluted by anthropogenic emissions of Asian origin. According to the FLEXPART simulations, contributions from industrial pollution sources from other continents or from biomass burning are negligible. The CO source contribution plot for 16:11 UTC (CO maximum) is given in **Fig. 6.3c**. This plot represents the product between the anthropogenic emission flux (taken from the emission inventories) and the

footprint emission sensitivity. The latter is proportional to the residence time of the particles over a unit area in the lowest 100 m (Stohl et al., 2005). The CO source contribution plot shows that the pollution mainly originates from the North China Plain, one of the most densely populated regions in China, with some minor contributions from the North East China Plain and Korea. According to the model, the pollution was emitted approximately 6-10 days before our measurements (not shown).

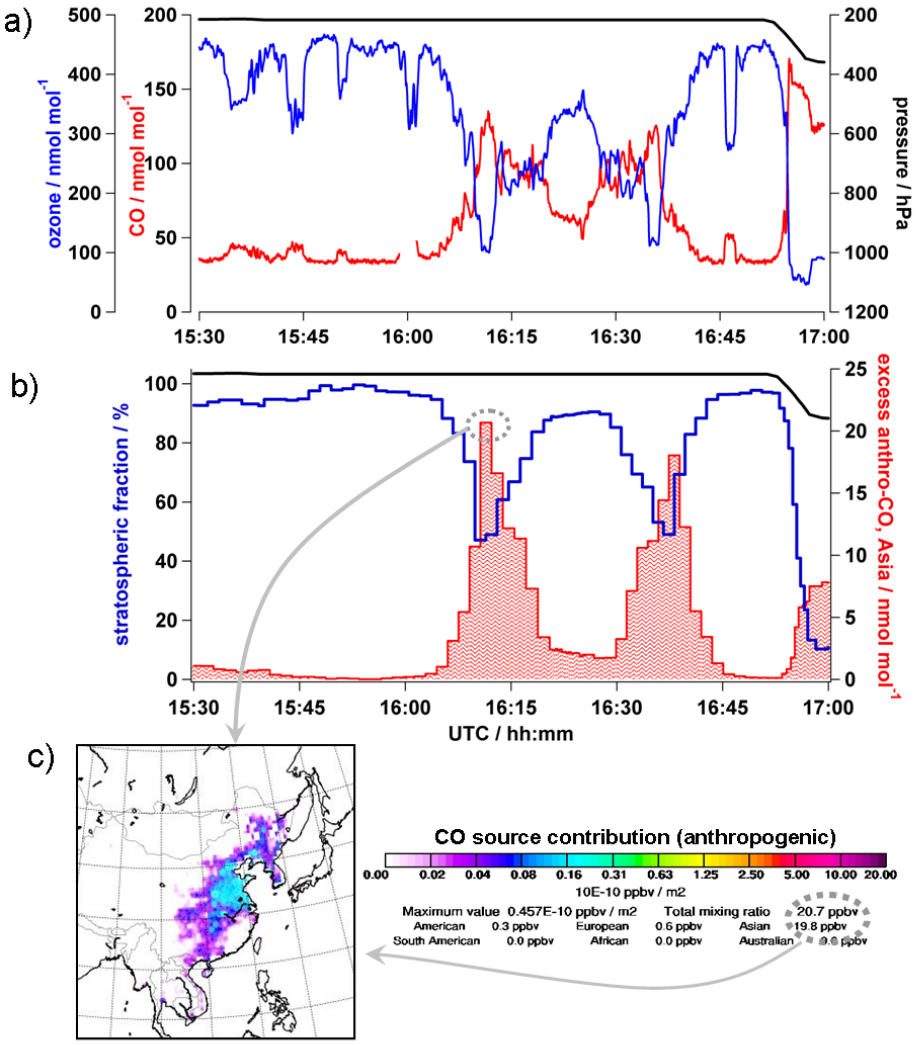

Figure 6.3: *a) Time-series of in-situ CO (red), O_3 (blue), and pressure at flight altitude (black) for the same time period shown in* ***Fig. 6.2****. b) Results of the FLEXPART backward analysis: The blue line gives the stratospheric fraction along the flight path. The red pattern represents the FLEXPART excess-CO originating from Asian anthropogenic pollution. c) CO source contribution plot for 16:11 UTC (maximum CO concentration at 11.3 km altitude) with color-scaling on the right.*

6.3.2 LAGRANTO backward trajectories

The **Lagr**angian **An**alysis **To**ol (LAGRANTO, Wernli and Davies (1997)) was used to investigate the origin of the observed air masses over Greenland. The calculations are based on three-dimensional wind fields of 6-hourly ECMWF operational analyses at a 1° horizontal grid resolution. Several variables characterizing the physical state of the air parcels including potential temperature, specific humidity and potential vorticity were traced along the trajectory paths. In order to analyze the transport history of the sampled "MR" and "LMS" air masses, an ensemble of 8 day LAGRANTO backward trajectories was calculated. The results are illustrated in **Fig. 6.4**. A total of 242 trajectories were released in an area from -60°E to 40°E and 75°N to 82°N (see black rectangle in **Fig. 6.4a**) at 217 hPa on 10 July, 18 UTC. The color-code gives the latitude of the starting position and the black line within the rectangle shows the Falcon flight track. **Figures 6.4b** to **d** show the temporal evolution of meteorological parameters along the trajectories (e.g. pressure, humidity, potential temperature, potential vorticity). In this area, two different air mass origins can be distinguished. Trajectories in the southern part of the box were transported from northern North America towards Greenland, remaining above 300 hPa. These trajectories characterize the pathway for the sampled "LMS" air masses.

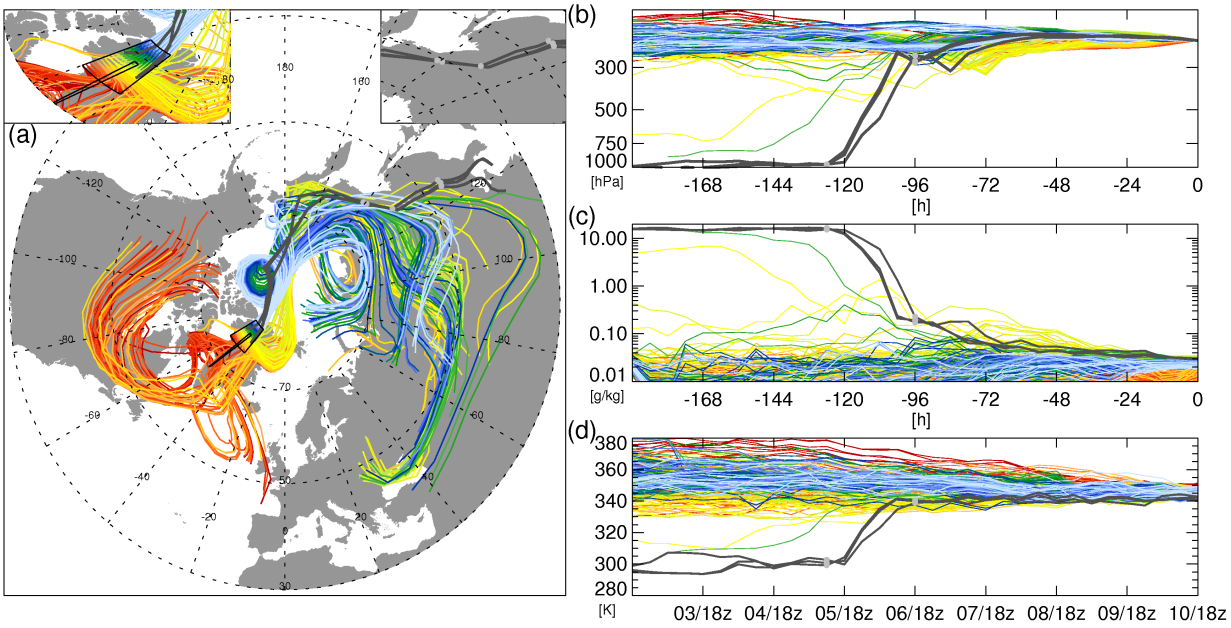

Figure 6.4: *LAGRANTO 8-day backward trajectories released on 10 July, 18 UTC, every 40 km inside the black box at 217 hPa. The box was centred around the encountered "MR". The flight track of the 10 July flight is shown as black line. The color-code of the trajectories represents the starting latitude of the trajectories. Green trajectories belong approx. to the region of the "MR". Panel a) gives a polar view of the pathways. Two sections are shown at a larger scale on the top: The release box (left) as well as the ascent over eastern Asia (right). The three panels b), c) and d) show the evolution of pressure, specific humidity, and potential temperature along the trajectories. The time on the x-axis is relative to 10 July, 18 UTC. The trajectories highlighted as thick grey lines experience a strong ascent over eastern Asia. Two time marks (gray dots) at -126 h (05 July, 12 UTC) and at -96 h (06 July, 18 UTC) indicate the location of this lifting process.*

The cyclonic curvature indicates transport within the large scale trough described in section 6.1 (see also **Fig. 6.1a**). Trajectories in the northern part of the box were traced back across the North Pole to Siberia/Russia. Some parcels moved directly over the pole (yellow), while others were influenced by the upper level high that caused an anti-cyclonic rotation (blue and green). The time-series of pressure along the trajectories shows that independent of their origin, most of the parcels were transported at high altitudes above 300 hPa (see **Fig. 6.4b**). Their PV values were predominantly larger than 2 PVU which points to stratospheric transport (not shown). Only a small number of the trajectories experienced a strong vertical displacement. Remarkably, three of these parcels (thick grey lines in **Fig. 6.4**) originate from the boundary layer in the industrialized coastal regions of China and Korea, where they had the possibility to take up anthropogenic pollution. This is in good agreement with the results of the FLEXPART analysis (see section 6.3.1). The subsequent fast and strong ascent from ground level to the upper troposphere is accompanied by a strong loss of humidity and an increase of the potential temperature as a result of latent heat release. The strong up-lift of the trajectories took place over eastern Russia between 05 July, 12 UTC (-126 h) and 06 July, 18 UTC (-96 h), as indicated by the grey dots in **Fig. 6.4**. According to FLEXPART, the pollution was emitted between ∼01 - 04 July, i. e. ∼6 - 10 days before our measurements. The polluted air mass was transported for a few days at low levels towards the north-east before it was exported from the boundary layer. The characteristics of strong and poleward ascent in combination with latent heat release suggests up-lift by a WCB, which is further investigated in the following section.

6.4 Meteorological situation in the source region

To study the ascent process within the warm conveyor belt, 48 h LAGRANTO forward trajectories were initiated on every grid point in a box over Asia (90°E to 150°E, 30°N to 75°N and between 1000 hPa and 750 hPa), as indicated in **Fig. 6.5**. Within the 8-day period from 02 July 2008, 18 UTC to 10 July 2008, 18 UTC, every 6 h a new set of trajectory calculations was initialised, and calculated for a 48 h interval. From all trajectories, only those showing a pressure decrease greater than 600 hPa within 24 h were selected, and considered as warm conveyor belt trajectories. The computation of all selected 48 h WCB trajectories was then completed over the entire 8-day period both by a forward and backward calculation. **Figure 6.5** shows the position of the WCB parcels during the evolution of a cyclone with an embedded WCB. As the up-lift of the relevant air mass took place between 05 and 06 of July (see **Fig. 6.4**), we only show WCB trajectories that ascended between 04 July, 00 UTC to 07 July, 18 UTC. On 05 July, 00 UTC (**Fig. 6.5a**), the WCB parcels were located over the coastal regions of China and Korea as well as above the Yellow Sea, predominantly at altitudes below 900 hPa, and transported by south-westerly winds. The distribution matches partly the FLEXPART CO source contribution (**Fig. 6.3c**), with a shift towards the north-east due to the preceding low-level transport.

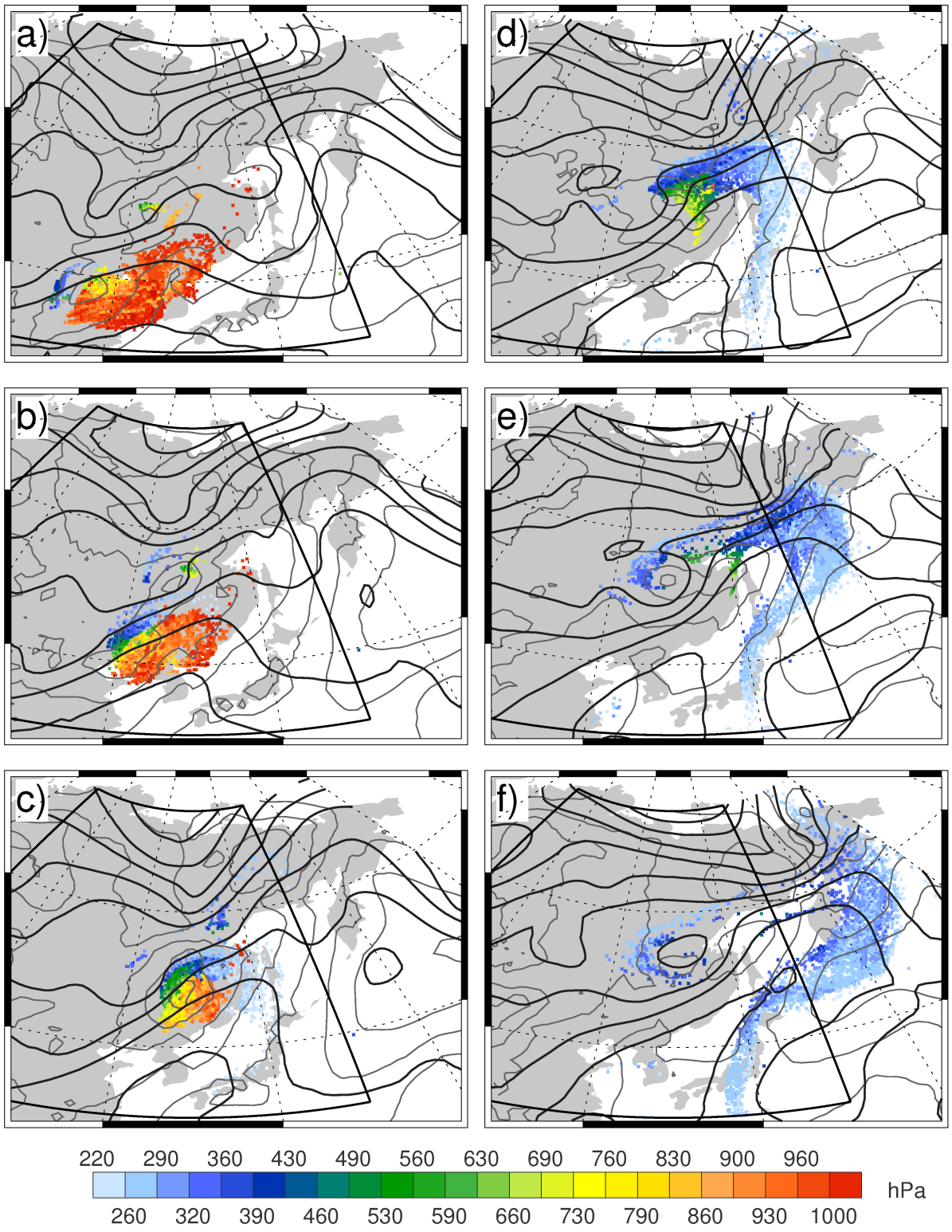

Figure 6.5: *Synoptic evolution from ECMWF analyses and position of WCB parcels at a) 05 July, 00 UTC b) 05 July, 12 UTC, c) 06 July, 00 UTC, d) 06 July, 12 UTC, e) 07 July, 00 UTC , and f) 07 July, 12 UTC. Thick black lines show geopotential height at 300 hPa (80 gpm interval). Thin grey lines illustrate the mean sea level pressure (4 hPa interval). The black polygon marks the region in which the trajectories were initialized. The color-coded dots show location and pressure of the parcels at the respective time step.*

Twelve hours later, the air mass was advected further north-eastward and a portion of the eastern parcels began rising when an upper level trough approached and caused cyclogenesis (**Fig. 6.5b**). At 06 July, 00 UTC a surface low developed and the parcels were situated close to the cyclone center and in the associated warm sector (**Fig. 6.5c**). North-east of the low, the parcels lined up along the warm front and reached the upper troposphere with pressure values up to 300 hPa. The parcels south of the surface low were located closer to the ground (**Fig. 6.5d**). Another 12 hours later (06 July, 12 UTC) the surface low propagated further north eastward (**Fig. 5e**). Except for some parcels located at mid-levels (500-800 hPa), the bulk reached the upper troposphere and was embedded in the jet stream located above the east coast of Asia. The majority of the WCB parcels were located in the diffluent exit region of the jet stream. Most parcels moved southward, however, those on the cyclonic side of the jet were embedded in the north-eastward flow on the leading edge of a trough approaching from the north (see **Fig. 6.5f**). These parcels subsequently moved over the pole following the pathways illustrated in **Fig. 6.4**. Of the 4,296 selected WCB trajectories, a subset of 191 trajectories (4.5%) was transported into the Arctic. 92% of these Arctic WCB trajectories intersected the dynamical tropopause (PVU $>$ 2), compared to only 18% of the remaining WCB trajectories. Most parcels reached the 2 PVU level right after the WCB ascent or when they were again lifted on the leading edge of the upper level trough. The latter ascent is also reflected in the pressure time-series of **Fig. 6.4** (see yellow and blue trajectories between -84 and -72 h). The trajectories most likely to reach the Arctic were those initialised from the cyclone centre (not shown).

6.5 Cross-polar transport and vertical distribution of the Asian pollution

The transport of the Asian pollution plume across the pole is illustrated in **Fig. 6.6**. The left panel shows satellite image composites for 4 points in time, covering the time period after the up-lift within the WCB (06 July, 2008) to the day of our measurements above northern Greenland (10 July, 2008). The images are color enhanced such that yellow and red colors highlight the cold upper-level cloud tops, green colors underscore the tops of the warmer mid-level and low-level clouds, and blue colors are the much warmer surface of the Earth (for description of the image retrievals, see appendix A8). The white contour lines represent the FLEXPART Asian anthropogenic CO tracer, but only for the column above 9 km. For the same points in time, the right panel shows maps of FLEXPART Asian CO tracer plotted on 340 K isentropes. The red line indicates where the 325 K isentropes crosses the 2 PVU surface, giving the approximate position of the jet stream. The red crosses indicate the location of a subset (every 8^{th}) of the pole-crossing WCB forward trajectories (see 6.4). According to this trajectory analysis, the WCB ascent ahead of the cold front took place over Eastern Russia approximately between 05 July, 18 UTC and 07 July, 00 UTC. On 06 July, 18 UTC, the WCB trajectories reached the upper troposphere, coinciding with an area of enhanced CO tracer columns above 9 km of 100 g m^{-2} ahead of the cold front (**Fig. 6.6a**).

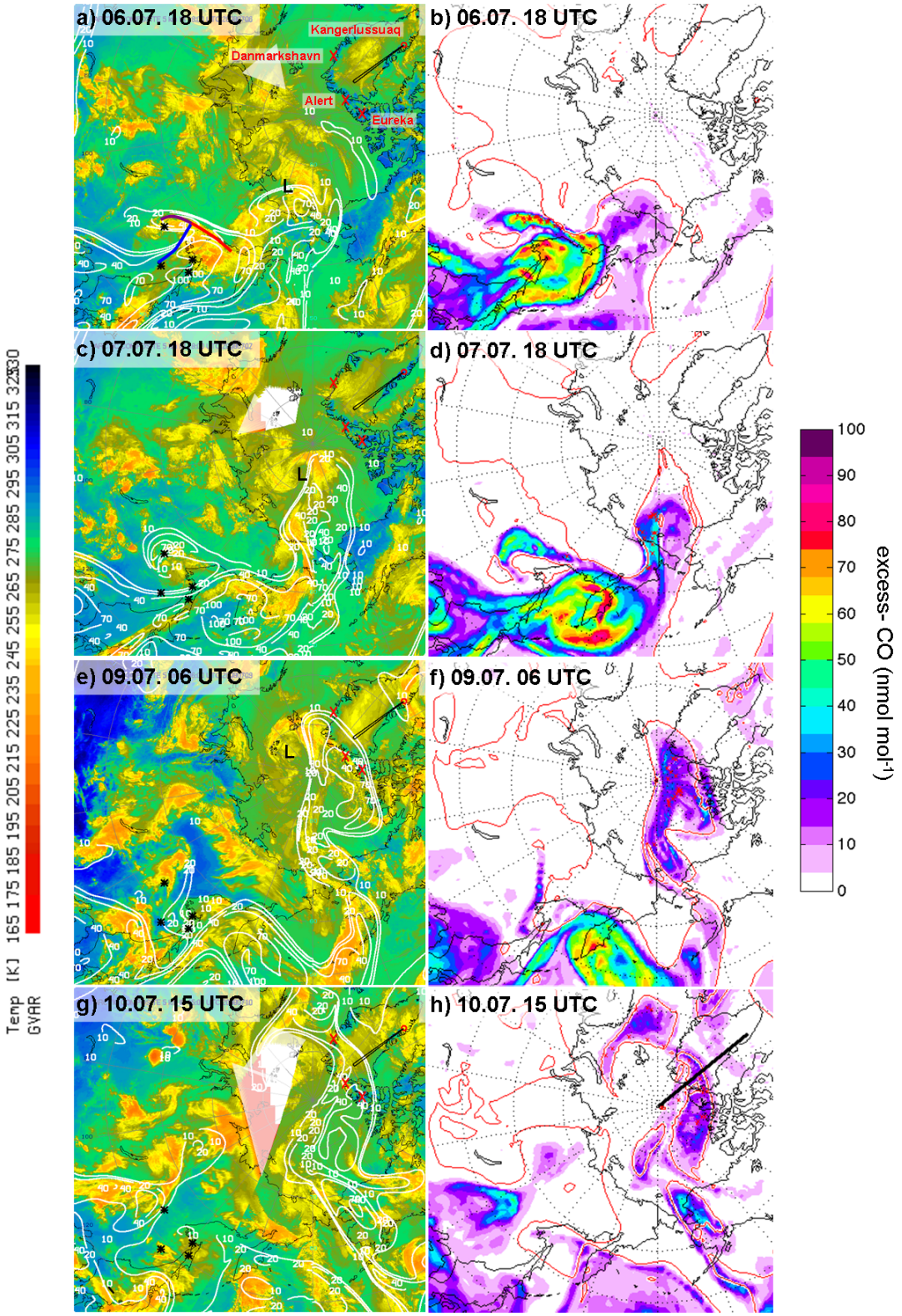

Figure 6.6: *Cross-polar transport of the Asian pollution. a) and b) 06 July, 18:00 UTC, c) and d) 07 July, 18:00 UTC, e) and f) 06 July, 09:00 UTC, g) and h) 10 July, 15:00 UTC. Left panels: Satellite composite images with color-coded cloud top temperatures (see color-scaling at the left). White contour lines show FLEXPART Asian CO for the column above 9 km. Black asterisks indicate locations of weather stations in the region of the WCB (marked by the fronts in panel a). The Falcon flight path is superimposed in* ***Fig. 6.6g****. Right panels: FLEXPART Asian CO tracer plotted on the 340 K isentrope (see color-scaling on the right). Red line gives the location of the dynamical tropopause (2 PVU) at the 325 K surface. The red crosses indicate the position of the WCB forward trajectories. The black line shows the location of the cross section presented in* ***Fig. 6.8****.*

Soundings from four weather stations (black asterisks in **Fig. 6.6a**) indicate that the minimum cloud top temperatures of ∼240 - 223 K within the WCB correspond to a maximum altitude of ∼11 km. CO is used as a passive tracer with a lifetime of 20 days in the FLEXPART model runs, therefore other CO pollution "remnants" north of Kamchatka / east of North Siberia are also visible in the upper troposphere, possibly from earlier lifting events. However, the polluted air mass lifted within the studied mid-latitude cyclone reached high potential temperatures of 340 K, shown in a comparison with **Fig. 6.6b**.

As indicated by the red line, a tropospheric streamer had already begun to intrude into the Arctic, ahead of an upper level trough. In the following hours and days, a low pressure system formed, deepened and moved further to the north (indicated with "L" in **Fig. 6.6a, c, e**). The polluted Asian air mass therefore was advected towards the North Pole (**Fig. 6.6c**, 07 July, 18 UTC). Whereas most of the Asian CO tracer was advected eastwards, some of the Asian CO was embedded in the streamer (**Fig. 6.6d**). A comparison of **Fig. 6.6c** and **Fig. 6.6d** shows that the region of enhanced FLEXPART tracer is accompanied partly by upper level clouds. During its journey, the polluted streamer was elongated and deformed (**Fig. 6.6e** and **f**, 09 July, 06 UTC). Finally, a portion of the polluted streamer reached northern Greenland, where it was sampled by the Falcon on 10 July (**Fig. 6.6g** and **h**, 10 July, 18 UTC). **Fig. 6.6h** illustrates the good agreement with our in-situ data, showing that the polluted streamer was located almost perpendicular to our flight track, and was not completely traversed.

During the cross-polar transport, the tropospheric streamer elevated the polar tropopause substantially (see also **Fig. 6.1a**). **Figure 6.7** illustrates the temporal evolution of the vertical temperature structure during the advection of the streamer. Temperature profiles from soundings before, during and after the passage of the polluted streamer are presented exemplary for Eureka, Canada (79.98°N, 85.95°W), and show a tropopause height variation of ∼2.5 km. Due to the mid-latitude origin of the polluted Asian air mass, the temperature at a fixed level in the middle to upper troposphere is ∼ to 10 K higher inside the Asian air mass (red solid lines) in comparison to the Artic air mass (blue dotted lines), whereas the tropopause temperature is up to ∼7 K lower. The region above ∼ 13 km is less affected by the dynamics of the tropospheric streamer. During the passage of the Asian air mass the tropopause is sharper than before and after. The maximum thermal tropopause is ∼ 11.5 km (11 July, 00 UTC), which is slightly above our flight altitude (11.3 km). Note however the considerable temporal and spatial difference between the soundings and our in-situ measurements. An analysis of ECMWF temperature profiles indicates that e. g. at the time of the observation, the thermal tropopause was ∼ 500 m lower in the sampled part of streamer than above Eureka.

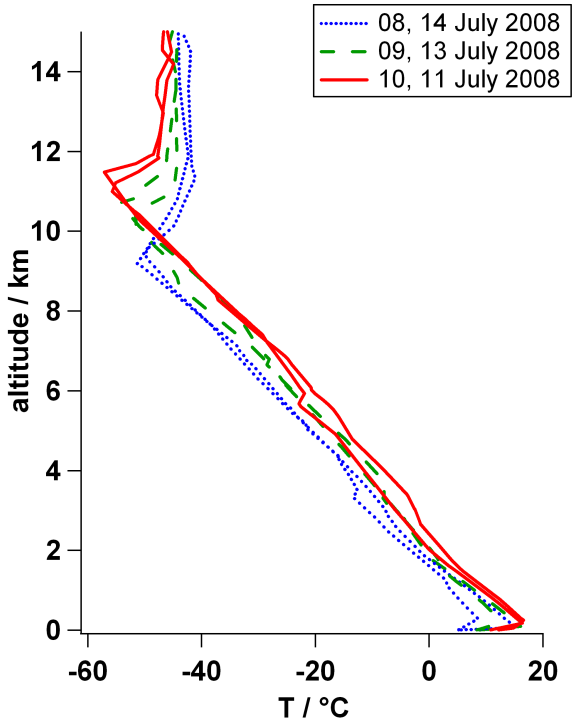

Figure 6.7: *Temperature profiles at Eureka, Canada (79.98° N, 85.95° W) as derived from radiosonde soundings on several days, each at 00 UTC (taken from http://weather.uwyo.edu/upperair/sounding.html) . The blue dotted lines represent profiles obtained before and after the polluted Asian air mass arrived at Eureka (08 July and 14 July 2008), respectively. The red solid lines show soundings during its passage (10 and 11 July 2008). The green dashed lines represent profiles from times between (09 and 13 July 2008).*

Figure 6.8 shows a vertical cross section of the FLEXPART Asian excess-CO tracer around the time of the flight (see black line in **Fig. 6.6h**). Also given are isentropes (black lines), the 2 PVU dynamical tropopause (thick black line), as obtained from the ECMWF analysis data, as well as isotaches (blue lines). The red crosses indicate the position of the WCB forward trajectories. Only WCB trajectory points located within 200 km of the Falcon flight path are shown (within 16:30 h ±3 h). Their abundance close to or above the 2 PVU tropopause reflects the strong selection criteria of the WCB forward analysis (600 hPa within 24 h). According to the FLEXPART model simulation, the Falcon probed the topmost part of an Asian pollution plume with a vertical extension of several km. The Asian excess-CO shows a maximum of ∼90 to 100 nmol mol^{-1} at about 9 km just below the dynamic tropopause, at the edges of the tropospheric streamer. A part of the pollution reached the lowermost stratosphere, as indicated both by the 2 PVU tropopause and the closer spacing between the isentropes. According to ECMWF analysis, the plume was sampled ∼800 m above the dynamic tropopause and ∼400 m above the thermal tropopause, respectively. The Falcon nearly reached the centre of the streamer which is indicated by the region of the elevated dynamical tropopause. The Falcon probed the part of the streamer where the modelled excess-CO reached the highest altitude (∼12.5 km), with values of ∼20 nmol mol^{-1} at our flight level (see also **Fig. 6.3b**). The FLEXPART runs further indicate that the Asian air mass also contained emissions from Siberian forest fires, but only at altitudes between ∼4 to 9 km and hence, below our flight level and below the 2 PVU tropopause (not shown).

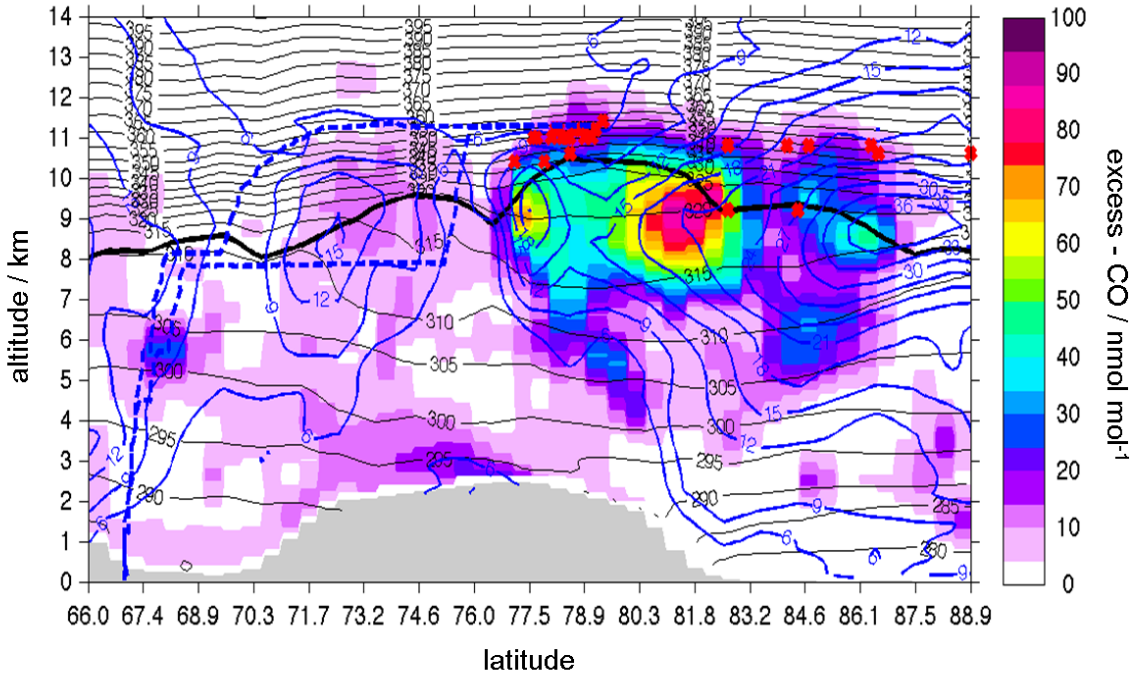

Figure 6.8: *Cross section of the FLEXPART Asian anthropogenic excess-CO tracer (see black line in* ***6.6h****). Colors represent the modelled Asian excess-CO above atmospheric background values (see color-scale on the right). The dashed blue line shows the Falcon flight path on 10 July. Also given are the 2 PVU dynamical tropopause (thick black line), isentropes (thin black lines), and isotaches*[2] *(thin blue lines), as calculated from ECMWF analysis.*

6.6 Discussion

6.6.1 Tracer-tracer correlations

As shown in sections 6.2 and 6.3, both in-situ measurements and the FLEXPART analysis indicate that we probed an air mass of both stratospheric and tropospheric origin. In this section the chemical properties of the sampled air mass are discussed using correlations between different trace gases. Tracer-tracer relationships are a common tool to investigate mixing, chemical and/or transport processes in the tropopause region (Hoor et al., 2002, 2004; Pan et al., 2004, 2007; Kunz et al., 2009). The red crosses in **Fig. 6.9a** to **d** represent the 10 July data observed inside the "MR". For comparison, the 10 July "LMS" data are also shown (black circles). The grey open circles represent all other GRACE data, as obtained from all 15 local flights.

Figure 6.9a shows an O_3-CO scatter plot. O_3-CO correlations help to diagnose STE (Stratosphere-Troposphere-Exchange) because both O_3 and CO show distinct vertical gradients in the vicinity of the extratropical tropopause, with higher O_3 in the stratosphere and higher CO in the troposphere, respectively. Ozone is mainly produced in the tropical stratosphere and has a lifetime of approx. 1 year in the lowermost stratosphere (Solomon et al., 1985). In the troposphere, O_3 values are highly variable due to in-situ photochemical production/destruction, dry deposition and import of stratospheric air (see also section 5.5).

The "MR" data in the O_3-CO scatter plot in **Fig. 6.9a** can be represented by a regression line, a so-called mixing line, which is formed by irreversible mixing of air parcels of both stratospheric and tropospheric origin. The slope of such a mixing line in a tracer-tracer space is dependent on the trace gas mixing ratios of the initial air masses (Plumb and Ko, 1992; Hoor et al., 2002). The tropospheric character is found to be highest in the center of the "MR" (see also **Fig. 6.1b**). Here, the CO mixing ratio of $\sim$138 nmol mol^{-1} suggests predominantly tropospheric origin whereas the ozone mixing ratio of $\sim$100 nmol mol^{-1} is already at the upper limit of typical tropospheric values. Although photochemical in-situ production in strongly polluted air masses may cause such high ozone values, this might indicate that also this part of the streamer had already mixed with ozone-rich stratospheric air masses. At the edges of the "MR", the entrainment of O_3-rich, stratospheric air is more prominent.

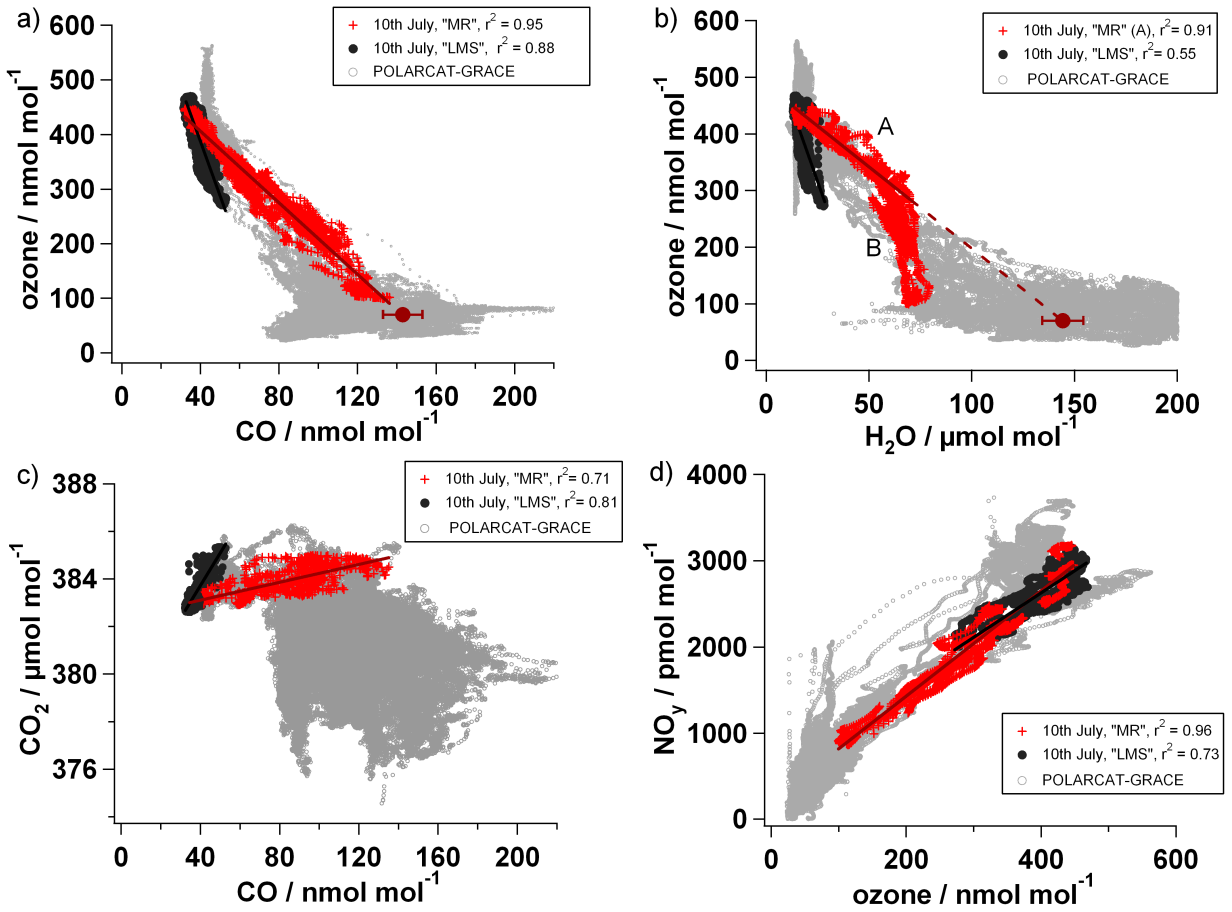

Figure 6.9: *Scatter plots of a) O_3 vs. CO, b) O_3 vs. H_2O, c) CO_2 vs. CO, and d) NO_y vs. O_3. Data of the 10 July "MR" are shown as red crosses, the 10 July "LMS" data are given as black circles. Grey open circles represent all POLARCAT-GRACE measurements. See text for more details.*

A comparison of the "MR" data with the remaining GRACE data shows that the "MR" CO values in the tropopause region and above (i.e. $O_3 > 100$ nmol mol^{-1}) are biased towards higher CO mixing ratios. This suggests that a CO-enriched air mass was mixed into the lowermost stratosphere, which

confirms the FLEXPART model results. If mixing and not chemical transformation is the dominant process, the extrapolation of the regression slope to an assigned tropospheric value of O_3 gives an indication of the CO concentration of the "tropospheric end-member" (Hintsa et al., 1998; Herman et al., 1999; Hoor et al., 2002). If we assume an upper tropospheric ozone mixing ratio of 70 ($\pm$30) nmol mol^{-1}, we can calculate an initial CO mixing ratio of 143 ($\pm$10) nmol mol^{-1}, as indicated by the dark red marker in **Fig. 6.9a**. It has to be pointed out that the tropospheric end-member represents only the tropospheric air mass just before it mixed with the stratospheric air. The WCB inflow regions however can be quite large (Wernli and Davies, 1997; Eckhardt et al., 2004), which means that the anthropogenic emissions certainly have been diluted with less polluted air already in the troposphere.

Figure 6.9b shows the relation between O_3 and H_2O. Water vapor data were obtained by a Lyman-alpha hygrometer (Zöger et al. (1999); $\pm$6 %, 0.1 μmol mol^{-1}). Water vapor mixing ratios show an even stronger gradient across the extratropical tropopause than O_3 and CO. The entry of H_2O into the stratosphere occurs primarily in the tropics, however in the extratropics a moist mixing layer in the lowermost stratosphere is an indicator of troposphere-to-stratosphere transport occurring at higher latitudes (e.g. (Krebsbach et al., 2006)). The moisture in the extratropical tropopause region is largely a function of the temperature at the cold point tropopause, but depends also on the relative strength of the different transport paths. Water vapor has a long chemical lifetime in the tropopause region, but it is not conserved if condensation followed by precipitation occurs.

Apparently the "MR" data are divided into two regimes A and B, which are separated approximately at O_3 and H_2O values of 280 nmol mol^{-1} and 65 μmol mol^{-1}, respectively. The data in group A form a mixing line which can be extrapolated towards assigned tropospheric ozone values of 70 ($\pm$30) nmol mol^{-1}. The corresponding H_2O end-member of 144 ($\pm$10) μmol mol^{-1} is indicated by the dark red marker in **Fig. 6.9b**. It gives an approximate value of the H_2O content of the air mass after it was up-lifted within the WCB, but before it mixed with drier air from the stratosphere. This water vapor mixing ratio is in the same range of values obtained from the backward trajectory calculations, suggesting that after the strong loss of moisture that is characteristic of WCB lifting events, H_2O mixing ratios of $\sim$0.06 - 0.1 g kg^{-1} (corresponding to $\sim$96 - 160 μmol mol^{-1}) remain within the air mass (see grey trajectories in **Fig. 6.4c**, at -72 h). The high water vapor mixing ratio in the WCB region raises the question whether this transport pathway may lead to an enhanced moistening of the extratropical lowermost stratosphere, though an upscaling cannot be done from our single event study. This might have implications for the temperature and chemistry of the UTLS, as water vapor plays an important role in the radiation budget and is a primary source of HO_x radicals (e.g. (Fueglistaler et al., 2009; Kunz et al., 2009). The data of group B correspond to the center of the "MR", and clearly deviate from the regression line. Obviously water vapor was removed in this part of the air mass due to phase transition followed by sedimentation. This assumption is supported by the occurrence of the high-level clouds in some parts of the streamer, visible in the satellite images (e.g. **Fig. 6.6c, e**).

A CO_2-CO scatter plot is presented in **Fig. 6.9c**. CO_2 has seasonal, diurnal, and spatial variations (see also section 5.5). The "MR" data show a linear dependence between CO_2 and CO. Positive

correlations between CO_2 and CO are typically observed for combustion sources, and the CO_2/CO emission ratio may provide information about the combustion efficiency. The CO_2/CO slope in this case is mainly driven by the mixing processes between the tropospheric and the stratospheric air masses, but it points clearly towards higher CO_2 values with increasing CO. The CO_2/CO ratio in this tropospheric pollution therefore was rather high compared to the ratios observed in all other CO plumes, which originated mainly from boreal biomass burning. This might be due to a combination of two effects. The fuel carbon conversion of biomass burning is relatively low, especially compared to industrial pollution, e.g. to power plants with high combustion efficiencies. This leads to initial CO_2/CO slopes of up to a magnitude lower than those from anthropogenic plumes Andreae and Merlet (2001); Suntharalingam et al. (2004). Additionally, the CO_2 "background" might differ for these two different source regions. In densely populated areas like the North China Plain, respiratory CO_2 of urban residents as well as agricultural soils and livestock is part of the anthropogenic plume and increases the CO_2/CO ratio (Wang et al., 2010). On the contrary, CO_2 plant uptake in boreal regions during summer leads to a decrease of this ratio.

Figure 6.9d shows a NO_y-O_3 scatter plot. In the stratosphere, NO_y is primarily composed of HNO_3 and NO_x, produced mainly in the tropics by the photolysis of N_2O followed by oxidation (Murphy et al., 1993). The NO_y composition in the troposphere might differ considerably depending on sources/sinks, as well as region and altitude (see section 2.2.1 and 5.5). As obvious in the GRACE data, correlations between NO_y and O_3 are typically steeper in the troposphere than in the stratosphere (Murphy et al., 1993). The NO_y values of the "MR" data do not stand out from the remaining GRACE measurements, suggesting that although the air mass was influenced by anthropogenic pollution and hence, by emission of NO_x, the main part of the emitted NO_y did not reach high altitudes. This is in agreement with earlier studies which show that the export of NO_y from the boundary layer is not very efficient (Stohl et al., 2003; Koike et al., 2003; Nowak et al., 2004), mainly because of the removal of water-soluble HNO_3 due to precipitation processes. Furthermore, the polluted air mass resided a few days in the boundary layer before it ascended within the WCB (see section 6.4), which means that also dry deposition at the surface might have played a role.

Beyond HNO_3, PAN is the most dominant NO_y species found in aged pollution. In the region of weakest stratospheric influence (i. e. at highest CO), a maximum PAN/NO_y ratio of $\sim$0.3 is observed. This ratio is rather low, PAN/NO_y ratios of up to $\sim$0.85 have been measured in other CO plumes during GRACE (see section5.4.2), and ratios of $\sim$0.65 in aged Asian pollution (Nowak et al., 2004). PAN is not affected by dry deposition and survives the up-lift in a mid-latitude cyclone (Miyazaki et al., 2003), but it has a lifetime of only a few hours at the warm temperatures prevalent in the boundary layer (see section 2.2.2). The low PAN content therefore is very likely the result of thermal decomposition during the low-level transport in the first days after emission. PAN may reform especially during night-time. However, in the humid boundary layer the released NO_2 is efficiently oxidized to HNO_3 (e.g. Bradshaw et al. (2000)), especially during summer at these latitudes (see also model simulations in section 5.7). As discussed earlier, most of the HNO_3 in the WCB was presumably removed by wet deposition. Compared to the "MR" slopes, the regression lines of the "LMS" data are much steeper for all correlations. The CO values of up to 50 nmol mol^{-1}

are well above the stratospheric equilibrium value of 12 to 15 nmol mol^{-1} (Flocke et al., 1999) which suggests also for these air masses recent influence from the troposphere (e.g. Hoor et al. (2002, 2004),Tilmes et al. (2010)), but to a lesser extent. Compared to the tropospheric air mass mixed into the "MR", the tropospheric air in the "LMS" case contained much less H_2O, PAN and CO, but slightly higher NO_y and much higher CO_2.

6.6.2 Mixing of Asian pollution with Arctic stratospheric air

As discussed before, the polluted Asian air mass had already mixed with stratospheric air when it was probed by the Falcon, although some interleaved filaments were still observed (see section 6.2). An interesting question is of course, when and why did these air masses mix? As mentioned in section 6.4, most air parcels reached the 2 PVU level during the up-lift within the WCB, or later during the ascent at the leading edge of the upper level trough. It is possible that during this up-lift some mixing took place between the ascending Asian pollution and the lowermost stratospheric air located above, especially at the top of the lifted air mass. However, the main part of the mixing happened very likely during the period of cross-polar transport at elevated levels. As mentioned in section 6.5, the polar tropopause was vertically displaced during the passage of the tropospheric streamer. Temperature soundings from several weather stations (Eureka, Alert and Danmarkshavn, see red crosses in **Fig. 6.6g**) show an up-lift of the thermal tropopause of 2.5 to 3 km. This in turn implies that the polluted air mass was above ∼9 to 10 km embedded by stratospheric air from the Arctic, while it was advected across the pole. As discussed in section 6.5, the tropospheric streamer was elongated and stretched into long and narrow filaments during its journey. Therefore the most likely scenario is that horizontal shear induced mass exchange, and as a result, turbulent mixing across the air mass boundaries took place. As suggested by the "MR" in-situ data, O_3-rich and CO-poor stratospheric air masses were entrained at the boundaries of the polluted air mass. However, one has to keep in mind that our data only represent a "snap-shot" in the temporal evolution of 3-dimensional mixing events, documenting the mixing stage only at one location and one point in time. The role of radiation (cooling/heating) is not discussed here, but may be relevant due to the existence of clouds, or at least humidity differences.

Another point worth mentioning is that not only does the chemical composition change through entrainment of stratospheric air, but also thermo-dynamic properties. The polar-crossing WCB trajectories show for example a slight but continuous increase in potential temperature and PV, as do forward trajectories initialized from the locations of our observation. This possibly reflects the entrainment of warmer stratospheric air, at least to some extent, and this gain in Θ and PV suggests in turn that the pollution might have been completely mixed into the lowermost stratosphere.

Chapter 7

Conclusions and Outlook

The present thesis aimed to accomplish two primary objectives:

- to modify and characterize an isotopically calibrated airborne CI-ITMS system for fast and high accuracy measurements of PAN.
- to answer a number of scientific questions in relation to the Arctic nitrogen budget and pollution transport based on observations during the POLARCAT-GRACE campaign 2008, during which PAN measurements were conducted for the first time aboard the DLR Falcon research aircraft.

All these objectives were successfully achieved. In summary, the results of this thesis can be separated into three main parts:

1. An existing CI-ITMS instrument was modified in order to provide PAN measurements with a high time resolution of $\sim$2 s and a low detection limit of $\sim$25 pmol mol^{-1}. Due to the employment of a newly set-up isotopically labelled PAN calibration source, an accuracy of $\pm$10% for PAN mixing ratios greater than 200 pmol mol^{-1} was achieved. The new FASTPEX instrument (**Fast** Measurement of **Pe**rox**x**yacyl nitrates) was successfully deployed during 18 scientific flights within GRACE campaign 2008, and is described also in Roiger et al. (2011a).

2. The POLARCAT-GRACE measurements in summer 2008 showed that the Arctic free troposphere was quite heavily perturbed by the import of aged pollution, which originated mainly from boreal forest fires. This showed up not only in the presence of individual pollution plumes, but rather in a significantly enhanced background of the pollution tracers PAN and CO, being comparable or even higher than typically observed in the industrialized mid-latitudes. It is remarkable that the common notion of the Arctic troposphere being polluted in winter and spring season, and being clean in summer, is only true from the viewpoint of surface observations. This work has shown clearly, that in the summer season strongly polluted air masses are present in the Arctic troposphere, but only above 4 to 5 km, well separated from the boundary layer. In the free troposphere, PAN was observed to be the most dominant reactive nitrogen species, which is in good agreement with the only available earlier measurements conducted

in this region during the ABLE-3A and B campaigns 1988 (Singh et al., 1992b). Our in-situ measurements indicate low photochemical ozone formation inside the sampled biomass burning plumes. This is in good agreement with the results recently reported by (Alvarado et al., 2010), who used remote observations from the TES (**T**ropospheric **E**mission **S**pectrometer)[1] instrument to study the chemical evolution downstream of the fire regions. The observed low ozone formation is related to efficient conversion of primary emitted NO_x into PAN in fire emissions, which is highly stable at the low temperatures of the Arctic.

3. A detailed case study based on in-situ observations of the Falcon flight on 10 July 2008 showed that Asian surface emissions may reach the Arctic lowermost stratosphere within a few days, if being exported from the boundary layer within a strong warm conveyor belt (WCB). This is the first time experimental evidence was found for this transport pattern, which was already suggested by climatological studies. The results are also published in Roiger et al. (2011b).

In the following, the achievements of this thesis with respect to the three main results above are reviewed in some more detail. This is followed by an outlook summarizing next steps and recommendations for future work.

The new FASTPEX instrument

Due to its thermal instability, PAN cannot be stored in gas bottles. For this reason, a suitable PAN calibration source (PCS) first had to be set-up and characterized in detail. The new PCS uses a photolytic method for the in-situ production of PAN (Warneck and Zerbach, 1992). Nitrogen monoxide (NO) is efficiently converted to PAN via several reactions, initiated by the photolysis of acetone (CH_3COCH_3). A maximum NO to PAN conversion efficiency of $92\,(\pm 5)\,\%$ was reached, which is comparable to similar photolytic PAN sources described in the literature (Volz-Thomas et al., 2002; Flocke et al., 2005b). For permanent in-flight calibrations during ambient measurements, the PCS is supplied with isotopically labelled ^{13}C-acetone (instead of ambient ^{12}C-acetone).
For the first time, the I^-- chemistry for the measurement of PAN was coupled with an ion trap mass spectrometer (ITMS). Ion trap mass spectrometers offer certain advantages, such as for example a high mass resolution of $\sim$0.3 amu, which leads to an unambiguous detection of neighboring mass peaks. This is especially important if an isotopic calibration is used as in the present work, since in this case the calibration peak is generally only one or two mass units apart from the ambient mass peak (dependent on the isotope used).
The FASTPEX system was tested in the laboratory by optimizing the ion-molecule reaction (using I^- reagent ions) and the parameters of the ITMS for a high time resolution and low detection limit. Pre- and post campaign laboratory experiments were conducted in order to study the selectivity of the used ion detection scheme. These showed that the PAN measurements did not suffer from cross-sensitivities to other main constituents of the atmosphere, such as for example ozone, acetic acid or nitrogen oxides.

[1] TES is an infrared spectrometer flying aboard the Aura satellite

During GRACE, the isotopic standard turned out to be especially important to account for the water vapor dependence of the PAN sensitivity, as well as for the high reactivity of the product ion. Two different kinds of in-flight background determinations were performed regularly. No trends in different types of air masses or any other drifts have been observed. An in-flight intercomparison during the GRACE campaign 2008 showed good agreement within the combined measurement uncertainties between the PAN measurements of the FASTPEX instrument aboard the Falcon, and a similar CIMS measurement system aboard the NASA DC8 (equipped with an linear quadrupole mass spectrometer).

The ion detection scheme used in this work allows for the simultaneous detection of higher homologues of the PAN family, such as PPN (peroxypropionyl nitrate). The PPN measurement is complicated due to a water-vapor dependent background, which was accounted for with an empirically derived correction. The obtained PPN mole fractions were most of the time close to the detection limit, but for polluted situations it is possible to determine accurate PPN/PAN ratios: In an aged Siberian biomass burning plume, the observed ratio of 0.11 was much lower than the PPN/PAN ratio of 0.18 measured in fresh anthropogenic pollution over southern Germany. This points to different hydrocarbon precursors involved in photochemistry. Future work should focus on calibration of PPN and higher homologues as a function of ambient water vapor, in order to provide also high-accuracy measurements of other PAN-type compounds.

Influence of imported pollution on the chemical composition of the summer time Arctic free troposphere

The GRACE field deployment of the DLR Falcon research aircraft was a German contribution to the POLARCAT (**Pol**ar study using **a**ircraft, **r**emote sensing, surface measurements and modelling of **c**limate, chemistry, **a**erosols and **t**ransport) activity, a core project of the International Polar Year (IPY) in 2007 and 2008. During GRACE (30 June–18 July 2008), the DLR Falcon was based in Kangerlussuaq, Greenland (67.01° N, 50.7° W). A total of 15 local flights were performed, covering latitudes from 57° N to 81.5° N, longitudes from 66° W to 16° E and altitudes up to 11.8 km. In-situ observations showed that the free troposphere ($\sim$ 4 - 9 km) contained elevated concentrations of pollution tracers such as PAN and CO.

A combined analysis using in-situ measurements and the FLEXPART transport model showed that the Arctic free troposphere was impacted mainly by aged biomass burning emissions from the boreal fire regions in Canada and eastern Siberia. Surprisingly, the pollution influence from Siberian fires was as important than those from the much closer fire regions in Saskatchewan (Canada). The main part of the pollution from the Asian continent was transported directly across the North Pole into the European sector of the Arctic, associated with Arctic low-pressure systems. Conditions during GRACE campaign can be classified as quite typical: The summer 2008 showed in general low to moderate biomass burning activity in Canada (van der Werf et al., 2010; Singh et al., 2010), but high fire activity in the northern part of the province Saskatchewan (Soja et al., 2008). In Siberia, boreal fires burned mainly in the eastern regions, and were the most intense ones since the record-breaking year in 2003 (van der Werf et al., 2010). Detailed analyses showed that during the

summer period 2008, meteorological conditions over the northern hemisphere were quite close to climatological average (Fuelberg et al., 2010).

A series of prominent pollution plumes was encountered by the Falcon having typical CO mixing ratios of ∼200 nmol mol^{-1}. However, imported emissions were found to be more or less mixed into the Arctic also on much larger scales: CO background values were about ∼40 nmol mol^{-1} higher in the free troposphere than in the boundary layer. In this altitude region, median values of CO were even ∼20 nmol mol^{-1} higher than those observed during the CONTRACE[2] campaign, which was conducted in the industrialized mid-latitudes of western Europe in spring 2003. During GRACE, PAN was abundant at average mixing ratios of ∼300 pmol mol^{-1} in the free troposphere, where it was the dominant NO_y compound (∼50 - 60%). Nitrogen monoxide (NO) however was present only at low mixing ratios of several pmol mol^{-1}.

According to the Lagrangian particle dispersion model FLEXPART, biomass burning plumes from Siberia also often contained mixed-in urban pollution from East Asia, whereas plumes originating in Canada typically carried only emissions from forest fires. These FLEXPART results however cannot be validated by our in-situ measurements, because the Falcon measured neither a direct tracer for anthropogenic emissions (e. g. SF_6), nor for biomass burning pollution (e. g. HCN, CH_3CN). As derived with analyses from the FLEXPART model, transport times for pollution plumes to Greenland were 5 - 10 days for emissions originating from North America, compared to 10 - 20 days for those arriving from Siberia/Asia.

The chemical composition did not differ significantly in plumes from the two different source regions (e. g. PAN vs. CO, PAN/NO_y ratios), and PAN/CO enhancement ratios in distinct biomass burning plumes (2.61 ± 0.36) were found to be consistently lower than those reported from earlier studies focusing on younger forest fire plumes (< 5 days). A possible explanation is the much stronger dilution of the aged plumes with surrounding PAN-poor air masses during the comparatively long transport time to Greenland. Polluted air masses were often found in close proximity to UTLS air masses, which might be explained by the fact that stratospheric intrusions frequently occur within the same mid-latitude cyclone in which emission are vented from the boundary layer.

O_3-CO correlation analyses of distinct fire plumes suggest that photochemical ozone production was generally low. This is in good agreement with other measurements conducted in the framework of POLARCAT. Alvarado et al. (2010) reports from rapid conversion of nitrogen oxides into PAN in fresh fire emissions, which suppresses ozone formation in young plumes. The GRACE observations of small NO mixing ratios in combination with the measured high fraction of PAN suggests that ozone formation during transport to Greenland was NO_x-limited. At the cold temperatures of the Arctic, NO_x is efficiently conserved in the temporary reservoir species PAN.

The ozone production potential of sampled forest fire plumes subsiding downstream of Greenland was studied exemplary for one case with the help of a Lagrangian box model (CiTTyCaT). NO_x released due to PAN thermolysis was found to induce if any, only very small net photochemical O_3 production, especially if the air mass descends into the humid boundary layer where photochemical

[2] **Con**vective Transport of **Trac**e Gases into the Middle and Upper Troposphere over **E**urope: Budget and Impact on Chemistry

O_3 destruction is especially efficient. It is however important to note that NO_x input from PAN decomposition at least slows down photochemical O_3 destruction. Future simulations with the TOMCAT model (**T**oulouse **O**ff-line **M**odel of **C**hemistry **a**nd **T**ransport) will help to evaluate the large scale effect of PAN thermolysis on ozone concentrations in remote regions.

Case study of Asian pollution transport into the Arctic lowermost stratosphere

Using FLEXPART forecasts, the Falcon probed on the 10th July flight an air mass containing unusually high CO and PAN mixing ratios of 138 nmol mol^{-1} and 330 pmol mol^{-1} in the Arctic tropopause region at 11.3 km, $\sim$800 m above the dynamical tropopause (2 PVU). In-situ tracer correlations and FLEXPART backward simulations confirmed that the Falcon sampled the topmost part of an air mass with recent tropospheric origin, containing anthropogenic pollution from East Asia mixed with O_3-rich stratospheric air. A detailed trajectory analysis suggests that the Asian pollution was up-lifted within a warm conveyor belt (WCB) which was associated with a low pressure system over Northern Russia. The analysis also showed that 92 % of the pole-crossing WCB trajectories reached the dynamical tropopause, mainly within the WCB ascent or shortly later. A part of the Asian pollution was embedded in a tropospheric streamer, which subsequently was advected across the pole. During its journey, the top of the polluted air mass was surrounded by Arctic stratospheric air. Mixing most likely took place laterally along the sides of the plume, when the tropospheric streamer was stretched into long and narrow filaments. A correlation analysis of tracer concentrations indicated that the polluted tropospheric air mass was enriched mainly in CO, CO_2 and H_2O before it was mixed into the stratosphere, whereas PAN and NO_y have been efficiently removed before and during the up-lift within the WCB. While the wet removal of HNO_3 is a common occurrence in the discussed transport pathway, PAN generally has the potential to reach the tropopause region within WCB ascents, if the up-lift is not preceded by multi-day-transport in the warm boundary layer as in this case.

Outlook

This thesis presented the first in-situ measurement of WCB-lifted Asian pollution being stirred and finally irreversibly mixed into the polar lowermost stratosphere. In the context of these observations several questions arise: is this transport process a common scenario that brings pollution to the polar lowermost stratosphere? What are the consequences on the chemical and radiative budget? And how relevant are these transport patterns in the context of climate change, and rising Asian emissions? The planned DLR measurement campaign HYMEX-NADEX (**Hy**drological cycle in the **m**editerranean **ex**periment - **N**orth **A**tlantic Waveguide and **D**ownstream impact **ex**periment) will focus on some of these aspects. HYMEX-NADEX will be conducted in fall 2012 and aims to investigate the efficiency of trace gas transport within WCBs. Air masses with different boundary layer conditions therefore will be probed before, during and after being up-lifted within WCBs in order to analyze the influence of starting conditions on the WCB development.

The GRACE in-situ measurements will be further used for the validation of 3D CTM models within the POLMIP project (**POL**ARCAT **M**odel **I**ntercom**p**arison). First comparisons of a range of 3D chemistry - transport models (CTMs) with a particular focus on Arctic tropospheric composition showed a large difference between the model´s NO_y budgets (Sarah Monks, University of Leeds, personal communication). A particular large spread was observed in the partitioning between HNO_3 and PAN, which is attributed to differences in the hydrocarbon emission and chemistry schemes of the models. The aircraft measurements will be useful to help to compare the CTMs with a hope of understanding these model differences. After improving the emission and chemistry schemes, the TOMCAT model will be used to study the sensitivity of ozone production to PAN mixing ratios, and the large-scale influence of PAN decomposition on ozone mixing ratios.
Pollution from the Asian continent was observed to be regularly transported across the Pole into the European sector of the Arctic, which is associated with Arctic low-pressure systems. Such cyclone events in the proximity of the North Pole are regular phenomena of the polar circulation, especially during summer (Serreze and Barrett, 2008; Orsolini and Sorteberg, 2009). Future Arctic measurement activities therefore should try to cover even higher latitudes of the Arctic in summer, which would require a campaign base farther north (e. g. Spitsbergen). The scientific payload should be extended to measure also direct tracers for industrial pollution, such as SF_6, and/or biomass burning emissions, like HCN or CH_3CN. This would help to distinguish between anthropogenic and forest fire pollution, and allow for a more detailed validation of the FLEXPART model.

PAN measurements are not only relevant for Arctic science questions. Therefore, DLR plans further deployments of the FASTPEX instrument which in the meantime was configured and certified for application on the new German research aircraft HALO (**H**igh **A**ltitude and **Lo**ng Range). For instance, PAN measurements are essential for the scientific objectives of one of the first HALO missions, the OMO (**O**xidation **M**echanism **O**bservations) campaign. OMO will take place in 2013 and aims to determine the oxidation rates of natural and anthropogenic emissions in the upper troposphere. A key question is the influence of transport and local photochemistry on radical chemistry: What are the differences in different types of air masses, which are influenced either by convective pollution (i. e. high VOCs/NO_x), by intercontinental pollutant transport (i. e. moderate VOCs/NO_x) or by lightning (i. e. low VOCs/high NO_x)?

Appendix A

Appendix

A1. Potential vorticity

The potential vorticity (PV) is the absolute circulation of an air parcel that is enclosed between two isentropic surfaces, and is given in PVU (Potential Vorticity Units, $10^{-6}\,\mathrm{m^2\,K\,s^{-1}\,kg^{-1}}$). PV is the product of absolute vorticity on an isentropic surface and static stability.

$$PV = \frac{1}{\varphi}(\vec{\nabla} \times \vec{v} + 2\vec{\Omega})\vec{\nabla}\Theta\,. \tag{A.1}$$

where φ is the air density, v the wind speeds, Ω the rotation of the Earth and Θ the potential temperature (see also section A.6). In the atmosphere, PV is a conserved quantity in the absence of adiabatic and frictionless processes. Due to the high static stability in the stratosphere, the PV gradient shows a sharp increase across the tropopause. A PV threshold value thus can be utilized for the definition of the dynamic tropopause, with values ranging between 1.6 to 3.5 PVU. As most other studies, the present work uses a value of 2 PVU. For more details see e. g. (Holton et al., 1995).

A2. Critical orifice

Critical orifices are a reliable tool to control flow rates while offering certain advantages: They are compact, robust, accurate and inexpensive. In the simplest case, a critical orifice is a thin plate with a hole in the middle, or it consists of a smooth rounded inlet section converging to a minimum throat area. A constant volume flow rate is ensured through the orifice, if the upstream pressure is constant and the downstream pressure is less than 0.53 of the upstream pressure. The critical orifice then is operated under "sonic state conditions". Under these conditions the velocity in the throat is the speed of sound, and a further reduction in the downstream pressure does not increase the flow velocity through the throat. The mass flow rate the linearly depends on the upstream pressure p

and the diameter A of the critical orifice. It is given by

$$q_m = Ap\left(\frac{2}{\kappa+1}\right)^{\frac{1}{\kappa-1}}\left(\frac{2\kappa}{\kappa+1}\frac{M}{RT}\right)^{\frac{1}{2}} \tag{A.2}$$

where κ represents the isentropic exponent ($\kappa=\frac{C_p}{C_v}$), M the molar mass, R the universal gas constant and T the ambient temperature. For more details see e. g. (Wutz et al., 1988).

A3. In-flight background determinations

Figure A.1 summarizes all GRACE in-flight background determinations. The upper panel shows the background values of the ion intensity at mass 59 amu, and the lower panel those of mass 61 amu.

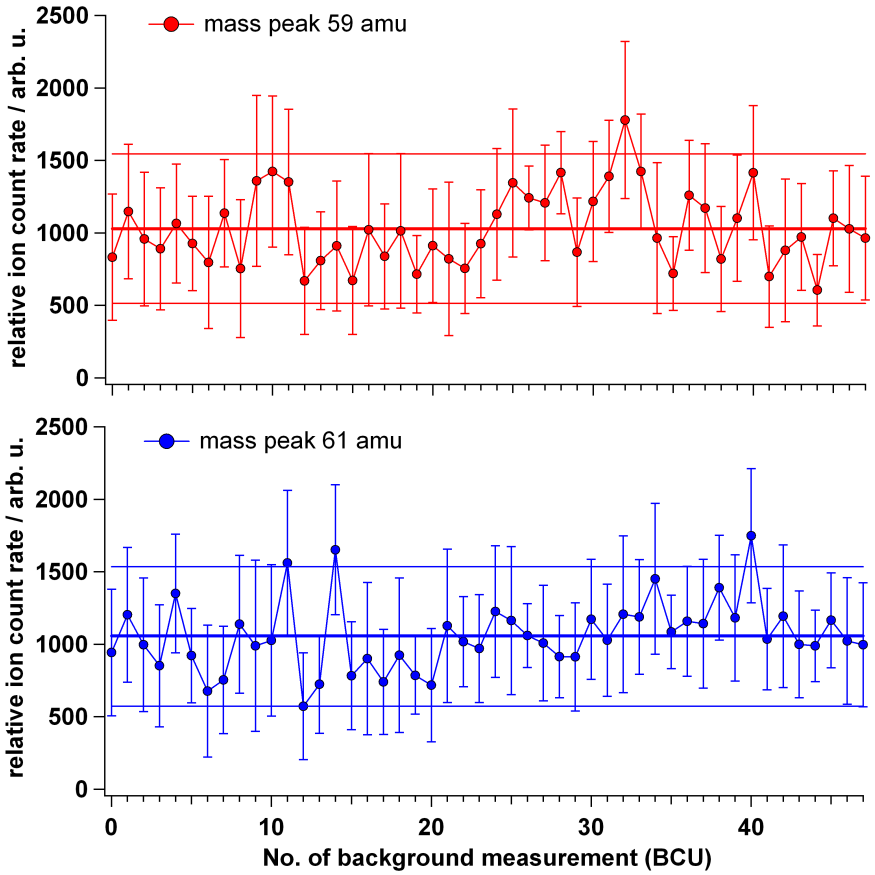

Figure A.1: *Instrumental background at mass 59 amu (upper panel) and 61 amu (lower panel) as derived from all in-flight background calibrations. The vertical error bars indicate the standard deviation of each single background determination. The thick lines represent the mean of all calibrations, whereas the thin lines indicate the standard deviation calculated from all mean background values.*

A4. Measurement uncertainty of FASTPEX

The ambient PAN mixing ratio is calculated via equation A.3 (see also equation 4.4). Basically, the signal of the isotopically labelled PAN standard is multiplied with a scaling factor B:

$$C_a = C_{ILS} \times B\,. \tag{A.3}$$

C_{ILS} represents the PAN mixing ratio C_{PAN} which is produced in the PAN calibration source (see equation 4.2). The PCS flow Q_{PCS} (Q_{PCS}=Q_{NO}+$Q_{acetone}$) is diluted with the total sample flow Q_s:

$$C_{ILS} = C_{PAN} \times \frac{Q_{PCS}}{Q_S} = \frac{Q_{NO} \times NO_b \times CE_{PCS}}{Q_s}\,. \tag{A.4}$$

The scaling factor B is given by (see equation 4.5):

$$B = \frac{K_{ss} \times R - K_{as}}{K_{aa} - K_{sa} \times R}\,. \tag{A.5}$$

The total accuracy of FASTPEX $\triangle_{FASTPEX}$ comprises the uncertainty of the isotopically labelled standard $\triangle_{ILS}$, as well as the error of the scaling factor B, $\triangle_B$:

$$\triangle_{FASTPEX} = \triangle_{ILS} + \triangle_B\,. \tag{A.6}$$

Using the Gaussian error propagation, $\triangle_{ILS}$ is given by:

$$\triangle_{ILS} = \sqrt{(\frac{\delta PAN}{\delta Q_{NO}}\triangle Q_{NO})^2 + (\frac{\delta PAN}{\delta NO_b}\triangle NO_b)^2 + (\frac{\delta PAN}{CE_{PCS}}\triangle CE_{PCS})^2 + (\frac{\delta PAN}{\delta Q_s}\triangle Q_s)^2}\,. \tag{A.7}$$

$$\begin{aligned}\triangle_{ILS} = ((\frac{NO_b \times CE_{PCS}}{Q_s} \times \triangle Q_{NO})^2 + (\frac{Q_{NO} \times CE_{PCS}}{Q_s} \times \triangle NO_b)^2 + \ldots \\ \ldots + (\frac{Q_{NO} \times NO_b}{Q_s} \times \triangle CE_{PCS})^2 + (\frac{Q_{NO} \times NO_b \times CE_{PCS}}{Q_s^2} \times \triangle Q_s)^2)^{\frac{1}{2}}\,.\end{aligned} \tag{A.8}$$

The uncertainty of the scaling factor B, $\triangle_B$, is calculated with:

$$\triangle_B = \sqrt{(\frac{\delta B}{\delta S_{59}}\triangle S_{59})^2 + (\frac{\delta B}{\delta S_{61}}\triangle S_{61})^2 + (\frac{\delta B}{BG_{59}}\triangle BG_{59})^2 + (\frac{\delta B}{\delta BG_{61}}\triangle BG_{61})^2}\,. \tag{A.9}$$

$$\triangle_B = ((\frac{1}{0.9731 \times (S_{61} - UG_{61})} \times \sqrt{S_{59}})^2 + (\frac{(S_{59} - UG_{59})}{0.9731 \times (S_{61} - UG_{61})^2} \times \sqrt{S_{61}})^2 + \ldots \quad \text{(A.10)}$$
$$\ldots + (\frac{1}{0.9731 \times (S_{61} - UG_{61})} \times \triangle UG_{59})^2 + (\frac{(S_{59} - UG_{59})}{0.9731 \times (S_{61} - UG_{61})} \times \triangle UG_{61})^2)^{\frac{1}{2}} .$$

The resulting total uncertainty under typical measurement conditions is illustrated in **Fig. 4.21.**

A5. Blue light converter(BLC)

The blue light converter is a nitrogen dioxide converter using LED´s (light emitting diodes) as a light source in order to achieve an interference-free conversion of NO_2 into NO at high efficiency. Interferences to other nitrogen compounds are minimized because the light source emits only in a narrow spectral band. In addition, the short residence time of only $\sim$1 s in the measurement cell minimizes the cross-sensitivity to PAN due to thermal dissociation of PAN into peroxyacetyl radicals and NO_2. **Figure A.2** gives the absorption cross sections of relevant nitrogen species. Also indicated is the approximate output wavelength region of the LED´s. In this region, the absorption cross section of NO_2 (σ_{NO_2}) is relatively high, whereas HONO and NO_3 do not absorb significantly. For more details see http://www.metcon.com.

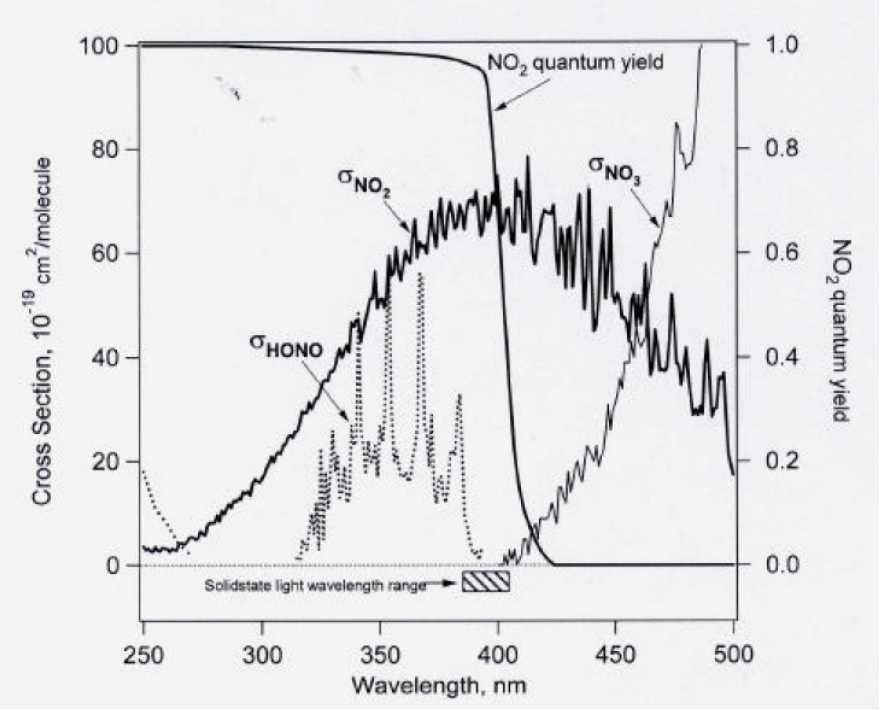

Figure A.2: *Absorption cross sections of HONO (dotted line), NO_2 (thick line) and NO_3 (thin line) as a function of wavelength (250 - 500 nm), along with the NO_2 quantum yield. Also indicated is the approximate output wavelength range of the BLC light source ($\sim$ 380 - 405 nm).*

A6. Mean vertical distribution of potential temperature Θ during GRACE

The potential temperature Θ is defined as the temperature an air parcel with temperature T and pressure p would acquire, if adiabatically brought down to the surface ($p_0 = 1000\,\mathrm{hPa}$):

$$\Theta = T \left(\frac{p_0}{p} \right)^{\frac{\kappa-1}{\kappa}} . \tag{A.11}$$

κ denotes the isentropic exponent ($\kappa = \frac{C_p}{C_v}$). Θ is a useful meteorological tracer: In the absence of diabatic processes (such as latent heat release, sensible heating, or the absorption and emission of long and short wave radiation), an air parcel will be transported along constant isentropic surfaces - not across them. Note however that throughout most of the free troposphere slow radiational cooling decreases Θ by about 1 K/day. **Figure A.3** shows the mean vertical distribution of Θ as obtained from all local GRACE flights. Under stable stratified conditions, Θ increases with height. Due to the higher static stability in the stratosphere, the potential temperature increases even stronger above the tropopause.

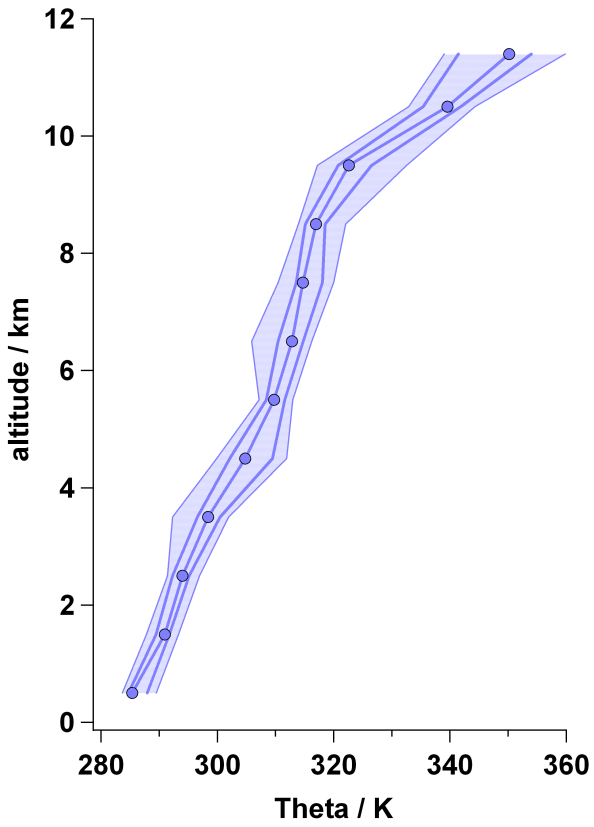

Figure A.3: *Vertical distribution of potential temperature Θ during GRACE campaign. The profiles were calculated from data of all 15 GRACE flights, each for 1-km altitude bins. Given are median (thick line plus markers), upper and lower quartiles (thick lines) as well as 10th/90th percentiles (thin lines).*

A7. Chemical properties of BB plumes sampled during GRACE

As discussed in section 5, the Arctic troposphere was influenced by pollution plumes originating from Canada and Siberia. In order to discuss similarities and/or differences in the chemical composition of pollution from different source regions, the most prominent plumes were selected and analyzed. The plumes first had to be separated from the generally enhanced CO background, which also varied strongly with height (**see Fig. 5.8a**). A pollution episode was defined as "plume" when the CO mixing ratio was higher than the 75th-percentile of the corresponding altitude bin. Most of the plumes were encountered on horizontal legs, in this case the CO value had to stay for at least 50 km above the defined CO limit. With this prerequisite, 29 distinct plumes were selected from all data of the 15 local GRACE flights. The plumes were classified with the help of FLEXPART analysis data. The FLEXPART model captured most of the plumes quite well. Source region, age and approximate contribution of anthropogenic emissions were determined for each plume. Main differences between the pollution plumes originating from the two source regions Canada and Siberia were found for plume ages and the anthropogenic fraction. Siberian plumes on average were found to be ∼1 week older when they were probed by the Falcon. This can be attributed to the much larger distance to our measurement area. Asian plumes most of the time were found to carry not only biomass burning emissions, but also anthropogenic pollution.
Table A.1 summarizes the properties of all sampled plumes, including average (±std) values for the measured trace gas species. The mean trace gas concentrations varied from plume to plume, but there no obvious trend with different source regions was found. The differences in emission ratios certainly are driven more by the fire-to-fire variability due to changing burning conditions (smoldering vs. flaming), than due to different fuel types. Possibly slightly different emission ratios might have been smeared out due to dilution into the Arctic background.

A8. Composite satellite images

The Antarctic Meteorological Research Center (AMRC) provides Arctic composite satellite images every three hours, creating a total of eight images per day (Lazzara, 2011). Geostationary and polar-orbiting satellites are used to generate the composite and, depending on the geographical location, can include observations from the following: Polar Orbiting Environmental Satellite (POES), Geostationary Operational Environmental Satellites (GOES-East and GOES–West), Meteosat, Multifunction Transport Satellite (MTSAT-1R), Feng Yun-2 (FY-2), Kalpana-1, and Terra/Aqua. The source observations that are used in the composite are within plus or minus 50 min to the top of the synoptic hour, although most of the observations fall within a plus or minus 15-min window. The imagery has the space background removed, and the data remapped into a polar stereographic projection. The data are merged with the geostationary observations combined first, followed by the polar orbiting observations. In general terms, the composite satellite images depict the temperature of the Earth as seen by the imagers on board the satellites, which measure the intensity of the radiation emitted by the Earth at approximately 11.0 μm, the infra-red window channel. The images are colour enhanced such that yellow and red colours highlight the cold upper-level cloud tops,

green colours underscore the tops of the warmer mid-level and low-level clouds, and blue colours are the much warmer surface of the Earth. In the present paper, the composites are combined with overlays of the FLEXPART Asian anthropogenic CO tracer fields. The passive CO tracers with a lifetime of 20 days were obtained from the FLEXPART forward model runs (see section 5.2.2) and are represented in the satellite images by white contour lines.

Table A.1: *Plume origin and selected properties of all sampled biomass burning plumes.*

plume ID	origin	age (days)	altitude (m)	anthrop. contrib.	CO (nmol mol^{-1})	O_3 (nmol mol^{-1})	CO_2 (μmol mol^{-1})	NO (pmol mol^{-1})	PAN (pmol mol^{-1})	NO_y (pmol mol^{-1})
04a-1	Canada	3-5	4870	∼50%	129.3±9.6(702)	50.3±9.4(702)	382.8±0.7(702)	below DL	421±55(123)	730±141(535)
07a-1	Canada	5-6	7910	none	160.6±7.8(494)	38.4±3.3(494)	378.2±0.6(494)	below DL	329±32(248)	485±43(300)
07a-2	Canada	3-6	7910	none	160.2±8(238)	43.6±6.4(238)	380.0±1.2(164)	below DL	376±35(238)	570±51(206)
07a-3	Canada	5-6	7760	none	152.9±6.9(890)	39.1±5.5(1024)	377.9±1.6(930)	below DL	351±41(515)	580±58(812)
07a-4	Canada	6	7910	none	164.2±6.2(304)	44.5±3.5(304)	379.5±0.5(304)	below DL	390±35(152)	654±17(302)
08a-1	Canada	6-9	6320-7700	∼50%	135.8±7.8(202)	64.3±5.2(202)	382.7±0.2(114)	below DL	337±62(178)	753±86(202)
08a-2	Canada	3-6	7270-6910	none	148.0±4.5(450)	46.8±7.5(450)	378.5±0.9(310)	below DL	327±28(123)	578±36(298)
08a-3	Canada	4-7	7790	none	153.5±2.3(347)	40.9±1.9(347)	378.4±0.6(347)	below DL	330±26(185)	573±29(347)
09a-1	Canada	6-8	5800	none	145.4±5.8(1025)	55.1±2.5(1025)	382.0±0.4(1025)	below DL	381±42(364)	771±60(801)
09a-2	Canada	8-11	5780	none	137.3±4.6(268)	63.7±4.8(268)	382.2±0.4(268)	below DL	378±26(107)	707±57(268)
09b-1	Canada	5-8	7910	none	150.1±9.2(1446)	69.2±3.6(1446)	381.1±0.3(1362)	below DL	420±37(701)	655±59(1044)
09b-2	Asia	8-11	7910	∼15%	158.7±4(654)	93.6±7.8(654)	381.2±0.3(654)	20±8(510)	435±29(327)	910±95(510)
09b-3	Asia	7-10	7910	∼20%	180.0±10.2(1124)	80.7±2.2(1124)	380.5±0.3(1004)	22±4(924)	470±40(527)	1034±78(942)
09b-4	Asia	10-15	7910	∼50%	271.1±24.1(544)	86.6±2.1(544)	381.0±0.4(544)	17±5(440)	690±70(272)	1435±69(440)
09b-5	Asia	7-9	7860-7080	none	318.7±26.9(108)	86.6±2.8(108)	380.7±0.3(108)	38±2(44)	844±100(108)	1976±100(96)
09b-6	Canada	6-9	7300	∼25%	158.8±6.2(370)	75.7±6.4(370)	381.3±0.2(334)	19±8(542)	504±34(544)	1018±200(540)
09b-7	Asia	7-10	9120	∼20%	165.1±4.6(682)	71.4±2.6(682)	381.1±0.2(682)	below DL	337±45(123)	611±52(123)
10a-1[a]	Asia	7-9	11260	∼95%	102.1±12.8(607)	203±51(607)	384.3±0.5(607)	81±33(451)	197±22(256)	1414±280(451)
10a-2	–	–	9160-7910	–	150.2±8.5(203)	64.1±24.6(203)	381.4±0.8(203)	below DL	337±45(123)	1157±438(171)
10a-3	–	–	7910	–	174.1±13.2(466)	74.7±4.5(466)	381.1±0.5(326)	below DL	485±59(241)	878±89(413)
10a-4	Asia	8-11	7910	∼10%	161.9±4.9(465)	85.4±5.3(465)	380.7±0.4(465)	below DL	473±34(176)	843±59(465)
12a-1	Asia	11-15	5600-3500	∼25%	150.1±40.7(2004)	66.7±6.1(2004)	380.7±0.7(1584)	below DL	369±49(292)	520±51(1536)
13a-1	Asia	11-15	5000-5600	∼20%	144.9±11.4(184)	60.6±2.2(184)	381.3±0.2(184)	below DL	305±47(25)	468±23(145)
13b-2	–	–	7440-6220	–	152.3±19.5(146)	88.3±3.5(146)	382.2±0.6(146)	below DL	333±31(73)	705±37(123)
14b-1	Asia	7-10	9120	∼50%	147.2±9.0(432)	96.5±10.4(432)	382.3±0.3(432)	26±6(290)	384±29(216)	996±64(290)
15b-1	Asia	7-9	8520	∼10%	144.3±10.4(226)	110.0±7.6(226)	381.1±0.1(226)	16±2(68)	377±27(123)	855±22(68)
15b-2	Asia	15-20	6930-6120	none	139.2±9.2(1078)	81.0±3.2(1078)	381.3±0.2(850)	below DL	304±26(489)	515±24(794)
15b-3	Asia	15-20	8210	∼20%	138.2±5.4(420)	76.4±4.0(420)	382.5±0.2(420)	below DL	277±22(268)	490±26(280)
17a-1	Asia	15-20	5770	∼25%	140.0±13.8(381)	73.0±5.4(381)	380.8±0.3(381)	16±2(381)	271±22(190)	507±23(381)

[a]Anthropogenic plume in UTLS, see section 6

Abbreviations

Abbreviation	Description
ABL	**A**tmospheric **B**oundary **L**ayer
ACIMS	**A**ctive **C**hemical **I**onization **M**ass **S**pectrometry
BB	**B**iomass **B**urning
CiTTyCaT	**C**ambr**i**dge **T**roposperic **T**rajecto**y** model of **C**hemistry **a**nd **T**ransport
CI - ITMS	**C**hemical **I**onization – **I**on **T**rap **M**ass **S**pectrometer
CIMS	**C**hemical **I**onization **M**ass **S**pectrometry
DLR	**D**eutsches Zentrum für **L**uft- und **R**aumfahrt
ECMWF	**E**uropean **C**entre for **M**edium-Range **W**eather **F**orecasting
FASTPEX	**Fast** Measurement of **Pe**rox**y**acyl nitrates
FLEXPART	Lagrangian particle dispersion model
FLEXTRA	Lagrangian trajectory model
FT	**F**ree **T**roposphere
GRACE	**Gr**eenland **A**erosol and **C**hemistry **E**xperiment
IASI	**I**nfrared **A**tmospheric **S**ounding **I**nterferometer
IPA	**I**nstitut für **P**hysik der **A**tmosphäre
ITMS	**I**on **T**rap **M**ass **S**pectrometer
LRT	**L**ong-**R**ange **T**ransport
MBL	**M**arine **B**oundary **L**ayer
MODIS	**Mod**erate Resolution **I**maging **S**pectroradiometer
NASA	**N**ational **A**eronautics and **S**pace **A**dministration
PACIMS	**P**assive **C**hemical **I**onization **M**ass **S**pectrometry
PAN	**P**eroxy**a**cetyl **n**itrate
PFA	**P**erfluoro**a**lkoxy
POLARCAT	**POL**ar study using **A**ircraft, **R**emote sensing, surface measurements and modeling of **C**limate, chemistry, **A**erosols and **T**ransport
sccm	**s**tandard **c**ubic **c**m per **m**inute
slm	**s**tandard **l**iter per **m**inute
TOMCAT	**T**oulouse **O**ff-line **M**odel of **C**hemistry **A**nd **T**ransport
UTLS	**u**pper **t**roposphere/**l**owermost **s**tratosphere
VOC	**v**olatile **o**rganic **c**ompounds

List of Figures

List of Tables

Bibliography

Altshuller, A. (1993). PANs in the atmosphere. *J. Air Waste Manege.*, 43:1221–1230.

Alvarado, M. J., Logan, J. A., Mao, J., Apel, E., Riemer, D., Blake, D., Cohen, R. C., Min, K.-E., Perring, A. E., Browne, E. C., Wooldridge, P. J., Diskin, G. S., Sachse, G. W., Fuelberg, H., Sessions, W. R., Harrigan, D. L., Huey, G., Liao, J., Case-Hanks, A., Jimenez, J. L., Cubison, M. J., Vay, S. A., Weinheimer, A. J., Knapp, D. J., Montzka, D. D., Flocke, F. M., Pollack, I. B., Wennberg, P. O., Kurten, A., Crounse, J., Clair, J. M. S., Wisthaler, A., Mikoviny, T., Yantosca, R. M., Carouge, C. C., and Le Sager, P. (2010). Nitrogen oxides and PAN in plumes from boreal fires during ARCTAS-B and their impact on ozone: an integrated analysis of aircraft and satellite observations. *Atmospheric Chemistry and Physics*, 10(20):9739–9760.

Andreae, M. O. and Merlet, P. (2001). Emission of trace gases and aerosols from biomass burning. *Global Biogeochem. Cycles*, 15(4):955–966.

Arnold, F., Böhringer, H., and Henschen, G. (1978). Composition measurements of stratospheric positive ions. *Geophys. Res. Lett.*, 5:653–655.

Arnold, F. and Fabian, R. (1980). First measurements of gas phase sulfuric acid in the stratosphere. *Nature*, 283:55–57.

Arnold, F. and Hauck, G. (1985). Lower stratosphere trace gas detection using aircraft-borne active chemical ionization mass spectrometry. *Nature*, 315(6017):307–309.

Arnold, S. R., Methven, J., Evans, M. J., Chipperfield, M. P., Lewis, A. C., Hopkins, J. R., McQuaid, J. B., Watson, N., Purvis, R. M., Lee, J. D., Atlas, E. L., Blake, D. R., and Rappenglück, B. (2007). Statistical inference of OH concentrations and air mass dilution rates from successive observations of nonmethane hydrocarbons in single air masses. *J. Geophys. Res.*, 112(D10):D10S40–.

Atkinson, R., Baulch, D. L., Cox, R. A., Crowley, J. N., Hampson, R. F., Hynes, R. G., Jenkin, M. E., Rossi, M. J., and Troe, J. (2004). Evaluated kinetic and photochemical data for atmospheric chemistry: Volume I - gas phase reactions of O_x, HO_x, NO_x and SO_x species. *Atmospheric Chemistry and Physics*, 4(6):1461–1738.

Atkinson, R., Baulch, D. L., Cox, R. A., Crowley, J. N., Hampson, R. F., Hynes, R. G., Jenkin, M. E., Rossi, M. J., Troe, J., and Subcommittee, I. (2006). Evaluated kinetic and photochemical

data for atmospheric chemistry: Volume II - gas phase reactions of organic species. *Atmospheric Chemistry and Physics*, 6(11):3625–4055.

Auby, A., Lax, K. S., Ravetta, F., Bauer, S., Schlager, H., Roiger, A., Pommier, M., Turquety, S., and Szopa, S. (2010). Estimations of free tropospheric mixing rates in the arctic using lagrangian reconstructions. Poster. IGAC conference.

Aufmhoff, H., Hanke, M., Uecker, J., Schlager, H., and Arnold, F. (2011). Atmospheric measurements of gaseous sulfuric acid and OH: Deployment of an Ion Trap CIMS-instrument. *Intern. Journal of Mass Spectrometry*, in press.

Bandy, A. R., Thornton, D., and Driedger, A. (1993). Airborne measurements of sulfur dioxide, dimethyl sulfide carbon disulfide, and carbonyl sulfide by isotope dilution gas chromatography/mass spectrometry. *Journal of Geophysical Research*, 98:23423–23433.

Bond, T. C., Streets, D. G., Yarber, K. F., Nelson, S. M., Woo, J.-H., and Klimont, Z. (2004). A technology-based global inventory of black and organic carbon emissions from combustion. *J. Geophys. Res.*, 109(D14):D14203–.

Bönisch, H., Engel, A., Curtius, J., Birner, T., and Hoor, P. (2009). Quantifying transport into the lowermost stratosphere using simultaneous in-situ measurements of SF_6 and CO_2. *Atmospheric Chemistry and Physics*, 9(6):5905–5919.

Bottenheim, J. (2004). *"Long Range Transport of Air pollution to the Arctic" in: Intercontinental Transport of Air Pollution.* Springer-Verlag Berlin Heidelberg New York.

Bradshaw, J., Davis, D., Grodzinsky, G., Smyth, S., Newell, R., Sandholm, S., and Liu, S. (2000). Observed distributions of nitrogen oxides in the remote free troposphere from the Nasa Global Tropospheric Experiment Programs. *Rev. Geophys.*, 38(1):61–116.

Brioude, J., Cooper, O. R., Trainer, M., Ryerson, T. B., Holloway, J. S., Baynard, T., Peischl, J., Warneke, C., Neuman, J. A., De Gouw, J., Stohl, A., Eckhardt, S., Frost, G. J., McKeen, S. A., Hsie, E.-Y., Fehsenfeld, F. C., and Nédélec, P. (2007). Mixing between a stratospheric intrusion and a biomass burning plume. *Atmospheric Chemistry and Physics*, 7(16):4229–4235.

Brown, S. S., Ryerson, T. B., Wollny, A. G., Brock, C. A., Peltier, R., Sullivan, A. P., Weber, R. J., Dubac, W. P., Trainer, M., Meagher, J. F., Fehsenfeld, F. C., and Ravishankara, A. R. (2006). Variability in nocturnal nitrogen oxide processing and its role in regional air quality. *Science*, 311(5757):67–70.

Cammas, J.-P., Brioude, J., Chaboureau, J.-P., Duron, J., Mari, C., Mascart, P., Nedelec, P., Smit, H., Pätz, H.-W., Volz-Thomas, A., Stohl, A., and Fromm, M. (2009). Injection in the lower stratosphere of biomass fire emissions followed by long-range transport: a MOZAIC case study. *Atmospheric Chemistry and Physics*, 9(15):5829–5846.

Chapin, F. S., I. and Shaver, G. R. (1985). *Arctic, in "Physiological Ecology of North American Plant Communities"*. Chapman and Hall, New York.

Christensen, J., Hewitson, B., Busuioc, A., Chen, A., Gao, X., Held, I., Jones, R., Kolli, R., Kwon, W.-T., Laprise, R., Magaña Rueda, V., Mearns, L., Menéndez, C., Räisänen, J., Rinke, A., Sarr, A., and Whetton, P. (2007). *Regional Climate Projections. In: Climate Change 2007: The Physical Science Basis. Contribution of Working Group I to the Fourth Assessment Report of the Intergovernmental Panel on Climate Change.* Cambridge University Press, Cambridge, United Kingdom and New York, NY, USA.

Cooper, O. R., Forster, C., Parrish, D., Trainer, M., Dunlea, E., Ryerson, T., Hübler, G., Fehsenfeld, F., Nicks, D., Holloway, J., de Gouw, J., Warneke, C., Roberts, J. M., Flocke, F., and Moody, J. (2004). A case study of transpacific warm conveyor belt transport: Influence of merging airstreams on trace gas import to North America. *J. Geophys. Res.*, 109(D23):D23S08–.

Cooper, O. R., Moody, J. L., Parrish, D. D., Trainer, M., Ryerson, T. B., Holloway, J. S., Hübler, G., Fehsenfeld, F. C., and Evans, M. J. (2002). Trace gas composition of midlatitude cyclones over the western North Atlantic Ocean: A conceptual model. *J. Geophys. Res.*, 107(D7):4056–.

Crowley, J. N., Schuster, G., Pouvesle, N., Parchatka, U., Fischer, H., Bonn, B., Bingemer, H., and Lelieveld, J. (2010). Nocturnal nitrogen oxides at a rural mountain-site in south-western Germany. *Atmospheric Chemistry and Physics*, 10(6):2795–2812.

Damoah, R., Spichtinger, N., Forster, C., James, P., Mattis, I., Wandinger, U., Beirle, S., Wagner, T., and Stohl, A. (2004). Around the world in 17 days - hemispheric-scale transport of forest fire smoke from Russia in May 2003. *Atmospheric Chemistry and Physics*, 4(5):1311–1321.

Damoah, R., Spichtinger, N., Servranckx, R., Fromm, M., Eloranta, E. W., Razenkov, I. A., James, P., Shulski, M., Forster, C., and Stohl, A. (2006). A case study of pyro-convection using transport model and remote sensing data. *Atmospheric Chemistry and Physics*, 6(1):173–185.

Davis, D. D., Crawford, J., Chen, G., Chameides, W., Liu, S., Bradshaw, J., Sandholm, S., Sachse, G., Gregory, G., Anderson, B., Barrick, J., Bachmeier, A., Collins, J., Browell, E., Blake, D., Rowland, S., Kondo, Y., Singh, H., Talbot, R., Heikes, B., Merrill, J., Rodriguez, J., and Newell, R. E. (1996). Assessment of ozone photochemistry in the western North Pacific as inferred from PEM-West A observations during the fall 1991. *J. Geophys. Res.*, 101(D1):2111–2134.

de Gouw, J. A., Goldan, P. D., Warneke, C., Kuster, W. C., Roberts, J. M., Marchewka, M., Bertman, S. B., Pszenny, A. A. P., and Keene, W. C. (2003). Validation of proton transfer reaction-mass spectrometry (PTR-MS) measurements of gas-phase organic compounds in the atmosphere during the New England Air Quality Study (NEAQS) in 2002. *J. Geophys. Res.*, 108(D21):4682–.

de Gouw, J. A., Warneke, C., Stohl, A., Wollny, A. G., Brock, C. A., Cooper, O. R., Holloway, J. S., Trainer, M., Fehsenfeld, F. C., Atlas, E. L., Donnelly, S. G., Stroud, V., and Lueb, A. (2006).

Volatile organic compounds composition of merged and aged forest fire plumes from alaska and western canada. *J. Geophys. Res.*, 111(D10):D10303–.

Duncan, B. N., Martin, R. V., Staudt, A. C., Yevich, R., and Logan, J. A. (2003). Interannual and seasonal variability of biomass burning emissions constrained by satellite observations. *J. Geophys. Res.*, 108(D2):4100–.

Eckhardt, S., Stohl, A., Beirle, S., Spichtinger, N., James, P., Forster, C., Junker, C., Wagner, T., Platt, U., and Jennings, S. G. (2003). The North Atlantic Oscillation controls air pollution transport to the Arctic. *Atmospheric Chemistry and Physics*, 3(5):1769–1778.

Eckhardt, S., Stohl, A., Wernli, H., James, P., Forster, C., and Spichtinger, N. (2004). A 15-Year Climatology of Warm Conveyor Belts. *Journal of Climate*, 17(1):218–237.

Esler, J. G., Tan, D. G. H., Haynes, P. H., Evans, M. J., Law, K. S., Plantevin, P.-H., and Pyle, J. A. (2001). Stratosphere-troposphere exchange: Chemical sensitivity to mixing. *J. Geophys. Res.*, 106(D5):4717–4731.

Evans, M. J., Shallcross, D. E., Law, K. S., Wild, J. O. F., Simmonds, P. G., Spain, T. G., Berrisford, P., Methven, J., Lewis, A. C., McQuaid, J. B., Pilling, M. J., Bandy, B. J., Penkett, S. A., and Pyle, J. A. (2000). Evaluation of a Lagrangian box model using field measurements from EASE (Eastern Atlantic Summer Experiment) 1996. *Atmospheric Environment*, 34(23):3843 – 3863.

Fahey, D. W., Eubank, C. S., HÃ$\frac{1}{4}$bler, G., and Fehsenfeld, F. C. (1985). Evaluation of a catalytic reduction technique for the measurement of total reactive odd-nitrogen NOy in the atmosphere. *Journal of Atmospheric Chemistry*, 3:435–468. 10.1007/BF00053871.

Feigl, C. (1998). *Aufbau und Charakterisierung eines Meßsystems for NO, NO_2 und NO_y: Laboruntersuchungen und Einsatz in der unteren arktischen Stratosphäere*. PhD thesis, Faculty of Physics, LMU, Munich.

Fiedler, V., Dal Maso, M., Boy, M., Aufmhoff, H., Hoffmann, J., Schuck, T., Birmili, W., Hanke, M., Uecker, J., Arnold, F., and Kulmala, M. (2005). The contribution of sulphuric acid to atmospheric particle formation and growth: a comparison between boundary layers in northern and central europe. *Atmospheric Chemistry and Physics*, 5(7):1773–1785.

Fiedler, V., Nau, R., Ludmann, S., Arnold, F., Schlager, H., and Stohl, A. (2009). East Asian SO_2 pollution plume over Europe; Part 1: Airborne trace gas measurements and source identification by particle dispersion model simulations. *Atmospheric Chemistry and Physics*, 9(14):4717–4728.

Fischer, H., de Reus, M., Traub, M., Williams, J., Lelieveld, J., de Gouw, J., Warneke, C., Schlager, H., Minikin, A., Scheele, R., and Siegmund, P. (2003). Deep convective injection of boundary layer air into the lowermost stratosphere at midlatitudes. *Atmospheric Chemistry and Physics*, 3(3):739–745.

Fischer, H., Lawrence, M., Gurk, C., Hoor, P., Lelieveld, J., Hegglin, M. I., Brunner, D., and Schiller, C. (2006). Model simulations and aircraft measurements of vertical, seasonal and latitudinal o_3 and co distributions over europe. *Atmospheric Chemistry and Physics*, 6(2):339–348.

Fischer, H., Wienhold, F. G., Hoor, P., Bujok, O., Schiller, C., Siegmund, P., Ambaum, M., Scheeren, H. A., and Lelieveld, J. (2000). Tracer correlations in the northern high latitude lowermost stratosphere: Influence of cross-tropopause mass exchange. *Geophys. Res. Lett.*, 27(1):97–100.

Flannigan, M. D., Logan, K. A., Amiro, B. D., Skinner, W. R., and Stocks, B. J. (2005). Future area burned in canada. *Climatic Change*, 72:1–16.

Flocke, F., A., S., Roberts, J., Pfister, G., L., E., Lamarque, J.-F., Hess, P., Huey, G., Tanner, D., Ryerson, T., Neuman, A., Holloway, J., de Gouw, J., and Warneke, C. (2005a). Results from fast airborne measurements of PANs during the 2004 New England Air Quality Study. volume A54C-03. AGU Fall Meeting.

Flocke, F., Herman, R. L., Salawitch, R. J., Atlas, E., Webster, C. R., Schauffler, S. M., Lueb, R. A., May, R. D., Moyer, E. J., Rosenlof, K. H., Scott, D. C., Blake, D. R., and Bui, T. P. (1999). An examination of chemistry and transport processes in the tropical lower stratosphere using observations of long-lived and short-lived compounds obtained during strat and polaris. *J. Geophys. Res.*, 104(D21):26625–26642.

Flocke, F. M., Weinheimer, A. J., Swanson, A. L., Roberts, J. M., Schmitt, R., and Shertz, S. (2005b). On the measurements of PANs by Gas Chromatography and Electron Capture Detection. *J. Atmos. Chem.*, 52:19–43.

Forster, C., Wandinger, U., Wotawa, G., James, P., Mattis, I., Althausen, D., Simmonds, P., O'Doherty, S., Jennings, S. G., Kleefeld, C., Schneider, J., Trickl, T., Kreipl, S., Jäger, H., and Stohl, A. (2001). Transport of boreal forest fire emissions from Canada to Europe. *J. Geophys. Res.*, 106(D19):22887–22906.

Forster, P., Ramaswamy, V., Artaxo, P., Berntsen, T., Betts, R., Fahey, D. W., Haywood, J., Lean, L., Lowe, D. C., Myhre, G., Nganga, J., Prinn, R., Raga, G., Schulz, M., and Van Dorland, R. (2007). *Changes in Atmospheric Constituents and in Radiative Forcing. In: Climate Change 2007: The Physical Science Basis. Contribution of Working Group I to the Fourth Assessment Report of the Intergovernmental Panel on Climate Change.* Cambridge University Press, Cambridge, United Kingdom and New York, NY, USA.

Fromm, M., Alfred, J., Hoppel, K., Hornstein, J., Bevilacqua, R., Shettle, E., Servranckx, R., Li, Z., and Stocks, B. (2000). Observations of boreal forest fire smoke in the stratosphere by POAM III, SAGE II, and lidar in 1998. *Geophys. Res. Lett.*, 27(9):1407–1410.

Fromm, M. D. and Servranckx, R. (2003). Transport of forest fire smoke above the tropopause by supercell convection. *Geophys. Res. Lett.*, 30(10):1542–.

Frost, G. J., McKeen, S. A., Trainer, M., Ryerson, T. B., Neuman, J. A., Roberts, J. M., Swanson, A., Holloway, J. S., Sueper, D. T., Fortin, T., Parrish, D. D., Fehsenfeld, F. C., Flocke, F., Peckham, S. E., Grell, G. A., Kowal, D., Cartwright, J., Auerbach, N., and Habermann, T. (2006). Effects of changing power plant NO_x emissions on ozone in the eastern United States: Proof of concept. *J. Geophys. Res.*, 111(D12):D12306–.

Fueglistaler, S., Dessler, A. E., Dunkerton, T. J., Folkins, I., Fu, Q., and Mote, P. W. (2009). Tropical tropopause layer. *Rev. Geophys.*, 47(1):RG1004–.

Fuelberg, H. E., Harrigan, D. L., and Sessions, W. (2010). A meteorological overview of the ARCTAS 2008 mission. *Atmospheric Chemistry and Physics*, 10(2):817–842.

Gerbig, C., Schmitgen, S., Kley, D., Volz-Thomas, A., Dewey, K., and Haaks, D. (1999). An improved fast-response vacuum-UV resonance fluorescence CO instrument. *J. Geophys. Res.*, 104(D1):1699–1704.

Giglio, L., Randerson, J. T., van der Werf, G. R., Kasibhatla, P. S., Collatz, G. J., Morton, D. C., and DeFries, R. S. (2010). Assessing variability and long-term trends in burned area by merging multiple satellite fire products. *Biogeosciences*, 7(3):1171–1186.

Goode, J. G., Yokelson, R. J., Ward, D. E., Susott, R. A., Babbitt, R. E., Davies, M. A., and Hao, W. M. (2000). Measurements of excess O_3, CO_2, CO, CH_4, C_2H_4, C_2H_2, HCN, NO, NH_3, HCOOH, CH_3COOH, HCHO, and CH_3OH in 1997 Alaskan biomass burning plumes by airborne Fourier transform infrared spectroscopy (AFTIR). *J. Geophys. Res.*, 105(D17):22147–22166.

Greenaway, K. R. (1950). Experiences with arctic flying weather. Royal Meteorol. Soc. Can. Branch, Toronto, Ont., Canada.

Grooß, J.-U., Brühl, C., and Peter, T. (1998). Impact of aircraft emissions on tropospheric and stratospheric ozone. Part I: chemistry and 2-D model results. *Atmospheric Environment*, 32(18):3173 – 3184.

Gurk, C., Fischer, H., Hoor, P., Lawrence, M. G., Lelieveld, J., and Wernli, H. (2008). Airborne insitu measurements of vertical, seasonal and latitudinal distributions of carbon dioxide over europe. *Atmospheric Chemistry and Physics*, 8(21):6395–6403.

Haagen-Smit, A. J. (1950). The air pollution problem in Los Angeles. *Engineering and science*, 14:1.

Hanke, M., Umann, B., Uecker, J., Arnold, F., and Bunz, H. (2003). Atmospheric measurements of gas-phase HNO_3 and SO_2 using chemical ionization mass spectrometry during the MINATROC field campaign 2000 on Monte Cimone. *Atmospheric Chemistry and Physics*, 3(2):417–436.

Harwood, M., Roberts, J., Frost, G., Ravishankara, A., and Burkholder, J. (2003). Photochemical Studies of $CH_3C(O)OONO_2$ (PAN) and $CH_3CH_2C(O)OONO_2$ (PPN): NO_3 Quantum Yields. *J. Phys. Chem. A*, 107(8):1148–1154.

Hauf, T., Schulte, P., Alheit, R., and Schlager, H. (1995). Rapid vertical trace gas transport by an isolated midlatitude thunderstorm. *J. Geophys. Res.*, 100(D11):22957–22970.

Herman, R. L., Webster, C. R., May, R. D., Scott, D. C., Hu, H., Moyer, E. J., Wennberg, P. O., Hanisco, T. F., Lanzendorf, E. J., Salawitch, R. J., Yung, Y. L., Margitan, J. J., and Bui, T. P. (1999). Measurements of CO in the upper troposphere and lower stratosphere. *Chemosphere - Global Change Science*, 1(1-3):173 – 183.

Hintsa, E. J., Boering, K. A., Weinstock, E. M., Anderson, J. G., Gary, B. L., Pfister, L., Daube, B. C., Wofsy, S. C., Loewenstein, M., Podolske, J. R., Margitan, J. J., and Bui, T. P. (1998). Troposphere-stratosphere transport in the lowermost stratosphere from measurements of H_2O, CO_2, N_2O and O_3. *Geophys. Res. Lett.*, 25(14):2655–2658.

Holton, J. R., Haynes, P. H., McIntyre, M. E., Douglass, A. R., Rood, R. B., and Pfister, L. (1995). Stratosphere-troposphere exchange. *Rev. Geophys.*, 33(4):403–439.

Holzinger, R., Williams, J., Salisbury, G., Klöpfel, T., de Reus, M., Traub, M., Crutzen, P. J., and Lelieveld, J. (2005). Oxygenated compounds in aged biomass burning plumes over the Eastern Mediterranean: evidence for strong secondary production of methanol and acetone. *Atmospheric Chemistry and Physics*, 5(1):39–46.

Hoor, P., Fischer, H., Lange, L., Lelieveld, J., and Brunner, D. (2002). Seasonal variations of a mixing layer in the lowermost stratosphere as identified by the CO-O3 correlation from in situ measurements. *J. Geophys. Res.*, 107(D5):4044–.

Hoor, P., Gurk, C., Brunner, D., Hegglin, M. I., Wernli, H., and Fischer, H. (2004). Seasonality and extent of extratropical TST derived from in-situ CO measurements during SPURT. *Atmospheric Chemistry and Physics*, 4(5):1427–1442.

Hoskins, B. J. (1991). Towards a PV-Theta view of the general circulation. *Tellus A*, 43(4):27–35.

Hudman, R. C., Jacob, D. J., Cooper, O. R., Evans, M. J., Heald, C. L., Park, R. J., Fehsenfeld, F., Flocke, F., Holloway, J., Hübler, G., Kita, K., Koike, M., Kondo, Y., Neuman, A., Nowak, J., Oltmans, S., Parrish, D., Roberts, J. M., and Ryerson, T. (2004). Ozone production in transpacific Asian pollution plumes and implications for ozone air quality in California. *J. Geophys. Res.*, 109(D23):1–14.

Huey, L. G., Hanson, D. R., and Howard, C. J. (1995). Reactions of SF_6^- and I^- with Atmospheric Trace Gases. *J. Phys. Chem.*, 99(14):5001–5008.

Huntrieser, H., Heland, J., Schlager, H., Forster, C., Stohl, A., Aufmhoff, H., Arnold, F., Scheel, H. E., Campana, M., Gilge, S., Eixmann, R., and Cooper, O. (2005). Intercontinental air pollution transport from North America to Europe: Experimental evidence from airborne measurements and surface observations. *J. Geophys. Res.*, 110(D1):D01305–.

Jacob, D. J., Crawford, J. H., Maring, H., Clarke, A. D., Dibb, J. E., Emmons, L. K., Ferrare, R. A., Hostetler, C. A., Russell, P. B., Singh, H. B., Thompson, A. M., Shaw, G. E., McCauley, E., Pederson, J. R., and Fisher, J. A. (2010). The Arctic Research of the Composition of the Troposphere from Aircraft and Satellites (ARCTAS) mission: design, execution, and first results. *Atmospheric Chemistry and Physics*, 10(11):5191–5212.

Jacob, D. J., Wofsy, S. C., Bakwin, P. S., Fan, S.-M., Harriss, R. C., Talbot, R. W., Bradshaw, J. D., Sandholm, S. T., Singh, H. B., Browell, E. V., Gregory, G. L., Sachse, G. W., Shipham, M. C., Blake, D. R., and Fitzjarrald, D. R. (1992). Summertime Photochemistry of the Troposphere at High Northern Latitudes. *J. Geophys. Res.*, 97(D15):16421–16431.

Jaffe, D., Anderson, T., Covert, D., Kotchenruther, R., Trost, B., Danielson, J., Simpson, W., Berntsen, T., Karlsdottir, S., Blake, D., Harris, J., Carmichael, G., and Uno, I. (1999). Transport of Asian air pollution to North America. *Geophys. Res. Lett.*, 26(6):711–714.

Jaffe, D., McKendry, I., Anderson, T., and Price, H. (2003). Six 'new' episodes of trans-Pacific transport of air pollutants. *Atmospheric Environment*, 37(3):391 – 404.

Jost, H.-J., Drdla, K., Stohl, A., Pfister, L., Loewenstein, M., Lopez, J. P., Hudson, P. K., Murphy, D. M., Cziczo, D. J., Fromm, M., Bui, T. P., Dean-Day, J., Gerbig, C., Mahoney, M. J., Richard, E. C., Spichtinger, N., Pittman, J. V., Weinstock, E. M., Wilson, J. C., and Xueref, I. (2004). In-situ observations of mid-latitude forest fire plumes deep in the stratosphere. *Geophys. Res. Lett.*, 31:–.

Jurkat, T., Voigt, C., Arnold, F., Schlager, H., Kleffmann, J., Aufmhoff, H., Schäuble, D., Schaefer, M., and Schumann, U. (2011). Measurements of HONO, NO, NO_y and SO_2 in aircraft exhaust plumes at cruise. *Geophys. Res. Lett.*, 38(10):L10807–.

Justice, C. O., Giglio, L., Korontzi, S., Owens, J., Morisette, J. T., Roy, D., Descloitres, J., Alleaume, S., Petitcolin, F., and Kaufman, Y. (2002). The MODIS fire products. *Remote Sensing of Environment*, 83(1-2):244 – 262.

Kasischke, E. S., Hyer, E. J., Novelli, P. C., Bruhwiler, L. P., French, N. H. F., Sukhinin, A. I., Hewson, J. H., and Stocks, B. J. (2005). Influences of boreal fire emissions on Northern Hemisphere atmospheric carbon and carbon monoxide. *Global Biogeochem. Cycles*, 19(1):GB1012–.

Kiendler, A., Aberle, S., and Arnold, F. (2000). Positive ion chemistry in the exhaust plumes of an air craft jet engine and a burner: investigations with a quadrupole ion trap mass spectrometer. *Atmospheric Environment*, 34(28):4787 – 4793.

Kim, S., Huey, L. G., Stickel, R. E., Tanner, D. J., Crawford, J. H., Olson, J. R., Chen, G., Brune, W. H., Ren, X., Lesher, R., Wooldridge, P. J., Bertram, T. H., Perring, A., Cohen, R. C., Lefer, B. L., Shetter, R. E., Avery, M., Diskin, G., and Sokolik, I. (2007). Measurement of HO_2NO_2 in the free troposphere during the Intercontinental Chemical Transport Experiment-North America 2004. *J. Geophys. Res.*, 112(D12):D12S01–.

Klonecki, A., Hess, P., Emmons, L., Smith, L., Orlando, J., and Blake, D. (2003). Seasonal changes in the transport of pollutants into the Arctic troposphere-model study. *J. Geophys. Res.*, 108(D4):8367–.

Klonecki, A. and Levy, H., I. (1997). Tropospheric chemical ozone tendencies in CO-CH4-NOy-H2O system: Their sensitivity to variations in environmental parameters and their application to a global chemistry transport model study. *J. Geophys. Res.*, 102(D17):21221–21237.

Knop, G. and Arnold, F. (1987). Atmospheric acetonitrile measurements in the tropopause region using aircraft-borne active chemical ionization mass spectrometry. *Planetary and Space Science*, 35(2):259 – 266.

Koike, M., Kondo, Y., Kita, K., Takegawa, N., Masui, Y., Miyazaki, Y., Ko, M. W., Weinheimer, A. J., Flocke, F., Weber, R. J., Thornton, D. C., Sachse, G. W., Vay, S. A., Blake, D. R., Streets, D. G., Eisele, F. L., Sandholm, S. T., Singh, H. B., and Talbot, R. W. (2003). Export of anthropogenic reactive nitrogen and sulfur compounds from the East Asia region in spring. *J. Geophys. Res.*, 108(D20):8789–.

Krebsbach, M., Schiller, C., Brunner, D., Günther, G., Hegglin, M. I., Mottaghy, D., Riese, M., Spelten, N., and Wernli, H. (2006). Seasonal cycles and variability of O_3 and H_2O in the UT/LMS during SPURT. *Atmospheric Chemistry and Physics*, 6(1):109–125.

Kunz, A., Konopka, P., Müller, R., Pan, L. L., Schiller, C., and Rohrer, F. (2009). High static stability in the mixing layer above the extratropical tropopause. *J. Geophys. Res.*, 114(D16):D16305–.

LaFranchi, B. W., Wolfe, G. M., Thornton, J. A., Harrold, S. A., Browne, E. C., Min, K. E., Wooldridge, P. J., Gilman, J. B., Kuster, W. C., Goldan, P. D., de Gouw, J. A., McKay, M., Goldstein, A. H., Ren, X., Mao, J., and Cohen, R. C. (2009). Closing the peroxy acetyl nitrate budget: observations of acyl peroxy nitrates (PAN, PPN, and MPAN) during BEARPEX 2007. *Atmospheric Chemistry and Physics*, 9(19):7623–7641.

Lapina, K., Honrath, R. E., Owen, R. C., Val Martín, M., Hyer, E. J., and Fialho, P. (2008). Late summer changes in burning conditions in the boreal regions and their implications for NO_x and CO emissions from boreal fires. *J. Geophys. Res.*, 113(D11):D11304–.

Lapina, K., Honrath, R. E., Owen, R. C., Val Martín, M., and Pfister, G. (2006). Evidence of significant large-scale impacts of boreal fires on ozone levels in the midlatitude Northern Hemisphere free troposphere. *Geophys. Res. Lett.*, 33(10):L10815–.

Lavoué, D., Liousse, C., Cachier, H., Stocks, B. J., and Goldammer, J. G. (2000). Modeling of carbonaceous particles emitted by boreal and temperate wildfires at northern latitudes. *J. Geophys. Res.*, 105(D22):26871–26890.

Law, K. S. and Stohl, A. (2007). Arctic Air Pollution: Origins and Impacts. *Science*, 315(5818):1537–1540.

Lawrence, M. G., Jöckel, P., and von Kuhlmann, R. (2001). What does the global mean OH concentration tell us? *Atmospheric Chemistry and Physics*, 1(1):37–49.

Lazzara, M. A, K. S. L. (2011). Arctic and Antarctic Satellite Composite Imagery. *Polar Science*, in preparation.

Levy, H. (1971). Normal Atmosphere: Large Radical and Formaldehyde Concentrations Predicted. *Science*, 173(3992):141–143.

Li, G., Lei, W., Zavala, M., Volkamer, R., Dusanter, S., Stevens, P., and Molina, L. T. (2010). Impacts of HONO sources on the photochemistry in Mexico City during the MCMA-2006/MILAGO Campaign. *Atmospheric Chemistry and Physics*, 10(14):6551–6567.

Liang, Q., Rodriguez, J. M., Douglass, A. R., Crawford, J. H., Apel, E., Bian, H., Blake, D. R., Brune, W., Chin, M., Colarco, P. R., da Silva, A., Diskin, G. S., Duncan, B. N., Huey, L. G., Knapp, D. J., Montzka, D. D., Nielsen, J. E., Olson, J. R., Pawson, S., Weinheimer, A. J., and Reimer, D. D. (2011). Reactive nitrogen, ozone and ozone production in the Arctic troposphere and the impact of stratosphere-troposphere exchange. *Atmospheric Chemistry and Physics Discussions*, 11(4):10721–10767.

Logan, J. A. (1983). Nitrogen Oxides in the Troposphere: Global and Regional Budgets. *J. Geophys. Res.*, 88(C15):10785–10807.

March, R. and Hughes, R. (1989). *Quadrupole Storage Mass Spectrometry*. John Wiley & Sons, New York.

March, R. and Todd, J. (1995). *Practical Aspects of Ion Trap Mass Spectrometry*. CRC Press.

Mari, C., Evans, M. J., Palmer, P. I., Jacob, D. J., and Sachse, G. W. (2004). Export of Asian pollution during two cold front episodes of the TRACE-P experiment. *J. Geophys. Res.*, 109(D15):D15S17–.

Mathieu, E. (1868). Memoire sur le mouvement vibratoire d´une membrane de forme elliptique. *J. Math. Pures Appl.*, 13:137.

Mauzerall, D. L., Jacob, D. J., Fan, S.-M., Bradshaw, J. D., Gregory, G. L., Sachse, G. W., and Blake, D. R. (1996). Origin of tropospheric ozone at remote high northern latitudes in summer. *J. Geophys. Res.*, 101(D2):4175–4188.

Mauzerall, D. L., Logan, J. A., Jacob, D. J., Anderson, B. E., Blake, D. R., Bradshaw, J. D., Heikes, B., Sachse, G. W., Singh, H., and Talbot, B. (1998). Photochemistry in biomass burning plumes and implications for tropospheric ozone over the tropical South Atlantic. *J. Geophys. Res.*, 103:–.

McLachlan, N. (1947). *Theory and Applications of Mathieu Functions*. Clarendon, Oxford.

Mitchell, J. M. (1957). Visual range in the polar regions with particular refernce to the Alaskan Arctic. *J. Atmos. Terr. Phys. Spec. Suppl.*, pages 195–211.

Miyazaki, Y., Kondo, Y., Koike, M., Fuelberg, H. E., Kiley, C. M., Kita, K., Takegawa, N., Sachse, G. W., Flocke, F., Weinheimer, A. J., Singh, H. B., Eisele, F. L., Zondlo, M., Talbot, R. W., Sandholm, S. T., Avery, M. A., and Blake, D. R. (2003). Synoptic-scale transport of reactive nitrogen over the western Pacific in spring. *J. Geophys. Res.*, 108(D20):8788–.

Moehler, O. and Arnold, F. (1991). Flow reactor and triple quadrupole mass spectrometer investigations of negative ion reactions involving nitric acid: Implications for atmospheric HNO_3 detection by Chemical Ionization Mass Spectrometry. *Atmospheric Chemistry*, 13:33–61.

Murphy, D. M., Fahey, D. W., Proffitt, M. H., Liu, S. C., Chan, K. R., Eubank, C. S., Kawa, S. R., and Kelly, K. K. (1993). Reactive Nitrogen and Its Correlation With Ozone in the Lower Stratosphere and Upper Troposphere. *J. Geophys. Res.*, 98(D5):8751–8773.

National Research Council (2009). *Global Sources of Local Pollution: An Assessment of Long-Range Transport of Key Air Pollutants to and from the United States.* The National Academies Press, Washington D. C.

Neuman, J. A., Gao, R. S., Schein, M. E., Ciciora, S. J., Holecek, J. C., Thompson, T. L., Winkler, R. H., McLaughlin, R. J., Northway, M. J., Richard, E. C., and Fahey, D. W. (2000). A fast-response chemical ionization mass spectrometer for in situ measurements of HNO_3 in the upper troposphere and lower stratosphere. *Review of Scientific Instruments*, 71(10):3886–3894.

Neuman, J. A., Nowak, J. B., Zheng, W., Flocke, F., Ryerson, T. B., Trainer, M., Holloway, J. S., Parrish, D. D., Frost, G. J., Peischl, J., Atlas, E. L., Bahreini, R., Wollny, A. G., and Fehsenfeld, F. C. (2009). Relationship between photochemical ozone production and NOx oxidation in Houston, Texas. *J. Geophys. Res.*, 114:D00F08–.

Neuman, J. A., Parrish, D. D., Trainer, M., Ryerson, T. B., Holloway, J. S., Nowak, J. B., Swanson, A., Flocke, F., Roberts, J. M., Brown, S. S., Stark, H., Sommariva, R., Stohl, A., Peltier, R., Weber, R., Wollny, A. G., Sueper, D. T., Hubler, G., and Fehsenfeld, F. C. (2006). Reactive nitrogen transport and photochemistry in urban plumes over the North Atlantic Ocean. *J. Geophys. Res.*, 111:–.

Novelli, P. C., Masarie, K. A., Lang, P. M., Hall, B. D., Myers, R. C., and Elkins, J. W. (2003). Reanalysis of tropospheric CO trends: Effects of the 1997 and 1998 wildfires. *J. Geophys. Res.*, 108(D15):4464–.

Novelli, P. C., Steele, L. P., and Tans, P. P. (1992). Mixing Ratios of Carbon Monoxide in the Troposphere. *J. Geophys. Res.*, 97(D18):20731–20750.

Nowak, J. B., Huey, L. G., Eisele, F. L., Tanner, D. J., Mauldin, R. L., I., Cantrell, C., Kosciuch, E., and Davis, D. D. (2002). Chemical ionization mass spectrometry technique for detection of dimethylsulfoxide and ammonia. *J. Geophys. Res.*, 107(D18):4363.

Nowak, J. B., Parrish, D. D., Neuman, J. A., Holloway, J. S., Cooper, O. R., Ryerson, T. B., Nicks, D. K., J., Flocke, F., Roberts, J. M., Atlas, E., de Gouw, J. A., Donnelly, S., Dunlea, E., Hübler, G., Huey, L. G., Schauffler, S., Tanner, D. J., Warneke, C., and Fehsenfeld, F. C. (2004). Gas-phase chemical characteristics of Asian emission plumes observed during ITCT 2K2 over the eastern North Pacific Ocean. *J. Geophys. Res.*, 109(D23):D23S19–.

Orlando, J. J., Tyndall, G. S., Bertman, S. B., Chen, W., and Burkholder, J. B. (2002). Rate coefficient for the reaction of OH with CH_2=C(CH_3)C(O)OONO_2 (MPAN). *Atmospheric Environment*, 36:1895–1900.

Orsolini, Y. I. and Sorteberg, A. (2009). Projected changes in eurasian and arctic summer cyclones under global warming in the bergen climate model. *Atmospheric and Oceanic Science Letters*, 2(1):62–67.

Pan, L. L., Bowman, K. P., Shapiro, M., Randel, W. J., Gao, R. S., Campos, T., Davis, C., Schauffler, S., Ridley, B. A., Wei, J. C., and Barnet, C. (2007). Chemical behavior of the tropopause observed during the Stratosphere-Troposphere Analyses of Regional Transport experiment. *J. Geophys. Res.*, 112(D18):D18110–.

Pan, L. L., Randel, W. J., Gary, B. L., Mahoney, M. J., and Hintsa, E. J. (2004). Definitions and sharpness of the extratropical tropopause: A trace gas perspective. *J. Geophys. Res.*, 109(D23):D23103–.

Paris, J.-D., Stohl, A., Nedelec, P., Arshinov, M. Y., Panchenko, M. V., Shmargunov, V. P., Law, K. S., Belan, B. D., and Ciais, P. (2009). Wildfire smoke in the Siberian Arctic in summer: source characterization and plume evolution from airborne measurements. *Atmospheric Chemistry and Physics*, 9(23):9315–9327.

Parrish, D. D., Holloway, J. S., Jakoubek, R., Trainer, M., Ryerson, T. B., Hübler, G., Fehsenfeld, F. C., Moody, J. L., and Cooper, O. R. (2000). Mixing of anthropogenic pollution with stratospheric ozone: A case study from the North Atlantic wintertime troposphere. *J. Geophys. Res.*, 105(D19):24363–24374.

Paul, W. and Raether, M. (1955). Das elektrische Massenfilter. *Zeitschrift für Physik*, 140:161–273.

Paul, W. and Steinwedel, H. (1953). Ein neues Massenspektrometer ohne Magnetfeld. *Zeitschrift für Naturforschung*, pages 448–450.

Pfister, G. G., Emmons, L. K., Hess, P. G., Honrath, R., Lamarque, J.-F., Val Martin, M., Owen, R. C., Avery, M. A., Browell, E. V., Holloway, J. S., Nedelec, P., Purvis, R., Ryerson, T. B., Sachse, G. W., and Schlager, H. (2006). Ozone production from the 2004 North American boreal fires. *J. Geophys. Res.*, 111(D24):D24S07–.

Platt, U., LeBras, G., Poulet, G., Burrows, J. P., and Moortgat, G. (1990). Peroxy radicals from night-time reaction of NO_3 with organic compounds. *Nature*, 348(6297):147–149.

Platt, U., Perner, D., Harris, G. W., Winer, A. M., and Pitts, J. N. (1980). Observations of nitrous acid in an urban atmosphere by differential optical absorption. *Nature*, 285:312–314.

Plumb, R. A. and Ko, M. K. W. (1992). Interrelationships between mixing ratios of longlived stratospheric constituents. *J. Geophys. Res.*, 97(D9):10145–10156.

Pommier, M., Law, K. S., Clerbaux, C., Turquety, S., Hurtmans, D., Hadji-Lazaro, J., Coheur, P.-F., Schlager, H., Ancellet, G., Paris, J.-D., Nédélec, P., Diskin, G. S., Podolske, J. R., Holloway, J. S., and Bernath, P. (2010). IASI carbon monoxide validation over the Arctic during POLARCAT spring and summer campaigns. *Atmospheric Chemistry and Physics*, 10(21):10655–10678.

Poulida, O., Dickerson, R. R., and Heymsfield, A. (1996). Stratosphere-troposphere exchange in a midlatitude mesoscale convective complex 1. Observations. *J. Geophys. Res.*, 101(D3):6823–6836.

Quinn, P. K., Shaw, G., Andrews, E., Dutton, E. G., Ruoho-Airola, T., and Gong, S. L. (2007). Arctic haze: current trends and knowledge gaps. *Tellus B*, 59(1):99–114.

Real, E., Law, K. S., Schlager, H., Roiger, A., Huntrieser, H., Methven, J., Cain, M., Holloway, J., Neuman, J. A., Ryerson, T., Flocke, F., de Gouw, J., Atlas, E., Donnelly, S., and Parrish, D. (2008). Lagrangian analysis of low altitude anthropogenic plume processing across the North Atlantic. *Atmospheric Chemistry and Physics*, 8(24):7737–7754.

Real, E., Law, K. S., Weinzierl, B., Fiebig, M., Petzold, A., Wild, O., Methven, J., Arnold, S., Stohl, A., Huntrieser, H., Roiger, A., Schlager, H., Stewart, D., Avery, M., Sachse, G., Browell, E., Ferrare, R., and Blake, D. (2007). Processes influencing ozone levels in Alaskan forest fire plumes during long-range transport over the North Atlantic. *J. Geophys. Res.*, 112:–.

Reeves, C. E., Penkett, S. A., Bauguitte, S., Law, K. S., Evans, M. J., Bandy, B. J., Monks, P. S., Edwards, G. D., Phillips, G., Barjat, H., Kent, J., Dewey, K., Schmitgen, S., and Kley, D. (2002). Potential for photochemical ozone formation in the troposphere over the North Atlantic as derived from aircraft observations during ACSOE. *J. Geophys. Res.*, 107(D23):4707–.

Reiner, T., Moehler, O., and Arnold, F. (1998). Measurements of acetone, acetic acid, and formic acid in the northern midlatitude upper troposphere and lower stratosphere. *J. Geophys. Res.*, 104:–.

Ren, X., Olson, J. R., Crawford, J. H., Brune, W. H., Mao, J., Long, R. B., Chen, Z., Chen, G., Avery, M. A., Sachse, G. W., Barrick, J. D., Diskin, G. S., Huey, L. G., Fried, A., Cohen, R. C., Heikes, B., Wennberg, P. O., Singh, H. B., Blake, D. R., and Shetter, R. E. (2008). HOx chemistry during INTEX-A 2004: Observation, model calculation, and comparison with previous studies. *J. Geophys. Res.*, 113(D5):D05310–.

Roberts, J. M. (1990). The atmospheric chemistry of organic nitrates. *Atmospheric Environment*, 24A:243–287.

Roberts, J. M. (2005). Measurement of the Henry's law coefficient and first order loss rate of PAN in n-octanol. *Geophys. Res. Lett.*, 32(8):L08803–.

Roberts, J. M. and Bertman, S. B. (1992). The thermal decomposition of peroxyacetic nitric anhydride (PAN) and peroxymethacrylic nitric anhydride (MPAN). *International Journal of Chemical Kinetics*, 24(3):297–307.

Roberts, J. M., Flocke, F., Chen, G., de Gouw, J., Holloway, J. S., Hübler, G., Neuman, J. A., Jr., D. K. N., Nowak, J. B., Parrish, D. D., Ryerson, T. B., Sueper, D. T., Warneke, C., and Fehsenfeld, F. C. (2004). Measurement of peroxycarboxylic nitric anhydrides (PANs) during the ITCT 2K2 aircraft intensive experiment. *J. Geophys. Res.*, 109(D23):1–13.

Roberts, J. M., Flocke, F., Stroud, C. A., Hereid, D., Williams, E., Fehsenfeld, F., Brune, W., Martinez, M., and Harder, H. (2002). Ground-based measurements of peroxycarboxylic nitric anhydrides (PANs) during the 1999 Southern Oxidants Study Nashville Intensive. *J. Geophys. Res.*, 107(D21):ACH 1–1–ACH 1–10.

Roberts, J. M., Marchewka, M., Bertman, S. B., Sommariva, R., Warneke, C., de Gouw, J., Kuster, W., Goldan, P., Williams, E., Lerner, B. M., Murphy, P., and Fehsenfeld, F. C. (2007). Measurements of PANs during the New England Air Quality Study 2002. *J. Geophys. Res.*, 112(D20):1–14.

Roberts, J. M., Veres, P., Warneke, C., Neuman, J. A., Washenfelder, R. A., Brown, S. S., Baasandorj, M., Burkholder, J. B., Burling, I. R., Johnson, T. J., Yokelson, R. J., and de Gouw, J. (2010). Measurement of HONO, HNCO, and other inorganic acids by negative-ion proton-transfer chemical-ionization mass spectrometry (NI-PT-CIMS): application to biomass burning emissions. *Atmospheric Measurement Techniques*, 3(4):981–990.

Roberts, J. M., Williams, J., Baumann, K., Buhr, M. P., Goldan, P. D., Holloway, J., Hübler, G., Kuster, W. C., McKeen, S. A., Ryerson, T. B., Trainer, M., Williams, E. J., Fehsenfeld, F. C., Bertman, S. B., Nouaime, G., Seaver, C., Grodzinsky, G., Rodgers, M., and Young, V. L. (1998). Measurements of PAN, PPN, and MPAN made during the 1994 and 1995 Nashville Intensives of the Southern Oxidant Study: Implications for regional ozone production from biogenic hydrocarbons. *J. Geophys. Res.*, 103(D17):22473–22490.

Roiger, A., Aufmhoff, H., Stock, P., Arnold, F., and Schlager, H. (2011a). An aircraft-borne chemical ionization - ion trap mass spectrometer (CI-ITMS) for fast PAN and PPN measurements. *Atmospheric Measurement Techniques*, 4(2):173–188.

Roiger, A., Schlager, H., Schäfler, A., Huntrieser, H., Scheibe, M., Aufmhoff, H., Cooper, O. R., Sodemann, H., Stohl, A., Burkhart, J., Lazzara, M., Schiller, C., Law, K. S., and Arnold, F. (2011b). In-situ observation of Asian pollution transported into the Arctic lowermost stratosphere. *Atmospheric Chemistry and Physics Discussions*, 11(5):16265–16310.

Sandholm, S. T., Bradshaw, J. D., Chen, G., Singh, H. B., Talbot, R. W., Gregory, G. L., Blake, D. R., Sachse, G. W., Browell, E. V., Barrick, J. D. W., Shipham, M. A., Bachmeier, A. S., and

Owen, D. (1992). Summertime Tropospheric Observations Related to N_xO_y Distributions and Partitioning Over Alaska: Arctic Boundary Layer Expedition 3A. *J. Geophys. Res.*, 97(D15):16481–16509.

Sawa, Y., Machida, T., and Matsueda, H. (2008). Seasonal variations of CO_2 near the tropopause observed by commercial aircraft. *J. Geophys. Res.*, 113(D23):D23301–.

Schlager, H. and Arnold, F. (1987). On stratospheric acetonitrile detection by passive chemical ionization mass spectrometry. *Planetary and Space Science*, 35(6):715 – 725.

Schlager, H., Konopka, P., Schulte, P., Schumann, U., Ziereis, H., Arnold, F., Klemm, M., Hagen, D. E., Whitefield, P. D., and Ovarlez, J. (1997). In situ observations of air traffic emission signatures in the North Atlantic flight corridor. *J. Geophys. Res.*, 102(D9):10739–10750.

Schlager, H. e. a. (2011). First results of the PFC release and resampling experiment during POLARCAT-GRACE. *Geophys. Res. Lett.*, in preparation.

Schröder, D., Soldi-Lose, H., Semialjac, M., Loos, J., Schwarz, H., Eerdekens, G., and Arnold, F. (2003). On gaseous c4h6o2 compounds in the atmosphere: new insights from collision experiments of the protonated molecules in the laboratory and on aircraft. *International Journal of Mass Spectrometry*, 228(1):35 – 47.

Seinfeld, J. H. and Pandis, S. N. (1998). *Atmospheric Chemistry and Physics*. John Wiley & Sons, Inc.

Serreze, M. C. and Barrett, A. P. (2008). The summer cyclone maximum over the central arctic ocean. *J. Climate*, 21(5):1048–1065.

Shindell, D., Faluvegi, G., Lacis, A., Hansen, J., Ruedy, R., and Aguilar, E. (2006). Role of tropospheric ozone increases in 20th-century climate change. *J. Geophys. Res.*, 111(D8):D08302–.

Shindell, D. T., Chin, M., Dentener, F., Doherty, R. M., Faluvegi, G., Fiore, A. M., Hess, P., Koch, D. M., MacKenzie, I. A., Sanderson, M. G., Schultz, M. G., Schulz, M., Stevenson, D. S., Teich, H., Textor, C., Wild, O., Bergmann, D. J., Bey, I., Bian, H., Cuvelier, C., Duncan, B. N., Folberth, G., Horowitz, L. W., Jonson, J., Kaminski, J. W., Marmer, E., Park, R., Pringle, K. J., Schroeder, S., Szopa, S., Takemura, T., Zeng, G., Keating, T. J., and Zuber, A. (2008). A multi-model assessment of pollution transport to the Arctic. *Atmospheric Chemistry and Physics*, 8(17):5353–5372.

Singh, H., Anderson, B., Brune, W., Cai, C., Cohen, R., Crawford, J., Cubison, M., Czech, E., Emmons, L., Fuelberg, H., Huey, G., Jacob, D., Jimenez, J., Kaduwela, A., Kondo, Y., Mao, J., Olson, J., Sachse, G., Vay, S., Weinheimer, A., Wennberg, P., and Wisthaler, A. (2010). Pollution influences on atmospheric composition and chemistry at high northern latitudes: Boreal and California forest fire emissions. *Atmospheric Environment*, 44(36):4553 – 4564.

Singh, H. and Salas, L. (1983). Methodology for the analysis of peroxyacetyl nitrate (PAN) in the unpolluted atmosphere. *Atmospheric Environment - Part A General Topics*, 17(8):1507–1516.

Singh, H. B. and Hanst, P. L. (1981). Peroxyacetyl Nitrate (PAN) in the Unpolluted Atmosphere; An Important Reservoir for Nitrogen Oxides. *Geophys. Res. Lett.*, 8(8):941–944.

Singh, H. B., Herlth, D., O'Hara, D., Zahnle, K., Bradshaw, J. D., Sandholm, S. T., Talbot, R., Crutzen, P. J., and Kanakidou, M. (1992a). Relationship of Peroxyacetyl Nitrate to Active and Total Odd Nitrogen at Northern High Latitudes: Influence of Reservoir Species on NO_x and O_3. *J. Geophys. Res.*, 97:–.

Singh, H. B., O'Hara, D., Herlth, D., Bradshaw, J. D., Sandholm, S. T., Gregory, G. L., Sachse, G. W., Blake, D. R., Crutzen, P. J., and Kanakidou, M. A. (1992b). Atmospheric Measurements of Peroxyacetyl Nitrate and other Organic Nitrates at High Latitudes: Possible Sources and Sinks. *J. Geophys. Res.*, 97:–.

Singh, H. B., Salas, L., Herlth, D., Kolyer, R., Czech, E., Avery, M., Crawford, J. H., Pierce, R. B., Sachse, G. W., Blake, D. R., Cohen, R. C., Bertram, T. H., Perring, A., Wooldridge, P. J., Dibb, J., Huey, G., Hudman, R. C., Turquety, S., Emmons, L. K., Flocke, F., Tang, Y., Carmichael, G. R., and Horowitz, L. W. (2007). Reactive nitrogen distribution and partitioning in the North American troposphere and lowermost stratosphere. *J. Geophys. Res.*, 112(D12):1–15.

Singh, H. B., Salas, L. J., Chatfield, R. B., Czech, E., Fried, A., Walega, J., Evans, M. J., Field, B. D., Jacob, D. J., Blake, D., Heikes, B., Talbot, R., Sachse, G., Crawford, J. H., Avery, M. A., Sandholm, S., and Fuelberg, H. (2004). Analysis of the atmospheric distribution, sources, and sinks of oxygenated volatile organic chemicals based on measurements over the Pacific during TRACE-P. *J. Geophys. Res.*, 109:–.

Slusher, D. L., Huey, L. G., Tanner, D. J., Flocke, F. M., and Roberts, J. M. (2004). A thermal dissociation chemical ionization mass spectrometry (TD-CIMS) technique for the simultaneous measurement of peroxyacyl nitrates and dinitrogen pentoxide. *J. Geophys. Res.*, 109(D19):1–13.

Sodemann, H., Pommier, M., Arnold, S. R., Monks, S. A., Stebel, K., Burkhart, J. F., Hair, J. W., Diskin, G. S., Clerbaux, C., Coheur, P.-F., Hurtmans, D., Schlager, H., Blechschmidt, A.-M., Kristjánsson, J. E., and Stohl, A. (2011). Episodes of cross-polar transport in the Arctic troposphere during July 2008 as seen from models, satellite, and aircraft observations. *Atmospheric Chemistry and Physics*, 11(8):3631–3651.

Soja, A. J., Stocks, B., Maczeck, P., Fromm, M., Servranckx, R., Turetsky, M., and Bensoter, B. (2008). Arctas: the perfect smoke. The Canadian Smoke Newsletter.

Soja, A. J., Tchebakova, N. M., French, N. H., Flannigan, M. D., Shugart, H. H., Stocks, B. J., Sukhinin, A. I., Parfenova, E., III, F. S. C., Stackhouse, P. W., and Jr. (2007). Climate-induced boreal forest change: Predictions versus current observations. *Global and Planetary Change*, 56(3-4):274 – 296. Northern Eurasia Regional Climate and Environmental Change.

Solomon, S., Garcia, R., and Stordal, F. (1985). Transport Processes and Ozone Perturbations. *J. Geophys. Res.*, 90(D7):12981–12989.

Speidel, M., Nau, R., Arnold, F., Schlager, H., and Stohl, A. (2007). Sulfur dioxide measurements in the lower, middle and upper troposphere: Deployment of an aircraft-based chemical ionization mass spectrometer with permanent in-flight calibration. *Atmospheric Environment*, 41(11):2427 – 2437.

Stafford, G.C.and Kelley, P., Syka, J., Reynolds, W., and Todd, J. (1984). Recent improvements in and analytical applications of advanced ion trap technology. *International Journal of Mass Spectrometry and Ion Processes*, 60(1):85 – 98.

Stephens, E. R., Hanst, P. L., Doerr, R. C., and Scott, W. E. (1956a). Reactions of Nitrogen Dioxide and Organic Compounds in Air. *Industrial & Engineering Chemistry*, 48(9):1498–1504.

Stephens, E. R., Scott, W. E., Hanst, P. L., and Doerr, R. C. (1956b). Auto exhaust: Composition and photolysis products. *J. Air Poll. Control. Assoc.*, 6:159.

Stocks, B. J., Fosberg, M. A., Lynham, T. J., Mearns, L., Wotton, B. M., Yang, Q., Jin, J.-Z., Lawrence, K., Hartley, G. R., Mason, J. A., and McKENNEY, D. W. (1998). Climate Change and Forest Fire Potential in Russian and Canadian Boreal Forests. *Climatic Change*, 38:1–13. 10.1023/A:1005306001055.

Stohl, A. (2001). A 1-year Lagrangian climatology of airstreams in the Northern Hemisphere troposphere and lowermost stratosphere. *J. Geophys. Res.*, 106(D7):7263–7279.

Stohl, A. (2006). Characteristics of atmospheric transport into the Arctic troposphere. *J. Geophys. Res.*, 111(D11):D11306–.

Stohl, A., Eckhardt, S., Forster, C., James, P., Spichtinger, N., and Seibert, P. (2002). A replacement for simple back trajectory calculations in the interpretation of atmospheric trace substance measurements. *Atmospheric Environment*, 36(29):4635–4648.

Stohl, A., Forster, C., Eckhardt, S., Spichtinger, N., Huntrieser, H., Heland, J., Schlager, H., Wilhelm, S., Arnold, F., and Cooper, O. (2003). A backward modeling study of intercontinental pollution transport using aircraft measurements. *J. Geophys. Res.*, 108(D12):4370–.

Stohl, A., Forster, C., Frank, A., Seibert, P., and Wotawa, G. (2005). Technical note: The Lagrangian particle dispersion model FLEXPART version 6.2. *Atmospheric Chemistry and Physics*, 5(9):2461–2474.

Stohl, A., Forster, C., Huntrieser, H., Mannstein, H., McMillan, W. W., Petzold, A., Schlager, H., and Weinzierl, B. (2007). Aircraft measurements over Europe of an air pollution plume from Southeast Asia; aerosol and chemical characterization. *Atmospheric Chemistry and Physics*, 7(3):913–937.

Stohl, A. and Thomson, D. J. (1999). A density correction for Lagrangian particle dispersion models. *Boundary-Layer Meteorology*, 90:155–167.

Stohl, A. and Trickl, T. (1999). A textbook example of long-range transport: Simultaneous observation of ozone maxima of stratospheric and north american origin in the free troposphere over europe. *J. Geophys. Res.*, 104(D23):30445–30462.

Suntharalingam, P., Jacob, D. J., Palmer, P. I., Logan, J. A., Yantosca, R. M., Xiao, Y., Evans, M. J., Streets, D. G., Vay, S. L., and Sachse, G. W. (2004). Improved quantification of Chinese carbon fluxes using CO2/CO correlations in Asian outflow. *J. Geophys. Res.*, 109(D18):D18S18–.

Talbot, R., Vijigen, A. S., and Harris, R. C. (1990). Measuring Tropospheric HNO_3: Problems and Prospects for Nylon Filter and Mist Chamber Techniques. *J. Geophys. Res.*, 95(D6):7553–7561.

Talukdar, R. K., Burkholder, J. B., Schmoltner, A.-M., Roberts, J. M., Wilson, R. W., and Ravishankara, A. R. (1995). Investigation of the loss processes for peroxyacetyl nitrate in the atmosphere: UV photolysis and reaction with OH. *J. Geophys. Res.*, 100(D7):14163–14174.

Thornton, D. C., Bandy, A. R., Tu, F. H., Blomquist, B. W., Mitchell, G. M., Nadler, W., and Lenschow, D. H. (2002). Fast airborne sulfur dioxide measurements by Atmospheric Pressure Ionization Mass Spectrometry (APIMS). *J. Geophys. Res.*, 107(D22):4632.

Tilmes, S., Pan, L. L., Hoor, P., Atlas, E., Avery, M. A., Campos, T., Christensen, L. E., Diskin, G. S., Gao, R.-S., Herman, R. L., Hintsa, E. J., Loewenstein, M., Lopez, J., Paige, M. E., Pittman, J. V., Podolske, J. R., Proffitt, M. R., Sachse, G. W., Schiller, C., Schlager, H., Smith, J., Spelten, N., Webster, C., Weinheimer, A., and Zondlo, M. A. (2010). An aircraft-based upper troposphere lower stratosphere O_3, CO, and H_2O climatology for the Northern Hemisphere. *J. Geophys. Res.*, 115(D14):D14303–.

Trenberth, K.E., J. P. D., Ambenje, P., Bojariu, R., Easterling, D., Klein Tank, A., Parker, D., Rahimzadeh, F., Renwick, J. a., Rusticucci, M., Soden, B., and Zhai, P. (2007). *Observations: Surface and Atmospheric Climate Change. In: Climate Change 2007: The Physical Science Basis. Contribution of Working Group I to the Fourth Assessment Report of the Intergovernmental Panel on Climate Change.* Cambridge University Press, Cambridge, United Kingdom and New York, NY, USA.

Val Martin, M., Logan, J. A., Kahn, R. A., Leung, F.-Y., Nelson, D. L., and Diner, D. J. (2010). Smoke injection heights from fires in North America: analysis of 5 years of satellite observations. *Atmospheric Chemistry and Physics*, 10(4):1491–1510.

Val Martín, M., Honrath, R. E., Owen, R. C., Pfister, G., Fialho, P., and Barata, F. (2006). Significant enhancements of nitrogen oxides, black carbon, and ozone in the North Atlantic lower free troposphere resulting from North American boreal wildfires. *J. Geophys. Res.*, 111(D23):D23S60–.

van der Werf, G. R., Randerson, J. T., Giglio, L., Collatz, G. J., Mu, M., Kasibhatla, P. S., Morton, D. C., DeFries, R. S., Jin, Y., and van Leeuwen, T. T. (2010). Global fire emissions and the contribution of deforestation, savanna, forest, agricultural, and peat fires (1997-2009). *Atmospheric Chemistry and Physics*, 10(23):11707–11735.

Veres, P., Roberts, J., Warneke, C., Welsh-Bona, D., Zahniserd, M., Herndond, S., Falla, R., and de Gouw, J. (2008). Development of negative-ion proton-transfer chemical-ionization mass spectrometry (NI-PT-CIMS) for the measurement of gas-phase organic acids in the atmosphere. *Intern. J. of Mass Spectrometry*, 1-3(274):48–55.

Verma, S., Worden, J., Pierce, B., Jones, D. B. A., Al-Saadi, J., Boersma, F., Bowman, K., Eldering, A., Fisher, B., Jourdain, L., Kulawik, S., and Worden, H. (2009). Ozone production in boreal fire smoke plumes using observations from the Tropospheric Emission Spectrometer and the Ozone Monitoring Instrument. *J. Geophys. Res.*, 114(D2):D02303–.

Villalta, P. and Howard, C. (1996). Direct Kinetics Study of the $CH_3C(O)O_2$ + NO Reaction Using Chemical Ionization Mass Spectrometry. *J. Phys. Chem.*, 100(32):13624–13628.

Volz-Thomas, A., Xueref, I., and Schmitt, R. (2002). An Automatic Gas Chromatograph and Calibration System for Ambient Measurements of PAN and PPN. *Env. Sci. & Pollut. Res.*, 4:72–76.

Waibel, A. E., Fischer, H., Wienhold, F. G., Siegmund, P. C., Lee, B., Ström, J., Lelieveld, J., and Crutzen, P. J. (1999). Highly elevated carbon monoxide concentrations in the upper troposphere and lowermost stratosphere at northern midlatitudes during the STREAM II summer campaign in 1994. *Chemosphere - Global Change Science*, 1(1-3):233 – 248.

Wang, Y., Munger, J. W., Xu, S., McElroy, M. B., Hao, J., Nielsen, C. P., and Ma, H. (2010). CO_2 and its correlation with CO at a rural site near Beijing: implications for combustion efficiency in China. *Atmospheric Chemistry and Physics*, 10(18):8881–8897.

Warneck, P. and Zerbach, T. (1992). Synthesis of peroxyacetyl nitrate in air by acetone photolysis. *Environ. Sci. Technol.*, 26(1):74–79.

Wernli, B. H. and Davies, H. C. (1997). A lagrangian-based analysis of extratropical cyclones. I: The method and some applications. *Quarterly Journal of the Royal Meteorological Society*, 123(538):467–489.

Wernli, H. and Bourqui, M. (2002). A Lagrangian 1-year climatology of (deep) cross-tropopause exchange in the extratropical Northern Hemisphere. *J. Geophys. Res.*, 107(D2):4021–.

Wigley, T. M. L. and Schimel, T. S. (7-36, 2000). *The carbon cycle*. Cambridge University Press.

Wild, O. and Akimoto, H. (2001). Intercontinental transport of ozone and its precursors in a three-dimensional global CTM. *J. Geophys. Res.*, 106(D21):27729–27744.

Wild, O., Law, K. S., McKenna, D. S., Bandy, B. J., Penkett, S. A., and Pyle, J. A. (1996). Photochemical trajectory modeling studies of the North Atlantic region during August 1993. *J. Geophys. Res.*, 101(D22):29269–29288.

Williams, J., Roberts, J. M., Bertman, S. B., Stroud, C. A., Fehsenfeld, F. C., Baumann, K., Buhr, M. P., Knapp, K., Murphy, P. C., Nowick, M., and Williams, E. J. (2000). A method for the airborne measurement of PAN, PPN, and MPAN. *J. Geophys. Res.*, 105(D23):28943–28960.

Williams, J., Roberts, J. M., Fehsenfeld, F. C., Bertman, S. B., Buhr, M. P., Goldan, P. D., Hübler, G., Kuster, W. C., Ryerson, T. B., Trainer, M., and Young, V. (1997). Regional Ozone from Biogenic Hydrocarbons Deduced from Airborne Measurements of PAN, PPN, and MPAN. *Geophys. Res. Lett.*, 24:–.

Wofsy, S. C., Sachse, G. W., Gregory, G. L., Blake, D. R., Bradshaw, J. D., Sandholm, S. T., Singh, H. B., Barrick, J. A., Harriss, R. C., Talbot, R. W., Shipham, M. A., Browell, E. V., Jacob, D. J., and Logan, J. A. (1992). Atmospheric Chemistry in the Arctic and Subarctic: Influence of Natural Fires, Industrial Emissions, and Stratospheric Inputs. *J. Geophys. Res.*, 97(D15):16731–16746.

Wolfe, G. M., Thornton, J. A., McNeill, V. F., Jaffe, D. A., Reidmiller, D., Chand, D., Smith, J., Swartzendruber, P., Flocke, F., and Zheng, W. (2007). Influence of trans-Pacific pollution transport on acyl peroxy nitrate abundances and speciation at Mount Bachelor Observatory during INTEX-B. *Atmospheric Chemistry and Physics*, 7(20):5309–5325.

Wollny, A. (1998). Flugzeugmessungen atmosphärischer Spurengase mittels Ionen-Molekül-Reaktions-Massenspektrometrie: Methodische Untersuchungen zur Reaktionskinetik. Master's thesis, Universität Heidelberg.

Wotawa, G. and Trainer, M. (2000). The Influence of Canadian Forest Fires on Pollutant Concentrations in the United States. *Science*, 288(5464):324–328.

Wutz, M., Adam, H., and Walcher, W. (1988). *Theore und Praxis der Vakuumtechnik*. Friedr. Vieweg & Sohn, Braunschweig/Wiesbaden.

Yokelson, R. J., Griffith, D. W. T., and Ward, D. E. (1996). Open-path Fourier transform infrared studies of large-scale laboratory biomass fires. *J. Geophys. Res.*, 101(D15):21067–21080.

Zahn, A. and Brenninkmeijer, C. A. M. (2003). New Directions: A Chemical Tropopause Defined. *Atmospheric Environment*, 37(3):439 – 440.

Zahn, A., Brenninkmeijer, C. A. M., Maiss, M., Scharffe, D. H., Crutzen, P. J., Hermann, M., Heintzenberg, J., Wiedensohler, A., Güsten, H., Heinrich, G., Fischer, H., Cuijpers, J. W. M., and van Velthoven, P. F. J. (2000). Identification of extratropical two-way troposphere-stratosphere mixing based on CARIBIC measurements of O_3, CO, and ultrafine particles. *J. Geophys. Res.*, 105(D1):1527–1535.

Zhang, L., Jacob, D. J., Boersma, K. F., Jaffe, D. A., Olson, J. R., Bowman, K. W., Worden, J. R., Thompson, A. M., Avery, M. A., Cohen, R. C., Dibb, J. E., Flock, F. M., Fuelberg, H. E., Huey, L. G., McMillan, W. W., Singh, H. B., and Weinheimer, A. J. (2008). Transpacific transport of ozone pollution and the effect of recent Asian emission increases on air quality in North America: an integrated analysis using satellite, aircraft, ozonesonde, and surface observations. *Atmospheric Chemistry and Physics*, 8(20):6117–6136.

Zheng, W., Flocke, F. M., Tyndall, G. S., Swanson, A., Orlando, J. J., Roberts, J. M., Huey, L. G., and Tanner, D. J. (2011). Characterization of a thermal decomposition chemical ionization mass spectrometer for the measurement of peroxy acyl nitrates (PANs) in the atmosphere. *Atmospheric Chemistry and Physics*, 11(13):6529–6547.

Ziereis, H., Minikin, A., Schlager, H., Gayet, J. F., Auriol, F., Stock, P., Baehr, J., Petzold, A., Schumann, U., Weinheimer, A., Ridley, B., and Ström, J. (2004). Uptake of reactive nitrogen on cirrus cloud particles during inca. *Geophys. Res. Lett.*, 31:–.

Zöger, M., Afchine, A., Eicke, N., Gerhards, M.-T., Klein, E., McKenna, D. S., Mörschel, U., Schmidt, U., Tan, V., Tuitjer, F., Woyke, T., and Schiller, C. (1999). Fast in situ stratospheric hygrometers: A new family of balloon-borne and airborne Lyman-photofragment fluorescence hygrometers. *J. Geophys. Res.*, 104(D1):1807–1816.

Erklärung:

Ich versichere, dass ich vorliegende Arbeit selbständig verfasst und keine anderen als die angegebenen Quellen und Hilfsmittel benutzt habe.

Heidelberg, den 12.08.2011

Acknowledgement

I would like to thank Prof. Ulrich Platt for accepting to be the first referee of the present thesis. I´m especially thankful to the second referee of this work, Prof. Frank Arnold, for his valuable support in many aspects of this thesis. I enjoyed our many inspiring discussions about a series of different topics in the Munich "Mongdratzerl".

I would like to thank Dr. Hans Schlager and Prof. Ulrich Schumann for the opportunity to work at DLR-IPA in an exciting research field, and for providing excellent working conditions.

I gratefully thank the ion trapper Dr. Heinfried Aufmhoff for his valuable assistance in all sort of problems when using an ion trap, and for his helpful hands during GRACE! Many thanks go also to Paul Stock, especially for his support in the building of the PAN calibration source. This is also the place to acknowledge Michael Lichtenstern and Monika Scheibe for providing the trace gas measurements during GRACE.

I am very grateful to Dr. Heidi Huntrieser who always took the time to discuss about everything - be it photochemical or meteorological problems. I benefited also a lot from the experience of Dr. Andreas Minikin and Dr. Helmut Ziereis, who helped me "greenhorn" a lot in all scientific issues. Many thanks go in particular to Andreas Schäfler for his tireless efforts to familiarize me with WCBs. I greatly acknowledge Dr. Tina Jurkat for discussing many important topics - not only about mass spectrometry. I also want to thank Dr. Gebhard Günther, Dr. Harald Sodemann, Dr. Andreas Stohl and Dr. Owen Cooper for their endurance in discussing pollutant transport into the lowermost stratosphere: when, how and - why at all?

Many thanks go to Kathy Law and Antoine Auby for their support during my research stay at CNRS Paris. Merci Antoine pour de m´avoir instruire a CiTTyCat!

Thanks to the whole POLARCAT - GRACE team for wonderful moments in wonderful Greenland: I´ll never forget our barbecue at the icecap of Greenland, and certainly I´ll remember also our a never-ending bike tour with completely undamped "bikes".

I also would like to acknowledge all proof-readers of my thesis: Dr. Heidi Huntrieser, Dr. Tina Jurkat, Stefan Kaufmann, Dr. Andreas Minikin, Dr. Heinfried Aufmhoff, Dr. Helmut Ziereis and Anja Reiter! Thanks a lot also to all other IPA collegues for the nice working atmosphere: My roommate Greta Stratmann, Dr. Dominik Schäuble, Dr. Simon Unterstrasser and many others which I cannot all mention here.

Thanks also to all my friends, especially for understanding that I have sometimes strange working-times - although nobody of you understands what I´m exactly doing all the time (by the way, PAN is no dangerous germ!). I´m especially grateful to "*ma petite sourette*": Your dedication and confidence in me often has taken the load off my shoulder. Last but not least, I´d like to thank my mother - for nothing in special but for all in general.